Spin-photon interfaces enabled by Group-IV quantum memory in diamond and silicon color centers

Single Rubidium Atoms

顾 风磊
GU Fenglei

不知周之梦为胡蝶与，胡蝶之梦为周与?
(He could not tell whether Zhou was dreaming he was a butterfly, or whether the butterfly was dreaming it was Zhou.)
--庄周 (ZHUANG Zhou, c. 369–286 BCE)

Spin-photon interfaces Enabled by Group-IV-Vacancy Color Centers in Diamond and Single Rubidium Atoms

Dissertation

for the purpose of obtaining the degree of doctor
at Delft University of Technology
by the authority of the Rector Magnificus,
Prof. dr. ir. H. Bijl,
chair of the Board for Doctorates
to be defended publicly on
Wednesday 4th, March 2026 at 15:00 o'clock

by

Fenglei GU

This dissertation has been approved by the (co)promotors.

Composition of the doctoral committee:

Rector Magnificus,	chairperson
Prof. dr. ir. R. Hanson,	Delft University of Technology, *promotor*
Dr. V. V. Dobrovitski,	Delft University of Technology, *copromotor*
Dr. J. Borregaard	Harvard University, USA, *External adviser*

Independent members:

Prof. dr. S. Groeblacher	Delft University of Technology
Prof. dr. M. Blaauboer	Delft University of Technology
Prof. dr. Y. M. Blanter	Delft University of Technology
Prof. dr. N. T. Zinner,	Aarhus University, Denmark
Dr. ir. T. H. Taminiau,	Delft University of Technology, *reserve member*

Keywords: Spin-Photon interface, quantum communication, modular quantum computation, trapped Rb atom, Group-IV vacancy center, surface code
Printed by: Segers Printing House
Cover by: Fenglei Gu

ISBN/EAN: 978-94-6518-256-8

An electronic copy of this dissertation is available at
https://repository.tudelft.nl/.

CONTENTS

SUMMARY

Spin-photon interfaces play a crucial role in the realization of large-scale quantum computation and quantum communication. In this thesis, we investigate two types of spin-photon interfaces, Group-IV color centers in diamond and trapped Rubidium atoms, and evaluate their potential to enable long-distance quantum communication and modular quantum computation.

Group-IV vacancy color centers (G4V, or XV, where X = Si, Ge, Sn, Pb) in diamonds have recently emerged as promising candidates for quantum technologies. Compared to the widely studied nitrogen-vacancy (NV) center, they exhibit reversal symmetry, large ground-state splitting, and a high proportion of light emitted in the zero-phonon line (ZPL). These characteristics enhance robustness against charge noise and thermal excitations and improve the efficiency of coherent quantum light emission.

Leveraging the excellent spin-photon interface properties of XV centers, we explore their potential applications in long-distance quantum communication and modular quantum computing. Through analytical studies and numerical simulations, we find that when integrated with quantum dot photon emitters, a quantum secret key rate of 100 bit/s over 1000 km is achievable using near-term techniques (Ch. 2). Moreover, XV centers can be used to decompose a monolithic quantum chip into multiple modules connected via optical fibers. Our study shows that this modular architecture, based on a typical surface-code quantum error correction scheme, can tolerate single-qubit operation error rates below 0.4% (Ch. 3).

On the other side, trapped rubidium (Rb) atoms represent a unique spin-photon interface compatible with both visible and telecom-wavelength photons. We additionally explore a hybrid scheme combining Rb atoms with thulium (Tm)-doped crystal atomic frequency comb (AFC) quantum memories to enable long-distance quantum communication. We demonstrate that this approach can achieve an entanglement distribution rate of approximately 10 bits/s over a distance of 1000 km (Ch. 4) with minimal of Rb atoms.

In summary, the theoretical insights and schemes presented in this thesis highlight the versatility and potential of spin-photon interfaces based on XV centers and trapped Rubidium atoms. These results contribute to the advancement of practical, long-distance quantum communication and modular quantum computation.

SAMENVATTING

Spin-fotoninterfaces spelen een cruciale rol bij de realisatie van grootschalige kwantumcomputatie en kwantumcommunicatie. In dit proefschrift onderzoeken we twee types spin-fotoninterfaces: kleurcentra van groep IV in diamant en gevangen rubidiumatomen, en evalueren we hun potentieel om kwantumcommunicatie over lange afstanden en modulaire kwantumcomputatie mogelijk te maken.

Groep-IV-vacantiekleurcentra (G4V, of XV, waarbij X = Si, Ge, Sn, Pb) in diamant zijn recentelijk naar voren gekomen als veelbelovende kandidaten voor kwantumtechnologieën. In vergelijking met het veel bestudeerde stikstof-vacantiecentrum (NV-centrum) vertonen ze omkeersymmetrie, een grote splitsing van de grondtoestand en een hoog aandeel licht dat wordt uitgezonden in de zero-fononlijn (ZPL). Deze eigenschappen vergroten de robuustheid tegen ladingsruis en thermische excitatie, en verbeteren de efficiëntie van het uitzenden van coherent kwantumlicht.

Wij maken gebruik van de uitstekende spin-fotoninterface-eigenschappen van XV-centra om hun potentiële toepassingen in kwantumcommunicatie over lange afstanden en modulaire kwantumberekeningen te onderzoeken. Uit analytische studies en numerieke simulaties blijkt dat, wanneer ze worden geïntegreerd met fotonenemitters op basis van kwantumpunten, een kwantumgeheime-sleutelsnelheid van 10 bit/s over een afstand van 1000km haalbaar is met behulp van de korte termijn technieken (Hoofdstuk 2). Bovendien kunnen XV-centra worden gebruikt om een monolithische kwantumchip op te splitsen in meerdere modules die verbonden zijn via optische vezels. Onze studie toont aan dat deze modulaire architectuur, gebaseerd op een typisch surface-code kwantumfoutcorrectieschema, foutpercentages voor enkelqubitbewerkingen tot onder 0,4% kan verdragen (Hoofdstuk 3).

Aan de andere kant vertegenwoordigen gevangen rubidium (Rb)-atomen een unieke spin-fotoninterface die compatibel is met zowel zichtbare als telecom-golflengtefotonen. We onderzoeken bovendien een hybride schema waarin Rb-atomen worden gecombineerd met thulium (Tm)- gedoteerde kristallen die functioneren als een atomaire frequentiekam (AFC)-kwantumgeheugen, om kwantumcommunicatie over lange afstanden mogelijk te maken. We tonen aan dat met deze aanpak een verstrengelingsverdelingssnelheid van ongeveer 10 bits/s over een afstand van 1000 km (Ch. 4) kan worden bereikt met minimale Rb-atomen.

Samenvattend benadrukken de theoretische inzichten en schema's die

in dit proefschrift worden gepresenteerd de veelzijdigheid en het potentieel van spin-fotoninterfaces gebaseerd op XV-centra en gevangen rubidiumatomen. Deze resultaten dragen bij aan de ontwikkeling van praktische kwantumcommunicatie over lange afstanden en modulaire kwantumcomputatie.

1

INTRODUCTION

欲穷千里目，更上一层楼。 *(To see as far as a thousand miles, one must climb one level higher.)*

–王之涣(WANG Zhihuan, c. 688–742 CE)

Artificial intelligence (AI) and quantum technologies represent two of the most significant technological paradigm shifts of the 21st century. While AI has demonstrated remarkable success through revolutionary tools such as Midjourney and ChatGPT, quantum technologies still face substantial challenges, primarily in error control and scalability. This thesis outlines several promising paths to overcome these issues by leveraging efficient spin-photon interfaces, wherein photons serve multiple purposes: first, as a detection mechanism to identify erroneous qubits; second, as a medium to establish distant entanglement and realize multiple qubit operations; and third, as a means of achieving massive multiplexing due to their abundant availability. These capabilities foster large-scale quantum computing through modularization and support long-distance quantum communication.

1

The early 21st century has witnessed the emergence of two transformative technologies: artificial intelligence (AI) and quantum technology. In March 2016, Google DeepMind's AlphaGo system reached a historic milestone by defeating the world-renowned Go player Lee Sedol, marking the first time a computer had bested a human champion in one of the world's most complex board games. In 2022, Midjourney gained prominence for generating highly creative and often photorealistic images, showcasing AI's growing potential in artistic and visual domains. Later that year, OpenAI's ChatGPT revolutionized conversational AI, engaging in human-like interactions and demonstrating sophisticated language understanding and reasoning. These advances have profoundly shaped research directions, industrial practices, and the ways we produce and consume information, making AI an integral part of modern life.

In retrospect, it took 75 years for these revolutionary technologies to materialize after the AI pioneer Alan Turing posed the initial question, 'Can machines think?' in 1950. In contrast, it has been 100 years since Werner Heisenberg, Max Born, and Pascual Jordan developed matrix mechanics, and Erwin Schrödinger introduced wave mechanics and the non-relativistic Schrödinger equation in 1925, marking the birth of modern quantum mechanics. Since then, quantum technology has steadily advanced, giving rise to various platforms, including optics (photons), superconducting circuits, trapped neutral atoms, trapped ions, crystal defects, and quantum dots. Each platform has achieved significant breakthroughs in applications such as quantum computing, quantum communication, quantum sensing, and quantum simulations. The past decade has witnessed groundbreaking advancements, with two remarkable milestones standing out. The first is the launch of the Micius satellite in 2016, which successfully demonstrated quantum key distribution for secure communication and quantum teleportation over a distance of 1200 km [1–3]. The second is the presentation of Google's Willow quantum chip in 2024, which showcased the capability to execute error correction on quantum bits (qubits) [4], a critical step toward realizing general quantum computation. Nowadays, nearly every nation is investing heavily in quantum technologies, and the United Nations General Assembly has declared 2025 the International Year of Quantum Science and Technology (IYQ) to raise public awareness of the profound importance and impact of quantum science and its applications across all aspects of life. The revolutionary moment of the quantum technology revolution is eagerly anticipated.

Despite these remarkable advancements, practical universal quantum computing and a cost-effective, high-rate quantum internet spanning continental distances remain elusive. Quantum computing faces significant challenges in error mitigation and scalability, while quantum communication grapples with photon loss and decoherence. A robust

spin-photon interface is pivotal in addressing these obstacles. In quantum computing, photons provide a means to detect erroneous qubits, support long-distance interactions, and facilitate the development of large-scale quantum processors. In quantum communication, photons and quantum memories are essential for long-distance entanglement distribution. Therefore, fast and reliable spin-photon interfaces are critical for progress in both domains.

This thesis explores two promising spin-photon interfaces: Group-IV vacancy (XV, where X=Si, Ge, Sn, Pb) color centers in diamond and trapped Rubidium (Rb) atoms. XV centers can couple to photons in the visible-light spectrum and exhibit strong robustness to charge noise and thermalization. Notably, they emit photons from direct transitions between electronic orbital levels—without involving any phonons—with a probability of 40–70%[5–7], representing a significant improvement over the widely studied nitrogen-vacancy (NV) center, which achieves only 3%[8]. This work develops protocols that leverage XV centers for quantum communication (Ch. 2) and modular quantum computing (Ch. 3).

Trapped rubidium (Rb) atoms, on the other hand, can emit photons at both telecom and visible wavelengths, making them compatible with ensemble-based and multiplexed quantum memories and optical fibers for transmission, thereby eliminating the need for frequency conversion. Combined with thulium-doped crystal quantum memories serving as photon buffers, this thesis demonstrates how single Rb atoms are harnessed to generate entangled photons at the two wavelengths, enabling long-distance (~ 1000 km) quantum communication (Ch. 4).

Together, these contributions advance the practical utility of spin-photon interfaces, bringing us closer to scalable quantum computing architectures and effective global quantum communication networks.

1.1. DOCUMENT STRUCTURE

This thesis is structured as follows:

- Chapter 2 demonstrates the suitability of XV centers for long-distance quantum communication. In this chapter, incorporating the quantum-dot photon emitter, we develop a protocol for realizing a quantum repeater chain and predict a 100 bit/s quantum secret key rate over 1000 km based on near-term technologies.

- Chapter 3 explores a promising application of the XV center in modularizing a monolithic quantum chip, which helps scale up quantum computing. The chapter presents a proposed method to realize the surface code, a standard quantum error correction code, in a modularized architecture, providing simulations showing that

the modularized surface code can efficiently tolerate single-qubit gate error up to 0.4%, comparable to the monolithic case.

- Chapter 4 introduces another spin-photon interface enabled by the trapped rubidium (Rb) atom possessing a distinctive ability to be compatible with both the visible-light and telecommunications spectra. There, we show, incorporating the Tm-doped atomic frequency comb (AFC) quantum memory, how a quantum repeater chain can be realized, reaching a quantum secret key rate of 10 bit/s over a distance of 1000 km with minimal Rb atoms.

REFERENCES

[1] S.-K. Liao, W.-Q. Cai, W.-Y. Liu, L. Zhang, Y. Li, J.-G. Ren, J. Yin, Q. Shen, Y. Cao, Z.-P. Li, *et al.* “Satellite-to-ground quantum key distribution”. In: *Nature* 549.7670 (2017), pp. 43–47.

[2] J.-G. Ren, P. Xu, H.-L. Yong, L. Zhang, S.-K. Liao, J. Yin, W.-Y. Liu, W.-Q. Cai, M. Yang, L. Li, *et al.* “Ground-to-satellite quantum teleportation”. In: *Nature* 549.7670 (2017), pp. 70–73.

[3] C.-Y. Lu, Y. Cao, C.-Z. Peng, and J.-W. Pan. “Micius quantum experiments in space”. In: *Reviews of Modern Physics* 94.3 (2022), p. 035001.

[4] D. Castelvecchi. “’A truly remarkable breakthrough’: Google’s new quantum chip achieves accuracy milestone”. In: *Nature* ().

[5] A. Gorokhovsky, A. Turukhin, R. Alfano, and W. Phillips. “Photoluminescence vibrational structure of Si center in chemical-vapor deposited diamond”. In: *Applied physics letters* 66.1 (1995), pp. 43–45.

[6] Y. N. Palyanov, I. N. Kupriyanov, Y. M. Borzdov, and N. V. Surovtsev. “Germanium: a new catalyst for diamond synthesis and a new optically active impurity in diamond”. In: *Scientific reports* 5.1 (2015), p. 14789.

[7] J. Görlitz, D. Herrmann, G. Thiering, P. Fuchs, M. Gandil, T. Iwasaki, T. Taniguchi, M. Kieschnick, J. Meijer, M. Hatano, *et al.* “Spectroscopic investigations of negatively charged tin-vacancy centres in diamond”. In: *New Journal of Physics* 22.1 (2020), p. 013048.

[8] D. Riedel, I. Söllner, B. J. Shields, S. Starosielec, P. Appel, E. Neu, P. Maletinsky, and R. J. Warburton. “Deterministic enhancement of coherent photon generation from a nitrogen-vacancy center in ultrapure diamond”. In: *Physical Review X* 7.3 (2017), p. 031040.

2

HYBRID QUANTUM REPEATER CHAINS WITH SEMICONDUCTOR QUANTUM DOTS AND GROUP-IV COLOR CENTERS IN DIAMOND

Yannick Strocka*, Fenglei Gu*, Gregor Pieplow, Johannes Borregaard, Tim Schröder

身无彩凤双飞翼，心有灵犀一点通 *(Though we lack the paired wings of the jeweled phoenix to fly across great distances, our hearts remain linked by a shared, intuitive bond.)*

–李商隐(LI Shangyin, c. 813–858 CE)

*These authors contributed equally to this work. Y.S. made imperfect bandwidth-matching-related derivations and simulations. F.G. provided analysis for the performance of the repeater chain. G.P., J.B., and T.S. developed the idea and supervised the project. All authors contributed to writing the manuscript.

2

We propose and analyze a hybrid quantum repeater architecture that combines two leading hardware platforms: quantum dots (QDs) as bright, deterministic sources of entangled photon pairs and group-IV-vacancy centers in diamond as efficient, heralded quantum memories. This combination leverages high-rate entanglement generation together with long-lived storage, enabling scalable entanglement distribution over long distances. A key challenge is the large bandwidth mismatch between QD photons and the narrow optical transitions of the memories. We combine a comprehensive model of the spin-photon interface, including full spin-photon coupling dynamics, and explore mitigation strategies such as frequency filtering and optimized magnetic-field orientation. Our results show that with optimized designs, photon-to-memory transfer can be achieved with high efficiency and fidelity, supporting the feasibility of such hybrid systems. Finally, we analyze a full repeater chain using experimentally achievable parameters and find that a network with thousands of memories across several repeater nodes could achieve a secret-key rate of 500 *bit/s over* 1,000 *km, demonstrating the strong potential of this approach for next-generation quantum networks.*

2.1. INTRODUCTION

Quantum networks [1–6] capable of distributing high-fidelity entanglement are essential for applications such as distributed quantum sensing [7–10], secure communication [11–13], and networking of quantum computers [14, 15]. A major challenge for the construction of extended quantum networks is photon loss in optical fibers: 99% of photons are lost over every 100 km of transmission [16]. Since quantum states cannot be amplified like classical signals [17], quantum repeaters [18] are required to extend entanglement over continental distances.

A variety of hardware platforms have been explored for quantum repeaters, including atomic ensembles [19], trapped ions [20], solid-state defect centers [21], and semiconductor quantum dots [22]. Each offers distinct strengths: quantum dots (QDs) can generate entangled photons at high rates with excellent fidelity [23], while group-IV-vacancy (G4V) centers in diamond provide long-lived, optically addressable spins for efficient and heralded photon storage [24, 25]. These complementary capabilities naturally motivate hybrid repeater architectures that combine the best features of different hardware systems.

Here, we propose and analyze such a hybrid scheme, integrating QDs as entangled photon-pair sources with G4V centers as efficient single-spin memories. A key challenge is the bandwidth mismatch: QDs emit photons with ∼10 GHz bandwidths [23, 26, 27], while G4Vs have narrow optical transitions of order 100 MHz [28, 29]. To address this challenge, we use a comprehensive model in [30] of the cavity-mediated spin–photon interaction that includes polarization effects, magnetic-field-induced level splitting, and cross-talk between transitions. Having expanded beyond more simplified models [31], our approach enables the identification of practical mitigation strategies and provides a realistic assessment of their effectiveness. In particular, we investigate techniques such as frequency filtering and magnetic-field optimization to determine the conditions under which efficient, high-fidelity photon storage can be achieved.

Building on this, we evaluate the performance of a full repeater chain with entanglement distillation using an operational protocol based on BB84 quantum key distribution [32]. Our results show that a network with thousands of G4V memories across multiple nodes can reach secret-key rates on the order of hundreds to thousands of bits per second over continental distances. This demonstrates the strong potential of this hybrid QD–G4V platform as a path toward scalable long-distance quantum networks.

The remainder of this paper is organized as follows: Sec. 2.2 introduces the operating principles of the scheme, Sec. 2.3 presents the photon-cavity-G4V model, Sec. 2.4 evaluates repeater chain performance, and

Sec. 2.5 concludes with a discussion of future directions.

2.2. HARDWARE IMPLEMENTATION

The hybrid repeater chain protocol is illustrated in Fig. 2.1. The two end nodes, Alice and Bob, are separated by a large distance. The repeater nodes divide the total distance into multiple segments, each containing a QD emitter in the middle for sending photons to the two neighboring nodes. Each repeater node contains two memory modules, one of each segment. Depending on whether entanglement distillation is applied, the end node contains one or no memory modules. When there is no entanglement distillation, the received photons are directly measured, hence no quantum memories at the end nodes are required. Each memory module contains multiple memory cells, each of which contains a G4V electron spin serving as the communication qubit and a nuclear spin, *e.g.*, ^{13}C [35, 36], ^{29}Si [37], ^{117}Sn [38], or ^{119}Sn, serving as the storage qubit. Here, the G4V electron spin refers to the collection of electrons in the unsaturated covalent bonds [39, 40]. It is effectively equivalent to a hole with spin-$\frac{1}{2}$.

Our two-way repeater chain protocol consists of three key operations: elementary link establishment, entanglement distillation [33, 41–44], and entanglement swapping [19, 45]. Elementary link establishment generates entanglement between neighboring nodes separated by a short distance. Entanglement distillation enhances the fidelity of Bell pairs at the cost of consuming multiple pairs. Two possibilities, entanglement distillation for the elementary links and the end-to-end links, are examined in this work. Entanglement swapping extends entanglement by merging two adjacent links into a longer one. We describe these three operations in detail below.

2.2.1. ELEMENTARY-LINK ESTABLISHMENT

The operation of elementary link establishment contains four steps: entangled photon pair generation, photon transmission, quantum information transfer, and photon-reception heralding. The concrete protocol is illustrated in Fig. 2.2a.

The quantum dot (QD) generates entangled photon pairs with polarization correlations [23, 46–50]. Photon absorption and emission in the QD correspond to an electron transitioning between the conduction and valence bands. As a result, the four lowest-energy quantum states of the QD are: the ground state $|0\rangle$, the two single-exciton states $|X\rangle$ and $|X'\rangle$ of opposite spin orientations, and the biexciton state $|XX\rangle$, as illustrated in Fig. 2.3a. Under suitable laser irradiation, the QD is initialized in the biexciton state $|XX\rangle$. From this state, it can decay via two possible cascaded paths: $|XX\rangle \to |X\rangle \to |0\rangle$ and $|XX\rangle \to |X'\rangle \to |0\rangle$.

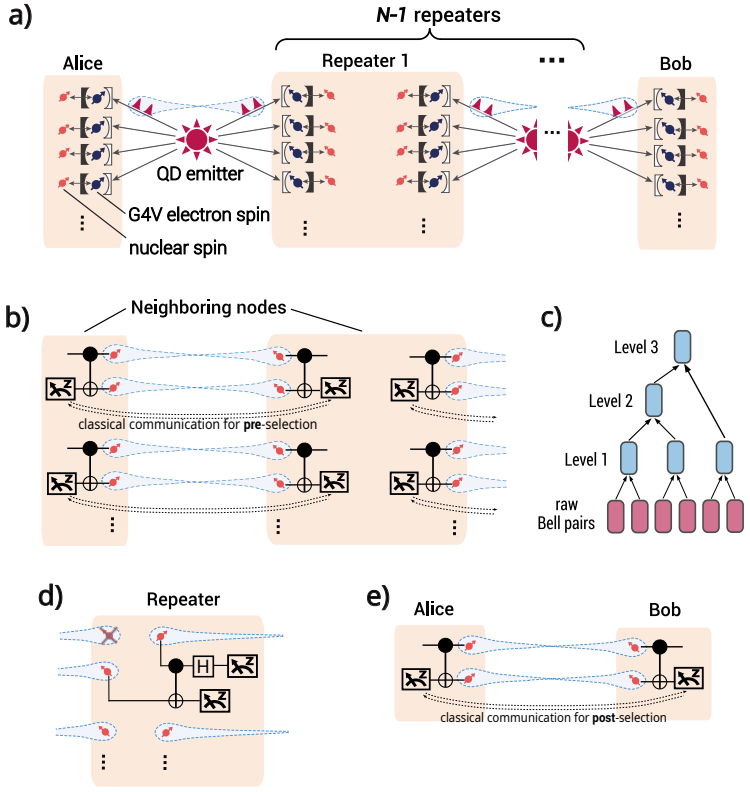

Figure 2.1.: QD-G4V hybrid repeater chain protocol. **a)** Elementary-link establishment. The chain consists of two end nodes, Alice and Bob, and $N-1$ intermediate repeater nodes, each represented by an orange rectangle color block. QD emitters (red stars) are positioned midway between neighboring nodes and distribute entangled photons (red bell shapes) between them. In each node, G4V electron spins (dark blue) serve as interfaces for loading qubits from the incoming entangled photons, while nuclear spins (orange) provide long-term qubit storage. **b)** The fundamental operations of the elementary-link entanglement distillation. They involve local nucleus-nucleus cnot gates and qubit measurement and classical communications between the two nodes. **c)** The entanglement distillation protocol following Ref. [33]. It has four options: level-0: using directly the raw Bell pairs; level-1, -2, and -3: each distilled Bell pair is made up from 2, 4, and 6 raw ones, respectively. Single-qubit gates (not shown) are applied before the level-2 and -3 distillations. **d)** Entanglement swapping. It contains a cnot gate between the two nuclear spins from different memory modules in a repeater node, followed by a Hadamard gate and qubit measurements. **e)** The end-to-end entanglement distillation is similar to the elementary-link distillation, except that, due to its time-consuming nature, classical communication is employed for post-selection rather than as a precondition in the level-2 and level-3 operations.

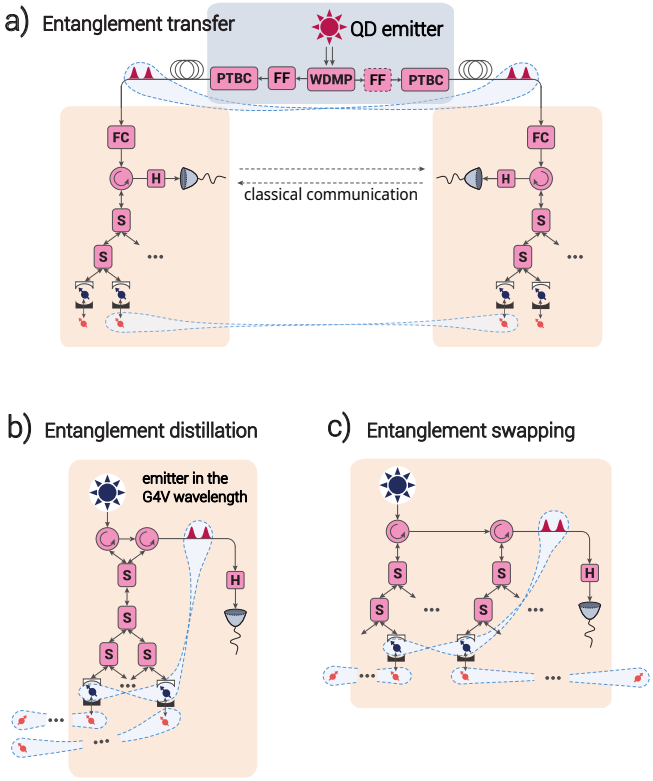

Figure 2.2.: Optical circuits for the repeater-chain operations. **a)** Entanglement transfer from the photons to the nuclear spins as in the elementary-link establishment step. QDs emit frequency-distinct, polarization-entangled photon pairs, which are separated by a wavelength-division multiplexer (WDMP). Frequency filters (FFs) are used on one side or both for narrowing the bandwidth of the photon(s) in a Bell pair. Polarization-to-time-bin converters (PTBCs), implemented with polarizing beam splitters, encode polarization qubits into time-bin qubits for fiber transmission. At each repeater node, frequency converters (FCs) shift photons from telecommunication to visible wavelengths for G4V compatibility. Optical switches (S) direct photons to designated memory cells. Through controlled photon–spin interactions and subsequent photon detection, the photon qubit is mapped onto a G4V electron spin (dark blue) and then transferred to a nuclear spin (orange). Successful detection heralds photon receipt, which is confirmed via classical communication between nodes. **b)** and **c)** Optical circuit for the local nucleus-nucleus cont gates in the entanglement distillation and swapping steps, respectively. A single photon source (implemented with a separate G4V [34]) generates a photon, which is guided by circulators and optical switches (S). It interacts sequentially with two target G4V electron spins until heralded photon measurements confirm entanglement between them. Nucleus–nucleus cnot gates are then realized using local electron–nuclear gates.

The first (second) path produces two vertically (horizontally) polarized photons of different frequencies.

Here, we consider the ideal case where the intermediate states $|X\rangle$ and $|X'\rangle$ are energetically degenerate, making the two decay paths indistinguishable by photon frequencies. This results in the generation of a maximally entangled polarization Bell-state:

$$|\psi_{QD}\rangle = \frac{1}{\sqrt{2}}\left(|HH'\rangle + |VV'\rangle\right), \tag{2.1}$$

where $|H\rangle$ and $|V\rangle$ denote the horizontally and vertically polarized photon states, respectively, and the presence and absence of the prime symbol denote different frequencies. We assume QD photon wavelengths in the telecom spectral range.

The two emitted photons have different frequencies and can thus be separated using a wavelength-division multiplexer (WDMP) [51] and be directed to the two different nodes of the segment. To mitigate polarization instability during fiber transmission, before transmission, a polarization-to-time-bin converter (PTBC) [52] is used to convert the polarization states $|H\rangle$ and $|V\rangle$ ($|H'\rangle$ and $|V'\rangle$) into early and late time-bin states $|E\rangle$ and $|L\rangle$ ($|E'\rangle$ and $|L'\rangle$), respectively.

After the polarization-to-time-bin conversion, the two photons will be sent to the two nodes adjacent to the QD emitter, respectively. When a photon arrives at a repeater node, a frequency converter [53] shifts its frequency from the telecom band to the frequency of the G4V spin-photon interface in the visible light regime. The photon is then routed to a designated memory cell by an optical switching network. Through a tailored interaction between the photon and the target G4V electron spin [6, 54], the quantum information (qubit) carried by the photon is transferred to the electron spin. This interaction is discussed in detail further down.

Photons experience significant loss during transmission through optical fibers and on-chip circuits. Therefore, heralding their successful arrival is essential for identifying the memory cells that have been successfully entangled and are ready for the subsequent operation of entanglement swapping. At each repeater node, local heralding is achieved by measuring the photon in the X-basis, $|\pm\rangle = \frac{1}{\sqrt{2}}(|E\rangle \pm |L\rangle)$, after the quantum state transfer operation [6, 54], i.e. the interaction between the photon and the target electron spin. Moreover, a successfully transferred qubit is further transferred to a nuclear spin via an electron-nuclear entanglement gate [36] for long-time storage. Lastly, to determine whether the other photon of the same pair has also been received at the opposite node, classical communication between the two nodes is required to exchange heralding signals.

2.2.2. ENTANGLEMENT DISTILLATION AND SWAPPING

We examine the possibilities to apply entanglement distillations for the elementary entanglement links and the end-to-end links as shown in Fig. 2.1b and e. The distillation protocol we adopted is presented in Ref. [33]. It introduces three levels of purification. By applying single-qubit rotations, different error types in the entangled state are corrected at successive levels. A level-1, -2, and -3 distilled Bell pair requires at least two, four, and six raw Bell pairs, respectively, as shown in Fig. 2.1c. The basic operation in this scheme is the fusion of two Bell pairs into one. Firstly, two pairs of remotely entangled qubits are established between two nodes. Then a cnot gate is implemented locally at each node.

A direct nuclear-nuclear cnot gate could be implemented if both spins belong to the same crystal and are coupled to a comon G4V center [55]. However, due to extensive optical multiplexing requirement, we consider the local nuclear-nuclear cnot gates mediated by the two G4V electron spins and additional photons. The reason is as follows. While coupling to tens of ^{13}C spins has been demonstrated in NV centers [35], high-fidelity operations are typically feasible only with a small subset of strongly coupled spins. Moreover, because G4V centers exhibit long reset times and slower G4V–^{13}C gates compared to fast quantum dot emitters, hundreds of G4Vs are required for sufficient multiplexing. Thus, the probability that two targeted spins reside at the same site is low, making inter-G4V operations necessary for scalable architectures. We therefore focus on on a scenario where each nuclear spin is hosted by a separate G4V.

A schematic optical circuit for the fusion operation is shown in Fig. 2.2b. The procedure consists of two steps. First, entanglement is generated between the two electron spins [56]. This step can be retried until either success or a maximum number of attempts is reached. A cap in the number of attempts ensures synchronization across the repeater chain and limits decoherence in the nuclear memory. In each attempt, a single photon—emitted by a G4V source or another compatible emitter—is prepared as a time-bin qubit and routed through an optical circuit containing two circulators. The photon sequentially interacts with the electron spins of both G4V-memories before being measured in the X basis. Successful detection heralds entanglement between the electron spins. If no heralding event is observed, the G4Vs are re-initialized while the nuclear spin states remain preserved.

Once entanglement between two electron spins is established, the second step performs local Bell-state measurements between each electron and its adjacent nuclear spin. These measurements, enabled by electron–nuclear entangling gates, realize a near-deterministic cnot gate between the two nuclear spins [36].

Before advancing to the second and third levels of distillation, classical

communication is used to verify the success of the preceding step. Over long distances, however, the communication delay can cause significant decoherence in the quantum states. For the final distillation between Alice and Bob, we therefore consider a post-selection procedure to minimize the the decoherence errors. In this case, the distillation procedure continues without waiting for confirmation from the other node about the success of the measurement. Since Alice and Bob will ultimately measure their qubits to distill a secret key, they can post-select which of the measurements were successful at the end and thereby minimize the effect of decoherence errors.

Entanglement swapping is realized by performing a Bell-state measurement (BSM) on two selected nuclear spins within a repeater node, each already entangled with a remote node, as shown in Fig. 2.1d. In this setting, the BSM between the two nuclear spins again relies on a cnot gate, implemented by the method described above. The relevant optical circuit is similar and shown in Fig. 2.2c.

2.3. SYSTEM COMPATIBILITY

Compatibility between the QD photon emitter and the G4V single-spin quantum memory is a central challenge in our protocol. While the central frequencies of the two systems can be aligned using frequency converters, matching their bandwidths and lineshapes remains a formidable task. The QD emitter has a natural lifetime of 125–250 ps [23], corresponding to a bandwidth on the order of 10 GHz. In contrast, the G4V spin has a natural lifetime of 1.7–4.5 ns [29], implying a bandwidth on the order of 100 MHz—only about 1% of that of the QD. This mismatch implies that the G4V would fail to interact efficiently with approximately 99% of the QD-emitted photons. Nevertheless, this issue can be mitigated by coupling the G4V and the broadband photon via an intermediate cavity with an optimized total energy decay rate and central mode frequency relative to the G4V transition [31].

Following a decay cascade from the biexcitation state to the ground state, the experimentally investgated QD considered here emits two photons with Lorentzian spectral profiles [57] and bandwidths $\gamma_{XX} = 8.33$ GHz and $\gamma_X = 4.34$ GHz, respectively [23], as shown in Fig. 2.3(b). Each photon can optionally pass through a Fabry–Perot interferometer for frequency filtering [58] (see App. A.4.4 for details) and is routed to one of the two adjacent nodes containing a G4V spin, thereby distributing entanglement. Since the two photons have different bandwidths, using two distinct cavities optimized for each photon would yield the best performance. However, for simplicity and practical implementation, we adopt a symmetric design for both cavities, balancing system complexity and performance. As a result, only three

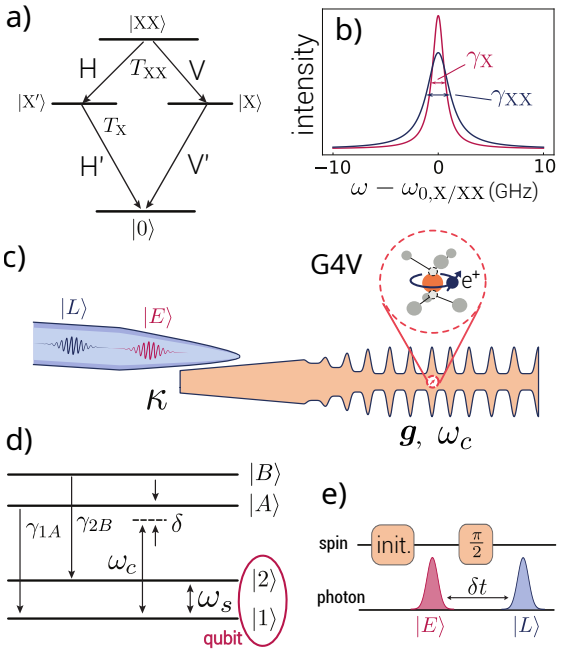

Figure 2.3.: QD and G4V hardware profiles. **a)** Energy levels and decay paths of a quantum dot (QD). The QD includes a ground state $|0\rangle$, two approximately degenerate single-excitation states, $|X\rangle$ and $|X'\rangle$, and a biexcitation state, $|XX\rangle$, which together give rise to two cascade decay paths. The decay times T_X and T_{XX} of the single- and biexcitation states correspond to linewidths γ_X and γ_{XX}, respectively. Photons are emitted with horizontal (H) or vertical (V) polarization, depending on the decay path; the presence or absence of a prime symbol for the labels H and V denotes different photon frequencies. **b)** Frequency profile of photons emitted by the QD. According to the experiment presented in [23], the photons from both $|XX\rangle$, $|X\rangle$ and $|X'\rangle$ exhibit Lorentzian spectral profiles centered at $\omega_{0,X}$ and $\omega_{0,XX}$, with bandwidths $\gamma_{XX} = 8.33$ GHz and $\gamma_X = 4.34$ GHz, respectively. **c)** Fiber–cavity interface and integration of a group-IV-vacancy color center (G4V) into the sawfish nanophotonic crystal cavity [29]. The incoming photon from the fiber is in a superposition of early and late time-bin states, encoding a qubit. The cavity supports a single optical mode with resonance frequency ω_c, coupling strength $\boldsymbol{g} = [g_{1A}, g_{2B}, g_{2A}, g_{1B}]$ to the G4V, and a total loss rate κ. **d)** Energy levels of the G4V center (SiV or SnV), modeled as a four-level system with ground states $|1\rangle$ and $|2\rangle$ and excited states $|A\rangle$ and $|B\rangle$. The optical transitions $|1\rangle \leftrightarrow |A\rangle$ and $|2\rangle \leftrightarrow |B\rangle$ have linewidths γ_{1A} and γ_{2B}, respectively. The cavity resonance ω_c is detuned by δ from the $|1\rangle \leftrightarrow |A\rangle$ transition. The ground-states $|1\rangle$ and $|2\rangle$ circled by the orange line make up the qubit of the G4V spin, whose splitting is denoted as ω_s. **e)** Operational sequence for implementing the spin–photon entanglement gate via the reflection-based scheme (see App. A.1). The protocol consists of four steps: (1) initialize the G4V spin in state $|1\rangle$; (2) scatter the early time-bin photon; (3) apply a $\pi/2$ rotation around the y−axis to the spin; (4) scatter the late time-bin photon. Fig. e) is adapted from [54].

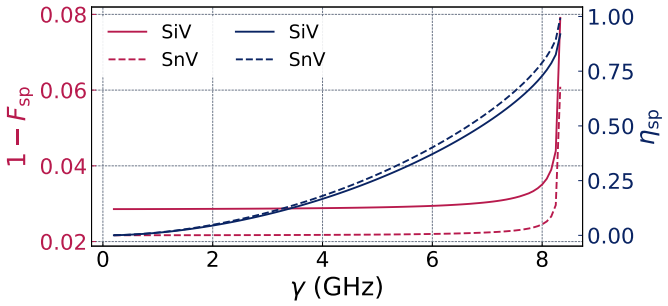

Figure 2.4.: Infidelity $1-F_{sp}$ and efficiency η_{sp} of the spin-spin entangled state as a function of the filtered bandwidth $\gamma := \tilde{\gamma}_{XX}$ while keeping $\gamma_X = 4.34$ GHz the same. The relevant parameters for both the SiV and SnV are shown in Tab. A.1 in App. A.4.2.

parameters require optimization: the photon central frequency ω_0 (as targeted by the frequency converters), the cavity resonance frequency ω_c, and the cavity loss rate κ.

Because the challenge of low success probability of entanglement transfer, mainly caused by photon loss during fiber transmission and local optical circuits, is addressed through multiplexing, quantum state and gate fidelities become the dominant factor limiting repeater performance. Therefore, our objective is to maximize the fidelity of the resulting G4V spin-spin state relative to the raw G4V electron-electron Bell-state, $|\text{Bell}\rangle = \frac{1}{\sqrt{2}}(|11\rangle + |22\rangle)$, where $|ij\rangle$ $(i,j \in \{1,2\})$ is the quantum state where the left(right) G4V electron in an elementary link is in the $|i(j)\rangle$ state. This leads to the objective function [59]

$$F_{sp} = \langle \text{Bell}| \rho_{sp} |\text{Bell}\rangle \tag{2.2}$$

where ρ_{sp} denotes the density matrix of the quantum state of the two G4V spins.

To examine the quantum state transfer from one of the two photons in the pair to the G4V spin, we consider the setup shown in Fig. 2.3(c). Via the polarization to time-bin converter, the photonic qubit is encoded in early and late time bins. The photon is guided through a fiber into a single-sided, overcoupled nanophotonic crystal cavity [29], where it interacts with the G4V spin. After interaction, the photon is reflected back into the fiber and directed to a measurement device. In the simplest case spin-photon entanglement succeeds when the phase contrast fulfills $\Delta\phi(\omega) := \phi_1(\omega) - \phi_2(\omega) = \pi$ on a frequency range around the central frequency of the incoming photon where the expressions ϕ_i are the phases of the reflected photon when the spin is initialized in $|i\rangle$ for $i = 1, 2$. The phase contrast $\Delta\phi$ is determined by the optical splitting

$\Delta\omega_s$ of the G4V, which corresponds to the energy difference between the optical transitions connecting the excited states $|A\rangle$ and $|B\rangle$, and the ground states $|1\rangle$ and $|2\rangle$.

Four G4V energy levels are relevant for spin-photon interaction: two spin states in the ground state manifold, $|1\rangle$ and $|2\rangle$, and the other two in the excited state manifold, $|A\rangle$ and $|B\rangle$, as shown in Fig. 2.3(d). Their level splittings depend on the applied magnetic field and local strain. The spin qubit is encoded in $|1\rangle$ and $|2\rangle$, and optical transitions occur between the ground- and excited state manifolds. Of the four allowed transitions, those connecting $|1\rangle \leftrightarrow |A\rangle$ and $|2\rangle \leftrightarrow |B\rangle$ dominate due to favorable dipole strengths and selection rules.

We operate in the weak-driving regime, where the product of the photon's electric field amplitude and the G4V transition dipole moments is much weaker than the spin's optical decay rates $\{\gamma_{1A}, \gamma_{2B}\}$. In this regime, the photon induces no population transfer but imparts a conditional phase on the spin qubit, implementing a photon-induced phase gate [30].

Since spectrally degenerate photons are resonant with only one of the optical transitions, simply applying identical phase gates to both time bins would not generate entanglement. However, entanglement can still be created by inserting a spin rotation between the two photon arrivals [see Fig. 2.3(e)], provided that the spin rotation does not commute with the phase gates [54, 60]. Here, we consider a $\pi/2$ rotation around the $y-$axis acting on the G4V spin, which can be implemented via a microwave pulse [61] with an error rate below 10^{-4} [62]. Following a projective measurement of the photonic qubit, the photonic state is effectively transferred to the spin. Details are provided in App. A.1.

When evaluating the objective function in Eq. (2.2), we account for the broadband nature of the QD photons. A detailed analysis of the associated effects is presented in App. A.2. To enhance the frequency contrast between the $|1\rangle \leftrightarrow |A\rangle$ and $|2\rangle \leftrightarrow |B\rangle$ transitions, we apply an off-axis 1 T magnetic field to both the SiV and SnV centers, which we investigate as light and heavy representatives of G4V, respectively. In addition, a compressive strain of $E_x = 5.38 \cdot 10^{-5}$, perpendicular to the G4V symmetry axis, is applied to the SiV but not the SnV as an outcome of parameter optimization [61] (see App. A.4.1 for details). As the angle between the magnetic field and the symmetry axis increases, the spectral contrast between the intended transitions improves, leading to better performance. However, this also increases cross-coupling, the unintended coupling between transitions $|1\rangle \leftrightarrow |B\rangle, |2\rangle \leftrightarrow |A\rangle$, which introduces nonlinearities in the system's equations of motion. These are included in our modeling and additionally utilized to minimize entanglement infidelities (see App. A.4.2). Such cross-coupling terms that have not been addressed yet for G4Vs.

We determine optimal magnetic field orientations for both SiV and

SnV subject to the given conditions and utilize crosstalk to minimize the spin-spin entanglement infidelity using state-of-the-art optimization techniques for the rates $\gamma_X = 4.34$ GHz and $\gamma_{XX} = 8.33$ GHz (see App. A.4.2). Assuming a perfect photonic Bell state and no filtering, the resulting minimum infidelity and success probability for the SiV are $1 - F_{\mathrm{sp,SiV}} = 7.91 \cdot 10^{-2}$ and $\eta_{\mathrm{sp,SiV}} = 0.9187$, achieved by a SiV-cooperativity $C_{\mathrm{SiV}} = g_{1A}^2/(2\gamma_{1A}\kappa)\big|_{\mathrm{SiV}} \approx 11$ (see App. A.4.2 for the optimized parameters). However, the spin splitting for the considered magnetic field configuration is $\omega_s \approx 26$ GHz, which is challenging to address using microwave spin control. To address realistic parameters, we also consider a magnetic field strength that produces a spin splitting closer to the experimentally achieved value [62]. We choose $B = 0.3$ T yielding $\omega_s \approx 8$ GHz. One limitation of the reduced magnetic field strength is a reduction of the maximum feasible bandwidth of the QD photons.

To investigate the influence of the photon bandwidths, we use the achievable $1 - F_{\mathrm{sp,SiV}} = 7.91 \cdot 10^{-2}$ as reference value and optimize for bandwidth requirements. A quantum dot pair source with photon bandwidths $\gamma < 1.56$ GHz is necessary to achieve the infidelity $1 - F_{\mathrm{sp,SiV}} < 7.91 \cdot 10^{-2}$. Instead of reducing bandwidth and repetition rate, we now introduce filtering of the fast yet broadband QD with $\gamma_X = 4.34$ GHz and $\gamma_{XX} = 8.33$ GHz. We find that filtering boosts performance for reduced magnetic fields. For bandwidths $\gamma_X < 4$ GHz and $\gamma_{XX} < 7.3$ GHz the high magnetic field value for the infidelity of $1 - F_{\mathrm{sp,SiV}} = 7.91 \cdot 10^{-2}$ can be achieved. This is, however, achieved on a reduced overall efficiency $\eta_{\mathrm{sp}} < 0.33$ which is lower than in the unfiltered case. We conclude that broadband QDs including filtering are compatible with SiV cavities and experimental magnetic field constraints, enabling high-fidelity spin $\pi/2$ microwave rotations (see App. A.4.4 for details). Moreover, as we will show later, keeping a high fidelity on cost of the efficiency is advantageous for the repeater performance.

For the SnV, we obtain $1 - F_{\mathrm{sp,SnV}} = 6.09 \cdot 10^{-2}$, $\eta_{\mathrm{sp,SnV}} = 0.9935$, and $C_{\mathrm{SnV}} = 160$. A higher cooperativity C_{SnV} compared to C_{SiV} is required due to the much smaller natural atomic decay rate $\gamma_{1A,\mathrm{SnV}}$. Since such a high cooperativity for the SnV has not yet been experimentally demonstrated, we evaluate the case where $C_{\mathrm{SnV}} = 25$, matching already experimentally demonstrated values [54]. For this relatively low cooperativity, a bandwidth as low as $\gamma < 480$ MHz is required to achieve an infidelity similar to the SiV's spin-spin entangled state infidelity $1 - F_{\mathrm{sp}} < 7.9 \cdot 10^{-2}$. We conclude that broadband photons, with rates comparable to those of the quantum dot considered here, are compatible with future SnV cavities with cooperativities on the order of 100. Achieving such high cooperativities may be enabled by advances in high-purity diamond growth [63], isotopic purification [64], and optimized surface termination [65]. Current state-of-the-art SnV

cavities can already interface with broadband QDs through bandwidth compression [66] or spectral filtering. Alternatively, one could employ a QD with intrinsically narrower bandwidth.

Next, we examine the infidelity $1-F_{\text{sp}}$ and efficiency η_{sp} as a function of γ_{XX} fixing $\gamma_X = 4.34$ GHz for a given magnetic and strain field induced optical splitting using frequency filtering, which we show in Fig. 2.4. The infidelity increases slightly with bandwidth and then rises sharply at larger bandwidths. This behavior reflects the finite contrast of the system; since the cavity and frequency of the incoming photons were previously optimized based on the QD properties, the steep increase occurs near that range. Below we go more into detail of that behavior. As the bandwidth increases, the phase contrast between $|1\rangle \longleftrightarrow |A\rangle$ and $|2\rangle \longleftrightarrow |B\rangle$ is washed out as was explained in [31]. The phase contrast can be recovered by increasing the optical splitting $\Delta\omega_s$, which depends on the magnetic field strength, orientation, and strain configuration. Interestingly, the cooperativity cannot be increased indefinitely at a given splitting for increasing the infidelity. This arises because the phase contrast results from a competition between the contrast itself and its first-order derivative with respect to the cooperativity [31]. As higher cooperativities reduce the magnitude of the first-order derivative, the overall fidelity increases at the price of a reduced phase difference.

Having discussed the impact of bandwidth and contrast, we next consider the influence of the photon's temporal profile. Here, the infidelity rise remains small, owing to the spectral shape of the incoming mode. That is of higher order due to spectral filtering. As a consequence, the tails of the spectrum approach zero faster than a Lorentzian. Within the considered bandwidth range the filtered mode remains within the range where $\Delta\phi(\omega) \approx \pi$ and the infidelity has only a slight increase. However, the more the bandwidth of the filtered mode approaches the QD bandwidth the broader the filter gets. The advantageous effect of the higher order spectral mode gets washed out and the infidelity steeply increases. We conclude from our observation that temporal mode shaping without reducing efficiency would be a powerful tool to significantly reduce infidelities.

In contrast to the infidelity, the efficiency rises monotonically as the bandwidth increases. That is due to the increasing total throughput of the filter across all frequencies as the bandwidth increases. It is important to mention that the infidelity for the SnV at $\gamma_X = 4.34$ GHz, $\gamma_{XX} = 6$ GHz is $1-F_{\text{sp}} = 0.05$ when no filtering is applied while the infidelity $1-F_{\text{sp}} = 0.022$ is reached at the mentioned bandwidth when we apply a filter to reduce the bandwidth from $\gamma_{XX} = 8.33$ GHz to $\gamma_{XX} = 6$ GHz. The vast infidelity difference is due to the incoming intensity spectrum being fourth order instead of second order without a filter.

Lastly, we analyze the spin-spin entanglement fidelity at the optimized

cavity and magnetic field configuration in a local environment of the optimized cavity parameters. For a deviation of maximally 1 GHz for the cavity loss rate κ and cavity mode detuning $\delta := \omega_{1A} - \omega_c$ the spin-spin entanglement infidelity for the SiV (SnV) stays below $8.11 \cdot 10^{-2}$ ($10.0 \cdot 10^{-2}$) and efficiency above 0.9175 (0.9931) (see App. A.4.3 for details). For this particular example, we find that the SiV's spin–spin entangled state is more robust to fabrication uncertainties than the SnV's. This does not need to be generally true, but only for this set of local minima of the optimization. We conclude that the spin-spin entanglement fidelity at the optimized cavity and magnetic field configuration is also robust to fabrication uncertainties.

2.4. REPEATER CHAIN PROTOCOL

To assess the repeater chain performance, we consider a symmetric node configuration and a cyclical operational protocol. This configuration and protocol may not be optimal, but they provide a lower bound on the secret-key rate. Specifically, we consider $N-1$ repeater nodes that evenly divide the total communication distance L into N segments. Each repeater node contains two quantum memory modules, used to establish elementary entanglement links with adjacent segments (see Fig. 2.1). The two end nodes have either one or zero memory modules, depending on whether entanglement distillation is applied. When no entanglement distillation is applied, the incoming photons are measured directly, so no quantum memories are required. Each memory module consists of m memory cells, with each cell composed of a G4V electron spin and a nearby nuclear spin. The nuclear spin serves as long-term storage for a single qubit, while the electron spin provides the interface to photonic qubits. Here, we consider $m \in \{100, 1{,}000\}$.

Based on the working principle introduced in Sec. 2.2, a memory cell undergoes three operational phases: qubit loading, entanglement distillation, and entanglement swapping. In each memory module, m_{loa} cells are always dedicated to the qubit-loading phase, while the remaining $m_{\text{pro}} = m - m_{\text{loa}}$ cells are engaged in either entanglement distillation or entanglement swapping.

The qubit-loading phase contains three steps: cell initialization, photon registering, and classical communication. In the initialization step, the G4V electron spin is reset to a specific quantum state, which takes $t_{\text{res}} = 1\,\mu\text{s}$. In the photon-registering step, qubits carried by photons emitted from the QD source are transferred to electron spins. This step has a fixed period T_{str}. During this period, the memory modules continuously receive photons from the QD emitter, and m_{loa} cells in each module attempt to load the qubits. Because of the high emission rate of the QD source, the photon stream is distributed quasi-parallelly across the targeted electron spins. Due to transmission loss in fibers

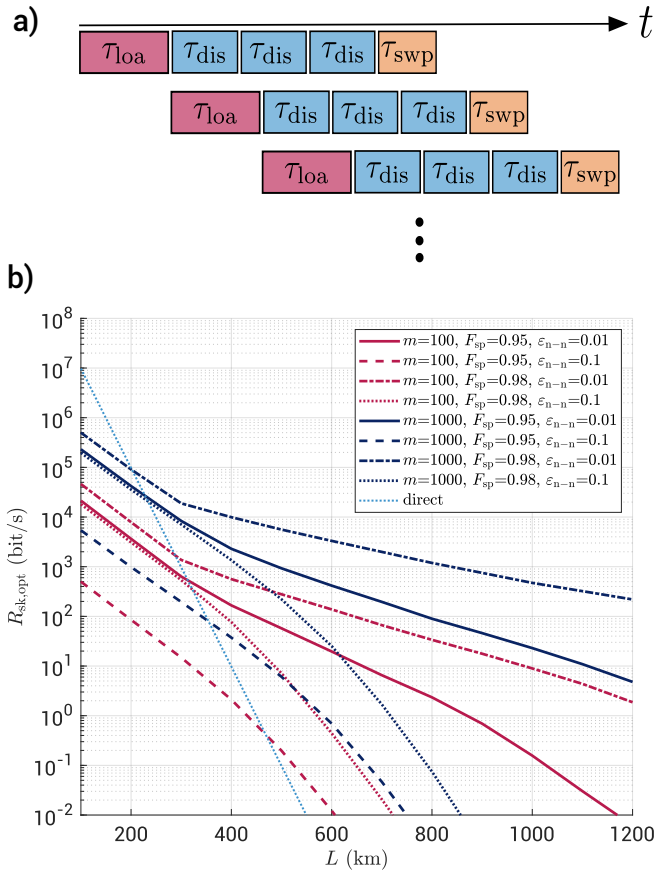

Figure 2.5.: Operational protocol and optimal secret-key rate for a QD-SiV quantum repeater chain. **a)** Operation timeline of the repeater chain. The red, blue, and yellow boxes represent the qubit-loading phase, one round of entanglement-distillation operation, and the entanglement swapping phase. Each chain of boxes represents an operational thread of a memory cell. **b)** Maximal secret-key rate ($R_{\mathrm{sk,opt}}$) as a function of total distance L under certain memory cell number per module (m), QD photon bandwidth presented as spin Bell pair fidelity (F_{sp}), and the photon-mediated nuclear-nuclear gate error rate $\varepsilon_{\mathrm{n-n}}$. The spin Bell pair fidelities $F_{\mathrm{sp}} = 0.95$ and 0.98 correspond to the QD photon bandwidth after the frequency filtering of $[\tilde{\gamma}_{\mathrm{X}}, \tilde{\gamma}_{\mathrm{XX}}] = [4.34, 8.17]$ GHz and $[\tilde{\gamma}_{\mathrm{X}}, \tilde{\gamma}_{\mathrm{XX}}] = [4.33, 6.50]$ GHz, respectively. Note that for the $F_{\mathrm{sp}} = 0.95$ case, only one photon in a Bell pair is filtered ($\tilde{\gamma}_{\mathrm{X}} = \gamma_{\mathrm{X}} = 4.34$ GHz). The optimal values of N, n_{loa}, $n_{\mathrm{dis,n}}$, and $n_{\mathrm{dis,e}}$, which give the maximal secret-key rate, can be found in App. A.6.

and local optics, many photons are lost before reaching the spins. If an electron spin fails to register a photon, it is reset for the next attempt. This process is repeated n_{loa} times, so that each targeted electron

Table 2.1.: System parameters assumed in simulations of the QD-SiV hybrid repeater chain.

QD emitter duty cycle (t_{QD})	1 ns [23, 49, 50]
nuclear spin coherence time (T_{nu})	0.1 s [67–69]
fiber attenuation rate (γ_{fib})	0.2 dB/km [16]
classical-signal transmitting speed (c)	2×10^5 km/s
number of memory cells per memory module (m)	100, 1000
G4V electron spin reset time (t_{res})	1 μs [29]
electron-nuclear gate time (t_{nu})	10 μs [67–69]
chance of causing decoherence of the nuclear spin for each electron-electron entanglement establishing attempt ($\varepsilon_{\mathrm{nu}}$)	5×10^{-5} [67–69]
QD Photon Bell pair fidelity after WDMP and PTBC (F_{ph})	0.99 [50]
QD photon bandwidths ($\{\tilde{\gamma}_X, \tilde{\gamma}_{XX}\}$)	$\{4.34, 8.17\}$ GHz [23] $\{4.33, 6.50\}$ GHz
Spin Bell pair fidelity (F_{sp})	0.95, 0.98
nucleus-nucleus gate error rate ($\varepsilon_{\mathrm{n-n}}$)	0.01, 0.1
maximal number of attempt to establish electron-electron entanglement for both entanglement distillation and swapping ($n_{\mathrm{e-e}}$)	32
cavity-fiber coupling efficiency ($\eta_{\mathrm{c-f}}$)	0.864 [54]
quantum dot photon emitter efficiency ($\eta_{\mathrm{em,qd}}$)	0.974 [29]
group-IV-vacancy color center photon emitter efficiency ($\eta_{\mathrm{em,g4v}}$)	0.98 [29]
frequency converter efficiency (η_{fc})	0.73 [70]
photon detection efficiency (η_{pd})	0.99 [54]
circulator port-1-to-2/2-to-3 efficiency ($\eta_{\mathrm{cir12/cir23}}$)	0.83 [71]
optical switch efficiency (η_{swi})	0.95 [72]

spin has n_{loc} opportunities to register a photon. Consequently, the photon-registering step has a duration

$$T_{\mathrm{str}} = (n_{\mathrm{loc}} - 1)\,\max(t_{\mathrm{res}}, m_{\mathrm{loc}} t_{\mathrm{QD}}) + m_{\mathrm{loc}} t_{\mathrm{QD}}, \tag{2.3}$$

where $t_{\mathrm{QD}} = 1\,\mathrm{ns}$ [23, 49, 50] is the duty cycle of the QD emitter.

Once a photon is successfully registered, the cell immediately enters the classical-communication step. Two processes occur simultaneously. First, a classical signal is sent to the opposite node of the segment to

announce the success, which takes

$$t_{\mathrm{com}} = \frac{L}{cN}, \tag{2.4}$$

where $c = 2 \times 10^5$ km/s is the transmission speed of a classical signal. At the same time, the qubit is transferred from the electron spin to the nuclear spin, which has a longer coherence time $T_{\mathrm{nu}} = 0.1\,\mathrm{s}$ [67–69]. The electron-nuclear transfer requires $t_{\mathrm{nu}} = 10\,\mu\mathrm{s}$ [67–69]. Therefore, the duration of the qubit-loading phase is

$$\tau_{\mathrm{loa}} = t_{\mathrm{res}} + T_{\mathrm{str}} + \max(t_{\mathrm{com}}, t_{\mathrm{nu}}). \tag{2.5}$$

During this phase, the expected number of cells that successfully register a photon is

$$m_{\mathrm{reg}} = m_{\mathrm{loa}}\left[1-(1-p_{\mathrm{arm}})^{\eta_{\mathrm{loa}}}\right]. \tag{2.6}$$

Out of these, only

$$m_{\mathrm{p}} = \mathrm{round}(m_{\mathrm{reg}} p_{\mathrm{arm}}) \tag{2.7}$$

are expected to be successfully entangled with a partner cell in the opposite node of the segment. Here round$(\cdot)$ denotes rounding to the nearest integer, and

$$p_{\mathrm{arm}} = 10^{-\frac{\gamma_{\mathrm{fib}}}{10}\cdot\frac{L}{2N}}\, p_{\mathrm{trn}} \tag{2.8}$$

is the probability of loading one qubit into one arm of a segment, where $\gamma_{\mathrm{fib}} = 0.2$ dB/km [16] is the fiber attenuation rate, and

$$p_{\mathrm{trn}} = \sqrt{\eta_{\mathrm{em,qd}}}\,\eta_{\mathrm{fc}}\,\eta_{\mathrm{cir12}}\,\eta_{\mathrm{cir23}}\,\eta_{\mathrm{c-f}}^{2(4)}\,\sqrt{\eta_{\mathrm{sp}}}\,\eta_{\mathrm{swi}}^2\,\eta_{\mathrm{pd}} \tag{2.9}$$

accounts for all optical transmission and detection efficiencies (see Tab. 2.1). The exponent of $\eta_{\mathrm{c-f}}$ is 2 or 4 depending if the Fabry-Pérot interferometer for frequency filtering is applied or not.

At the end of the qubit-loading phase, the m_{p} entangled cells hold qubits and proceed to entanglement distillation. Meanwhile, under proper scheduling, at least m_{p} additional cells are released from the m_{pro} pool (previously in distillation or swapping). This ensures that each module can again allocate m_{loa} cells for the next qubit-loading round. Consequently, the cycle period of the entire repeater chain is τ_{loa}. The timeline of operations is shown in Fig. 2.5a.

As mentioned above, we adopt the entanglement distillation protocol of Ref. [33]. In this protocol, one can distill raw Bell pairs to the first, second, or third level. Level-1, -2, and -3 distillation consume two, four, and six raw Bell pairs, respectively, and require one, two, and three sequential distillation rounds, as shown in Fig. 2.1c. Each round involves similar operations: single-qubit rotations on the nuclear

spins, intra-module nucleus–nucleus gates, nuclear-spin readout, and cross-module classical communication.

Similar to the entanglement-swapping procedure described in Sec. 2.2.2, we employ two G4V electron spins as the medium to implement nucleus–nucleus gates. The procedure is as follows: first, establish entanglement between the two electron spins; then perform local electron–nucleus gates. The electron–electron entanglement is photon-mediated and attempted $n_{\mathrm{e-e}}$ times. Each attempt consumes time t_{res} and carries a probability $\varepsilon_{\mathrm{nu}} = 5 \times 10^{-5}$ [67–69] of inducing nuclear-spin decoherence. The success probability per attempt is

$$p_{\mathrm{e-e}} = \eta_{\mathrm{em,g4v}}\, \eta_{\mathrm{cir12}}^{2}\, \eta_{\mathrm{cir23}}^{2}\, \eta_{\mathrm{c-f}}^{4}\, \eta_{\mathrm{swi}}^{4}\, \eta_{\mathrm{pd}}\,, \tag{2.10}$$

where the parameters are explained and listed in Tab. 2.1. We set $n_{\mathrm{e-e}} = 32$, chosen to maximize the objective function

$$f_{\mathrm{e-e}} = P_{\mathrm{e-e}}^{2}\, P_{\mathrm{nu}}^{4}\, \mathrm{e}^{-\frac{4 t_{\mathrm{res}} n_{\mathrm{e-e}}}{T_{\mathrm{nu}}}}. \tag{2.11}$$

Here,

$$P_{\mathrm{e-e}} = \left[1 - (1 - p_{\mathrm{e-e}})^{n_{\mathrm{e-e}}}\right] \tag{2.12}$$

is the overall success probability of establishing electron–electron entanglement, and

$$P_{\mathrm{nu}} = (1 - \varepsilon_{\mathrm{nu}})^{n_{\mathrm{e-e}}} \tag{2.13}$$

is the probability that the nuclear spin remains error-free during the $n_{\mathrm{e-e}}$ attempts.

A nuclear single-qubit rotation or nuclear-spin readout each requires time t_{nu}. Thus, the duration of one distillation round is

$$\tau_{\mathrm{dis}} = 3 t_{\mathrm{nu}} + t_{\mathrm{res}} n_{\mathrm{e-e}} + t_{\mathrm{com}}. \tag{2.14}$$

Once the memory cells complete distillation, they enter the entanglement-swapping phase, which involves one nucleus–nucleus gate and nuclear-spin readout. Its duration is

$$\tau_{\mathrm{swp}} = 2 t_{\mathrm{nu}} + t_{\mathrm{res}} n_{\mathrm{e-e}}. \tag{2.15}$$

At the end of each cycle, the number of established end-to-end links is determined by the minimum number of elementary links across all segments. The expected number of end-to-end links is (see App. A.5)

$$\mathrm{E}[n_{\mathrm{end}}] = P_{\mathrm{e-e}}^{N-1} \sum_{l=1}^{m_{\mathrm{s}}} \left(\sum_{k=l}^{m_{\mathrm{s}}} f_{\mathrm{b}}(k, m_{\mathrm{s}}, p_{\mathrm{arm}}) \right)^{N}, \tag{2.16}$$

where m_{s} is the number of Bell pairs distilled from the m_{p} raw pairs, and

$$f_{\mathrm{b}}(k, m_{\mathrm{s}}, p_{\mathrm{arm}}) = \binom{m_{\mathrm{s}}}{k} p_{\mathrm{arm}}^{k} (1 - p_{\mathrm{arm}})^{m_{\mathrm{s}} - k} \tag{2.17}$$

is the binomial distribution.

After entanglement swapping, the end-to-end links undergo another round of entanglement distillation. Unlike segment-level distillation, this round suffers from long classical-communication delays between end nodes, which cause significant nuclear-spin decoherence. Therefore, the second and third distillation levels are executed without the classical communication for identifying which Bell pair is errant. Errant pairs are allowed to propagate to higher levels, but are identified and discarded later by post-selection.

Using superoperators, the average density matrix of the final end-to-end Bell pairs is

$$\rho_{\mathrm{f}} = \mathcal{D}_{\mathrm{e}}\Big(\mathcal{S}_{N-1}\big([\mathcal{D}_{\mathrm{n}}(\rho_{\mathrm{sp}})]^{\otimes N}\big)\Big), \tag{2.18}$$

where ρ_{sp} is the density matrix of two entangled SiVs in an elementary link (App. A.3), $\mathcal{D}_{\mathrm{n}}(\cdot)$ and $\mathcal{D}_{\mathrm{e}}(\cdot)$ denote distillation for elementary links and end-to-end links, respectively, and $\mathcal{S}_{N-1}(\cdot)$ represents $N-1$ entanglement swappings. Each operation includes both intrinsic decoherence and environmental noise. Specifically, each distillation round requires two nucleus–nucleus gates, while each swapping requires one. We examine the cases when these gate error rates take values $\varepsilon_{\mathrm{n-n}} \in \{0.1, 0.01\}$.

From ρ_{f} we compute the average qubit error rates (QBERs) for Z- and X-basis measurements:

$$Q_{\mathrm{Z}} = 1 - \langle 11|\rho_{\mathrm{f}}|11\rangle - \langle 22|\rho_{\mathrm{f}}|22\rangle, \tag{2.19}$$

$$Q_{\mathrm{X}} = 1 - \langle ++|\rho_{\mathrm{f}}|++\rangle - \langle --|\rho_{\mathrm{f}}|--\rangle, \tag{2.20}$$

where $|1/2\rangle$ and $|+/-\rangle$ are the Z- and X-basis states of the end-node qubit. According to the BB84 protocol [32], the secret-key rate per entangled pair is

$$r_{\mathrm{sk}}(\rho_{\mathrm{f}}) = \max(0,\ 1 - H(Q_{\mathrm{X}}) - H(Q_{\mathrm{Z}})), \tag{2.21}$$

where $H(\cdot)$ is the binary entropy [73]. The ultimate secret-key rate is therefore

$$R_{\mathrm{sk}} = \frac{r_{\mathrm{sk}}\,\eta_{\mathrm{dis,e}}\,\mathrm{E}[n_{\mathrm{end}}]}{\tau_{\mathrm{loa}}}, \tag{2.22}$$

where $\eta_{\mathrm{dis,e}}$ is the success probability of end-to-end distillation.

All system parameters are summarized in Tab. 2.1. Based on these, we simulate the performance of the QD–SiV hybrid repeater chain. We consider two cases of QD photon bandwidths: $\{\gamma_{\mathrm{X}} = 4.34\,\mathrm{GHz}, \gamma_{\mathrm{XX}} = 8.17\,\mathrm{GHz}\}$ and $\{\gamma_{\mathrm{X}} = 4.33\,\mathrm{GHz}, \gamma_{\mathrm{XX}} = 6.50\,\mathrm{GHz}\}$. For both cases, the entangled-photon fidelity is assumed to be 0.99, corresponding to spin–spin fidelities of $F_{\mathrm{sp}} = 0.95$ and 0.98, respectively

(see Fig. 2.4). We optimize the secret-key rate $R_{\mathrm{sk,opt}}$ by scanning over the engineering parameters $\{N, n_{\mathrm{loq}}, n_{\mathrm{dis,n}}, n_{\mathrm{dis,e}}\}$, where $n_{\mathrm{dis,n}}, n_{\mathrm{dis,e}} \in \{0, 1, 2, 3\}$ denote the distillation levels for elementary and end-to-end links (level zero meaning no distillation). The simulated maximal $R_{\mathrm{sk,opt}}$ as a function of L, under different $\{m, F_{\mathrm{sp}}, \varepsilon_{\mathrm{n-n}}\}$, is shown in Fig. 2.5b, with optimal parameters listed in App. A.6. As an example, a secret-key rate of 500 bit/s over 1,000 km is achievable with $m = 1{,}000$, $\{\gamma_{\mathrm{X}} = 4.34\,\mathrm{GHz}, \gamma_{\mathrm{XX}} = 8.17\,\mathrm{GHz}\}$, $\varepsilon_{\mathrm{n-n}} = 0.01$, and a division of the total distance into seven segments.

2.5. DISCUSSION AND OUTLOOK

In this work, we have studied the performance of a hybrid quantum repeater enabled by negatively charged G4Vs as quantum memories and quantum dots as photon pair sources. Our model incorporates dominant imperfections associated with the system. Within this framework, we optimize the cavity design that is required to realize a controlled-phase gate between a broadband photon emitted from a QD and a narrowband qubit system provided by either the SiV or SnV. These gates enable the transfer of quantum states from entangled photons to the SiV or SnV spins.

For the reported photon bandwidths $\gamma_{\mathrm{X}} = 4.34$ GHz and $\gamma_{\mathrm{XX}} = 8.33$ GHz [23], the spin-spin entanglement infidelities within one section are 7.91×10^{-2} and 6.09×10^{-2} for the SiV and SnV, respectively. Using spectral filtering we can additionally interface the G4V's cavity with photons that are narrower than the reported photon bandwidth. For those we find a higher fidelity than without filtering at the same bandwidth due to the steeper shape of the spectrum after the filter compared to a Lorentzian. This shows that temporal photon shaping is an important tool for improving reflective spin-photon interfaces.

We further analyze a specific repeater chain with a chosen node configuration and operational protocol. Taking into account reported efficiencies of quantum-optical devices, nucleus–nucleus gate errors, spin rotation errors, depolarization errors in photonic states, and bandwidth mismatch between QD photons and G4Vs, we derive the maximal secret key rate as a function of the total distance, under constraints set by photon bandwidth, nucleus–nucleus gate errors, and the number of memory cells. Our estimation suggests the feasibility of building a functional repeater chain covering a distance at the order of 1,000 km based on state-of-the-art technology.

Finally, given the versatility of color centers in diamond, we anticipate that our approach is compatible with next-generation repeaters that employ quantum error correction [29, 74, 75].

REFERENCES

[1] P. Zhang, N. Chen, S. Shen, S. Yu, S. Wu, and N. Kumar. “Future Quantum Communications and Networking: A Review and Vision”. In: *IEEE Wirel. Commun.* 31.1 (Feb. 2024), pp. 141–148.

[2] S.-H. Wei, B. Jing, X.-Y. Zhang, J.-Y. Liao, C.-Z. Yuan, B.-Y. Fan, C. Lyu, D.-L. Zhou, Y. Wang, G.-W. Deng, H.-Z. Song, D. Oblak, G.-C. Guo, and Q. Zhou. “Towards Real-World Quantum Networks: A Review”. en. In: *Laser Photonics Rev.* 16.3 (2022), p. 2100219.

[3] D. D. Sukachev. “Large Quantum Networks”. In: *Phys. Usp.* 64.10 (Oct. 2021), p. 1021.

[4] M. Ruf, N. H. Wan, H. Choi, D. Englund, and R. Hanson. “Quantum networks based on color centers in diamond”. In: *J. Appl. Phys.* 130.7 (Aug. 2021), p. 070901.

[5] P. Lodahl. “Quantum-dot based photonic quantum networks”. en. In: *Quantum Sci. Technol.* 3.1 (Oct. 2017), p. 013001.

[6] A. Reiserer and G. Rempe. “Cavity-based quantum networks with single atoms and optical photons”. In: *Rev. Mod. Phys.* 87.4 (Dec. 2015), pp. 1379–1418.

[7] D.-H. Kim, S. Hong, Y.-S. Kim, Y. Kim, S.-W. Lee, R. C. Pooser, K. Oh, S.-Y. Lee, C. Lee, and H.-T. Lim. “Distributed quantum sensing of multiple phases with fewer photons”. en. In: *Nat. Commun.* 15.1 (Jan. 2024), p. 266.

[8] Z. Zhang and Q. Zhuang. “Distributed quantum sensing”. en. In: *Quantum Sci. Technol.* 6.4 (July 2021), p. 043001.

[9] X. Guo, C. R. Breum, J. Borregaard, S. Izumi, M. V. Larsen, T. Gehring, M. Christandl, J. S. Neergaard-Nielsen, and U. L. Andersen. “Distributed quantum sensing in a continuous-variable entangled network”. en. In: *Nat. Phys.* 16.3 (Mar. 2020), pp. 281–284.

[10] C. L. Degen, F. Reinhard, and P. Cappellaro. “Quantum sensing”. In: *Rev. Mod. Phys.* 89.3 (July 2017).

[11] R. Ramya, P. Kumar, D. Dhanasekaran, R. S. Kumar, and S. A. Sharavan. “A review of quantum communication and information networks with advanced cryptographic applications using machine learning, deep learning techniques”. In: *Frankl. Open* 10 (Mar. 2025), p. 100223.

[12] J. Chen. “Review on Quantum Communication and Quantum Computation”. In: *J. Phys. Conf. Ser.* 1865.2 (Apr. 2021), p. 022008.

[13] N. Gisin and R. Thew. “Quantum communication”. en. In: *Nat. Photonics* 1.3 (Mar. 2007), pp. 165–171.

[14] S. Sunami, S. Tamiya, R. Inoue, H. Yamasaki, and A. Goban. “Scalable Networking of Neutral-Atom Qubits: Nanofiber-Based Approach for Multiprocessor Fault-Tolerant Quantum Computers”. In: *PRX Quantum* 6.1 (Feb. 2025), p. 010101.

[15] A. R. et al. “Scaling and networking a modular photonic quantum computer”. en. In: *Nature* 638.8052 (Feb. 2025), pp. 912–919.

[16] T. Miya, Y. Terunuma, T. Hosaka, and T. Miyashita. “Ultimate low-loss single-mode fibre at 1.55 μm”. In: *Electron. Lett.* 15.4 (Feb. 1979), pp. 106–108.

[17] W. K. Wootters and W. H. Zurek. “A single quantum cannot be cloned”. en. In: *Nature* 299.5886 (Oct. 1982), pp. 802–803.

[18] H.-J. Briegel, W. Dür, J. I. Cirac, and P. Zoller. “Quantum Repeaters: The Role of Imperfect Local Operations in Quantum Communication”. In: *Phys. Rev. Lett.* 81.26 (Dec. 1998), pp. 5932–5935.

[19] N. Sangouard, C. Simon, H. de Riedmatten, and N. Gisin. “Quantum repeaters based on atomic ensembles and linear optics”. In: *Rev. Mod. Phys.* 83.1 (Mar. 2011), pp. 33–80.

[20] V. Krutyanskiy, M. Canteri, M. Meraner, J. Bate, V. Krcmarsky, J. Schupp, N. Sangouard, and B. P. Lanyon. “Telecom-Wavelength Quantum Repeater Node Based on a Trapped-Ion Processor”. In: *Phys. Rev. Lett.* 130 (21 May 2023), p. 213601.

[21] H. Wang, M. E. Trusheim, L. Kim, H. Raniwala, and D. R. Englund. “Field programmable spin arrays for scalable quantum repeaters”. In: *Nat. Commun.* 14.1 (Feb. 2023).

[22] T.-J. Wang, S.-Y. Song, and G. L. Long. “Quantum repeater based on spatial entanglement of photons and quantum-dot spins in optical microcavities”. In: *Phys. Rev. A* 85.6 (June 2012).

[23] C. Schimpf, M. Reindl, D. Huber, B. Lehner, S. F. Covre Da Silva, S. Manna, M. Vyvlecka, P. Walther, and A. Rastelli. “Quantum cryptography with highly entangled photons from semiconductor quantum dots”. In: *Science Advances* 7.16 (Apr. 2021).

[24] C.-P. M. H. Knaut. “A Quantum Memory Network Based on Diamond Nanophotonics”. Ph.D. United States – Massachusetts: Harvard University, 2024.

[25] I. B. W. Harris and D. Englund. “Coherence of group-IV color centers”. In: *Phys. Rev. B* 109.8 (Feb. 2024), p. 085414.

[26] J. Neuwirth, F. B. Basset, M. B. Rota, E. Roccia, C. Schimpf, K. D. Jöns, A. Rastelli, and R. Trotta. “Quantum dot technology for quantum repeaters: from entangled photon generation toward the integration with quantum memories”. In: *Materials for Quantum Technology* 1.4 (Dec. 2021), p. 043001.

[27] J. M. Zajac, T. Huber-Loyola, and S. Hofling. “Quantum dots for quantum repeaters”. In: *arXiv:2503.13775* ().

[28] D. D. Sukachev, A. Sipahigil, C. T. Nguyen, M. K. Bhaskar, R. E. Evans, F. Jelezko, and M. D. Lukin. “Silicon-Vacancy Spin Qubit in Diamond: A Quantum Memory Exceeding 10 ms with Single-Shot State Readout”. In: *Phys. Rev. Lett.* 119.22 (Nov. 2017).

[29] J. M. Bopp, M. Plock, T. Turan, G. Pieplow, S. Burger, and T. Schröder. “‘Sawfish’ Photonic Crystal Cavity for Near-Unity Emitter-to-Fiber Interfacing in Quantum Network Applications”. en. In: *Adv. Opt. Mater.* 12.13 (2024), p. 2301286.

[30] Y. Strocka, M. Belhassen, T. Schröder, and G. Pieplow. “Software Framework for Optically Accessible Quantum Memory Using Group-IV Color Centers in Diamond”. In: *arXiv:2510.07045* ().

[31] F. Omlor, B. Tissot, and G. Burkard. “Entanglement generation using single-photon pulse reflection in realistic networks”. In: *Phys. Rev. A* 111.1 (Jan. 2025).

[32] P. W. Shor and J. Preskill. “Simple Proof of Security of the BB84 Quantum Key Distribution Protocol”. In: *Phys. Rev. Lett.* 85.2 (July 2000), pp. 441–444.

[33] R. Nigmatullin, C. J. Ballance, N. De Beaudrap, and S. C. Benjamin. “Minimally complex ion traps as modules for quantum communication and computing”. In: *New J. Phys.* 18.10 (2016), p. 103028.

[34] E. N. Knall, C. M. Knaut, R. Bekenstein, D. R. Assumpcao, P. L. Stroganov, W. Gong, Y. Q. Huan, P.-J. Stas, B. Machielse, M. Chalupnik, D. Levonian, A. Suleymanzade, R. Riedinger, H. Park, M. Lon čar, M. K. Bhaskar, and M. D. Lukin. “Efficient Source of Shaped Single Photons Based on an Integrated Diamond Nanophotonic System”. In: *Phys. Rev. Lett.* 129 (5 July 2022), p. 053603.

[35] G. Van de Stolpe, D. Kwiatkowski, C. Bradley, J. Randall, M. Abobeih, S. Breitweiser, L. Bassett, M. Markham, D. Twitchen, and T. Taminiau. “Mapping a 50-spin-qubit network through correlated sensing”. In: *Nat. Commun.* 15.1 (2024), p. 2006.

[36] H. K. C. Beukers, C. Waas, M. Pasini, H. B. van Ommen, Z. Ademi, M. Iuliano, N. Codreanu, J. M. Brevoord, T. Turan, T. H. Taminiau, and R. Hanson. “Control of solid-state nuclear spin qubits using an electron spin-1/2”. In: *arXiv:2409.08977* ().

[37] P.-J. Stas, Y. Q. Huan, B. Machielse, E. N. Knall, A. Suleymanzade, B. Pingault, M. Sutula, S. W. Ding, C. M. Knaut, D. R. Assumpcao, *et al.* “Robust multi-qubit quantum network node with integrated error detection”. In: *Science* 378.6619 (2022), pp. 557–560.

[38] R. A. Parker, J. Arjona Martínez, K. C. Chen, A. M. Stramma, I. B. Harris, C. P. Michaels, M. E. Trusheim, M. Hayhurst Appel, C. M. Purser, W. G. Roth, D. Englund, and M. Atatüre. “A diamond nanophotonic interface with an optically accessible deterministic electronuclear spin register”. In: *Nat. Photonics* 18.2 (Nov. 2023), pp. 156–161.

[39] F. Gu. “The Group-IV-Vacancy Color Center in Diamond”. In: *arXiv preprint arXiv:2509.00443* (2025).

[40] C. Hepp. “Electronic Structure of the Silicon Vacancy Color Center in Diamond”. Advisor: Christoph Becher. PhD thesis. Saarbrücken, Germany: Saarland University, 2014.

[41] F. Rozpędek, T. Schiet, L. P. Thinh, D. Elkouss, A. C. Doherty, and S. Wehner. “Optimizing practical entanglement distillation”. In: *Physical Review A* 97.6 (June 2018). Publisher: American Physical Society, p. 062333.

[42] S. Bratzik, S. Abruzzo, H. Kampermann, and D. Bruß. “Quantum repeaters and quantum key distribution: The impact of entanglement distillation on the secret key rate”. en. In: *Physical Review A* 87.6 (June 2013), p. 062335.

[43] R. Horodecki, P. Horodecki, M. Horodecki, and K. Horodecki. “Quantum entanglement”. In: *Reviews of Modern Physics* 81.2 (June 2009). Publisher: American Physical Society, pp. 865–942.

[44] W. Dür, H.-J. Briegel, J. I. Cirac, and P. Zoller. “Quantum repeaters based on entanglement purification”. In: *Phys. Rev. A* 59.1 (Jan. 1999), pp. 169–181.

[45] P.-S. Yan, L. Zhou, W. Zhong, and Y.-B. Sheng. “A survey on advances of quantum repeater”. en. In: *EPL* 136.1 (Nov. 2021), p. 14001.

[46] M. E. Reimer, G. Bulgarini, N. Akopian, M. Hocevar, M. B. Bavinck, M. A. Verheijen, E. P. Bakkers, L. P. Kouwenhoven, and V. Zwiller. “Bright single-photon sources in bottom-up tailored nanowires”. In: *Nat. Commun.* 3.1 (2012), p. 737.

[47] D. Heinze, D. Breddermann, A. Zrenner, and S. Schumacher. “A quantum dot single-photon source with on-the-fly all-optical polarization control and timed emission”. In: *Nat. Commun.* 6.1 (2015), p. 8473.

[48] M. Müller, S. Bounouar, K. D. Jöns, M. Glässl, and P. Michler. “On-demand generation of indistinguishable polarization-entangled photon pairs”. In: *Nat. Photonics* 8.3 (2014), pp. 224–228.

[49] T. Strobel, S. Kazmaier, T. Bauer, M. Schäfer, A. Choudhary, N. Lal Sharma, R. Joos, C. Nawrath, J. H. Weber, W. Nie, *et al.* “High-fidelity distribution of triggered polarization-entangled telecom photons via a 36 km intra-city fiber network”. In: *Opt. Quantum* 2.4 (2024), pp. 274–281.

[50] D. Huber, M. Reindl, J. Aberl, A. Rastelli, and R. Trotta. “Semiconductor quantum dots as an ideal source of polarization-entangled photon pairs on-demand: a review”. In: *Journal of Optics* 20.7 (June 2018), p. 073002.

[51] K.-i. Aoyama and J.-i. Minowa. “Optical demultiplexer for a wavelength division multiplexing system”. EN. In: *Appl. Opt.* 18.8 (Apr. 1979), pp. 1253–1258.

[52] C. Kupchak, P. J. Bustard, K. Heshami, J. Erskine, M. Spanner, D. G. England, and B. J. Sussman. “Time-bin-to-polarization conversion of ultrafast photonic qubits”. In: *Phys. Rev. A* 96.5 (Nov. 2017), p. 053812.

[53] B. Albrecht, P. Farrera, X. Fernandez-Gonzalvo, M. Cristiani, and H. de Riedmatten. “A waveguide frequency converter connecting rubidium-based quantum memories to the telecom C-band”. en. In: *Nat. Commun.* 5.1 (Feb. 2014), p. 3376.

[54] M. K. Bhaskar, R. Riedinger, B. Machielse, D. S. Levonian, C. T. Nguyen, E. N. Knall, H. Park, D. Englund, M. Lončar, D. D. Sukachev, and M. D. Lukin. “Experimental demonstration of memory-enhanced quantum communication”. en. In: *Nature* 580.7801 (Apr. 2020), pp. 60–64.

[55] R. Reyes, T. Nakazato, N. Imaike, K. Matsuda, K. Tsurumoto, Y. Sekiguchi, and H. Kosaka. “Complete Bell state measurement of diamond nuclear spins under a complete spatial symmetry at zero magnetic field”. In: *Appl. Phys. Lett.* 120.19 (2022).

[56] C. M. Knaut, A. Suleymanzade, Y.-C. Wei, D. R. Assumpcao, P.-J. Stas, Y. Q. Huan, B. Machielse, *et al.* “Entanglement of Nanophotonic Quantum Memory Nodes in a Telecom Network”. In: *Nature* 629.8012 (May 2024), pp. 573–578.

[57] T. T. Tran, M. Kianinia, K. Bray, S. Kim, Z.-Q. Xu, A. Gentle, B. Sontheimer, C. Bradac, and I. Aharonovich. “Nanodiamonds with photostable, sub-gigahertz linewidth quantum emitters”. In: *APL Photonics* 2.11 (Nov. 2017), p. 116103.

[58] N. Ismail, C. C. Kores, D. Geskus, and M. Pollnau. “Fabry-Pérot resonator: spectral line shapes, generic and related Airy distributions, linewidths, finesses, and performance at low or frequency-dependent reflectivity”. In: *Opt. Express* 24.15 (July 2016), p. 16366.

[59] Y.-C. Liang, Y.-H. Yeh, P. E. M. F. Mendonça, R. Y. Teh, M. D. Reid, and P. D. Drummond. “Quantum fidelity measures for mixed states”. In: *Rep. Prog. Phys.* 82.7 (June 2019), p. 076001.

[60] J. Borregaard, H. Pichler, T. Schröder, M. D. Lukin, P. Lodahl, and A. S. Sørensen. “One-Way Quantum Repeater Based on Near-Deterministic Photon-Emitter Interfaces”. en. In: *Phys. Rev. X* 10.2 (June 2020), p. 021071.

[61] G. Pieplow, M. Belhassen, and T. Schröder. “Efficient microwave spin control of negatively charged group-IV color centers in diamond”. In: *Phys. Rev. B* 109.11 (Mar. 2024), p. 115409.

[62] I. Karapatzakis, J. Resch, M. Schrodin, P. Fuchs, M. Kieschnick, J. Heupel, L. Kussi, C. Sürgers, C. Popov, J. Meijer, C. Becher, W. Wernsdorfer, and D. Hunger. “Microwave Control of the Tin-Vacancy Spin Qubit in Diamond with a Superconducting Waveguide”. In: *Phys. Rev. X* 14.3 (Aug. 2024).

[63] T. Chakraborty, F. Lehmann, J. Zhang, S. Borgsdorf, N. Wöhrl, R. Remfort, V. Buck, U. Köhler, and D. Suter. “CVD growth of ultra-pure diamond, generation of NV centers by ion implantation, and their spectroscopic characterization for quantum technological applications”. In: *Phys. Rev. Mater.* 3.6 (June 2019).

[64] T. Teraji, T. Yamamoto, K. Watanabe, Y. Koide, J. Isoya, S. Onoda, T. Ohshima, L. J. Rogers, F. Jelezko, P. Neumann, J. Wrachtrup, and S. Koizumi. “Homoepitaxial diamond film growth: High purity, high crystalline quality, isotopic enrichment, and single color center formation”. In: *Phys. Status Solidi A* 212.11 (Oct. 2015), pp. 2365–2384.

[65] M. V. Hauf, B. Grotz, B. Naydenov, M. Dankerl, S. Pezzagna, J. Meijer, F. Jelezko, J. Wrachtrup, M. Stutzmann, F. Reinhard, and J. A. Garrido. “Chemical control of the charge state of nitrogen-vacancy centers in diamond”. In: *Phys. Rev. B* 83.8 (Feb. 2011).

[66] M. Allgaier, V. Ansari, L. Sansoni, C. Eigner, V. Quiring, R. Ricken, G. Harder, B. Brecht, and C. Silberhorn. “Highly Efficient Frequency Conversion with Bandwidth Compression of Quantum Light”. In: *Nat. Commun.* 8.1 (Jan. 2017), p. 14288.

[67] C. M. Knaut, A. Suleymanzade, Y.-C. Wei, D. R. Assumpcao, P.-J. Stas, Y. Q. Huan, B. Machielse, E. N. Knall, M. Sutula, G. Baranes, *et al.* “Entanglement of nanophotonic quantum memory nodes in a telecom network”. In: *Nature* 629.8012 (2024), pp. 573–578.

[68] Y.-C. Wei, P.-J. Stas, A. Suleymanzade, G. Baranes, F. Machado, Y. Q. Huan, C. M. Knaut, S. W. Ding, M. Merz, E. N. Knall, U. Yazlar, M. Sirotin, I. W. Wang, B. Machielse, S. F. Yelin, J. Borregaard, H. Park, M. Lončar, and M. D. Lukin. “Universal distributed blind quantum computing with solid-state qubits”. In: *Science* 388.6746 (May 2025), pp. 509–513.

[69] P.-J. Stas, Y. Q. Huan, B. Machielse, E. N. Knall, A. Suleymanzade, B. Pingault, M. Sutula, S. W. Ding, C. M. Knaut, D. R. Assumpcao, *et al.* “Robust multi-qubit quantum network node with integrated error detection”. In: *Science* 378.6619 (2022), pp. 557–560.

[70] S. Zaske, A. Lenhard, and C. Becher. “Efficient frequency downconversion at the single photon level from the red spectral range to the telecommunications C-band”. In: *Opt. Express* 19.13 (June 2011), p. 12825.

[71] Thorlabs. *Wideband Multimode Circulators*. Accessed: 2024-02-15.

[72] G. Zeng, D. Zhang, F. Wang, X. Wang, and Y. Yin. “1 × N All-Logic Optical Switch Based on Polymer Platform Using Multimode Interferometer”. In: *Adv. Photonics Res.* **8** 2400118 (Oct. 2024).

[73] D. MacKay. *Information Theory, Inference, and Learning Algorithms: The Book*. Feb. 2016.

[74] J. Borregaard, H. Pichler, T. Schröder, M. D. Lukin, P. Lodahl, and A. S. Sørensen. “One-Way Quantum Repeater Based on Near-Deterministic Photon-Emitter Interfaces”. In: *Phys. Rev. X* 10.2 (2020), p. 021071.

[75] M. Ruf, N. H. Wan, H. Choi, D. Englund, and R. Hanson. “Quantum networks based on color centers in diamond”. In: *J. Appl. Phys.* 130.7 (Aug. 2021), p. 070901.

3

MODULAR ARCHITECTURES AND ENTANGLEMENT SCHEMES FOR ERROR-CORRECTED DISTRIBUTED QUANTUM COMPUTATION*

Siddhant Singh*, Fenglei Gu*, Sébastian de Bone, Eduardo Villaseñor, David Elkouss, Johannes Borregaard

运筹帷幄之中，决胜千里之外 *(Devising strategies within the confines of a command tent, one determines victory a thousand miles away.)*

– 司马迁(SIMA Qian, c. 145–86 BCE)

*The work presented in this chapter is published on arXiv:2408.02837[1].

*These authors contributed equally to this work. Under the guidance of J.B., F.G. developed the theory and performed numerical simulations for the reflecting (RFL) and carving (CAR) schemes for GHZ state generation. He also authored the corresponding sections of the manuscript.

3

Connecting multiple smaller qubit modules by generating high-fidelity entanglement is a promising path for scaling quantum computing hardware. The performance of such a modular quantum computer is highly dependent on the quality and rate of entanglement generation. However, identifying optimal architectures and entanglement generation protocols remains an open question. How can modular quantum architectures be designed to achieve fault tolerance while requiring only feasible entanglement rates and hardware? Focusing on solid-state quantum hardware, we investigate the threshold and logical failure rate of a fully distributed surface code. We consider both emission-based and scattering-based entanglement schemes between the modules to link the performance of the surface code to the physical hardware and identify the regime for fault tolerance. We compare modular architectures with one or two data qubits per module. For some entanglement schemes, thresholds nearing the thresholds of non-distributed implementations (∼ 0.4%) appear feasible with future parameters minimizing the performance gap between modular and monolithic quantum processors.

3.1. INTRODUCTION

Error-corrected [2–4] modular quantum computers [5–10], offer a promising route to overcome the noise and scalability challenges of large-scale fault-tolerant quantum computing. A modular quantum computer consists of individual computing modules with separate control, which are linked together by means of quantum entanglement [5, 8, 10–12]. Modular architectures have been proposed for several types of quantum computing hardware, such as superconducting qubits [13, 14], neutral atoms [15, 16], and color centers [17–19]. However, several fundamental questions remain: What are the optimal ways to generate high-fidelity entanglement between modules? Can modular architectures achieve fault-tolerant thresholds comparable to those of monolithic systems? Previous work has hinted that the performance of a distributed QEC code heavily depends on the degree of modularity [20] and the specific choice of quantum entanglement generation protocol [19]. The many suitable protocols for entanglement generation [21], as well as specific choice of modular architecture and QEC codes [22, 23], amount to a vast and largely unexplored design space. How do different entanglement protocols compare in terms of performance for real hardware? What hardware constraints limit their applicability?

In this article, we explore this space for quantum hardware with efficient spin-photon interfaces such as color centers in diamond or silicon, which is a promising hardware for fully connected, modular quantum computers [24–35]. We investigate the performance of a specific surface code, the toric code [36–39] across two types of modularized architectures, considering both emission- [40] and scattering-based [31, 41] entanglement generation schemes.

We go beyond the generic circuit-level noise model and develop hardware-tailored noise models that allow us to link the modular QEC performance directly to the physical parameters of the quantum hardware. From this investigation, we specify the requirements of key parameters such as qubit coherence times, photonic link efficiency, and quality of the spin-photon interface for the existence of a circuit-level noise code threshold and identify the break-even point where the QEC suppresses errors beyond the physical error rates. We perform a comprehensive comparison of multiple GHZ-generation protocols for stabilizer measurements, including several direct GHZ-generation protocols. Crucially, we demonstrate that by avoiding the slow Bell pair combination and distillation process of emission-based (EM) protocols as considered in Ref. [19], one can achieve substantially higher error thresholds and reduce the required coherence times by over an order of magnitude. While we find that near-term experimental parameters are sufficient to realize fault-tolerant quantum computation, modest improvements in hardware performance result in QEC thresholds as high as $\sim 0.4\%$, which is comparable to the thresholds found for monolithic

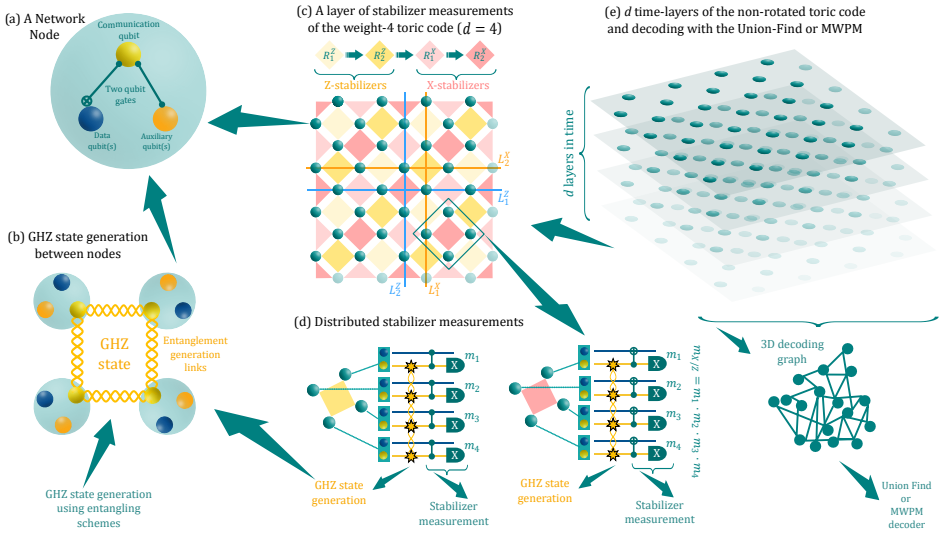

Figure 3.1.: Weight-4 toric code architecture with one data qubit per module. (a) The structure of a module. It consists of a single communication qubit that allows for optical connection to the other modules and some memory qubits acting as either data qubits of the code or auxiliary qubits for the stabilizer measurements. (b) Multipartite GHZ states used for measuring the stabilizers that spread among modules. (c) One round of Z and X type stabilizer measurements, each divided into two subroutines. The four colors of the squares in the toric-code lattice correspond to the four subroutines as shown in the sequence. The toric-code lattice encodes two qubits with logical operators ($L_{1,2}^{X,Z}$). The corresponding blue and orange lines indicate the qubit involved in implementing the logical operators. (d) Quantum circuits for implementing the distributed Z and X stabilizer measurement. A GHZ state is generated upon demand (star signs) and used to measure the joint parity $ZZZZ$ or $XXXX$ on the stabilizer data qubits via the application of local controlled-Z/X gates. The outcome of the stabilizer measurement is the joint parity outcome from the four measurements, i.e., $m_{X/Z} = m_1 \cdot m_2 \cdot m_3 \cdot m_4$. (e) Time layers of the stabilizer measurement. The stabilizer measurements are repeated d times, the same as the distance of the square toric code. These d layers constitute one full QEC cycle, and all syndrome data is then sent to a decoder. Thereafter, suitable corrections are applied to the qubits.

architectures of about half a percent under circuit-level noise [39]. Our findings provide a road map for designing scalable, fault-tolerant modular quantum computers and answer key questions about their feasibility with near-term and future quantum technology.

The chapter is organized as follows. In Sec. 3.2, we describe the modular architectures inspired by the toric surface code. Next, in Sec. 3.3, we describe the theory and analytical model of the entanglement generation schemes, including emission-based and scattering-based schemes. We construct detailed physical models for the hardware performance in Sec. 3.6. Finally, we describe the results on distributed code error thresholds and architecture implementation in Sec. 3.4.

3.2. MODULAR SURFACE CODE ARCHITECTURES

We consider a setup where each module of the computing architecture consists of a single communication qubit (CQ) and a few memory qubits, as shown in Fig. 3.1(a). The modules are arranged on a square lattice, and the communication qubits can establish entanglement with the nearest-neighboring modules through optical links. We will assign one or two of the memory qubits in a module as data qubits of the code, while additional memory qubits are assigned as auxiliary qubits that can be utilized for stabilizer measurements [13, 19, 42], as shown in Fig. 3.1(a).

Two-qubit interactions are allowed only between the communication qubit and a memory qubit within the same node, and only the communication qubit can be directly measured. This model is tailored to a broad range of quantum hardware based on color centers such as Nitrogen-Vacancy (NV) [43], Silicon-Vacancy (SiV) [26–29, 31], Tin-Vacancy (SnV) [32–34], and Silicon defect centers [18] where the electronic spin states of the defect are optically addressable and can couple through a dipolar interaction to nearby nuclear memory spins.

We consider the topological non-rotated toric surface code [13, 39, 44], which requires measurement of four-body stabilizers between neighboring data qubits. The stabilizers are measured by creating multi-qubit GHZ states between the modules, either through direct GHZ state generation or fusion of Bell pairs. For the architecture with one data qubit per module, we require the generation of 4-qubit GHZ states, while 3-qubit GHZ states are sufficient when 2 data qubits are hosted per module. We will refer to these as the weight-4 (WT4) [19] and weight-3 (WT3) architectures, respectively. WT4 architecture is a direct translation of monolithic surface code architecture to our modular design, which has been explored in [13, 19, 42]. We propose WT3 architecture in this work to lower the stringent entanglement generation requirements.

Since each module only contains one communication qubit, it is not possible to measure all the stabilizers simultaneously. This constraint

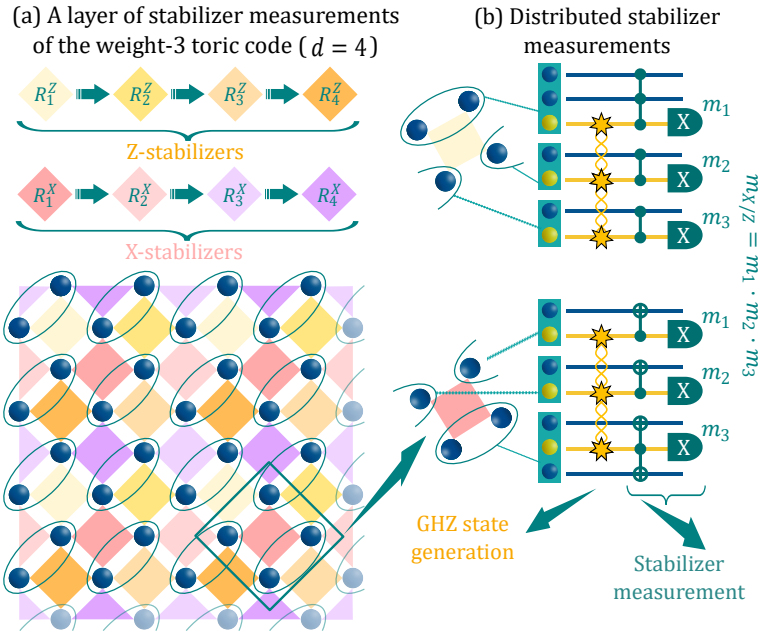

Figure 3.2.: Weight-3 toric code architecture of code distance $d = 4$ with two data qubits per module. (a) One round of stabilizer measurements, consisting of measurements for X and Z type stabilizers, each containing four subroutines. The logical qubits of the code are the same as for the WT4 architecture, as shown in Fig. 3.1(c). (b) Quantum circuits for the stabilizer measurement. The notation is the same as in Fig. 3.1

results in a checkerboard pattern of stabilizer measurement sub-rounds (each of X and Z types), which differs for the WT4 and WT3 architectures.

For the WT4 architecture, each X and Z-type stabilizer is divided into two sub-rounds, resulting in a four-sequence QEC cycle (see Fig. 3.1(c)). For the WT3 architecture, the modules are arranged obliquely on the code background array, such that one module contributes two data qubits on the code and exactly three modules span each stabilizer. We consider the even-distance (for each logical operator) WT3 toric code, as this allows all the modules to have exactly two data qubits. The topology of the WT3 architecture means that four sub-rounds for each stabilizer type (X, Z) are required, resulting in an 8-sequence QEC cycle (see Fig. 3.2).

(a) Schematic of the emission (fusion) scheme

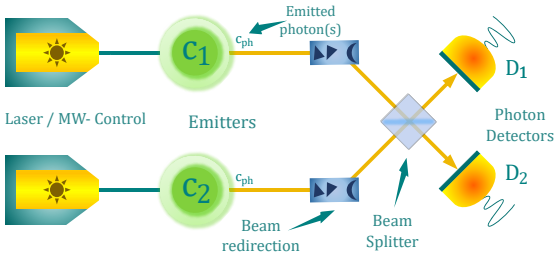

(b) Energy level diagram of the emitter

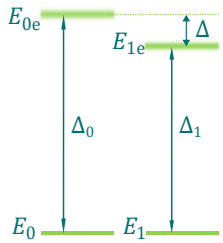

Figure 3.3.: Emission-based (EM) scheme. (a) An optical setup with two emitters as communication qubits can be initialized in a CQ-photon entangled state. Then, the emitted photons (c_{ph}) are sent to a middle station where an optical Bell measurement is performed using a balanced beam splitter and single photon detection. The detection of an early and a late photon at the detectors successfully heralds a Bell pair between the two CQs (c_i). (b) The energy levels of the photon-CQ system. The CQ has two sets of independent transitions: $E_0 \longleftrightarrow E_{0e}$ and $E_1 \longleftrightarrow E_{1e}$ with transition frequencies Δ_0 and Δ_1, respectively. Here, E_1 refers to the energy level of the bright-state $|1\rangle$ that emits a photon upon excitation.

3.3. GHZ-STATE GENERATION

We consider emission and scattering-based schemes for generating GHZ states between the modules. Each scheme can be adapted to generate either 4-qubit or 3-qubit GHZ states.

The EM scheme was first proposed in 1999 [45] and has been well developed to realize long-distance entangled Bell pairs [46]. However, for realizing the multipartite GHZ states, sequential generations of Bell pairs, intra-modular two-qubit gates [47] on the memory qubits, and

multiple-qubit readouts are required. These requirements present a significant time overhead in the QEC cycle with corresponding memory requirements on the data qubits.

Nevertheless, scattering-based entangling schemes [48] harness spin-dependent reflection/transmission, which is several orders of magnitude faster than the gates based on spin-spin interactions. Based on whether the reflected or transmitted photon is used to generate the heralding signal, we classify the scattering-based schemes into the reflection (RFL) scheme and the carving (CAR) scheme. The RFL scheme is inspired by previous studies of cavity-mediated spin-photon entanglement gates [49, 50] used for Bell-state realizations [51, 52]. On the other hand, the CAR scheme is closely related to carving schemes for Bell-state generation [53]. While the RFL scheme requires optical circulators and a delay line to guide and manipulate the photons, which raises challenges in on-chip integrated photonics, the CAR scheme circumvents these problems. However, the probabilistic-success nature lower its entanglement generation rates. The principles of these schemes are illustrated below.

Emission-based (EM) scheme: In this scheme, GHZ states are realized by the fusion of multiple Bell pairs [19]. For creating the Bell pairs, we consider both the single-click [45] and double-click (Barrett-Kok [54]) protocols, as they are suitable for the near-term parameters and boosted future parameters, respectively.

The single-click protocol works as follows. In each module, the CQ has a four-level structure with two ground states, as shown in Fig. 3.3(b). Ideally, one ground state can be selectively excited to emit a photon. Through a controlled operation, a photon is created and entangled with the CQ. The two photons from two modules are then sent and meet at a balanced beam splitter in a middle station. Then, after a single photon detection, the successful creation of an entangled state between the two CQs will be heralded, as shown in Fig. 3.3(a). In the double-click protocol, a second round of photon emission is used to boost the fidelity by eliminating terms that do not contribute to single photon emission after the first round, by applying local operations before the second emission. For the single-click (double-click) protocol, the overall success probability of the protocols depends linearly (quadratically) on the effective photon detection probability η_{ph}.

Due to imperfections of both the Bell states and the local gate operations, it is necessary to employ distillation protocols to boost the final fidelity of the GHZ state. Similar to the method illustrated in Ref. [19], we optimize over various distillation protocols where additional Bell pairs are used to increase the final GHZ state fidelity. Notably, we only consider distillation protocols where, at most, two auxiliary memory qubits per module are available to accommodate realistic hardware constraints. Full analytical details of the noisy EM schemes and the

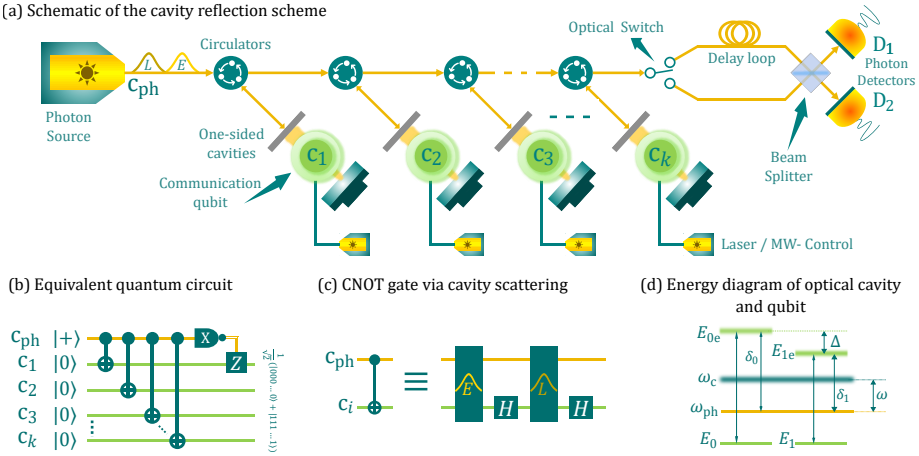

Figure 3.4.: Principles of the reflection (RFL) scheme. (a) System setup of the RFL scheme. It contains a series of atoms, each embedded within a single-side cavity. The fibers and circulators guide the photon to interact with each atom-cavity system successively. The delay loop, beam splitter, and photon detectors are used to detect the photonic qubit in the X basis. (b) Quantum circuit that the reflecting protocol implements. It contains cnot gates and a photon measurement in its X basis. (c) Physical implementation for the cnot gate. It contains four steps, including scattering the photon of the two time bins and implementing Hadamard gates on the atom. (d) The energy levels of the photon-atom-cavity system. The spin has two sets of independent transitions coupled to the input photon: $E_0 \leftrightarrow E_{0e}$ and $E_1 \leftrightarrow E_{1e}$. ω_c: cavity resonance frequency; ω_{ph}: input photon frequency.

distillation protocols can be found in App. B.4.

Reflection (RFL) scheme: In the RFL scheme, the GHZ state is realized by employing a photon as the flying auxiliary qubit, interacting sequentially with all the CQs involved, and finally being detected, as shown in Fig. 3.4(a). This procedure realized a quantum circuit as shown in Fig. 3.4(b). The photon-spin interaction realizes a cnot gate [55], where the photon encodes a qubit in its early and late time bins, and two qubit rotations are applied on the CQ, with one at the time between the scattering of the two time bins and the other after the late time-bin scattering, as shown in Fig. 3.4(c).

When examining the performance, we include various hardware

imperfections in our modeling of the RFL scheme, such as photon loss, finite cavity coupling, and unwanted optical couplings, considering the CQ level structure and photon and cavity frequencies, as shown in Fig. 3.4(d). We consider both a near-perfect single-photon source and an attenuated coherent light source for the photonic qubit. The details of our model are provided in App. B.5.

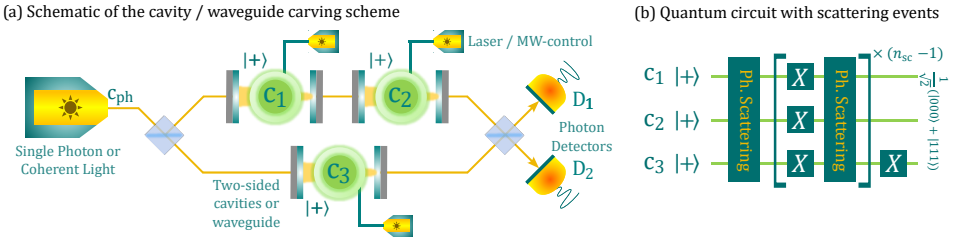

Figure 3.5.: Principle of the carving (CAR) scheme. (a) System setup of the CAR protocol. It consists of spins embedded inside a two-sided cavity (or waveguide), a light source, beam-splitters, and photon detectors. (b) The operating sequence of the CAR protocol. All the spins are initialized in $|+\rangle$ states. The operating sequence consists of scatterings of single photons through the optical circuit and not gates implemented on spins between every two sequential scattering rounds.

Carving (CAR) scheme:

The CAR scheme exploits the spin-dependent reflection or transmission mechanism of a qubit-coupled two-sided cavity or waveguide to realize the GHZ state. For an ideal mechanism, an incoming photon will be reflected (transmitted) when the CQ is in state $|1\rangle(|0\rangle)$. The GHZ state can be probabilistically carved out by means of a single photon scattering at the cavities or waveguides arranged in two routes, and finally getting detected, as shown in Fig. 3.5(a). The protocol can be repeated with not gates between every two successive rounds, as shown in Fig. 3.5(b), to increase the fidelity of the output GHZ state. Note that the CAR scheme is inherently probabilistic, with a probability of success that decreases exponentially with the number of CQs in the target GHZ state. The maximum success probability for a 3-CQ (4-CQ) GHZ state is 1/16 (1/32). For this scheme, we consider both a cavity (CAV) implementation and a waveguide (WG) implementation, where the cavity (waveguide) is of a finite (infinite) bandwidth. The level structure and the frequencies of the incoming photon and cavity are the same as those with the EM and RFL protocols. We include hardware imperfections, such as finite coupling strengths and unwanted transmission/reflection, in our modeling. The performance analysis for

the CAR scheme with a perfect single photon source (SPS) and an attenuated coherent light (COH) source is presented in App. B.6 and App.B.7, respectively.

3.4. PERFORMANCE

We consider the physical hardware parameter sets as described in our methods section. For each scheme, we have two sets of parameters: 1) the near-term parameters (NTP), which are based on experimental demonstrations and within the reach of present quantum technology, and 2) the future parameters (FP), where we boost some key parameters in the experiment. Three sets (Set-1, Set-2, and Set-3) of operational and coherence times are also considered, in the increasing order of the ratio between the coherence times and gate times (see the Methods section for details). We simulate a square toric surface code of code distance and number of time layers both equal to an even-number d, as shown in Fig. 3.1(e). Since entanglement generation is probabilistic, we consider a maximum time allowed (GHZ cut-off time t_{cut}) for GHZ generation for each stabilizer measurement to maintain synchronicity of the error correction sub-rounds.

The code thresholds are calculated for different physical error possibilities p, which account for both the gate and measurement errors, different coherence-time sets, and the NTP and FP scenarios. For each case, t_{cut} was swept to find the highest threshold p_{th} via a binary search. We report the optimized code threshold for each case using the weighted-growth version of the Union-Find decoder [56] is used to identify the qubit error.

Based on the numerical investigation with different parameter sets, we, in general, required $P_{\text{succ}}^{\text{link}} > 10^{-4}$ and a GHZ fidelity above 99%, for a threshold p_{th} to exist (see App. B.9). Coherence and operational times of Set-1 also serve as the lower bound for the existence of a threshold. Together, these bounds give a rough guide to determine the necessary hardware requirements.

We report that we do not find any code thresholds using a COH photon source for the CAR scheme. As similar performance for the RFL scheme is expected, we skip the simulation of the RFL scheme with a COH source, considering only a deterministic SPS instead. Note that the performance for a non-deterministic SPS can be estimated from this by absorbing the inefficiency of the photon source into the overall detection efficiency.

Thresholds for modular architectures: We present the WT4 architecture threshold results in Fig. 3.6 and WT3 thresholds in Fig. 3.7, where thresholds up to only two decimal places precision are shown. More accurate values can be found in App. B.9.3. We found no threshold for the EM scheme for the NTP, which we believe is primarily due to the

Weight - 4

Scheme	Parameters	$p_{\text{succ}}^{\text{link}}$	p_{th} (Set - 1)	p_{th} (Set - 2)	p_{th} (Set - 3)
Emission based	Near term	0.0001	NT	NT	NT
Emission based	Future	0.0999	NT	NT	0.1323 % ($k = 11$) ✓
Direct Scheme	**Parameters**	$p_{\text{succ}}^{\text{GHZ}}$	p_{th} (Set - 1)	p_{th} (Set - 2)	p_{th} (Set - 3)
Reflection	Near term	0.0147	0.1707	0.2807 % ✓	0.3285 %
Cavity Carving (SPS)	Near term	0.0013	NT	NT	0.3298 % ✓
Waveguide Carving (SPS)	Near term	0.0003	NT	NT	0.0180 % ✓
Reflection	Future	0.3782	0.3443 % ✓	0.3488 % ✓	0.3513 %
Cavity Carving (SPS)	Future	0.0164	0.2387 % ✓	0.3450 % ✓	0.4072 % ✓
Waveguide Carving (SPS)	Future	0.0047	NT	0.2158 % ✓	0.3541 % ✓

NT = No Threshold

Figure 3.6.: Weight-4 toric code thresholds. For every scheme and hardware parameter set, we report the code threshold for each coherence time set. We also report the optimal GHZ generation fusion-based protocol for the EM scheme via the number of Bell pairs (k) used in that protocol. The reported code thresholds (p_{th}), followed by a check mark, are the ones that are higher than the corresponding WT3 toric code threshold. NT represents “no threshold exist”.

Weight - 3

Scheme	Parameters	$p_{\text{succ}}^{\text{link}}$	p_{th} (Set - 1)	p_{th} (Set - 2)	p_{th} (Set - 3)
Emission based	Near term	0.0001	NT	NT	NT
Emission based	Future	0.0999	NT	NT	0.0928 % ($k = 7$)
Direct Scheme	**Parameters**	$p_{\text{succ}}^{\text{GHZ}}$	p_{th} (Set - 1)	p_{th} (Set - 2)	p_{th} (Set - 3)
Reflection	Near term	0.0423	0.1717 % ✓	0.2353 %	0.3350 % ✓
Cavity Carving (SPS)	Near term	0.0041	NT	0.0167 % ✓	0.3062 %
Waveguide Carving (SPS)	Near term	0.0009	NT	NT	NT
Reflection	Future	0.4823	0.2784 %	0.2849 %	0.3521 % ✓
Cavity Carving (SPS)	Future	0.0366	0.1787 %	0.2603 %	0.3678 %
Waveguide Carving (SPS)	Future	0.0098	NT	0.1522 %	0.3441 %

NT = No Threshold

Figure 3.7.: Weight-3 toric code thresholds. Refer to the caption of Fig. 3.6 for the explanation.

low success probability ($P_{\text{succ}}^{\text{link}}$) of Bell pair generation of 10^{-4}. However, even for future parameters (with $P_{\text{succ}}^{\text{link}} = 0.0999$), we get a threshold for only the best coherence times of Set-3. This threshold was found for the protocol with $k = 11(7)$ Bell pairs for the WT4 (WT3) architecture.

For the scattering-based (RFL and CAR) schemes with NTP parameters, we observe promising thresholds (∼0.3%) for some parameter sets. The RFL scheme supports thresholds for all the examined parameter sets. However, for the WT4 architecture, we only get a threshold value for the highest coherence times (Set-3) for the CAV-CAR and WG-CAR schemes with an SPS. For the WT3 architecture, we find no thresholds for WG-CAR scheme. This is associated with the low probability of success for the CAR scheme, around an order of magnitude lower than the RFL scheme. This result suggests that the decoherence noise becomes the dominant error source in this regime due to long waiting times.

In contrast, we see higher thresholds for FP. The RFL scheme has the highest success possibilities, $P_{\text{succ}}^{\text{GHZ}} = 0.3782\ (0.4823)$ for the WT4 (WT3) architecture, boosting the thresholds. The thresholds for the RFL scheme saturate around $\sim 0.35\%$ for WT4, meaning further improvements on the coherence parameters do not increase the threshold due to other noise sources present. However, for the WT3 case, due to the longer QEC cycles, the thresholds improve when the coherence parameters improve. Similarly, for the CAV-CAR protocol, we see a boost in the thresholds, with the highest value of 0.40% for WT4 with Set-3. This happens because the CAV-CAR scheme has higher GHZ state fidelity than the RFL scheme, and with Set-3, the coherence times are high enough for both schemes that the GHZ fidelity becomes the dominant factor in drawing the difference in the performance. Similar trend is seen for WT3. Finally, we get an even lower success probability for the WG-CAR scheme, with no thresholds for coherence times of Set-1. However, rapidly increasing thresholds for Set-2 and Set-3 indicate that the threshold is very sensitive to the coherence times in this regime for both WT4 and WT3 architectures.

Perspective on modular architectures and entangling schemes: The WT4 and WT3 architectures both give rise to competitive code thresholds for all the examined physical parameter sets. When the number of modules is a bottleneck for the experiment, the WT3 architecture can be chosen because it has half the number of modules that are required for the same code distance. However, the QEC cycle times of the WT3 architecture are twice as long for the same distance of the code. The bare WT3 architecture also has an adverse effect due to error propagation within each node, as it has two local data qubits per module that can have hook errors due to local operations within the module. Errors occurring between the stabilizer sub-rounds also affect the decoding of the two modular architectures. Numerically, we find that the WT4 architecture generally has about 5% lower logical error

rates than the WT3 architecture.

The threshold results show that the scattering-based schemes outperform the EM schemes. Two factors are responsible for this. One is that the EM schemes require two-qubit gates involving the memory qubits for Bell pair fusion operations, while the scattering-based schemes do not. The other factor is the high success possibilities $P^{\text{GHZ}}_{\text{succ}}$ for scattering-based schemes, which reduces the t_{cut} for the same ratio of GHZ generation rate. This thereby reduces the effect of decoherence noise on the memory qubits.

We conducted a separate investigation to verify the noise impact via the fusion process in the EM scheme. We considered a fictitious set of parameters for WT4 EM Set-3 (FP). We choose the boosted parameters $P^{\text{link}}_{\text{succ}} = 0.3782$ and Bell-pair fidelity $F_{\text{link}} = 99.75\%$ so that it matches the effective GHZ state fidelity and success probability to the WT4 RFL Set-3 (FP) (with $p_{\text{th}} = 0.35\%$). The new threshold only increased from 0.13% to $\approx 0.16\%$, and saturated around this value despite any further parameter improvements. This lack of improvement in the EM threshold can be explained via the noisy fusion process, which suppresses the performance of the EM scheme.

Sub-threshold performance of the architectures: Most reported thresholds are near $p = 10^{-3}$. We simulated the logical error probability (p_L) for physical error probability as low as $p = 10^{-5}$ and found the smallest code distance for NTP and FP, which gives break-even performance.

The logical error rates for code distance $d = 8$ lattice size are shown in Fig. 3.8(a) for NTP. It shows that $d = 8$ is the smallest code distance for which we get $p_L \ll p$ for at least one combination of architecture and scheme. We show the logical error rates in the FP case in Fig. 3.8(b). We do this for distance $d = 6$, for which we get better than break-even performance. For the smallest $d = 4$, WT4 RFL Set-3 shows just the break-even performance (with $p_L \approx p$) near $p = 10^{-4}$. A preferred scheme and architecture combination can be chosen for the minimal logical error rates. The plot shows that the logical error rates saturate and do not decrease when going near 10^{-5}. This is because the system has residual noise beyond the circuit-level noise, which originates from the hardware that remains constant in the plots.

Additionally, we increase the code distance to see how the logical error rates decrease. Shown in Fig. 3.8(c) for NTP parameters with $p = 10^{-3}$ and Fig. 3.8(d) for NF parameters with $p = 10^{-4}$, respectively. The logical error rates fall exponentially upon increasing the distance below the code threshold. For the NTP parameters, we see break-even performance for WT4 RFL Set-3 with only $d = 8$, and a few other schemes catch up with $d = 10$. We see improved sub-threshold performance for the FP case with a break-even starting lattice size of just $d = 6$. Most of the FP schemes demonstrate $p_L \leq p$ for distance 12 onward.

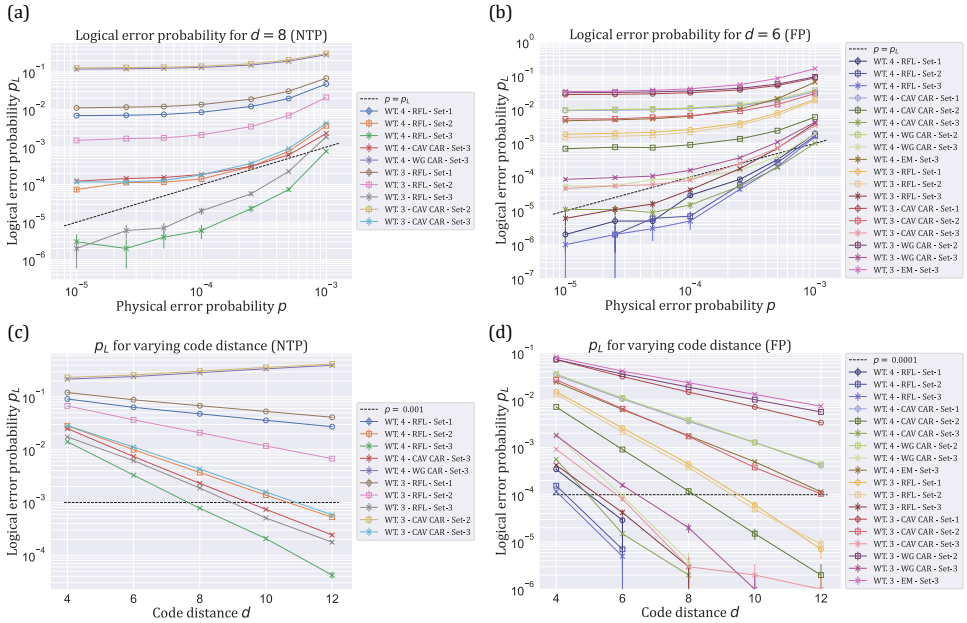

Figure 3.8.: Sub-threshold behavior of architectures that have an error threshold. For clarity, Set-1, Set-2, and Set-3 are shown with circle, square, and cross markers. All curves are checked for monotonicity, including the error bars. (a) Logical error probability (p_L) for NTP for the smallest even-sized code distance $d = 8$ shows better than break-even performance. (b) p_L with FP, for the smallest even-sized code distance $d = 6$, which shows better than break-even performance. (c) p_L for NTP, against varying code distance, with constant $p = 10^{-3}$. For WT4 WG-CAR Set-3 and WT3 CAV-CAR Set-2, we see an increase in p_L for an increase in p because the threshold for these architectures is less than 10^{-3}, which is about 0.01%. (d) p_L with FP, against varying code distance, with constant $p = 10^{-4}$. Some curves are discontinued after a certain code distance because no logical failure was recorded beyond this point, even with 10^6 iterations per data point. More iterations are required for accuracy, but it was beyond our computational resources' ability to estimate.

3.5. DISCUSSION

Our work has outlined several feasible approaches for modular error-corrected quantum computations with solid-state quantum hardware. Our results demonstrate that architectures with either one or two data qubits per module exhibit comparable code thresholds, which are strongly influenced by the choice of GHZ state generation schemes. Besides, we found that scattering-based schemes result in higher thresholds due to the faster and higher quality GHZ state generation for the distributed stabilizer measurements. This is because they circumvent the noisy and slow two-qubit gates and measurements required in the emission-based schemes. Furthermore, we have also provided bounds on the coherence times vs. operation times for the threshold performance of the modular architectures. Architectures with $T_{\text{link}}^{\text{dec}}/t_{\text{link}} < 10^4$ will not be a reliable candidate for distributed modular architectures as defined in our framework. A GHZ state success probability $P_{\text{succ}}^{\text{GHZ}} > 10^{-4}$ and GHZ fidelity $F_{\text{GHZ}} > 99\%$ are required to achieve a code threshold.

While we investigated the surface code due to its well-studied performance, it will be interesting to consider other codes that might better exploit the GHZ-state-enabled nonlocal stabilizer measurements. In particular, codes that could offer reduced qubit overhead, such as the recently introduced quantum low-density parity check (qLDPC) family known as the Bivariate Bicycle (BB) codes, by IBM [57]. Furthermore, extending the simulations to investigate the performance of logical gates and computation [58], even for the surface code, would be an interesting future direction.

3.6. METHODS

Cut-off times: The GHZ state generation is probabilistic for the distributed architecture due to the nature of GHZ generation protocols and due to photon loss and imperfect photon measurements. To maintain the stabilizer synchronicity on the code lattice, we consider a cut-off time (t_{cut}) that caps the maximum time duration allowed for GHZ state generation among the modules before stabilizers are measured. A low t_{cut} will lead to less syndrome measurement information and affect the detection of errors, and a larger t_{cut} will lead to more noise accumulation due to decoherence of the qubits while idle. Therefore, we optimize t_{cut} to find the highest error-correcting threshold of the code.

Operation and coherence times: We consider a broad set of coherence and operation time parameters as shown in Fig. 3.9. There, $T_{\text{link}}^{\text{dec}}$ and $T_{\text{idle}}^{\text{dec}}$ describe the coherence times applicable to the CQs and memory qubits when entanglement generation is attempted and during idling, respectively. Next, we describe the operational times with t_{link}

as the time for one entanglement generation attempt (either a Bell pair generation or direct GHZ state generation), and t_{meas} meaning the measurement time duration for the communication qubit. Further, $t_P^{\text{c/m}}$ is the time duration of a native single-qubit P gate with $P \in \{X, Y, Z, H\}$ acting on the communication (c)/memory (m) qubit. Lastly, we have the two-qubit gate times for controlled-Z, X, iY rotations t_{CZ}, t_{CX}, t_{CiY} and swap operation t_{SWAP}.

We express all the parameters w.r.t. t_{link} duration times. We consider three parameter sets with varying coherence times for link generation and idling. The first set has the lowest coherence times among the ones for which we find code thresholds. Set-2 has increased link coherence times by one order of magnitude, and finally, we consider Set-3, which has coherence times of 10^6.

Although our simulation model allows for distinct T_1 and T_2 times, for each communication and memory qubits, we considered $T^{\text{dec}}_{1,\text{ link}} = T^{\text{dec}}_{2,\text{ link}}$ and $T^{\text{dec}}_{1,\text{ idle}} = T^{\text{dec}}_{2,\text{ idle}}$, where the subscripts 1, 2 denote the T_1 and T_2 decay times. This model describes an effective depolarizing noise on the qubits. We choose this noise model against the optimistic case of pure dephasing where $T^{\text{dec}}_{1,\text{ link}} = \infty$ and $T^{\text{dec}}_{1,\text{ idle}} = \infty$.

Emission-based scheme parameters: We describe these parameters for the EM scheme in Fig. 3.10. Here, F_{prep} [59, 60] describes the fidelity of emitter-photon state preparation, p_{DE} [61] is the probability of the double excitation error on the emitter caused during emitter-photon state preparation, μ is the Hong-Ou-Mandel visibility of the photon interference [61][62], λ is the standard deviation in the path difference for the interference setup [61][63], and the effective photon detection probability is η_{ph} [64]. Furthermore, we have the probability of successful entanglement generation between two nodes $p^{\text{link}}_{\text{succ}}$ which depends on η_{ph} and has the approximate value of $p^{\text{link}}_{\text{succ}} \approx 10^{-4}$ and $p^{\text{link}}_{\text{succ}} \approx 0.099$ for NTP and FP, respectively. The FP sets are inspired by potential improvements in the experiments.

Reflection (RFL) scheme parameters: We simulate the performance of the RFL schemes based on the parameters of the diamond's silicon-vacancy (SiV) color center. The relevant parameters of the physical setup for the RFL scheme are shown in Fig. 3.11. The constrained parameters are based on NTP and FP, and the tunable parameters are based on maximizing the final GHZ state fidelity. The near-term parameters are modeled from recent experimental demonstrations in Refs. [30, 31, 55]. κ_{c} describes the cavity loss rate from the cavity to the coupling fiber. P_{dk} is the dark count rate of the photon detectors, assuming the dark count happens at 1 Hz and the photon detection window is 1 μs. γ denotes the natural linewidth of the spin, κ_{l} is the cavity loss rate from the cavity to the environment. Here, $\Delta = \delta_0 - \delta_1$, with $\delta_0 = E_{0\text{e}} - E_0 - \omega_{\text{ph}}$ and $\delta_1 = E_{1\text{e}} - E_1 - \omega_{\text{ph}}$. σ means the calibration

Parameter Sets	Set - 1	Set - 2	Set - 3
$T_{\text{link}}^{\text{dec}}$	10^4	10^5	10^6
$T_{\text{idle}}^{\text{dec}}$	10^5	10^5	10^6
Operation times			
t_{link}	1	1	1
t_{meas}	1	1	1
t_P^{c}	0.01	0.01	0.01
t_P^{m}	100	100	100
t_{CZ}, t_{CX}, t_{CiY}	100	100	100
t_{SWAP}	300	300	300

Figure 3.9.: Coherence times and operation times. All values are expressed w.r.t. t_{link}, which is assumed to take one unit of time.

EM	NTP	FP
F_{prep}	0.99	0.999
p_{DE}	0.04	0.01
μ	0.9	0.95
λ	0.984	1
η	0.0046	0.4472

Figure 3.10.: Parameter sets for the emission-based scheme.

error in δ_1 and δ_0. The cavity cooperativity, C_1, between the spin and the one-side cavity, is defined as $C_1 = \frac{g_1^2}{\gamma(\kappa_c+\kappa_l)}$, with g_1 the coupling strength of the spin and the one-side cavity. Finally, η_c is the circulator efficiency of preserving a photon and ω is defined as $\omega = \omega_{ph} - \omega_c$.

Cavity-carving (CAV-CAR) scheme parameters: The parameters for the CAV-CAR scheme are presented in Fig. 3.12, for both single-photon source (SPS) and coherent photon source (COH). Like the RFL scheme, NTP for the CAV-CAR scheme is also modeled from recent experimental demonstrations in Refs. [30, 31, 55]. Here, C_2 is the cooperativity between the spin and the two-side cavity defined as $C_2 = \frac{g_2^2}{\gamma(2\kappa_c+\kappa_l)}$, with g_2 the coupling strength of the spin and the two-side cavity. η_f captures the fiber efficiency of preserving a photon. n_{sc} indicates the number of total scattering times and α is the parameter of the coherent state $|\alpha\rangle$ (not to be confused with α as the bright-state parameter in the EM scheme). Other hardware parameters are similar to the RFL scheme. The detailed methods for calculating the final GHZ state with the SPS is shown in App. B.6, and the one with COH is shown in App. B.7.

Waveguide-carving (WG-CAR) scheme parameters: The parameters for the CAV-CAR scheme are shown in Fig. 3.13, respectively. Here, $P = \Gamma/\gamma$, with Γ being the intensity of the light emitted from the spin and going into the waveguide. Other variables are the same as the CAV-CAR scheme. The NTP sets are inspired from the same recent experiments as the RFL scheme parameters.

Logical error rates and thresholds: To calculate the logical error rates, we start with the noisy GHZ state (on the communication qubits) generated by the entangling schemes parameterized by all the input hardware parameters for that architecture. We simulate the X and Z stabilizer unit cell for the architecture's lattice using our source code CircuitSimulator. This is done by executing circuits in Fig. 3.1(d) and Fig. 3.2(b). It results in the density matrix of all the qubits involved in the stabilizer measurement, including all communication and memory qubits. All the qubits, except the data qubits of the code, are measured at the end. This projects the data qubits in the desired stabilizer state. We find this effective projector acting on the data qubits of the code, similar to Ref. [13]. The Pauli twirled representation of this superoperator is

$$\Pi_M^{\text{eff}}(\rho_D) = \sum_e (a_e^M E_e \Pi_M^{\text{ideal}}(\rho_D) E_e^\dagger + b_e^{\bar{M}} E_e \Pi_{\bar{M}}^{\text{ideal}}(\rho_D) E_e^\dagger) \tag{3.1}$$

where ρ_D is the data qubits' density matrix, and Π_M denotes the projector due to the measurement, acting on the state. E_e are all the possible Pauli errors acting on the data qubits in the unit cell of the code lattice, and the bar denotes a measurement error. Coefficients a_e and b_e are estimated by calculating the overlap of a given Pauli error string

RFL	Constrained parameters							Tuneable parameters	
	κ_c/γ	P_{dk}	$\frac{\kappa_c}{\kappa_c+\kappa_1}$	$\frac{\Delta}{\gamma}$	$\frac{\sigma}{\gamma}$	C_1	η_c	$\frac{\delta_1}{\gamma}$	$\frac{\omega}{\gamma}$
NTP	200	10^{-6}	0.90	16	0.46	30	0.5	16.3	283.0
FP	200	10^{-6}	0.95	122	0.32	40	0.9	32.2	130.7

Figure 3.11.: System parameters of the reflection scheme (RFL).

CAV CAR		Constrained parameters							Tuneable parameters					
		κ_c/γ	P_{dk}	$\frac{2\kappa_c}{2\kappa_c+\kappa_1}$	$\frac{\Delta}{\gamma}$	$\frac{\sigma}{\gamma}$	C_2	η_{f}	$\frac{\delta_1}{\gamma}$	$\frac{\omega}{\gamma}$	Weight-4		Weight-3	
											n_{sc}	α	n_{sc}	α
NTP	SPS	200	10^{-6}	0.9	16	0.46	30	0.5	0	832.5	2	-	2	-
	COH										2	0.54	2	0.41
FP	SPS	200	10^{-6}	0.95	122	0.32	40	0.9	0	138.0	2	-	2	-
	COH										2	0.54	2	0.24

Figure 3.12.: Hardware parameters of the cavity carving scheme (CAV-CAR).

WG CAR		Constrained parameters					Tuneable parameters				
		P_{dk}	$\frac{\Delta}{\gamma}$	$\frac{\sigma}{\gamma}$	P	η_{f}	$\frac{\delta_1}{\gamma}$	Weight-4		Weight-3	
								n_{sc}	α	n_{sc}	α
NTP	SPS	10^{-6}	16	0.46	5	0.5	0	4	-	4	-
	COH							2	0.29	2	0.28
FP	SPS	10^{-6}	122	0.32	20	0.9	0	4	-	4	-
	COH							2	0.26	2	0.22

Figure 3.13.: Hardware parameters of waveguide-carving (WG-CAR) scheme.

with the superoperator. This superoperator object is then represented as a table with all possible error configurations. Errors are then sampled from the superoperator onto the unit cells of a given code lattice of distance d. This task is done via our software package Qsurface that samples errors from the superoperator and then decodes for the errors using the UnionFind decoder to calculate the logical error rates. The logical error rates are then fitted to the curve $p_L = A + B\gamma + C\gamma^2$, where p_L is the logical error rate, $\gamma = (p - p_{\text{th}})L^{1/\nu_0}$, where L is the lattice size of the code, p is the physical error probability and $A, B, C, p_{\text{th}}, \nu_0$ are the fitting parameters. We estimate the threshold p_{th} using this fit.

ACKNOWLEDGMENTS

The authors thank Tim Taminiau, Ronald Hanson, Erwin van Zwet, and Barbara Terhal for helpful discussions and feedback. We gratefully acknowledge support from the joint research program “Modular quantum computers” by Fujitsu Limited and Delft University of Technology, co-funded by the Netherlands Enterprise Agency under project number PPS2007. D.E. was partially supported by the JST Moonshot R&D program under Grant JPMJMS226C. J.B. acknowledges support from The AWS Quantum Discovery Fund at the Harvard Quantum Initiative. We thank SURF (www.surf.nl) for the support in using the National Supercomputer Snellius.

SOURCE CODE AND DATA AVAILABILITY

The source code and simulation for this research’s findings are openly available in 4TU.ResearchData [65].

REFERENCES

[1] S. Singh, F. Gu, S. de Bone, E. Villaseñor, D. Elkouss, and J. Borregaard. “Modular Architectures and Entanglement Schemes for Error-Corrected Distributed Quantum Computation”. In: *arXiv preprint arXiv:2408.02837* (2024).

[2] S. J. Devitt, W. J. Munro, and K. Nemoto. “Quantum error correction for beginners”. In: *Reports on Progress in Physics* 76.7 (June 2013), p. 076001.

[3] J. Roffe. “Quantum error correction: an introductory guide”. In: *Contemporary Physics* 60.3 (July 2019), pp. 226–245.

[4] D. Bluvstein, S. J. Evered, A. A. Geim, S. H. Li, H. Zhou, T. Manovitz, S. Ebadi, M. Cain, M. Kalinowski, D. Hangleiter, J. P. Bonilla Ataides, N. Maskara, I. Cong, X. Gao, P. Sales Rodriguez, T. Karolyshyn, G. Semeghini, M. J. Gullans, M. Greiner, V. Vuletić, and M. D. Lukin. “Logical quantum processor based on reconfigurable atom arrays”. In: *Nature* 626.7997 (Feb. 2024), pp. 58–65.

[5] M. Caleffi, M. Amoretti, D. Ferrari, D. Cuomo, J. Illiano, A. Manzalini, and A. S. Cacciapuoti. *Distributed Quantum Computing: a Survey*. 2022.

[6] H. Aghaee Rad, T. Ainsworth, R. N. Alexander, B. Altieri, M. F. Askarani, R. Baby, L. Banchi, B. Q. Baragiola, J. E. Bourassa, R. S. Chadwick, I. Charania, H. Chen, M. J. Collins, P. Contu, N. D’Arcy, G. Dauphinais, R. De Prins, D. Deschenes, I. Di Luch, S. Duque, P. Edke, S. E. Fayer, S. Ferracin, H. Ferretti, J. Gefaell, S. Glancy, C. González-Arciniegas, T. Grainge, Z. Han, J. Hastrup, L. G. Helt, T. Hillmann, J. Hundal, S. Izumi, T. Jaeken, M. Jonas, S. Kocsis, I. Krasnokutska, M. V. Larsen, P. Laskowski, F. Laudenbach, J. Lavoie, M. Li, E. Lomonte, C. E. Lopetegui, B. Luey, A. P. Lund, C. Ma, L. S. Madsen, D. H. Mahler, L. Mantilla Calderón, M. Menotti, F. M. Miatto, B. Morrison, P. J. Nadkarni, T. Nakamura, L. Neuhaus, Z. Niu, R. Noro, K. Papirov, A. Pesah, D. S. Phillips, W. N. Plick, T. Rogalsky, F. Rortais, J. Sabines-Chesterking, S. Safavi-Bayat, E. Sazhaev, M. Seymour, K. Rezaei Shad, M. Silverman, S. A. Srinivasan, M. Stephan, Q. Y. Tang, J. F. Tasker, Y. S. Teo, R. B. Then, J. E. Tremblay, I. Tzitrin, V. D. Vaidya, M. Vasmer, Z. Vernon, L. F. S. S. M. Villalobos, B. W. Walshe, R. Weil, X. Xin, X. Yan, Y. Yao, M. Zamani Abnili, and Y. Zhang. “Scaling and networking

a modular photonic quantum computer". In: *Nature* 638.8052 (Feb. 2025), pp. 912–919.

[7] H. Bombin, I. H. Kim, D. Litinski, N. Nickerson, M. Pant, F. Pastawski, S. Roberts, and T. Rudolph. *Interleaving: Modular architectures for fault-tolerant photonic quantum computing*. 2021.

[8] R. VAN METER, T. D. LADD, A. G. FOWLER, and Y. YAMAMOTO. "DISTRIBUTED QUANTUM COMPUTATION ARCHITECTURE USING SEMICONDUCTOR NANOPHOTONICS". In: *International Journal of Quantum Information* 08.01n02 (Feb. 2010), pp. 295–323.

[9] D. Main, P. Drmota, D. P. Nadlinger, E. M. Ainley, A. Agrawal, B. C. Nichol, R. Srinivas, G. Araneda, and D. M. Lucas. "Distributed quantum computing across an optical network link". In: *Nature* 638.8050 (Feb. 2025), pp. 383–388.

[10] J. I. Cirac, A. K. Ekert, S. F. Huelga, and C. Macchiavello. "Distributed quantum computation over noisy channels". In: *Phys. Rev. A* 59 (6 June 1999), pp. 4249–4254.

[11] R. Van Meter and D. Horsman. "A blueprint for building a quantum computer". In: *Commun. ACM* 56.10 (Oct. 2013), pp. 84–93.

[12] D. Ferrari, S. Carretta, and M. Amoretti. "A Modular Quantum Compilation Framework for Distributed Quantum Computing". In: *IEEE Transactions on Quantum Engineering* 4 (2023), pp. 1–13.

[13] N. H. Nickerson, Y. Li, and S. C. Benjamin. "Topological quantum computing with a very noisy network and local error rates approaching one percent". In: *Nature Communications* 4.1 (Apr. 2013), p. 1756.

[14] S. Bravyi, O. Dial, J. M. Gambetta, D. Gil, and Z. Nazario. "The future of quantum computing with superconducting qubits". In: *Journal of Applied Physics* 132.16 (Oct. 2022), p. 160902.

[15] J. Ramette, J. Sinclair, Z. Vendeiro, A. Rudelis, M. Cetina, and V. Vuleti ć. "Any-To-Any Connected Cavity-Mediated Architecture for Quantum Computing with Trapped Ions or Rydberg Arrays". In: *PRX Quantum* 3 (1 Mar. 2022), p. 010344.

[16] Y. Li and J. Thompson. *High-rate and high-fidelity modular interconnects between neutral atom quantum processors*. 2024.

[17] L. Li, L. D. Santis, I. B. W. Harris, K. C. Chen, Y. Gao, I. Christen, H. Choi, M. Trusheim, Y. Song, C. Errando-Herranz, J. Du, Y. Hu, G. Clark, M. I. Ibrahim, G. Gilbert, R. Han, and D. Englund. "Heterogeneous integration of spin–photon interfaces with a CMOS platform". In: *Nature* (2024).

[18] F. Afzal, M. Akhlaghi, S. J. Beale, O. Bedroya, K. Bell, L. Bergeron, K. Bonsma-Fisher, P. Bychkova, Z. M. E. Chaisson, C. Chartrand, C. Clear, A. Darcie, A. DeAbreu, C. DeLisle, L. A. Duncan, C. D. Smith, J. Dunn, A. Ebrahimi, N. Evetts, D. F. Pinheiro, P. Fuentes, T. Georgiou, B. Guha, R. Haenel, D. Higginbottom, D. M. Jackson, N. Jahed, A. Khorshidahmad, P. K. Shandilya, A. T. K. Kurkjian, N. Lauk, N. R. Lee-Hone, E. Lin, R. Litynskyy, D. Lock, L. Ma, I. MacGilp, E. R. MacQuarrie, A. Mar, A. M. Khah, A. Matiash, E. Meyer-Scott, C. P. Michaels, J. Motira, N. K. Noori, E. Ospadov, E. Patel, A. Patscheider, D. Paulson, A. Petruk, A. L. Ravindranath, B. Reznychenko, M. Ruether, J. Ruscica, K. Saxena, Z. Schaller, A. Seidlitz, J. Senger, Y. S. Lee, O. Sevoyan, S. Simmons, O. Soykal, L. Stott, Q. Tran, S. Tserkis, A. Ulhaq, W. Vine, R. Weeks, G. Wolfowicz, and I. Yoneda. *Distributed Quantum Computing in Silicon*. 2024.

[19] S. de Bone, P. Möller, C. E. Bradley, T. H. Taminiau, and D. Elkouss. “Thresholds for the distributed surface code in the presence of memory decoherence”. In: *AVS Quantum Science* 6.3 (July 2024), p. 033801.

[20] J. Ramette, J. Sinclair, N. P. Breuckmann, and V. Vuletić. *Fault-Tolerant Connection of Error-Corrected Qubits with Noisy Links*. 2023.

[21] H. K. Beukers, M. Pasini, H. Choi, D. Englund, R. Hanson, and J. Borregaard. “Remote-Entanglement Protocols for Stationary Qubits with Photonic Interfaces”. In: *PRX Quantum* 5 (1 Mar. 2024), p. 010202.

[22] B. M. Terhal. “Quantum error correction for quantum memories”. In: *Rev. Mod. Phys.* 87 (2 Apr. 2015), pp. 307–346.

[23] N. P. Breuckmann and J. N. Eberhardt. “Quantum Low-Density Parity-Check Codes”. In: *PRX Quantum* 2 (4 Oct. 2021), p. 040101.

[24] M. H. Abobeih, Y. Wang, J. Randall, S. J. H. Loenen, C. E. Bradley, M. Markham, D. J. Twitchen, B. M. Terhal, and T. H. Taminiau. “Fault-tolerant operation of a logical qubit in a diamond quantum processor”. In: *Nature* 606.7916 (June 2022), pp. 884–889.

[25] C. E. Bradley, S. W. de Bone, P. F. W. Möller, S. Baier, M. J. Degen, S. J. H. Loenen, H. P. Bartling, M. Markham, D. J. Twitchen, R. Hanson, D. Elkouss, and T. H. Taminiau. “Robust quantum-network memory based on spin qubits in isotopically engineered diamond”. In: *npj Quantum Information* 8.1 (Oct. 2022), p. 122.

[26] A. Sipahigil, R. E. Evans, D. D. Sukachev, M. J. Burek, J. Borregaard, M. K. Bhaskar, C. T. Nguyen, J. L. Pacheco, H. A. Atikian, C. Meuwly, R. M. Camacho, F. Jelezko, E. Bielejec, H. Park, M. Lončar, and M. D. Lukin. “An integrated diamond nanophotonics platform

for quantum-optical networks". In: *Science* 354.6314 (2016), pp. 847–850.

[27] D. D. Sukachev, A. Sipahigil, C. T. Nguyen, M. K. Bhaskar, R. E. Evans, F. Jelezko, and M. D. Lukin. "Silicon-Vacancy Spin Qubit in Diamond: A Quantum Memory Exceeding 10 ms with Single-Shot State Readout". In: *Phys. Rev. Lett.* 119 (22 Nov. 2017), p. 223602.

[28] C. T. Nguyen, D. D. Sukachev, M. K. Bhaskar, B. Machielse, D. S. Levonian, E. N. Knall, P. Stroganov, C. Chia, M. J. Burek, R. Riedinger, H. Park, M. Lon čar, and M. D. Lukin. "An integrated nanophotonic quantum register based on silicon-vacancy spins in diamond". In: *Phys. Rev. B* 100 (16 Oct. 2019), p. 165428.

[29] C. T. Nguyen, D. D. Sukachev, M. K. Bhaskar, B. Machielse, D. S. Levonian, E. N. Knall, P. Stroganov, R. Riedinger, H. Park, M. Lon čar, and M. D. Lukin. "Quantum Network Nodes Based on Diamond Qubits with an Efficient Nanophotonic Interface". In: *Phys. Rev. Lett.* 123 (18 Oct. 2019), p. 183602.

[30] P.-J. Stas, Y. Q. Huan, B. Machielse, E. N. Knall, A. Suleymanzade, B. Pingault, M. Sutula, S. W. Ding, C. M. Knaut, D. R. Assumpcao, Y.-C. Wei, M. K. Bhaskar, R. Riedinger, D. D. Sukachev, H. Park, M. Lončar, D. S. Levonian, and M. D. Lukin. "Robust multi-qubit quantum network node with integrated error detection". In: *Science* 378.6619 (2022), pp. 557–560.

[31] C. M. Knaut, A. Suleymanzade, Y. .-. Wei, D. R. Assumpcao, P. .-. Stas, Y. Q. Huan, B. Machielse, E. N. Knall, M. Sutula, G. Baranes, N. Sinclair, C. De-Eknamkul, D. S. Levonian, M. K. Bhaskar, H. Park, M. Lončar, and M. D. Lukin. "Entanglement of nanophotonic quantum memory nodes in a telecom network". In: *Nature* 629.8012 (2024), pp. 573–578.

[32] T. Iwasaki, Y. Miyamoto, T. Taniguchi, P. Siyushev, M. H. Metsch, F. Jelezko, and M. Hatano. "Tin-Vacancy Quantum Emitters in Diamond". In: *Phys. Rev. Lett.* 119 (25 Dec. 2017), p. 253601.

[33] A. E. Rugar, S. Aghaeimeibodi, D. Riedel, C. Dory, H. Lu, P. J. McQuade, Z.-X. Shen, N. A. Melosh, and J. Vu čkovi ć. "Quantum Photonic Interface for Tin-Vacancy Centers in Diamond". In: *Phys. Rev. X* 11 (3 July 2021), p. 031021.

[34] R. Debroux, C. P. Michaels, C. M. Purser, N. Wan, M. E. Trusheim, J. Arjona Martínez, R. A. Parker, A. M. Stramma, K. C. Chen, L. de Santis, E. M. Alexeev, A. C. Ferrari, D. Englund, D. A. Gangloff, and M. Atatüre. "Quantum Control of the Tin-Vacancy Spin Qubit in Diamond". In: *Phys. Rev. X* 11 (4 Nov. 2021), p. 041041.

[35] S. Simmons. “Scalable Fault-Tolerant Quantum Technologies with Silicon Color Centers”. In: *PRX Quantum* 5 (1 Mar. 2024), p. 010102.

[36] A. Kitaev. “Fault-tolerant quantum computation by anyons”. In: *Annals of Physics* 303.1 (2003), pp. 2–30.

[37] S. B. Bravyi and A. Y. Kitaev. *Quantum codes on a lattice with boundary*. 1998.

[38] E. Dennis, A. Kitaev, A. Landahl, and J. Preskill. “Topological quantum memory”. In: *Journal of Mathematical Physics* 43.9 (Sept. 2002), pp. 4452–4505.

[39] A. G. Fowler, M. Mariantoni, J. M. Martinis, and A. N. Cleland. “Surface codes: Towards practical large-scale quantum computation”. In: *Phys. Rev. A* 86 (3 Sept. 2012), p. 032324.

[40] H. Bernien, B. Hensen, W. Pfaff, G. Koolstra, M. S. Blok, L. Robledo, T. H. Taminiau, M. Markham, D. J. Twitchen, L. Childress, and R. Hanson. “Heralded entanglement between solid-state qubits separated by three metres”. In: *Nature* 497.7447 (May 2013), pp. 86–90.

[41] S. Welte, B. Hacker, S. Daiss, S. Ritter, and G. Rempe. “Photon-Mediated Quantum Gate between Two Neutral Atoms in an Optical Cavity”. In: *Phys. Rev. X* 8 (1 Feb. 2018), p. 011018.

[42] N. H. Nickerson, J. F. Fitzsimons, and S. C. Benjamin. “Freely Scalable Quantum Technologies Using Cells of 5-to-50 Qubits with Very Lossy and Noisy Photonic Links”. In: *Phys. Rev. X* 4 (4 Dec. 2014), p. 041041.

[43] M. Ruf, M. Weaver, S. van Dam, and R. Hanson. “Resonant Excitation and Purcell Enhancement of Coherent Nitrogen-Vacancy Centers Coupled to a Fabry-Perot Microcavity”. In: *Phys. Rev. Appl.* 15 (2 Feb. 2021), p. 024049.

[44] E. Dennis, A. Kitaev, A. Landahl, and J. Preskill. “Topological quantum memory”. In: *Journal of Mathematical Physics* 43.9 (Sept. 2002), pp. 4452–4505.

[45] C. Cabrillo, J. I. Cirac, P. García-Fernández, and P. Zoller. “Creation of entangled states of distant atoms by interference”. In: *Phys. Rev. A* 59 (2 Feb. 1999), pp. 1025–1033.

[46] A. J. Stolk, K. L. van der Enden, M.-C. Slater, I. te Raa-Derckx, P. Botma, J. Van Rantwijk, J. B. Biemond, R. A. Hagen, R. W. Herfst, W. D. Koek, *et al.* “Metropolitan-scale heralded entanglement of solid-state qubits”. In: *Science advances* 10.44 (2024), eadp6442.

[47] L. Childress and R. Hanson. “Diamond NV centers for quantum computing and quantum networks”. In: *MRS Bulletin* 38.2 (Feb. 2013), pp. 134–138.

[48] R. E. Evans, M. K. Bhaskar, D. D. Sukachev, C. T. Nguyen, A. Sipahigil, M. J. Burek, B. Machielse, G. H. Zhang, A. S. Zibrov, E. Bielejec, *et al.* “Photon-mediated interactions between quantum emitters in a diamond nanocavity”. In: *Science* 362.6415 (2018), pp. 662–665.

[49] A. Reiserer, N. Kalb, G. Rempe, and S. Ritter. “A quantum gate between a flying optical photon and a single trapped atom”. In: *Nature* 508.7495 (2014), pp. 237–240.

[50] N. Kalb, A. Reiserer, S. Ritter, and G. Rempe. “Heralded storage of a photonic quantum bit in a single atom”. In: *Physical review letters* 114.22 (2015), p. 220501.

[51] M. K. Bhaskar, R. Riedinger, B. Machielse, D. S. Levonian, C. T. Nguyen, E. N. Knall, H. Park, D. Englund, M. Lončar, D. D. Sukachev, *et al.* “Experimental demonstration of memory-enhanced quantum communication”. In: *Nature* 580.7801 (2020), pp. 60–64.

[52] Y.-C. Wei, P.-J. Stas, A. Suleymanzade, G. Baranes, F. Machado, Y. Q. Huan, C. M. Knaut, W. S. Ding, M. Merz, E. N. Knall, *et al.* “Universal distributed blind quantum computing with solid-state qubits”. In: *arXiv preprint arXiv:2412.03020* (2024).

[53] S. Welte, B. Hacker, S. Daiss, S. Ritter, and G. Rempe. “Cavity Carving of Atomic Bell States”. In: *Phys. Rev. Lett.* 118 (21 May 2017), p. 210503.

[54] S. D. Barrett and P. Kok. “Efficient high-fidelity quantum computation using matter qubits and linear optics”. In: *Phys. Rev. A* 71 (6 June 2005), p. 060310.

[55] M. K. Bhaskar, R. Riedinger, B. Machielse, D. S. Levonian, C. T. Nguyen, E. N. Knall, H. Park, D. Englund, M. Lončar, D. D. Sukachev, and M. D. Lukin. “Experimental demonstration of memory-enhanced quantum communication”. In: *Nature* 580.7801 (2020), pp. 60–64.

[56] N. Delfosse and N. H. Nickerson. “Almost-linear time decoding algorithm for topological codes”. In: *Quantum* 5 (Dec. 2021), p. 595.

[57] S. Bravyi, A. W. Cross, J. M. Gambetta, D. Maslov, P. Rall, and T. J. Yoder. “High-threshold and low-overhead fault-tolerant quantum memory”. In: *Nature* 627.8005 (Mar. 2024), pp. 778–782.

[58] C. Gidney and M. Ekerå. “How to factor 2048 bit RSA integers in 8 hours using 20 million noisy qubits”. In: *Quantum* 5 (Apr. 2021), p. 433.

[59] B. Hensen, H. Bernien, A. E. Dréau, A. Reiserer, N. Kalb, M. S. Blok, J. Ruitenberg, R. F. L. Vermeulen, R. N. Schouten, C. Abellán, W. Amaya, V. Pruneri, M. W. Mitchell, M. Markham, D. J. Twitchen, D. Elkouss, S. Wehner, T. H. Taminiau, and R. Hanson. "Loophole-free Bell inequality violation using electron spins separated by 1.3 kilometres". In: *Nature* 526.7575 (Oct. 2015), pp. 682–686.

[60] F. Rozp ędek, R. Yehia, K. Goodenough, M. Ruf, P. C. Humphreys, R. Hanson, S. Wehner, and D. Elkouss. "Near-term quantum-repeater experiments with nitrogen-vacancy centers: Overcoming the limitations of direct transmission". In: *Phys. Rev. A* 99 (5 May 2019), p. 052330.

[61] P. C. Humphreys, N. Kalb, J. P. J. Morits, R. N. Schouten, R. F. L. Vermeulen, D. J. Twitchen, M. Markham, and R. Hanson. "Deterministic delivery of remote entanglement on a quantum network". In: *Nature* 558.7709 (June 2018), pp. 268–273.

[62] M. Pompili, S. L. N. Hermans, S. Baier, H. K. C. Beukers, P. C. Humphreys, R. N. Schouten, R. F. L. Vermeulen, M. J. Tiggelman, L. dos Santos Martins, B. Dirkse, S. Wehner, and R. Hanson. "Realization of a multinode quantum network of remote solid-state qubits". In: *Science* 372.6539 (2021), pp. 259–264.

[63] A. Dahlberg, M. Skrzypczyk, T. Coopmans, L. Wubben, F. Rozpundefineddek, M. Pompili, A. Stolk, P. Pawełczak, R. Knegjens, J. de Oliveira Filho, R. Hanson, and S. Wehner. "A link layer protocol for quantum networks". In: *Proceedings of the ACM Special Interest Group on Data Communication*. SIGCOMM '19. Beijing, China: Association for Computing Machinery, 2019, pp. 159–173.

[64] T. Coopmans, R. Knegjens, A. Dahlberg, D. Maier, L. Nijsten, J. de Oliveira Filho, M. Papendrecht, J. Rabbie, F. Rozpędek, M. Skrzypczyk, L. Wubben, W. de Jong, D. Podareanu, A. Torres-Knoop, D. Elkouss, and S. Wehner. "NetSquid, a NETwork Simulator for QUantum Information Using Discrete Events". In: *Communications Physics* 4.1 (July 2021), pp. 1–15.

[65] S. Singh, F. Gu, S. de Bone, E. Villaseñor, D. Elkouss, and J. Borregaard. *Source code and data underlying the publication "Modular Architectures and Entanglement Schemes for Error-Corrected Distributed Quantum Computation";* 2024.

4

HYBRID QUANTUM REPEATER BASED ON SINGLE-SPIN PHOTON TRANSDUCER AND ENSEMBLE-BASED QUANTUM MEMORY*

Fenglei Gu, Shankar G Menon, David Maier, Antariksha Das, Tanmoy Chakraborty, Wolfgang Tittel, Hannes Bernien, Johannes Borregaard

臭腐复化为神奇 *(From decay and corruption, the marvelous arises.)*

–庄周（ZHUANG Zhou, c. 369–286 BCE）

*The work presented in this chapter is published on arXiv 2401.12395[1]. F.G. modeled the Rb atom entangled photon source, performed the repeater modeling and optimization, and wrote the manuscript together with the co-authors.

4

Reliable quantum communication over hundreds of kilometers is a daunting yet necessary requirement for a quantum internet. To overcome photon loss, the deployment of quantum repeater stations between distant network nodes is necessary. A plethora of different quantum hardware is being developed for this purpose, each platform with its own opportunities and challenges. Here, we propose to combine two promising hardware platforms in a hybrid quantum repeater architecture to lower the cost and boost the performance of long-distance quantum communication. We outline how ensemble-based quantum memories combined with single-spin photon transducers, which can transfer quantum information between a photon and a single spin, can facilitate massive multiplexing, efficient photon generation, and quantum logic for amplifying communication rates. As a specific example, we describe how a single Rubidium (Rb) atom coupled to nanophotonic resonators can function as a high-rate, telecom-visible entangled photon source with the visible photon being compatible with storage in a Thulium-doped crystal memory (Tm-memory) and the telecom photon being compatible with low loss fiber propagation. We experimentally verify that the Tm and Rb transitions are in resonance with each other. Our analysis shows that by employing up to nine repeater stations, each equipped with two Tm-memories capable of holding up to 625 storage modes, along with four single Rb atoms, one can reach a quantum communication rate of about 10 secret bits per second across distances of up to 1000 km.

4.1. INTRODUCTION

The ability to transmit quantum information reliably between distant parties is a prerequisite for any useful application of a quantum internet [2, 3]. The primary challenge to achieve this is the exponential attenuation of optical signals in fiber-based networks. To overcome this challenge, quantum repeaters have been proposed where the distance is divided into shorter segments over which entanglement can be established in a heralded fashion. Once entanglement has been successfully established over the segments, entanglement swapping can extend the entanglement over the total distance [4, 5].

Different quantum hardware such as solid-state defect centers [6, 7], atomic ensembles [8–10], trapped ions [11, 12], rare-earth ions [13, 14], and quantum dots [15] are currently being developed to enable a functional quantum repeater. There exist numerous theoretical proposals for repeater architectures tailored to the specific features of each hardware [16–19].

Quantum repeaters with ensemble-based quantum memories, pioneered by the Duan-Lukin-Cirac-Zoller (DLCZ) protocol [20], have been pursued extensively experimentally due to their technological simplicity and multiplexing capabilities [21–23]. However, using ensembles makes it difficult to perform quantum logic on the stored information. Repeater protocols thus resort to probabilistic entanglement swapping schemes based on linear optics, severely limiting the performance. In addition, the probabilistic generation of approximate pairs of entangled photons from either the ensembles themselves or external Spontaneous Parametric Down Conversion (SPDC) sources leads to a fundamental trade-off between the rate and fidelity of the communication [24, 25] severely limiting the usefulness of repeaters.

Quantum repeaters based on individual atoms or atom-like defects represent an alternative route [6, 7, 26]. Near-deterministic single-spin photon transducers, which can transfer quantum information between a photon and a single spin, can be achieved by coupling the atomic system to optical resonators enabling efficient single-photon generation [27–29]. The ability to manipulate the hyperfine states of single atoms allows for quantum logic enabling deterministic entanglement swapping and purification techniques [30]. However, repeater protocols based on merely individually trapped atoms make large multiplexing a formidable challenge given current technology.

Here, we propose to combine ensemble-based quantum memories with single-spin photon transducers to enable a near-term hybrid quantum repeater with massive multiplexing, efficient photon generation, and near-deterministic entanglement swapping. In our scheme, a single-spin photon transducer is used for high-rate generation of entangled photon pairs where, for each pair, one photon is to be stored in a multi-mode ensemble-based memory in a repeater node and the other to be

transmitted through a fiber to generate distant entanglement over the elementary segment between the nodes. Successfully entangled stored photons are read out from the memories and near-deterministic entanglement swapping can be accomplished with the aid of extra single-spin photon transducers, thereby extending entanglement over neighboring elementary segments.

Furthermore, we outline a specific implementation with cavity-coupled single Rb atoms and Tm-doped crystal memories. We show how a single Rb atom coupled to two nanophotonic cavities with visible and telecom resonance frequencies, respectively, can function as a robust photon-pair source producing entangled visible and telecom photons. The telecom photon can propagate in standard optical fibers with minimum loss [31] and we experimentally verify that the visible photon is compatible with the resonance of the Tm-doped crystal. Thus no frequency conversion is required for the repeater. We simulate the performance of the repeater for quantum key distribution and show that rates of tens of secret bits per second over distances of up to 1000 km can be achieved with up to 9 repeater stations, each containing only two ensemble-based memories and four single Rb atoms. Further increase of the rate is possible through additional multiplexing.

The article is organized as follows: Section II introduces the overall protocol and the mechanism of the entanglement swapping. Section III discusses the mechanism by which Rb atoms emit both telecom and visible photons. Section IV presents an experimental study demonstrating the compatibility between the Rb photon source and quantum memory based on Tm:$LiNbO_3$. In Section V, we show the simulation results of the repeater chain. Finally, Section VI offers a general discussion and an outlook.

4.2. STRUCTURE OF THE REPEATER CHAIN PROTOCOL

The general structure of the quantum repeater, composed of the single-spin photon transducers and ensemble-based quantum memories, is depicted in Fig. 4.1. The protocol is designed to distribute entanglement between two distant end nodes, Alice and Bob. It divides the total distance between Alice and Bob into multiple segments. In each segment, we use photon transducers to repeatedly emit entangled photon pairs on each side, storing one photon from each pair in the ensemble-based memories and attempting heralded entanglement generation over the segment with the other photons. Upon success, the now entangled photons are retrieved from the memories on each side and mapped into single-atom systems in a heralded fashion. This is followed by entanglement swapping using local Bell measurements to generate entanglement between Alice and Bob. The protocol thus consists of three main steps: entanglement generation, entanglement

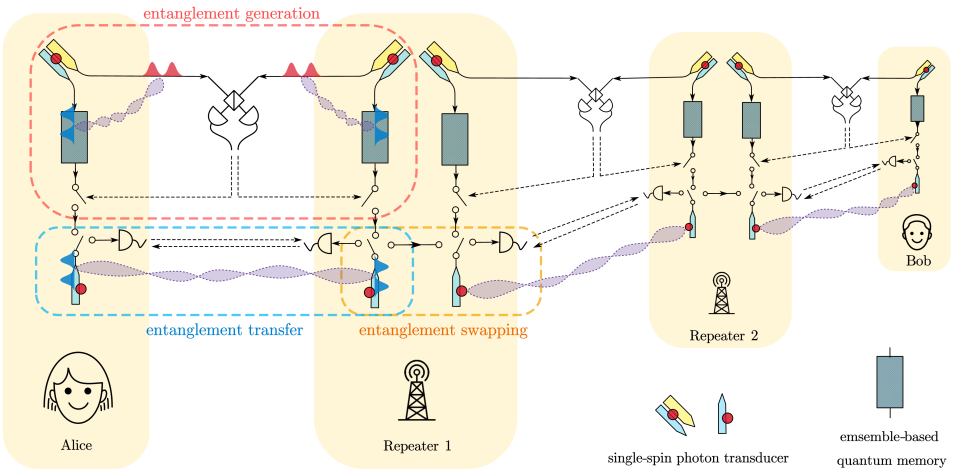

Figure 4.1.: Structure of the quantum repeater chain architecture. The whole system contains two end-nodes, Alice and Bob, connected by a series of repeater nodes. This figure depicts an example with two repeater nodes showcasing the key components involved. The yellow blocks represent the repeater nodes with the local devices depicted within. The protocol involves three main steps: entanglement generation, entanglement transfer, and entanglement swapping, as circled with dashed lines in different colors in the figure. The whole protocol harnesses two kinds of devices as the key components – the single-spin photon transducers and the ensemble-based quantum memories. The others are common devices including 50-50 optical beam splitters, photon detectors, and optical switches, as sketched with conventional symbols in the figure. The solid-line arrows represent the optical fibers and the dashed-line arrows the classical channels. Both the end nodes and the repeater nodes have symmetric layouts.

transfer, and entanglement swapping as circled separately in Fig. 4.1.

For the initial entanglement generation step, as shown within the dashed red boundary in Fig. 4.1, two identical single-spin photon transducers are employed to produce entangled photon pairs continuously. For each photon pair, one of the photons is to be stored in the multi-mode ensemble-based quantum memory while the other is sent via optical fiber to the middle station. At the middle station, a linear optics Bell measurement is performed to entangle the photons stored in the quantum memories. While the success of this operation is

probabilistic and subject to photon loss, information about which photon pairs were successfully entangled is sent back from the middle station to the nodes where quantum memories are located. The successfully entangled photons will be read out from the memories for further processing, while the failed ones will be discarded.

As illustrated in the area enclosed with the dashed blue line in Fig. 4.1, the successfully entangled photon pairs read out from the Tm-memories are transferred into the single-spin photon transducer systems. The entanglement is transferred from the photons to the spins by means of a cavity-mediated photon-spin gate [32–35], which also heralds successful retrieval of the photons from the ensemble-based memory and entanglement transfer to the spins. The gate operation leverages spin-dependent reflection from the cavity. In particular, for correctly tuned cavity parameters and a high cooperativity system, a photon will be reflected with/without a π-phase shift if the spin system is in qubit state $|0\rangle/|1\rangle$. This enables a direct entangling operation between a time-bin encoded photonic qubit and the atomic spin qubit by applying a spin rotation in between the scattering of the early and late time bins. Subsequently, measuring the photonic qubit in the X-basis using a time-bin interferometer heralds the successful entanglement transfer from the photon to the atom [18, 36].

The heralding signals are sent between the nodes to confirm the successful transfer. Once confirmed, the successfully entangled spins will be stored until entanglement swapping can take place with the neighboring link. Unsuccessfully entangled spins will be reset to attempt the next photonic transfer. Note that we employ separate spin systems for each memory to ensure that the unsuccessful retrieval of a photon from one memory does not influence the already successfully stored photon from the other.

Lastly, for the entanglement swapping between neighboring sections, one has to implement a Bell state measurement between the two adjacent spins in one repeater node. This can be achieved in several ways using, e.g., a linear optics Bell measurement between photons emitted from both atoms or employing the same cavity-based spin-photon gate used for the entanglement transfer [36]. The latter allows us to surpass the 50% efficiency limit of a linear optics Bell measurement [37], and we therefore choose to focus on this. In this case, one of the atoms emits a time-bin photon entangled with its qubit states. This can be achieved through spin-dependent, pulsed excitation as recently demonstrated in Ref. [38]. The emitted photon is then scattered from the second cavity-atom system, implementing the same cavity-mediated entangling operation described above. A final detection of the photon in both spins in suitable bases completes and heralds the successful Bell measurement. The success probability of this operation is determined solely by the efficiency of the operations,

which, in principle, can be almost deterministic.

Below, we outline a concrete implementation of this protocol with trapped single neutral Rb atoms and Tm-doped crystal quantum memory (Tm-memory) and assess its performance.

4.3. RB ENTANGLED-PHOTON EMITTER AND ENTANGLEMENT GENERATION PROTOCOL

The Rb entangled-photon emitter consists of a single neutral Rb atom trapped with optical tweezers and coupled to two nanophotonic cavities, one with a resonance wavelength at 1470 nm and the other at 795 nm. There have been previous designs for two-mode cavity coupling of emitters with crossed cavities or using both TE and TM modes in a waveguide [39, 40]. It is, however, challenging for such setups to maintain the required cavity quality factor while increasing the frequency separation of the two modes, which, in our case, corresponds to a wavelength difference of 675 nm.

Instead, we propose a parallel-cavity arrangement with the Rb atom located on the top of the two cavities, as shown in Fig. 4.2(a). Such an architecture enhances the independence of the two cavities and is feasible by integrating atoms with on-chip nanophotonic cavities [41, 42]. However, there are still many issues that need to be considered for choosing suitable system parameters. On the one hand, we need both cavities to be close enough to each other to reflect the tweezer light to form a stable trap for the Rb atoms [43, 44]. In addition, placing the cavities closer to each other also provides larger atom-cavity coupling strengths, resulting in Purcell-enhanced emissions into the desired cavity mode. On the other hand, as the cavities of 1470 nm and 795 nm get closer, photonic modes can leak into each other, reducing the achievable quality factors.

We address these challenges by carefully selecting the material with the optimum refractive index, cavity separation, and cavity thickness. In our design, we chose silicon-enriched silicon nitride, SiN, as the cavity material with a refractive index of 2.6. This selection enables better mode confinement compared to stoichiometric Si_3N_4, allowing for minimal separations between the cavities while maintaining high cavity quality factors. Similar cavities with high quality factors have been proposed and fabricated in silicon-enriched silicon nitride [45–47]. For practical fabrication considerations, both cavities are assumed to have a thickness of 300 nm. We perform simulations with a 1060 nm tweezer and 400 nm separation between the cavities and present the results in Fig. 4.2(b). Our findings demonstrate that this design enables the 1470 nm telecom-photon cavity to achieve a quality factor of 1.4×10^5 with an average cooperativity of 34 with the Rb atom, while

the 795 nm visible-photon cavity reaches a quality factor of 3.8×10^5 with an average cooperativity of 11. More details on the cavity design are provided in Appendix D.

We will now describe in detail how this Rb-dual-cavity setup can function as a source of entangled photon pairs with the two photons at telecom and visible wavelengths, respectively. To achieve this, we harness five specific electronic orbital states from the ^{87}Rb atom. They are: $|1\rangle$: $5^2S_{1/2}|F=2, m_F=2\rangle$, $|2\rangle$: $5^2P_{3/2}|F=3, m_F=3\rangle$, $|3\rangle$: $4^2D_{3/2}, |F=3, m_F=3\rangle$, $|4\rangle$: $5^2P_{1/2}, |F=2, m_F=2\rangle$, and $|5\rangle$: $5^2S_{1/2}, |F=1, m_F=1\rangle$. Fig. 4.2(c) shows the coupling and driving of these five levels. In each photon emission cycle, we initialize the Rb atom in state $|1\rangle$ and drive it first to the $|2\rangle$ state with the first laser and then to the $|3\rangle$ state with the second laser. From the $|3\rangle$ state, the Rb atom will decay initially to the $|4\rangle$ state, emitting a photon into the telecom cavity mode (1470 nm), followed by another decay to the $|5\rangle$ state, emitting a second photon into the visible cavity mode (795 nm).

The second laser is continuously driving the transition $|2\rangle \leftrightarrow |3\rangle$ at a Rabi frequency of the same order as the cavity couplings, however, the Rabi frequency of the $|1\rangle \leftrightarrow |2\rangle$ drive is chosen to be about an order of magnitude lower. Besides, the pulse of the $|1\rangle \leftrightarrow |2\rangle$ drive is modulated with a pause in the middle of the driving process as shown by the orange curve in Fig. 4.2(d). The paused driving is calibrated such that the telecom and visible photons have equal probabilities of being both generated in the early time-bin (E) and the late time-bin (L), as shown by the blue curve in Fig. 4.2(d). Ideally, this results in an entangled state of the form:

$$\psi_{vt} = \frac{1}{\sqrt{2}}(|E\rangle_v|E\rangle_t + |L\rangle_v|L\rangle_t), \tag{4.1}$$

where the subscripts refer to the visible (v) and telecom (t) photons. We note that the Rb atom is not entangled with the final photonic state and can repeatedly emit states of the form above. We simulated this emission procedure with the comprehensive Hamiltonian and parameters shown in Appendix A.

In each elementary segment, both end nodes are equipped with Rb emitters. The visible photons generated by the two Rb emitters are directly stored in quantum memories within the nodes, while the telecom photons are sent via optical fiber to a middle station. At the middle station, a beam splitter is used for erasing the which-way information, and photon detectors after the beam splitter are used to determine in which time bin the two photons arrive. In this way, with a maximum probability of 50% for the photon detectors to detect an early as well as a late photon, it ideally projects the two visible photons into a maximally entangled state

$$\psi_{vv} = \frac{1}{\sqrt{2}}(|E\rangle_{vl}|L\rangle_{vr} \pm |L\rangle_{vl}|E\rangle_{vr}), \tag{4.2}$$

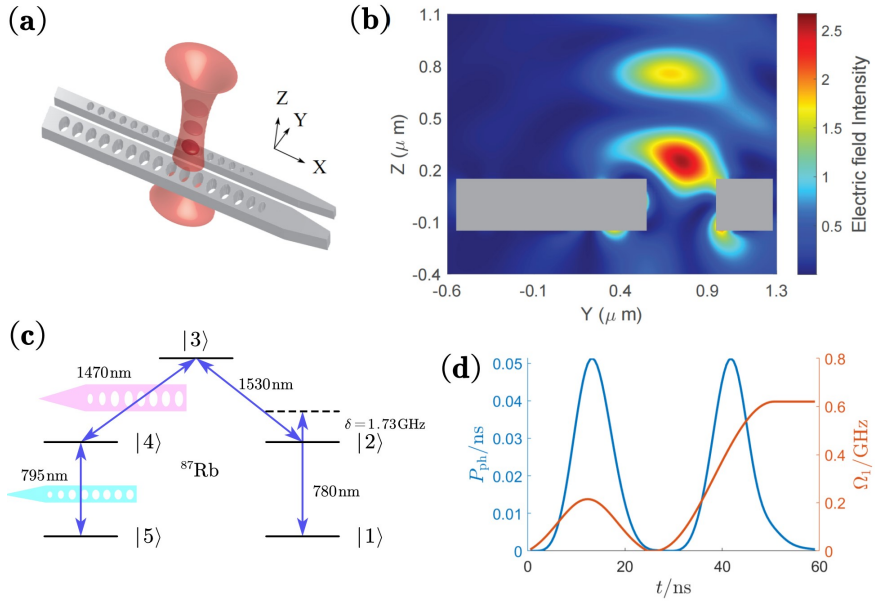

Figure 4.2.: Rb emitter design and mechanism. (a) Parallel dual cavity design. The wide and narrow gray strips placed along the X direction represent the nanophotonic cavities resonant with the telecom and visible photons emitted from the Rb atom, respectively. They are of a TE mode telecom wavelength cavity (1470 nm) and a TM mode visible wavelength cavity (795 nm) both with a refraction index of 2.6 and a thickness of 300 nm. The light-red cone denotes the combination of the incident and reflected trapping lights, forming antinodes of high light intensity marked as dark red. The Rb atom is trapped in the nearest node to the cavities. (b) The slice of the simulated relative electric field intensity of the trapping light of the Z-Y plane centered around the trapping light position. It is normalized to the incident tweezer beam intensity. The two solid gray rectangles indicate the two nanophotonic cavities viewed from the X direction. (c) The intended driving path, from $|1\rangle$ to $|5\rangle$, in the Rb atom. The first two couplings are laser-induced and the later two are cavity-induced. There is a detuning $\delta = 1.73$ GHz respecting the $|1\rangle - |2\rangle$ energy difference in the first laser driving. (d) Temporal profile of the driving pulse of the first laser (orange) and emitted telecom and visible photons (blue). The code of this Rb-cavity system simulation can be found in ref [48].

where the subscripts "l" and "r" denote the left and right ends, and the ± sign is determined by whether the same detector (+) or different detectors (-) measure the photons in the early and late time bins. This allows one to realize the heralded entanglement generation in each segment in a multiplexed fashion. We emphasize that we assume this Bell measurement to be based on the detection of two photons, but we note that more efficient schemes in which only a single photon is detected exist [21]. This extension of our investigation is left to the future. We also stress that, unlike cascaded emission schemes for single photon generation [49], our scheme does not suffer from a limitation on photonic interference due to the correlation of emission times between the optical and telecom photons. The precise detection of the telecom photons ensures the early-late time bin coherence of the optical photons, and any emission-time dependent phase shift will lead to a global phase of the entangled pair.

In actual implementations, there will be imperfections and noisy processes in the above procedure [44]. To investigate the effect of these, we develop a detailed quantum optical model that includes the many-level structure of the Rb-atoms, faulty laser polarization, finite and fluctuating cavity coupling, and various loss mechanisms. We refer to Appendix A for details of this model and discuss only some of the key insights here.

Ideally, the first driving laser should drive only the σ_+ transitions. However, due to the device geometry, good polarization-maintained driving can only be obtained by driving with linear polarization. This results in an equal driving of σ_+ and σ_- transitions. The σ_- components leak population to many other hyperfine levels as shown in Appendix A. This problem can, however, be mitigated by tuning the frequency of the first laser to match a specific resonance of a dressed state resulting from the continuous driving of the excited states from the second laser. The details of this method are presented in Appendix B.

Besides, the atoms will oscillate in the trapping potential due to finite temperature, which results in fluctuating cavity couplings. While this can in principle be mitigated by cooling the atomic motion [50–53], it is important to assess the robustness of our scheme to this.

Fluctuating cavity couplings mean that photons from different emitters will have varying amplitudes of the photonic time bins due to the fluctuations. This, in turn, will degrade the quality of the generated entanglement. While this cannot be completely circumvented, we identify certain ‘sweet spots’ of the frequency of the first driving laser where the effect of these fluctuations can be efficiently suppressed. This can be understood from the dressed states of the subspace $\{|2\rangle, |3\rangle, |4\rangle\}$ coupled by the telecom cavity field and the second laser. By tuning the frequency of the first driving laser, we can target one of the dressed states such that the effect from the fluctuation of $|3\rangle - |4\rangle$

coupling will be counteracted by the effective $|1\rangle - |2\rangle$ coupling. This procedure is described in more detail in Appendix C.

Adopting the error-suppression techniques described above, our simulation shows that entangled states with an average fidelity of 0.98 with respect to the target state in Eq. (4.2) can be achieved. This simulation is based on fluctuating cooperativities of 34 ± 5.0 for the telecom-photon cavity and 11 ± 2.2 for the visible-photon cavity. For the polarization purity of the optical fields, our simulation shows that the first laser, second laser, telecom-photon cavity, and visible-photon cavity have polarization purities of 98%, 99%, 83%, and 67%, respectively. With these input parameters, our simulation shows that the Rb atom can emit telecom-visible photon pairs within ~ 60 ns, as shown in Fig. 4.2(d). This is far shorter than the Rb state initialization time of roughly 1 μs. Hence we assume the Rb repetition rate to be $\nu_{\mathrm{eRb}} = 1$ MHz.

4.4. THULIUM-DOPED CRYSTAL QUANTUM MEMORY

In our proposal, multimode quantum memories (QMs) require an ensemble-based approach [54, 55]. Several possible methods exist, including electromagnetically induced transparency (EIT) [56], and photon-echo-related approaches [57], including the atomic frequency comb (AFC) protocol [58, 59]. Relevant hardware includes alkaline atoms [60–64] and rare-earth-ion-doped crystals (REID crystals) [65–68]. While the transition of Rb vapor or laser-cooled Rb is naturally resonant with the emission wavelengths of photons from a single Rb atom, here we focus on the use of REID crystals in conjunction with the atomic frequency comb (AFC) protocol. The reason is three-fold.

First, in contrast with other memory protocols, as long as the bandwidth of the optical signal to be stored is smaller than certain atomic level splittings, there is no trade-off between the bandwidth and the storage efficiency, nor between the number of the temporal modes that can be stored concurrently and the optical depth of the storage material [58]. This makes the AFC protocol directly compatible with the repeated emission of entangled photon pairs from the Rb-source described above. In fact, the multimode capacity is only limited by the total storage time and by the duration of each temporal mode; it can exceed 1000 temporal modes [23].

Second, another important point is that the 2-level AFC protocol in Tm-doped memory is noiseless, since atomic decoherence translates into a reduced readout efficiency rather than a reduction of the (post-selected) fidelity. However, for cold atoms, noise suppression techniques need to be incorporated to ensure high-fidelity operation.

Third, some Tm-doped crystals have matching resonance lines with ^{87}Rb, as shown in Fig. 4.3 with the example of Tm-doped $LiNbO_3$(Tm:$LiNbO_3$): We performed Doppler-free saturation spec-

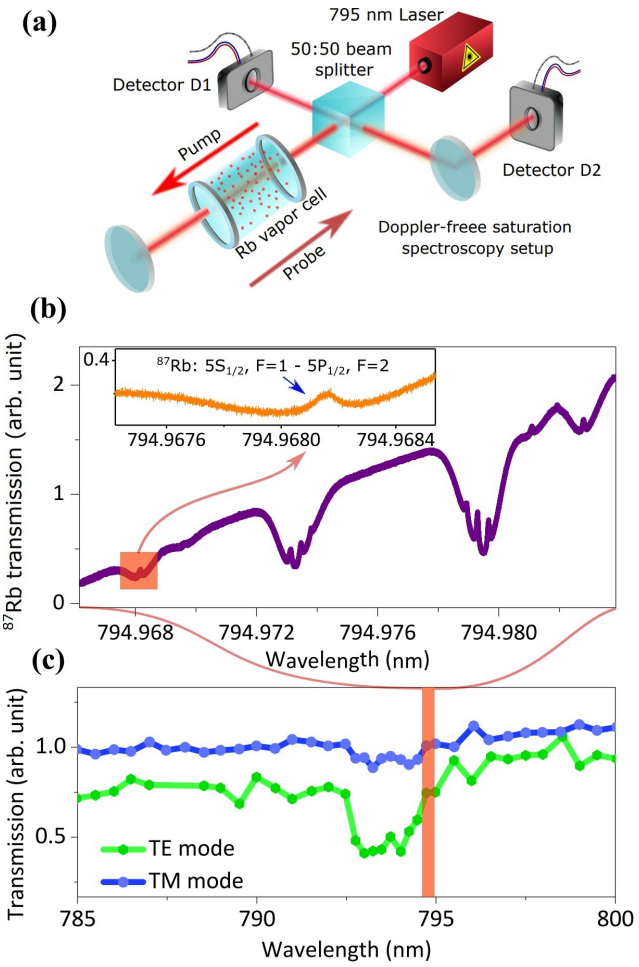

Figure 4.3.: (a) A simplified schematic of the Doppler-free saturation spectroscopy setup used to measure the absorption spectrum of rubidium. We use a laser with continuously sweeping frequency along with two light detectors (D1 to normalize the pump light, D2 to detect the probe light) to measure the absorption spectrum of the ^{87}Rb vapor. (b) Absorption spectrum of ^{87}Rb vapor. The inset shows an absorption peak corresponding to the $[5^2S_{1/2}, F = 1] \leftrightarrow [5^2P_{1/2}, F = 2]$ transition which is used in our single-spin photon transducer. (c) The absorption spectrum of Tm:$LiNbO_3$. The orange bar indicates the wavelength range in panel (b), identifying the spectral overlap between the Tm-memory absorption and Rb photon transducer emission.

troscopy [69] of the atomic ^{87} Rb vapor using an experimental setup schematically shown in a simplified form in Fig. 4.3(a). A pump beam propagates through the ^{87}Rb vapor cell and turns into a probe beam after reflecting from a mirror passing through the ^{87}Rb vapor cell again. The intensities of both beams are detected by two photon detectors, respectively. This gives the transmission of the ^{87}Rb vapor as a function of the wavelength of the laser, i.e. the spectrum of the ^{87}Rb atom as shown in Fig. 4.3(b). On the other hand, the transmission spectrum of a cryogenically cooled (T≈ 600 mK) Tm:$LiNbO_3$ crystal is depicted in Fig. 4.3(c), showing spectral overlap with the ^{87}Rb spectrum. Specifically, we show an enlarged view of the $[5^2S_{1/2}, F = 1] \leftrightarrow [5^2P_{1/2}, F = 2]$ resonance line in the inset of Fig. 4.3(b), which is used in our Rb single-spin photon transducer. Importantly, both spectra were taken simultaneously using the same laser and wavemeter. The resonance is therefore established free from calibration errors and ambient conditions that could, in principle, affect previously reported values.

Tm:$LiNbO_3$ has been used in several implementations of QM for light [70, 71]. Ignoring spectral diffusion, which will be discussed below [72], and assuming sufficient optical depth, e.g. by using an impedance-matched cavity [73–76], the storage efficiency for photons at 795 nm wavelength is determined by the optical coherence time T_2 of its $^3H_6 \leftrightarrow {}^3H_4$ transition. More precisely, the normalized retrieval rate decreases as $R_{\mathrm{rtr}} \propto \exp(-4t/T_2)$, where t is the storage time, resulting in $t_{1/e} = T_2/4$. The coherence time itself is upper bounded by $T_2^{\max} = 2T_1$ where T_1 is the lifetime of the excited state – in the case of Tm:$LiNbO_3$, around 100 μs. Experimentally, a T_2 time of 117 μs has been reported at a temperature of 810 mK [77], which limits $t_{1/e}$ to around 30μs. We note that other Tm-doped crystals with much longer coherence times are known. In particular, these include Tm:$Y_3Ga_5O_{12}$ (Tm:YGG), for which T_2=1.1 ms has been measured at 500 mK [10, 78].

In addition to coherence time, spectral diffusion is another factor that can limit the possible storage time [10, 72, 77–81]. However, there are several ways to mitigate the effect of spectral diffusion, including so-called zero first-order Zeeman (ZEFOZ) transitions [82, 83], a reduction of the temperature [77, 80], or co-doping with other ions [84, 85]. For the simulations in this paper, we assume that the storage efficiency is only determined by the coherence time, which we further assume to be given under optimized experimental conditions by its upper limit of $2T_1$. In the case of Tm:YGG, we thus find $R_{\mathrm{rtr}} \propto \exp(-4t/2.6\mathrm{ms})$. In addition, taking a maximum storage bandwidth at B=1T of around 50 MHz into account [83] (the bandwidth is limited by atomic-level splitting that determines the emergence of additional absorption features during the creation of the AFC), we calculate a temporal multiplexing capacity of around 10000.

As shown in Fig. 4.3, the $^3H_6 \leftrightarrow {}^3H_4$ transition line of Tm:$LiNbO_3$

spectrally overlaps with the $[5^2S_{1/2},\ F=1] \leftrightarrow [5^2P_{1/2},\ F=2]$ line in ^{87}Rb. However, the same line in Tm:YGG is slightly off-resonant (the Rb transition is centered at 794.97 nm and features a linewidth of $2\pi\cdot5.7$ MHz while the line of a 1% doped Tm:YGG crystal is centered at 795.32 nm with 56 GHz linewidth [86]). However, crystal engineering, e.g. by co-doping [84, 85], may solve this problem. Experiments show that a linear increase of the inhomogeneous linewidth in Tm:$Y_3Al_5O_{12}$(Tm:YAG) can be induced, for example, by 24 GHz/Scandium% [87] and by 3.6 GHz/Europium% [88] without detrimentally affecting the coherence properties of the crystal. It is reasonable to assume that these methods work for Tm:YGG as well. While more work remains to be done, it therefore appears feasible to match the Rb line with the absorption line of a Tm-doped crystal, allowing the creation of quantum memory for light with the desired specifications.

4.5. SIMULATED PERFORMANCE OF THE REPEATER CHAIN

To assess the performance of the quantum repeater chain, we carry out Monte Carlo-based simulations to evaluate the achievable secret key rate in the context of quantum key distribution (QKD). Each simulation involves multiple independent realizations of the stochastic behavior of the repeater chain. A single realization proceeds iteratively: in each iteration, events such as entanglement generation, transfer, swapping, and end-node measurement are simulated with the time of each event sampled from their corresponding probability distributions. A realization terminates either when 100 successful end-to-end entanglements are established or when 10,000 iterations have been completed.

For the ith realization, we record the total distribution time T_i and the number of successful end-to-end entanglements n_i established during that time. This yields an estimate of the average entanglement distribution rate, defined as $R_i = n_i/T_i$.

Several parameters influence R_i. The repetition rate of the Rb emitter is set to $\nu_{\mathrm{eRb}} = 1$ MHz and the fiber attenuation rate is 0.2 dB/km with the speed of light in the fiber assumed to be $c = 2 \times 10^5$ km/s, which determines the time of classical communication between the repeater stations. The retrieval efficiency of the Tm-memory, which depends on the storage time t, is

$$R_{\mathrm{rtr}} = \eta^2 \exp\left(-\frac{4t}{2.6\ \mathrm{ms}}\right), \tag{4.3}$$

where $\eta = 0.95$ is the assumed coupling efficiency to/from the fiber to the memory.

The entanglement transfer efficiency is assumed to be 0.95, primarily limited by photon loss in the optical circuit. The entanglement swapping efficiency is assumed to have an operation time of 0.2 μs and a success

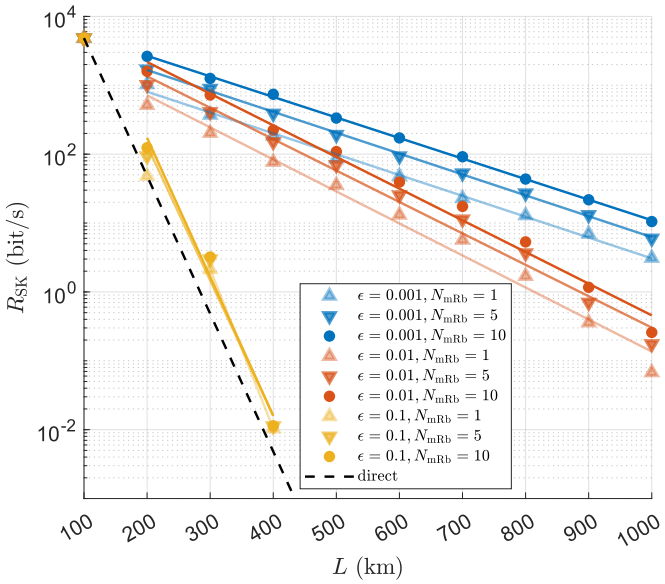

Figure 4.4.: Average secrete key rate (R_{SK}) as a function of distance (L) for different entanglement swap error probability (ϵ), and number of auxiliary Rb memory atoms (N_{mRb}). Note that the total number of Rb memory atoms in each repeater station is $2N_{\mathrm{mRb}}$. The dashed black line presents the secret key rate with no repeaters but only a direct link between the two end nodes. The solid lines are linear fits excluding the data points for L=100 km. The optimal number of repeater stations corresponding to each data point can be found in Appendix E. The simulation code is available in ref [48].

probability of 0.92. This results from a photon emission efficiency of 0.97 from one Rb atom (assuming a cooperativity of 30) and an entangling efficiency of 0.95 with the partner atom, the same as the entanglement transfer efficiency.

Lastly, the single-photon detection efficiency is taken as 0.99. Photon detection plays a role in entanglement generation, transfer, swapping, and the final measurements at the end nodes.

To model the decoherence affecting the evolution of the quantum states, we assume a depolarizing channel. For each of the n_i successful entanglement distributions in realization i, the final density matrix of the entangled qubits shared by Alice and Bob is described by

$$\rho_j = P_j \,\mathrm{Bell}_{N-1}(\rho_0^{\otimes N}) + \frac{1}{4}(1-P_j)I, \tag{4.4}$$

Rb emitter repetition rate (ν_{eRb})	1 MHz
Tm-memory typical photon preserving time ($T_2/4$)	0.65 ms
fiber attenuation rate	0.2 dB/km
light (classical signal) speed in fiber	2×10^5 km/s
fiber-cavity coupling efficiency (η)	0.95
entanglement transfer efficiency	0.95
entanglement swapping efficiency	0.92
entanglement swapping time	200 ns
photon detection efficiency	0.99
initial entangled photonic state (ρ_0) fidelity	0.98
operational error per repeater node (ϵ)	10^{-3}, 10^{-2}, 10^{-1}
Rb spin-memory storage cut-off time (t_{cut})	10 ms
Rb spin-memory coherence time (T_{mRb})	1 s

Table 4.1.: System parameters assumed in simulations of the hybrid repeater chain.

where ρ_0 (fidelity 0.98) is the estimated density matrix of an elementary link entangled state, shown in App. C.1, and N is the number of distance segments divided by $N-1$ repeater nodes. The operator $\mathrm{Bell}_{N-1}(\cdot)$ denotes $N-1$ perfect Bell-state measurements. The coefficient P_j is defined as

$$P_j = (1-\epsilon)^{N-1} \exp\left(-\frac{\sum_k^{2(N-1)} \tau_k^j}{T_{\mathrm{mRb}}}\right), \tag{4.5}$$

where ϵ quantifies the cumulative error per repeater station due to quantum-state operations of entanglement transfer and swapping. We consider values $\epsilon \in \{10^{-3}, 10^{-2}, 10^{-1}\}$. The set $\{\tau_k^j\}_k$ represents the sampled waiting times of the $2(N-1)$ qubits involved in Bell-state measurements. A memory cut-off policy is enforced such that $\tau_k \leq t_{\mathrm{cut}} = 10$ ms (optimized). The memory coherence time is assumed to be $T_{\mathrm{mRb}} = 1$ s. End-node qubits are assumed to be measured immediately upon arrival and are not subject to storage decoherence. To provide a concise overview of the different parameters assumed in our simulation, we summarize them in Table 4.1.

For each repeater configuration, characterized by a total distance L and a number of repeater stations $N_{\mathrm{rep}} = N-1$, we simulate 100 independent realizations. The final estimate of the average entanglement distribution

rate is

$$R_{\text{suc}} = \frac{1}{100} \sum_{i=1}^{100} R_i, \tag{4.6}$$

and the final estimated density matrix is given by

$$\rho = \frac{\sum_{i=1}^{100} \sum_{j=1}^{n_i} \rho_{i,j}}{\sum_{i=1}^{100} n_i}. \tag{4.7}$$

From the final state ρ, we derive the average quantum bit error rates (QBERs) for both Z- and X-basis measurements:

$$Q_{\text{Z}} = 1 - \langle 00|\rho|00\rangle - \langle 11|\rho|11\rangle, \tag{4.8}$$
$$Q_{\text{X}} = 1 - \langle ++|\rho|++\rangle - \langle --|\rho|--\rangle, \tag{4.9}$$

where $|0\rangle$ and $|1\rangle$ are the computational (Z-basis) states, and $|\pm\rangle = \frac{1}{\sqrt{2}}(|0\rangle \pm |1\rangle)$ are the X-basis states of the qubits held at the end nodes.

Based on the BB84 protocol [89], we estimate the raw secret key rate as

$$R_{\text{SK}} = \max(0,\ 1 - H(Q_{\text{X}}) - H(Q_{\text{Z}})) \times R_{\text{suc}}, \tag{4.10}$$

where $H(\cdot)$ denotes the binary entropy function. While the original BB84 protocol includes a factor of 1/2 due to random basis choices, this factor can be omitted in the asymptotic limit of infinitely long keys without compromising security [90, 91].

In addition to the baseline configuration where each end of a segment uses a single Rb photon transducer for qubit storage (as illustrated in Fig. 4.1), we also simulate scenarios incorporating multiple (N_{mRb}) Rb photon transducers per end. This second level of multiplexing enhances the entanglement swapping efficiency.

Fig. 4.4 presents the simulated average secret key rate R_{SK} as a function of total distance L, for various values of N_{mRb} and operational error per node, ϵ. For each configuration, we optimize the number of repeater stations N_{rep} and the memory cut-off time t_{cut} to maximize the per-segment secret key rate, defined as R_{SK}/N. Across all simulations, we find that a cut-off time of $t_{\text{cut}} = 10$ ms is near-optimal for an Rb spin coherence time of $T_{\text{mRb}} = 1$ s. The optimal value of N_{rep} used in each data point of Fig. 4.4 is reported in Appendix E.

Our results show that secret key rates on the order of 10 bit/s and 1 bit/s can be achieved over a distance of 1000 km for entanglement swapping error rates of $\epsilon = 10^{-3}$ and $\epsilon = 10^{-2}$, respectively. These results assume that Tm memories have sufficient multiplexing capacity to support continuous repeater operation. Specifically, the required

number of memory modes is given by

$$N_{\text{mod}} = \nu_{\text{eRb}} \cdot \frac{L}{N \cdot c}, \tag{4.11}$$

where ν_{eRb} is the photon generation rate, or the repetition rate of a single Rb emitter, and c is the speed of light in the fiber. Depending on the total distance and the optimal repeater configuration, N_{mod} ranges from 167 to 1000 in the simulations, which falls within the capabilities of rare-earth-doped quantum memories. Further increases in the secret key rate could be achieved by deploying additional Rb atoms as photon emitters to enhance the photon generation rate ν_{eRb}. We also performed simulations with a more modest operational error per node of 10% to reflect more near-term experimental implementations. Due to the error build-up across the repeater chain, such high operational errors limit the achievable distance to a few hundred kilometers and a single repeater node. However, we still observe a fourfold increase in the rate compared to direct transmission.

4.6. DISCUSSION

In summary, we have proposed a hybrid quantum repeater employing single-spin photon transducers and ensemble-based photonic memories to achieve a high-rate entanglement distribution over large distances. The hybrid architecture directs the massive multiplexing necessary for battling transmission loss in the optical fibers to the ensemble-based memories, while efficient and near-ideal photon pair generation and entanglement swapping are enabled by the single-spin photon transducers. Furthermore, we provided a specific example that utilizes Rb atoms coupled to nanophotonic cavities as single-spin photon transducers and Tm-doped crystals as ensemble-based memories for massive multiplexing.

Our simulations showed that operational errors at the %-level per repeater node are required to reach long distances. Although past experimental demonstrations of cavity-mediated spin-photon gates with atomic systems have been limited to fidelities of $\sim 80\%$ [92, 93], nano-photonic cavities, as considered here, or fiber-based cavities have demonstrated more than an order of magnitude higher cooperativities of the atom-cavity system [44, 94]. This shows the promise of such platforms to reach significantly higher fidelities comparable to similar gate operations with strongly coupled solid-state defect centers, where fidelities $> 95\%$ have been achieved [32]. Additionally, employing more complex operations such as entanglement purification techniques [30] to boost the fidelity could be envisioned through the quantum logic enabled by the single-spin photon transducers.

The overall framework presented here is relevant to other combinations of hardware besides the specific example analyzed in this work. Efficient single-spin photon transducers can be realized with diamond defect centers [7] and quantum dot systems [95], which can be matched with other ensemble-based memories based on AFC [58], Raman [96], or EIT [56] storage using impurity-doped crystals [68, 97] or atoms, either laser-cooled or at room temperature. We note that different hardware combinations may require frequency conversion to be compatible, which can be achieved through standard techniques based on non-linear waveguides [7, 31, 98, 99]. We have focused on the combination of the Rb entangled photon source with Tm-doped crystal memories due to their significant multiplexing potential. However, another interesting extension of this work would be to consider the combination of the entangled photon source with cold Rb atomic ensembles [100] in our repeater framework.

While combining different hardware is arguably more complex than a single hardware repeater, the overall requirements for reaching high-rate entanglement distribution may be substantially relaxed, as demonstrated in this work. We thus believe that further investigations of hybrid repeater architectures where ensemble-based memories are combined with single quantum emitters are a promising direction for future work.

4.7. ACKNOWLEDGMENTS

J.B. and F.G. acknowledge funding from the NWO Gravitation Program Quantum Software Consortium (Project QSC No. 024.003.037). J.B. acknowledges support from the AWS Quantum Discovery Fund at the Harvard Quantum Initiative. H.B. and S.G.M. gratefully acknowledge funding from the NSF QLCI for Hybrid Quantum Architectures and Networks (NSF award 2016136), and the NSF Quantum Interconnects Challenge for Transformational Advances in Quantum Systems (NSF award 2138068). W.T. acknowledges funding through the Netherlands Organization for Scientific Research and the European Union's Horizon 2020 Research and Innovation Program under Grant Agreement No. 820445 and Project Name Quantum Internet Alliance, as well as from the Swiss State Secretariat for Education, Research and Innovation (SERI) under contract number UeM019-3.

REFERENCES

[1] F. Gu, S. G. Menon, D. Maier, A. Das, T. Chakraborty, W. Tittel, H. Bernien, and J. Borregaard. “Hybrid Quantum Repeaters with Ensemble-based Quantum Memories and Single-spin Photon Transducers”. In: *arXiv:2401.12395* ().

[2] H. J. Kimble. “The quantum internet”. In: *Nature* 453.7198 (2008), pp. 1023–1030.

[3] S. Wehner, D. Elkouss, and R. Hanson. “Quantum internet: A vision for the road ahead”. In: *Science* 362.6412 (2018), eaam9288.

[4] W. J. Munro, K. Azuma, K. Tamaki, and K. Nemoto. “Inside Quantum Repeaters”. In: *IEEE Journal of Selected Topics in Quantum Electronics* 21.3 (2015), pp. 78–90.

[5] K. Azuma, S. E. Economou, D. Elkouss, P. Hilaire, L. Jiang, H.-K. Lo, and I. Tzitrin. “Quantum repeaters: From quantum networks to the quantum internet”. In: *Rev. Mod. Phys.* 95 (4 Dec. 2023), p. 045006.

[6] S. L. N. Hermans, M. Pompili, H. K. C. Beukers, S. Baier, J. Borregaard, and R. Hanson. “Qubit teleportation between non-neighbouring nodes in a quantum network”. In: *Nature* 605.7911 (2022), pp. 663–668.

[7] C. M. Knaut, A. Suleymanzade, Y.-C. Wei, D. R. Assumpcao, P.-J. Stas, Y. Q. Huan, B. Machielse, E. N. Knall, M. Sutula, G. Baranes, N. Sinclair, C. De-Eknamkul, D. S. Levonian, M. K. Bhaskar, H. Park, M. Lončar, and M. D. Lukin. *Entanglement of Nanophotonic Quantum Memory Nodes in a Telecommunication Network*. 2023.

[8] L. Heller, P. Farrera, G. Heinze, and H. de Riedmatten. “Cold-Atom Temporally Multiplexed Quantum Memory with Cavity-Enhanced Noise Suppression”. In: *Phys. Rev. Lett.* 124 (21 May 2020), p. 210504.

[9] Y.-F. Pu, S. Zhang, Y.-K. Wu, N. Jiang, W. Chang, C. Li, and L.-M. Duan. “Experimental demonstration of memory-enhanced scaling for entanglement connection of quantum repeater segments”. In: *Nature Photonics* 15.5 (2021), pp. 374–378.

[10] M. F. Askarani, A. Das, J. H. Davidson, G. C. Amaral, N. Sinclair, J. A. Slater, S. Marzban, C. W. Thiel, R. L. Cone, D. Oblak, and W. Tittel. “Long-Lived Solid-State Optical Memory for High-Rate Quantum Repeaters”. In: *Phys. Rev. Lett.* 127 (22 Nov. 2021), p. 220502.

[11] M. Bock, P. Eich, S. Kucera, M. Kreis, A. Lenhard, C. Becher, and J. Eschner. “High-fidelity entanglement between a trapped ion and a telecom photon via quantum frequency conversion”. In: *Nature Communications* 9.1 (2018), p. 1998.

[12] V. Krutyanskiy, M. Canteri, M. Meraner, J. Bate, V. Krcmarsky, J. Schupp, N. Sangouard, and B. P. Lanyon. “Telecom-Wavelength Quantum Repeater Node Based on a Trapped-Ion Processor”. In: *Phys. Rev. Lett.* 130 (21 May 2023), p. 213601.

[13] J. M. Kindem, A. Ruskuc, J. G. Bartholomew, J. Rochman, Y. Q. Huan, and A. Faraon. “Control and single-shot readout of an ion embedded in a nanophotonic cavity”. In: *Nature* 580.7802 (2020), pp. 201–204.

[14] S. Ourari, Ł. Dusanowski, S. P. Horvath, M. T. Uysal, C. M. Phenicie, P. Stevenson, M. Raha, S. Chen, R. J. Cava, N. P. de Leon, *et al.* “Indistinguishable telecom band photons from a single Er ion in the solid state”. In: *Nature* 620.7976 (2023), pp. 977–981.

[15] J. Neuwirth, F. B. Basset, M. B. Rota, E. Roccia, C. Schimpf, K. D. Jöns, A. Rastelli, and R. Trotta. “Quantum dot technology for quantum repeaters: from entangled photon generation toward the integration with quantum memories”. In: *Materials for Quantum Technology* 1.4 (Dec. 2021), p. 043001.

[16] N. Sangouard, C. Simon, H. de Riedmatten, and N. Gisin. “Quantum repeaters based on atomic ensembles and linear optics”. In: *Rev. Mod. Phys.* 83 (1 Mar. 2011), pp. 33–80.

[17] K. Nemoto, M. Trupke, S. J. Devitt, B. Scharfenberger, K. Buczak, J. Schmiedmayer, and W. J. Munro. “Photonic quantum networks formed from NV- centers”. In: *Scientific reports* 6.1 (2016), p. 26284.

[18] J. Borregaard, H. Pichler, T. Schröder, M. D. Lukin, P. Lodahl, and A. S. Sørensen. “One-Way Quantum Repeater Based on Near-Deterministic Photon-Emitter Interfaces”. In: *Phys. Rev. X* 10 (2 June 2020), p. 021071.

[19] K. Sharman, F. Kimiaee Asadi, S. C. Wein, and C. Simon. “Quantum repeaters based on individual electron spins and nuclear-spin-ensemble memories in quantum dots”. In: *Quantum* 5 (Nov. 2021), p. 570.

[20] L. .-. Duan, M. D. Lukin, J. I. Cirac, and P. Zoller. “Long-distance quantum communication with atomic ensembles and linear optics”. In: *Nature* 414.6862 (2001), pp. 413–418.

[21] D. Lago-Rivera, S. Grandi, J. V. Rakonjac, A. Seri, and H. de Riedmatten. “Telecom-heralded entanglement between multimode solid-state quantum memories”. In: *Nature* 594.7861 (2021), pp. 37–40.

[22] H. Li, J.-P. Dou, X.-L. Pang, T.-H. Yang, C.-N. Zhang, Y. Chen, J.-M. Li, I. A. Walmsley, and X.-M. Jin. “Heralding quantum entanglement between two room-temperature atomic ensembles”. In: *Optica* 8.6 (June 2021), pp. 925–929.

[23] M. Businger, L. Nicolas, T. S. Mejia, A. Ferrier, P. Goldner, and M. Afzelius. “Non-classical correlations over 1250 modes between telecom photons and 979-nm photons stored in 171Yb3+:Y2SiO5”. In: *Nature Communications* 13.1 (2022), p. 6438.

[24] H. Krovi, S. Guha, Z. Dutton, J. A. Slater, C. Simon, and W. Tittel. “Practical quantum repeaters with parametric down-conversion sources”. In: *Applied Physics B* 122.3 (2016), p. 52.

[25] D. Yoshida and T. Horikiri. *A multiplexed quantum repeater based on single-photon interference with mild stabilization*. 2024.

[26] S. Langenfeld, P. Thomas, O. Morin, and G. Rempe. “Quantum Repeater Node Demonstrating Unconditionally Secure Key Distribution”. In: *Phys. Rev. Lett.* 126 (23 June 2021), p. 230506.

[27] O. Morin, M. Körber, S. Langenfeld, and G. Rempe. “Deterministic Shaping and Reshaping of Single-Photon Temporal Wave Functions”. In: *Phys. Rev. Lett.* 123 (13 Sept. 2019), p. 133602.

[28] E. N. Knall, C. M. Knaut, R. Bekenstein, D. R. Assumpcao, P. L. Stroganov, W. Gong, Y. Q. Huan, P.-J. Stas, B. Machielse, M. Chalupnik, D. Levonian, A. Suleymanzade, R. Riedinger, H. Park, M. Lon čar, M. K. Bhaskar, and M. D. Lukin. “Efficient Source of Shaped Single Photons Based on an Integrated Diamond Nanophotonic System”. In: *Phys. Rev. Lett.* 129 (5 July 2022), p. 053603.

[29] M. Raha, S. Chen, C. M. Phenicie, S. Ourari, A. M. Dibos, and J. D. Thompson. “Optical quantum nondemolition measurement of a single rare earth ion qubit”. In: *Nature Communications* 11.1 (2020), p. 1605.

[30] N. Kalb, A. A. Reiserer, P. C. Humphreys, J. J. W. Bakermans, S. J. Kamerling, N. H. Nickerson, S. C. Benjamin, D. J. Twitchen, M. Markham, and R. Hanson. “Entanglement distillation between solid-state quantum network nodes”. In: *Science* 356.6341 (2017), pp. 928–932.

[31] S. Tanzilli, W. Tittel, M. Halder, O. Alibard, P. Baldi, N. Gisin, and H. Zbinden. “A photonic quantum information interface”. In: *Nature* 437 (2005), p. 116.

[32] M. K. Bhaskar, R. Riedinger, B. Machielse, D. S. Levonian, C. T. Nguyen, E. N. Knall, H. Park, D. Englund, M. Lončar, D. D. Sukachev, *et al.* “Experimental demonstration of memory-enhanced quantum communication”. In: *Nature* 580.7801 (2020), pp. 60–64.

[33] Y.-C. Wei, P.-J. Stas, A. Suleymanzade, G. Baranes, F. Machado, Y. Q. Huan, C. M. Knaut, S. W. Ding, M. Merz, E. N. Knall, U. Yazlar, M. Sirotin, I. W. Wang, B. Machielse, S. F. Yelin, J. Borregaard, H. Park, M. Lončar, and M. D. Lukin. “Universal distributed blind quantum computing with solid-state qubits”. In: *Science* 388.6746 (2025), pp. 509–513.

[34] A. Reiserer, N. Kalb, G. Rempe, and S. Ritter. “A quantum gate between a flying optical photon and a single trapped atom”. In: *Nature* 508.7495 (2014), pp. 237–240.

[35] N. Kalb, A. Reiserer, S. Ritter, and G. Rempe. “Heralded Storage of a Photonic Quantum Bit in a Single Atom”. In: *Phys. Rev. Lett.* 114 (22 June 2015), p. 220501.

[36] H. K. Beukers, M. Pasini, H. Choi, D. Englund, R. Hanson, and J. Borregaard. “Remote-Entanglement Protocols for Stationary Qubits with Photonic Interfaces”. In: *PRX Quantum* 5 (1 Mar. 2024), p. 010202.

[37] J. Calsamiglia and N. Lütkenhaus. “Maximum efficiency of a linear-optical Bell-state analyzer”. In: *Applied Physics B* 72.1 (2001), pp. 67–71.

[38] L. Li, X. Hu, Z. Jia, W. Huie, W. K. C. Sun, Aakash, Y. Dong, N. Hiri-O-Tuppa, and J. P. Covey. *Parallelized telecom quantum networking with a ytterbium-171 atom array*. 2025.

[39] Y. Zhang, M. W. McCutcheon, I. B. Burgess, and M. Loncar. “Ultra-high-Q TE/TM dual-polarized photonic crystal nanocavities”. In: *Opt. Lett.* 34.17 (Sept. 2009), pp. 2694–2696.

[40] J. Vučković, K. Rivoire, and S. Buckley. “Multiply resonant photonic crystal nanocavities for nonlinear frequency conversion”. In: *Optics Express, Vol. 19, Issue 22, pp. 22198-22207* 19 (22 Oct. 2011), pp. 22198–22207.

[41] S. G. Menon, N. Glachman, M. Pompili, A. Dibos, and H. Bernien. “An integrated atom array-nanophotonic chip platform with background-free imaging”. In: *arXiv:2311.02153* (2023).

[42] M. E. Kim, T.-H. Chang, B. M. Fields, C.-A. Chen, and C.-L. Hung. “Trapping single atoms on a nanophotonic circuit with configurable tweezer lattices”. In: *Nature Communications 2019 10:1* 10 (1 Apr. 2019), pp. 1–8.

[43] J. D. Thompson, T. G. Tiecke, N. P. de Leon, J. Feist, A. V. Akimov, M. Gullans, A. S. Zibrov, V. Vuletić, and M. D. Lukin. “Coupling a Single Trapped Atom to a Nanoscale Optical Cavity”. In: *Science* 340 (6137 June 2013), pp. 1202–1205.

[44] P. Samutpraphoot, T. Đorđević, P. L. Ocola, H. Bernien, C. Senko, V. Vuletić, and M. D. Lukin. “Strong Coupling of Two Individually Controlled Atoms via a Nanophotonic Cavity”. In: *Physical Review Letters* 124 (6 Feb. 2020), p. 063602.

[45] M. W. McCutcheon and M. Lončar. “Design of a silicon nitride photonic crystal nanocavity with a Quality factor of one million for coupling to a diamond nanocrystal”. In: *Optics express* 16.23 (2008), pp. 19136–19145.

[46] Z. Ye, A. Fülöp, Ó. B. Helgason, P. A. Andrekson, and V. Torres-Company. “Low-loss high-Q silicon-rich silicon nitride microresonators for Kerr nonlinear optics”. In: *Optics letters* 44.13 (2019), pp. 3326–3329.

[47] K. Debnath, M. Clementi, T. D. Bucio, A. Z. Khokhar, M. Sotto, K. M. Grabska, D. Bajoni, M. Galli, S. Saito, and F. Y. Gardes. “Ultrahigh-Q photonic crystal cavities in silicon rich nitride”. In: *Optics Express* 25.22 (2017), pp. 27334–27340.

[48] F. Gu. *Codes underlying the publication: "Hybrid Quantum Repeaters with Ensemble-based Quantum Memories and Single-spin Photon Transducers*". 2024.

[49] E. Schöll, L. Schweickert, L. Hanschke, K. D. Zeuner, F. Sbresny, T. Lettner, R. Trivedi, M. Reindl, S. F. Covre da Silva, R. Trotta, J. J. Finley, J. Vu čkovi ć, K. Müller, A. Rastelli, V. Zwiller, and K. D. Jöns. “Crux of Using the Cascaded Emission of a Three-Level Quantum Ladder System to Generate Indistinguishable Photons”. In: *Phys. Rev. Lett.* 125 (23 Dec. 2020), p. 233605.

[50] J. D. Thompson, T. Tiecke, A. S. Zibrov, V. Vuletić, and M. D. Lukin. “Coherence and Raman sideband cooling of a single atom in an optical tweezer”. In: *Physical review letters* 110.13 (2013), p. 133001.

[51] A. M. Kaufman, B. J. Lester, and C. A. Regal. “Cooling a single atom in an optical tweezer to its quantum ground state”. In: *Physical Review X* 2.4 (2012), p. 041014.

[52] X. Zhou, H. Tamura, T.-H. Chang, and C.-L. Hung. “Trapped atoms and superradiance on an integrated nanophotonic microring circuit”. In: *Physical Review X* 14.3 (2024), p. 031004.

[53] Y. Meng, A. Dareau, P. Schneeweiss, and A. Rauschenbeutel. “Near-ground-state cooling of atoms optically trapped 300 nm away from a hot surface”. In: *Physical Review X* 8.3 (2018), p. 031054.

[54] A. I. Lvovsky, B. C. Sanders, and W. Tittel. “Optical quantum memory”. In: *Nature Photonics* 3.12 (Dec. 2009), pp. 706–714.

[55] B. Jing and X.-H. Bao. “Ensemble-Based Quantum Memory: Principle, Advance, and Application”. In: *Photonic Quantum Technologies: Science and Applications* 2 (2023), pp. 433–462.

[56] L. Ma, O. Slattery, and X. Tang. “Optical quantum memory based on electromagnetically induced transparency”. In: *Journal of Optics* 19.4 (2017), p. 043001.

[57] F. Bussières, N. Sangouard, M. Afzelius, H. de Riedmatten, C. Simon, and W. Tittel. “Prospective applications of optical quantum memories”. In: *Journal of Modern Optics* 60.18 (2013), pp. 1519–1537.

[58] M. Afzelius, C. Simon, H. de Riedmatten, and N. Gisin. “Multimode quantum memory based on atomic frequency combs”. In: *Phys. Rev. A* 79 (5 May 2009), p. 052329.

[59] P. Jobez, N. Timoney, C. Laplane, J. Etesse, A. Ferrier, P. Goldner, N. Gisin, and M. Afzelius. “Towards highly multimode optical quantum memory for quantum repeaters”. In: *Phys. Rev. A* 93 (3 Mar. 2016), p. 032327.

[60] M. Bashkansky, F. K. Fatemi, and I. Vurgaftman. “Quantum memory in warm rubidium vapor with buffer gas”. In: *Optics Letters* 37.2 (2012), pp. 142–144.

[61] P. Vernaz-Gris, K. Huang, M. Cao, A. S. Sheremet, and J. Laurat. “Highly-efficient quantum memory for polarization qubits in a spatially-multiplexed cold atomic ensemble”. In: *Nature communications* 9.1 (2018), pp. 1–6.

[62] Y.-W. Cho, G. Campbell, J. Everett, J. Bernu, D. Higginbottom, M. Cao, J. Geng, N. Robins, P. Lam, and B. Buchler. “Highly efficient optical quantum memory with long coherence time in cold atoms”. In: *Optica* 3.1 (2016), pp. 100–107.

[63] M. Hosseini, B. M. Sparkes, G. Campbell, P. K. Lam, and B. C. Buchler. “High efficiency coherent optical memory with warm rubidium vapour”. In: *Nature communications* 2.1 (2011), pp. 1–5.

[64] J. Guo, X. Feng, P. Yang, Z. Yu, L. Chen, C.-H. Yuan, and W. Zhang. “High-performance Raman quantum memory with optimal control in room temperature atoms”. In: *Nature communications* 10.1 (2019), pp. 1–6.

[65] W. Tittel, M. Afzelius, T. Chaneliére, R. Cone, S. Kröll, S. Moiseev, and M. Sellars. “Photon-echo quantum memory in solid state systems”. In: *Laser & Photonics Reviews* 4.2 (2010), pp. 244–267.

[66] C. Thiel, T. Böttger, and R. Cone. “Rare-earth-doped materials for applications in quantum information storage and signal processing”. In: *Journal of luminescence* 131.3 (2011), pp. 353–361.

[67] T. Zhong and P. Goldner. “Emerging rare-earth doped material platforms for quantum nanophotonics”. In: *Nanophotonics* 8.11 (2019), pp. 2003–2015.

[68] G. Liu and B. Jacquier. *Spectroscopic properties of rare earths in optical materials*. Vol. 83. Springer Science & Business Media, 2006.

[69] D. W. Preston. “Doppler-free saturated absorption: Laser spectroscopy”. In: *American Journal of Physics* 64.11 (1996), pp. 1432–1436.

[70] N. Sinclair, E. Saglamyurek, H. Mallahzadeh, J. A. Slater, M. George, R. Ricken, M. P. Hedges, D. Oblak, C. Simon, W. Sohler, and W. Tittel. “Spectral Multiplexing for Scalable Quantum Photonics using an Atomic Frequency Comb Quantum Memory and Feed-Forward Control”. In: *Phys. Rev. Lett.* 113 (5 July 2014), p. 053603.

[71] M. l. G. Puigibert, M. F. Askarani, J. H. Davidson, V. B. Verma, M. D. Shaw, S. W. Nam, T. Lutz, G. C. Amaral, D. Oblak, and W. Tittel. “Entanglement and nonlocality between disparate solid-state quantum memories mediated by photons”. In: *Phys. Rev. Research* 2 (1 Jan. 2020), p. 013039.

[72] T. Böttger, C. Thiel, Y. Sun, and R. Cone. “Optical decoherence and spectral diffusion at 1.5 μ m in Er 3+: Y 2 SiO 5 versus magnetic field, temperature, and Er 3+ concentration”. In: *Physical Review B* 73.7 (2006), p. 075101.

[73] M. Afzelius and C. Simon. “Impedance-matched cavity quantum memory”. In: *Phys. Rev. A* 82 (2 Aug. 2010), p. 022310.

[74] J. H. Davidson, P. Lefebvre, J. Zhang, D. Oblak, and W. Tittel. “Improved light-matter interaction for storage of quantum states of light in a thulium-doped crystal cavity”. In: *Phys. Rev. A* 101 (4 Apr. 2020), p. 042333.

[75] A. Das, J. H. Davidson, T. Chakraborty, A. L. Tchebotareva, and W. Tittel. “Towards an Alignment-Free, Impedance-Matched Cavity Quantum Memory in a Thulium-Doped Crystal”. In: *CLEO 2023*. Optica Publishing Group, 2023, STh5C.6.

[76] S. Duranti, S. Wengerowsky, L. Feldmann, A. Seri, B. Casabone, and H. de Riedmatten. “Efficient cavity-assisted storage of photonic qubits in a solid-state quantum memory”. In: *arXiv preprint arXiv:2307.03509* (2023).

[77] N. Sinclair, D. Oblak, C. W. Thiel, R. L. Cone, and W. Tittel. “Properties of a rare-earth-ion-doped waveguide at sub-kelvin temperatures for quantum signal processing”. In: *Physical review letters* 118.10 (2017), p. 100504.

[78] A. Das, M. F. Askarani, J. H. Davidson, N. Sinclair, J. A. Slater, S. Marzban, D. Oblak, C. W. Thiel, R. L. Cone, and W. Tittel. “Optical investigations of coherence and relaxation dynamics of a thulium-doped yttrium gallium garnet crystal at sub-kelvin temperatures for optical quantum memory”. In: *Materials for Quantum Technology* 4.3 (Aug. 2024), p. 035202.

[79] Y. Sun, C. Thiel, and R. Cone. “Optical decoherence and energy level structure of 0.1% Tm 3+: LiNbO 3”. In: *Physical Review B* 85.16 (2012), p. 165106.

[80] N. Sinclair, D. Oblak, E. Saglamyurek, R. L. Cone, C. W. Thiel, and W. Tittel. “Optical coherence and energy-level properties of a Tm 3+-doped Li Nb O 3 waveguide at subkelvin temperatures”. In: *Physical Review B* 103.13 (2021), p. 134105.

[81] E. Saglamyurek, N. Sinclair, J. Jin, J. A. Slater, D. Oblak, F. Bussieres, M. George, R. Ricken, W. Sohler, and W. Tittel. “Conditional detection of pure quantum states of light after storage in a Tm-doped waveguide”. In: *Physical Review Letters* 108.8 (2012), p. 083602.

[82] D. McAuslan, J. Bartholomew, M. Sellars, and J. J. Longdell. “Reducing decoherence in optical and spin transitions in rare-earth-metal-ion–doped materials”. In: *Physical Review A* 85.3 (2012), p. 032339.

[83] J. H. Davidson, P. J. T. Woodburn, A. D. Marsh, K. J. Olson, A. Olivera, A. Das, M. F. Askarani, W. Tittel, R. L. Cone, and C. W. Thiel. “Measurement of the thulium ion spin Hamiltonian in an yttrium gallium garnet host crystal”. In: *Phys. Rev. B* 104 (13 Oct. 2021), p. 134103.

[84] C. W. Thiel, W. R. Babbitt, and R. L. Cone. “Optical decoherence studies of yttrium oxyorthosilicate Y_2SiO_5 codoped with Er^{3+} and Eu^{3+} for optical signal processing and quantum information applications at 1.5 microns”. In: *Phys. Rev. B* 85 (17 May 2012), p. 174302.

[85] T. Böttger, C. W. Thiel, R. L. Cone, and Y. Sun. “Controlled compositional disorder in $Er^{3+} : Y_2SiO_5$ provides a wide-bandwidth spectral hole burning material at 1.5 μm”. In: *Phys. Rev. B* 77 (15 Apr. 2008), p. 155125.

[86] C. W. Thiel, N. Sinclair, W. Tittel, and R. L. Cone. “Optical decoherence studies of Tm 3+: Y 3 Ga 5 O 12”. In: *Physical Review B* 90.21 (2014), p. 214301.

[87] A. Ferrier, S. Ilas, P. Goldner, and A. Louchet-Chauvet. “Scandium doped Tm: YAG ceramics and single crystals: Coherent and high resolution spectroscopy”. In: *Journal of Luminescence* 194 (2018), pp. 116–122.

[88] Z. Zhang, A. Louchet-Chauvet, L. Morvan, P. Berger, P. Goldner, and A. Ferrier. “Tailoring the 3F4 level lifetime in Tm3+: Y3Al5O12 by Eu3+ co-doping for signal processing application”. In: *Journal of Luminescence* 222 (2020), p. 117107.

[89] C. H. Bennett and G. Brassard. “Quantum Cryptography: Public Key Distribution and Coin Tossing”. In: *Theoretical Computer Science* 560 (Dec. 2014), pp. 7–11.

[90] H.-K. Lo, H. F. Chau, and M. Ardehali. “Efficient Quantum Key Distribution Scheme and a Proof of Its Unconditional Security”. In: *Journal of Cryptology* 18.2 (2005), pp. 133–165.

[91] V. Scarani, H. Bechmann-Pasquinucci, N. J. Cerf, M. Du šek, N. Lütkenhaus, and M. Peev. “The security of practical quantum key distribution”. In: *Rev. Mod. Phys.* 81 (3 Sept. 2009), pp. 1301–1350.

[92] S. Welte, B. Hacker, S. Daiss, S. Ritter, and G. Rempe. “Photon-Mediated Quantum Gate between Two Neutral Atoms in an Optical Cavity”. In: *Phys. Rev. X* 8 (1 Feb. 2018), p. 011018.

[93] S. Welte, P. Thomas, L. Hartung, S. Daiss, S. Langenfeld, O. Morin, G. Rempe, and E. Distante. “A nondestructive Bell-state measurement on two distant atomic qubits”. In: *Nature Photonics* 15.7 (2021), pp. 504–509.

[94] B. Grinkemeyer, E. Guardado-Sanchez, I. Dimitrova, D. Shchepanovich, G. E. Mandopoulou, J. Borregaard, V. Vuletić, and M. D. Lukin. “Error-detected quantum operations with neutral atoms mediated by an optical cavity”. In: *Science* 387.6740 (2025), pp. 1301–1305.

[95] D. Huber, M. Reindl, J. Aberl, A. Rastelli, and R. Trotta. “Semiconductor quantum dots as an ideal source of polarization-entangled photon pairs on-demand: a review”. In: *Journal of Optics* 20.7 (June 2018), p. 073002.

[96] L. Heller, J. Lowinski, K. Theophilo, A. Padrón-Brito, and H. de Riedmatten. “Raman Storage of Quasideterministic Single Photons Generated by Rydberg Collective Excitations in a Low-Noise Quantum Memory”. In: *Phys. Rev. Appl.* 18 (2 Aug. 2022), p. 024036.

[97] M. Guo, S. Liu, W. Sun, M. Ren, F. Wang, and M. Zhong. “Rare-earth quantum memories: The experimental status quo”. In: *Frontiers of Physics* 18.2 (2023), p. 21303.

[98] A. Tchebotareva, S. L. N. Hermans, P. C. Humphreys, D. Voigt, P. J. Harmsma, L. K. Cheng, A. L. Verlaan, N. Dijkhuizen, W. de Jong, A. Dréau, and R. Hanson. “Entanglement between a Diamond Spin Qubit and a Photonic Time-Bin Qubit at Telecom Wavelength”. In: *Phys. Rev. Lett.* 123 (6 Aug. 2019), p. 063601.

[99] M. Iuliano, M.-C. Roehsner, N. Alifasi, T. Chakraborty, A. J. Stolk, M. J. Weaver, M. O. Sholkina, E. Loukiantchenko, G. C. do Amaral, W. Tittel, and R. Hanson. “Interfacing an NV-center in diamond and a rare-earth ion compatible photonic time-bin qubit”. In: *Optica Quantum 2.0 Conference and Exhibition*. Optica Publishing Group, 2023, QW4A.7.

[100] N. Jiang, Y. .-. Pu, W. Chang, C. Li, S. Zhang, and L. .-. Duan. “Experimental realization of 105-qubit random access quantum memory”. In: *npj Quantum Information* 5.1 (2019), p. 28.

5

CONCLUSION

5.1. SUMMARY OF RESULTS

In this thesis, we explore the potential of XV color center in diamond in long-distance quantum communication and modular quantum computation. Additionally, we develop the protocol harnessing the trapped Rb atom serving as an entangled-photon emitter and photon memory, and examine its compatibility in realizing a long-distance quantum repeater chain.

Chapter 2 explores the application of group-IV vacancy color centers (G4V or XV) in quantum communication through a proposed hybrid protocol incorporating quantum dot entangled-photon emitters. The hole spin acts as an efficient spin-photon interface, serving as the communication qubit. When coupled to a nuclear spin serving as a data qubit, the XV center functions as a robust quantum memory cell. Our simulations show that, for the parameters of 14,000 XV units distributed in six repeater nodes and two end nodes, QD photon bandwidths of 2 GHz, and a photon mediated nucleus-nucleus gate error rate of 0.01, a secret-key rate of about 100 bit/s over 1,000 km is achievable.

In Chapter 3, we investigated the potential of XV centers as building blocks for modular quantum computing. Exploiting their seamless integration with optical circuits, we theoretically examine the possibility of implementing the surface code—one of the most robust quantum error correction schemes—within a modular architecture. In this design, each module contained only one or two qubits, interconnected through optical fibers, enabling scalable and distributed quantum computation. Our simulations revealed error tolerance up to 0.4%, demonstrating that this approach meets the fault-tolerance threshold and paving the way for large-scale quantum processors based on specifically NV, SiV, or SnV centers.

In Chapter 4, we introduced the trapped Rb atom as a promising spin-photon interface for quantum networking. A key advantage of

the trapped Rb atom is its ability to emit two entangled photons—one in the visible-light wavelength and the other in the telecommunication band—making it directly compatible with both atomic ensemble quantum memories and optical fiber transmission. With optimized control, its photon emission efficiency can reach up to 96%. Combined with the Tm-doped AFC quantum memory, which can store up to 1000 photonic modes simultaneously, our analysis shows that employing up to nine repeater stations—each equipped with two Tm memories and four single Rb atoms—can achieve a quantum communication rate of approximately 10 secret bits per second over distances up to 1000 km.

In summary, this thesis demonstrates the versatility and promise of spin-photon interfaces enabled by Group-IV vacancy centers in diamond and trapped Rb atoms, providing key insights into their theoretical foundations, practical implementations, and wide-ranging applications, paving the way for the next generation of scalable quantum technologies.

A

APPENDICES FOR CH. 2

A.1. QUANTUM STATE TRANSFER

To demonstrate the principle of quantum state transfer from the photon to a spin [1], we assume an arbitrary photonic state $\alpha|E\rangle + \beta|L\rangle$ and initialize the spin in the $|1\rangle$ state. The procedure includes four steps: early-time-bin photon reflection, first $\frac{\pi}{2}$ rotation, late-time-bin photon reflection, and second $\frac{\pi}{2}$ rotation. As a simplified example, we first look at a single-frequency photon, i.e. we assume $|E\rangle = |L\rangle = e^{i\omega_0 t}$ and a half-open cavity without photon loss. The evolution of the combined photon-spin state is as follows.

$$|\psi_0\rangle = (\alpha|E\rangle + \beta|L\rangle)|1\rangle \tag{A.1}$$

$$\xrightarrow{\text{early reflection}} e^{i\phi_1(\omega_0)}\alpha|E\rangle|1\rangle + \beta|L\rangle|1\rangle \tag{A.2}$$

$$\xrightarrow{\pi/2 \text{ rotation}} e^{i\phi_1(\omega_0)}\frac{\alpha}{\sqrt{2}}|E\rangle(|1\rangle + |2\rangle) + \frac{\beta}{\sqrt{2}}|L\rangle(|1\rangle + |2\rangle) \tag{A.3}$$

$$\xrightarrow{\text{late reflection}} e^{i\phi_1(\omega_0)}\frac{\alpha}{\sqrt{2}}|E\rangle(|1\rangle + |2\rangle) + \frac{\beta}{\sqrt{2}}|L\rangle\left(e^{i\phi_2(\omega_0)}|2\rangle + e^{i\phi_1(\omega_0)}|1\rangle\right) \tag{A.4}$$

$$\xrightarrow{\pi/2 \text{ rotation}} |\psi_{\text{id}}\rangle = e^{i\phi_1(\omega_0)}(\alpha|E2\rangle + \beta|L1\rangle) \tag{A.5}$$

By far, we have realized a maximally entangled state $|\psi_{\text{id}}\rangle$ between the photon and the spin. Here, we have assume $\phi_1(\omega_0) = \phi_2(\omega_0) + \pi$, which is the ideal condition. Note that the second $\pi/2$ rotation is just for converting the quantum state into the well-known Bell state. Before that, the photon and spin are already maximally entangled.

The state transfer is fulfilled if the state $|\psi_{\text{id}}\rangle$ undergoes a measurement for the photon on the X-basis, $|\pm\rangle = \frac{1}{\sqrt{2}}(|E\rangle \pm |L\rangle)$, followed by single-qubit phase correction for the spin depending on the measurement outcomes.

A

A.2. OPTIMIZING SPIN–PHOTON CPHASE GATES

To calculate a guess iterate for the controlled phase gate optimization, we neglect cross-talk. To derive the objective function, we first elaborate on the reflection scheme for broadband incoming photons. We model broadband incoming photons in the time domain by

$$a(t) = \epsilon_0 e^{(i\omega_0 - \gamma/2)t}. \tag{A.6}$$

The amplitude ϵ_0 is far smaller than the atomic decay rate so that no driving between the ground and excited state is steered. The spectrum is given by

$$S(\omega - \omega_0) = \frac{\epsilon_0}{i(\omega - \omega_0) + \gamma/2}. \tag{A.7}$$

The corresponding amplitude spectrum is lorentzian [2]. We perform the reflection scheme for entangled photons with emission rates γ_X, γ_{XX} and spectrum S_X, S_{XX}. It is

$$\begin{aligned}
|\psi\rangle &= (\alpha |EE'\rangle + \beta |LL'\rangle)|11\rangle \\
&= \iint S_X(\omega-\omega_0) S_{XX}(\nu-\omega_0)(\alpha|\omega_E \nu_E\rangle + \beta|\omega_L \nu_L\rangle)|11\rangle \, d\omega \, d\nu \\
&\xrightarrow{\text{early reflection}} \iint S_X(\omega-\omega_0) S_{XX}(\nu-\omega_0)(\alpha R_1(\omega) R_1(\nu)|\omega_E \nu_E\rangle + \beta|\omega_L \nu_L\rangle)|11\rangle \, d\omega \, d\nu \\
&\xrightarrow{\pi/2 \text{ rotation}} \frac{1}{2} \iint S_X(\omega-\omega_0) S_{XX}(\nu-\omega_0)(\alpha R_1(\omega) R_1(\nu)|\omega_E \nu_E\rangle + \beta|\omega_L \nu_L\rangle)(|11\rangle + |12\rangle + |21\rangle + |22\rangle) \, d\omega \, d\nu \\
&\xrightarrow{\text{late reflection}} \frac{1}{2} \iint S_X(\omega-\omega_0) S_{XX}(\nu-\omega_0)(\alpha R_1(\omega) R_1(\nu)|\omega_E \nu_E\rangle \\
&\quad + \beta|\omega_L \nu_L\rangle)(R_1(\omega) R_1(\nu)|11\rangle + R_1(\omega) R_2(\nu)|12\rangle + R_2(\omega) R_1(\nu)|21\rangle + R_2(\omega) R_2(\nu)|22\rangle) \, d\omega \, d\nu
\end{aligned} \tag{A.8}$$

with $\alpha, \beta \in \mathbb{C}$ such that $|\alpha|^2 + |\beta|^2 = 1$. Assuming that every photon gets detected with unity probability the X-measurement has the form [3]

$$\rho_{++} = \iint {}_{\omega\nu}\langle + + |\psi\rangle\langle\psi| + +\rangle_{\omega\nu} \, d\omega \, d\nu, \tag{A.9}$$

$$\rho_{+-} = \iint {}_{\omega\nu}\langle + - |\psi\rangle\langle\psi| + -\rangle_{\omega\nu} \, d\omega \, d\nu \tag{A.10}$$

with $|+\rangle_\omega = \frac{|\omega_E\rangle + |\omega_L\rangle}{\sqrt{2}}$. We find

$$\begin{aligned}
\langle + + |\psi\rangle = \frac{1}{4} S_X(\omega-\omega_0) S_{XX}(\nu-\omega_0) \Big(&\alpha R_1(\omega) R_1(\nu)(|11\rangle + |12\rangle + |21\rangle + |22\rangle) \\
&+ \beta(R_1(\omega) R_1(\nu)|11\rangle + R_1(\omega) R_2(\nu)|12\rangle + R_2(\omega) R_2(\nu)|21\rangle + R_2(\omega) R_2(\nu)|22\rangle) \Big),
\end{aligned} \tag{A.11}$$

$$\begin{aligned}
\langle + - |\psi\rangle = \frac{1}{4} S_X(\omega-\omega_0) S_{XX}(\nu-\omega_0) \Big(&\alpha R_1(\omega) R_1(\nu)(|11\rangle + |12\rangle + |21\rangle + |22\rangle) \\
&- \beta(R_1(\omega) R_1(\nu)|11\rangle + R_1(\omega) R_2(\nu)|12\rangle + R_2(\omega) R_2(\nu)|21\rangle + R_2(\omega) R_2(\nu)|22\rangle) \Big).
\end{aligned} \tag{A.12}$$

The resulting states ρ_{++} and ρ_{+-} depend on the integrals

$$I_{1X} = \frac{1}{4}\int_{\mathbb{R}} \tilde{S}_X(\omega-\omega_0)|R_1(\omega)|^2\,\mathrm{d}\omega, \qquad I_{1XX} = \frac{1}{4}\int_{\mathbb{R}} \tilde{S}_{XX}(\omega-\omega_0)|R_1(\omega)|^2\,\mathrm{d}\omega, \tag{A.13}$$

$$I_{2X} = \frac{1}{4}\int_{\mathbb{R}} \tilde{S}_X(\omega-\omega_0)R_1(\omega)R_2^*(\omega)\,\mathrm{d}\omega, \qquad I_{2XX} = \frac{1}{4}\int_{\mathbb{R}} \tilde{S}_{XX}(\omega-\omega_0)R_1(\omega)R_2^*(\omega)\,\mathrm{d}\omega, \tag{A.14}$$

$$I_{3X} = \frac{1}{4}\int_{\mathbb{R}} \tilde{S}_X(\omega-\omega_0)|R_2(\omega)|^2\,\mathrm{d}\omega, \qquad I_{1XX} = \frac{1}{4}\int_{\mathbb{R}} \tilde{S}_{XX}(\omega-\omega_0)|R_2(\omega)|^2\,\mathrm{d}\omega \tag{A.15}$$

where $\tilde{S}_k(\omega-\omega_0) = \mathcal{N}_k S_k(\omega-\omega_0)S_k^*(\omega-\omega_0)$ with normalization constants $\mathcal{N}_k = \gamma_k/(2\pi e_0^2)$ for $k = X, XX$ after measuring out the photon. The components of the spin-spin states are

$$\langle 0|\rho_{++}|0\rangle = |\alpha\pm\beta|^2 I_{1X}I_{1XX}, \tag{A.16}$$
$$\langle 0|\rho_{++}|1\rangle = (\alpha\pm\beta)I_{1X}(\alpha^* I_{1XX} + \beta^* I_{2XX}), \tag{A.17}$$
$$\langle 0|\rho_{++}|2\rangle = (\alpha\pm\beta)I_{1XX}(\alpha^* I_{1X} + \beta^* I_{2X}), \tag{A.18}$$
$$\langle 0|\rho_{++}|3\rangle = (\alpha\pm\beta)\alpha^* I_{1X}I_{1XX} + (\alpha\pm\beta)\beta^* I_{2X}I_{2XX}, \tag{A.19}$$
$$\langle 1|\rho_{++}|1\rangle = |\alpha|^2 I_{1X}I_{1XX} \pm \alpha\beta^* I_{1X}I_{2XX} \pm \alpha^*\beta I_{1X}I_{2XX}^* + |\beta|^2 I_{3XX}I_{1X}, \tag{A.20}$$
$$\langle 2|\rho_{++}|2\rangle = |\alpha|^2 I_{1X}I_{1XX} \pm \alpha\beta^* I_{1XX}I_{2X} \pm \alpha^*\beta I_{1XX}I_{2X}^* + |\beta|^2 I_{3X}I_{1XX}, \tag{A.21}$$
$$\langle 1|\rho_{++}|3\rangle = |\alpha|^2 I_{1X}I_{1XX} \pm \alpha\beta^* I_{2XX}I_{2X} \pm \alpha^*\beta I_{1X}I_{2XX}^* + |\beta|^2 I_{3XX}I_{2X}, \tag{A.22}$$
$$\langle 2|\rho_{++}|3\rangle = |\alpha|^2 I_{1X}I_{1XX} \pm \alpha\beta^* I_{2X}I_{2XX} \pm \alpha^*\beta I_{1XX}I_{2X}^* + |\beta|^2 I_{2XX}I_{3X}, \tag{A.23}$$
$$\langle 1|\rho_{++}|2\rangle = |\alpha|^2 I_{1X}I_{1XX} \pm \alpha\beta^* I_{2X}I_{1XX} \pm \alpha^*\beta I_{1X}I_{2XX}^* + |\beta|^2 I_{2X}I_{2XX}^*, \tag{A.24}$$
$$\langle 3|\rho_{++}|3\rangle = |\alpha|^2 I_{1X}I_{1XX} \pm \alpha\beta^* I_{2X}I_{2XX} \pm \alpha^*\beta I_{2X}^* I_{2XX}^* + |\beta|^2 I_{3X}I_{3XX}^*. \tag{A.25}$$

The remaining entries follow from the hermitian property of density matrices. On each measurement outcome we apply a $\pi/2$ rotation $U_{\pi/2} = R_y(\pi/2)\otimes R_y(\pi/2)$ to produce a known Bell-state, i.e. $\tilde{\rho}_{++} = U_{\pi/2}\rho_{++}U_{\pi/2}^\dagger$ and $\tilde{\rho}_{+-} = U_{\pi/2}\rho_{+-}U_{\pi/2}^\dagger$. The total spin state is

$$\tilde{\rho}_{\mathrm{sp}} = 2\tilde{\rho}_{++} + 2U_{\mathrm{CP}}\tilde{\rho}_{+-}U_{\mathrm{CP}}^\dagger \tag{A.26}$$

with the CPHASE gate $U_{\mathrm{CP}} = \mathrm{diag}(1,1,1,-1)$.

Atomic decay limits the efficiency of spin-spin entanglement, i.e. $\eta_{\mathrm{sp}} = \mathrm{tr}(\tilde{\rho}_{\mathrm{sp}}) < 1$. To evaluate the fidelity we consider the normalized state $\rho_{\mathrm{sp}} = \tilde{\rho}_{\mathrm{sp}}/\eta_{\mathrm{sp}}$. The ideal state is the Bell-state $|\mathrm{Bell}\rangle = 1/\sqrt{2}(|11\rangle + |22\rangle)$. The fidelity is

$$F_{\mathrm{sp}} = \langle \mathrm{Bell}|\,\rho_{\mathrm{sp}}\,|\mathrm{Bell}\rangle \tag{A.27}$$

A

For the repeater chain, we prefer high fidelity rather than success probability to be the objective function because the problem of low efficiency can be efficiently addressed by multiplexing. However, the entangled-state fidelity suffers from the significant nucleus-nucleus gate error rates in entanglement distillation and swapping. We find an optimal cavity configuration (ω_c, κ) and central frequency of the incoming mode ω_0 by solving the optimization problem

$$\min 1 - F_{\text{sp}}(\omega_0, \omega_c, \kappa) \tag{A.28}$$

using simplicial homology global optimization [4]. In [5] we developed a comprehensive spin-photon interaction model including crosstalk. To optimize subject to crosstalk, we have to convert the integrals shown in Eqs. (A.13)-(A.15) to time domain. For that purpose, we define $\mathcal{D}_k$ for $k = 1, 2$ as the map which maps an input signal a_{in} to the reflected signal a_{out} when the spin is initialized in $|k\rangle$. It holds

$$I_{1X} = \frac{\gamma_X}{4e_0^2}\int_0^T |\mathcal{D}_1(a_{\text{in},X}(t))|^2\,\mathrm{d}t, \qquad I_{1XX} = \frac{\gamma_{XX}}{4e_0^2}\int_0^T |\mathcal{D}_1(a_{\text{in},XX}(t))|^2\,\mathrm{d}t, \tag{A.29}$$

$$I_{2X} = \frac{\gamma_X}{4e_0^2}\int_0^T \mathcal{D}_1(a_{\text{in},X}(t))\mathcal{D}_2^*(a_{\text{in},X}(t))\,\mathrm{d}t, \qquad I_{2XX} = \frac{\gamma_{XX}}{4e_0^2}\int_0^T \mathcal{D}_1(a_{\text{in},XX}(t))\mathcal{D}_2^*(a_{\text{in},XX}(t))\,\mathrm{d}t, \tag{A.30}$$

$$I_{3X} = \frac{\gamma_X}{4e_0^2}\int_0^T |\mathcal{D}_2(a_{\text{in},X}(t))|^2\,\mathrm{d}t, \qquad I_{3XX} = \frac{\gamma_{XX}}{4e_0^2}\int_0^T |\mathcal{D}_2(a_{\text{in},XX}(t))|^2\,\mathrm{d}t \tag{A.31}$$

with a photon-emitting duration T. We choose T such that these integrals coincide with the integrals shown in Eqs. (A.29)-(A.31) when no crosstalk is assumed. The fidelity encountering crosstalk is modeled when evaluating the fidelity shown in Eq. (A.27) using the state from Eq. (A.26) with the integrals in the time domain shown in Eqs. (A.29)-(A.31).

To optimize the fidelity with crosstalk, we first solve the optimization problem in Eq. (A.28) without crosstalk. We initialize an optimization method like Nelder-Mead's algorithm [6] in the respective minimizer found from Eq. (A.28) and perform the optimization, encountering the time integrals shown in Eqs. (A.29)-(A.31).

A.3. SPIN-SPIN ENTANGLED STATE

We want to derive a closed integral expression for the spin-spin entangled state modeling imperfect and broadband photon pair generation, spin rotation, and crosstalk. Starting point is the entangled photonic qubit

$$|\psi_0\rangle = \frac{1}{\sqrt{2}}(|EE'\rangle + |LL'\rangle). \tag{A.32}$$

To model imperfect photon pair generation, we apply a depolarizing channel [7], i.e.

$$\rho = (1-\epsilon)\rho_0 + \epsilon I/4 \tag{A.33}$$

with $\epsilon = 4(1-F_{\text{ph}})/3$, the fidelity F_{ph} of the photon pair generated by the quantum dot and the pure state $\rho_0 = |\psi_0\rangle\langle\psi_0|$. For simplicity, we employ the notation

$$\rho = \sum \rho_{IJKM} |IJ\rangle\langle KM| \tag{A.34}$$

with $I, K = E, L$ and $J, M = E', L'$. We assume an imperfect spin $\pi/2$ rotation modeled by a map Λ, i.e.

$$\mathcal{D}_{\pi/2}(|11\rangle\langle 11|) = \sum \Lambda^{(mn,kl)} |mn\rangle\langle kl| . \tag{A.35}$$

The reflection scheme entails the early reflection, a spin $\pi/2$ rotation, and a late reflection, and reads

$$\sum \rho_{IJKM} |IJ\rangle\langle KM| 11\rangle\langle 11| = \sum \rho_{IJKM} a^I a^J \bar{a}^K \bar{a}^M |11\rangle\langle 11| \tag{A.36}$$

$$\xrightarrow{\text{early reflection}} \sum \rho_{IJKM} (\delta_{IE}\mathcal{D}_1(a^E) + \delta_{IL} a^L)(\delta_{JE'}\mathcal{D}_1(a^{E'}) + \delta_{JL'} a^{L'}) \tag{A.37}$$

$$(\delta_{KE}\bar{\mathcal{D}}_1(a^E) + \delta_{KL}\bar{a}^L)(\delta_{ME'}\bar{\mathcal{D}}_1(a^{E'}) + \delta_{ML'}\bar{a}^{L'})|11\rangle\langle 11| \tag{A.38}$$

$$\xrightarrow{\pi/2 \text{ rotation}} \sum \rho_{IJKM} \sum \Lambda^{(mn,kl)} (\delta_{IE}\mathcal{D}_1(a^E) + \delta_{IL} a^L)(\delta_{JE'}\mathcal{D}_1(a^{E'}) + \delta_{JL'} a^{L'}) \tag{A.39}$$

$$(\delta_{KE}\bar{\mathcal{D}}_1(a^E) + \delta_{KL}\bar{a}^L)(\delta_{ME'}\bar{\mathcal{D}}_1(a^{E'}) + \delta_{ML'}\bar{a}^{L'})|mn\rangle\langle kl| \tag{A.40}$$

$$\xrightarrow{\text{late reflection}} \sum \rho_{IJKM} \sum \Lambda^{(mn,kl)} (\delta_{IE}\mathcal{D}_1(a^E) + \delta_{IL}\mathcal{D}_m(a^L))(\delta_{JE'}\mathcal{D}_1(a^{E'}) + \delta_{JL'}\mathcal{D}_n a^{L'}) \tag{A.41}$$

$$(\delta_{KE}\bar{\mathcal{D}}_1(a^E) + \delta_{KL}\bar{\mathcal{D}}_k(\bar{a}^L))(\delta_{ME'}\bar{\mathcal{D}}_1(a^{E'}) + \delta_{ML'}\bar{\mathcal{D}}_l(\bar{a}^{L'}))|mn\rangle\langle kl| \tag{A.42}$$

where $\mathcal{D}_k(a)$ denotes the output mode a_{out} from the time evolution according to the Heisenberg-Langevin equations shown in [5] initializing $\sigma_{kk}(0) = 1$ for an input mode a_{in}. After measuring out the photon, the state reads

$$\tilde{\rho}_{\text{sp}} = (2\tilde{\rho}_{++} + 2U_{\text{CP}}\tilde{\rho}_{+-}U_{\text{CP}}) \tag{A.43}$$

with $U_{\text{CP}} = \text{diag}(1, 1, 1, -1)$, $\tilde{\rho}_{+\pm} = U_{\pi/2}\rho_{+\pm}U_{\pi/2}^\dagger$ Note that the additional $\pi/2$ rotation on each qubit is only a technical simplification for producing a known Bell-state, but is not necessary. and

$$\rho_{+\pm} = \sum_{\substack{I,K\in\{E,L\},\\ J,M\in\{E',L'\}}} \rho_{IJKM} \sum_{m,n,k,l=1}^{2} \Lambda^{(mn,kl)} \zeta_{IJKM}^{mnkl} |mn\rangle\langle kl| \tag{A.44}$$

A

with

$$\zeta_{IJKM}^{mnkl} = \delta_{IE}\delta_{JE'}\delta_{KE}\delta_{ME'}I_{X,1}I_{XX,1} + \delta_{IE}\delta_{JL'}\delta_{KE}\delta_{ML'}I_{X,1}I_{XX,2(n-1)+l} \tag{A.45}$$

$$+ \delta_{IL}\delta_{JE'}\delta_{KL}\delta_{ME'}I_{X,2(m-1)+k}I_{XX,1} + \delta_{IL}\delta_{JL'}\delta_{KL}\delta_{ML'}I_{X,2(m-1)+k}I_{XX,2(n-1)+l} \tag{A.46}$$

$$\pm \delta_{IE}\delta_{JE'}\delta_{KL}\delta_{ML'}I_{X,k}I_{XX,l} \pm \delta_{IL}\delta_{JL'}\delta_{KE}\delta_{ME'}I_{X,2m-1}I_{XX,2n-1} \tag{A.47}$$

where $I_{X,m}$ and $I_{XX,m}$ for $m = 1, 2, 3, 4$ denote the components of the vectors $\boldsymbol{I}_X = (I_{X1}, I_{X2}, I_{X2}^*, I_{X3})$ and $\boldsymbol{I}_{\mathrm{XX}} = (I_{XX1}, I_{XX2}, I_{XX2}^*, I_{XX3})$ with

$$I_{X1} = \mathcal{N}_{\mathrm{X}} \int_0^T |\mathcal{D}_1(a_{\mathrm{in,X}}(t))|^2 \, \mathrm{d}t, \qquad I_{XX1} = \mathcal{N}_{\mathrm{XX}} \int_0^T |\mathcal{D}_1(a_{\mathrm{in,XX}}(t))|^2 \, \mathrm{d}t, \tag{A.48}$$

$$I_{X2} = \mathcal{N}_{\mathrm{X}} \int_0^T \mathcal{D}_1(a_{\mathrm{in,X}}(t))\mathcal{D}_2^*(a_{\mathrm{in,X}}(t)) \, \mathrm{d}t, \qquad I_{XX2} = \mathcal{N}_{\mathrm{XX}} \int_0^T \mathcal{D}_1(a_{\mathrm{in,XX}}(t))\mathcal{D}_2^*(a_{\mathrm{in,XX}}(t)) \, \mathrm{d}t, \tag{A.49}$$

$$I_{X3} = \mathcal{N}_{\mathrm{X}} \int_0^T |\mathcal{D}_2(a_{\mathrm{in,X}}(t))|^2 \, \mathrm{d}t, \qquad I_{XX3} = \mathcal{N}_{\mathrm{XX}} \int_0^T |\mathcal{D}_2(a_{\mathrm{in,XX}}(t))|^2 \, \mathrm{d}t \tag{A.50}$$

with a sufficiently large photon emitting duration T, normalization constants $\mathcal{N}_k = \gamma_k/(2e_0^2)$ and $a_{\mathrm{in,k}}(t) = e_0 e^{(\mathrm{i}\omega_0 - \gamma_k/2)t}$ with $k = X, XX$. We choose T so large that the integrals shown in Eqs. (A.48)-(A.50) assuming no crosstalk coincide with the integrals in the frequency domain shown in Eqs. (A.13)-(A.15).

The success probability for spin-spin entanglement is $\eta_{\mathrm{sp}} = \mathrm{tr}(\tilde{\rho}_{\mathrm{sp}})$. The ideal state is the Bell-state $\sigma = |\mathrm{Bell}\rangle\langle\mathrm{Bell}|$ with $|\mathrm{Bell}\rangle = 1/\sqrt{2}(|11\rangle + |22\rangle)$. The fidelity of the spin-spin entangled state is

$$F_{\mathrm{sp}} = \langle \mathrm{Bell}| \rho_{\mathrm{sp}} |\mathrm{Bell}\rangle \tag{A.51}$$

with $\rho_{\mathrm{sp}} = \tilde{\rho}_{\mathrm{sp}}/\eta_{\mathrm{sp}}$.

We evaluate the spin-spin entangled state for the photon pair fidelity $F_{\mathrm{ph}} = 0.99$ assuming imperfect spin gates generated via microwaves with the gate fidelity of $F_{\mathrm{mw}} = 0.9999$ and the optimized cavity configuration and central frequency of the incoming photon for the SiV shown in Tab. A.1. We choose the photon-emitting duration $T = 10$ ns. We examine an experimental demonstrated case of $\gamma_{\mathrm{X}} = 4.34$ GHz, $\gamma_{\mathrm{XX}} = 8.33$ GHz and apply filtering as described in App. A.4.4 to produce narrower photons. Our calculation shows that the efficiencies for different cases are

$$\eta_{\mathrm{sp}} = \begin{cases} 0.9187, & \gamma_{\mathrm{X}} = 4.34 \text{ GHz}, \gamma_{\mathrm{XX}} = 8.33 \text{ GHz} \\ 0.7906, & \gamma_{\mathrm{X}} = 4.34 \text{ GHz}, \tilde{\gamma}_{\mathrm{XX}} = 8.1653 \text{ GHz} \\ 0.4167, & \tilde{\gamma}_{\mathrm{X}} = 4.3267 \text{ GHz}, \tilde{\gamma}_{\mathrm{XX}} = 6.5 \text{ GHz} \end{cases}. \tag{A.52}$$

It is important to mention that $\tilde{\gamma}$ means that filtering was applied and the bandwidth of the outcoming mode is written in Eq. (A.52). The density matrices for the three cases are

$$\rho_{\text{sp}}(\gamma_X = 4.34\ \text{GHz}, \gamma_{XX} = 8.33\ \text{GHz}) = \begin{pmatrix} 0.407 & 0.016\text{i} & 0.004\text{i} & 0.405+0.020\text{i} \\ -0.016\text{i} & 0.034 & 0 & 0.032-0.016\text{i} \\ -0.004\text{i} & 0 & 0.019 & 0.016-0.003\text{i} \\ 0.405-0.020\text{i} & 0.032+0.016\text{i} & 0.016+0.003\text{i} & 0.459 \end{pmatrix}, \tag{A.53}$$

$$\rho_{\text{sp}}(\gamma_X = 4.34\ \text{GHz}, \tilde{\gamma}_{XX} = 8.1653\ \text{GHz}) = \begin{pmatrix} 0.466 & 0.002+0.012\text{i} & 0.002+0.014\text{i} & 0.466+0.025\text{i} \\ 0.002-0.012\text{i} & 0.022 & 0 & 0.021-0.011\text{i} \\ 0.002-0.014\text{i} & 0 & 0.011 & 0.010-0.013\text{i} \\ 0.466-0.025\text{i} & 0.021+0.011\text{i} & 0.010+0.013\text{i} & 0.501 \end{pmatrix}, \tag{A.54}$$

$$\rho_{\text{sp}}(\tilde{\gamma}_X = 4.3267\ \text{GHz}, \tilde{\gamma}_{XX} = 6.5\ \text{GHz}) = \begin{pmatrix} 0.486 & 0.002+0.007\text{i} & 0.002+0.001\text{i} & 0.487+0.008\text{i} \\ 0.002-0.007\text{i} & 0.009 & 0 & 0.007-0.007\text{i} \\ 0.002-0.001\text{i} & 0 & 0.004 & 0.003-0.001\text{i} \\ 0.487-0.008\text{i} & 0.007+0.007\text{i} & 0.003+0.001\text{i} & 0.500 \end{pmatrix}. \tag{A.55}$$

A.4. SUPPORTING DATA

A.4.1. CONTRAST AND CROSS-TALK

The controlled phase gate between the incident photon and the G4V's spin is limited by the contrast $\Delta\omega_s = \omega_{2B} - \omega_{1A}$. The order of magnitude of the contrast depends on strain and the magnetic field. We choose the magnetic field strengths $B = 1$ T and $\theta_{\text{dc}} = 0$ to analyze the contrast's dependence on the extrinsic strain of the SiV and SnV. Fig. A.1 illustrates the contrast $\Delta\omega_s$ as a function of the axial strain E_x and shear strain ϵ_{xy}. The dependence of the G4V's Hamiltonian on strain is shown in [8]. The maximal contrast for the SiV is roughly $\Delta\omega_s \approx 1$ GHz at $E_x = 5.38 \cdot 10^{-4}$ and $\epsilon_{xy} = 0$. For the SnV, it is $\Delta\omega_s \approx 0.8$ GHz for negligible extrinsic strain. From an experimental perspective, it is not possible to control the extrinsic strain in such a precise manner. We observe a small change in the contrast in the local environment of the optimal strain configuration, making the choice of the optimal strain parameters reasonable for the following simulations.

In Fig. A.2 we visualize the contrast $\Delta\omega_s$, spin splitting ω_s, and the cross couplings g_{1B}, g_{2A} as a function of the magnetic field orientation θ_{dc}. On the left-hand side, we observe that the contrast decreases for a value of θ_{dc} until $\theta_{\text{dc}} \approx 0.4$. For $\theta_{\text{dc}} > 0.4$ the contrast increases

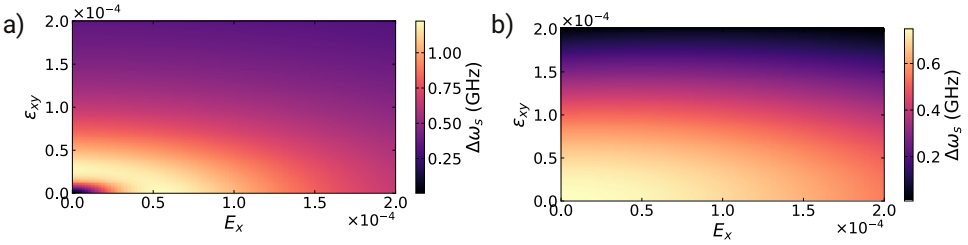

Figure A.1.: Contrast $\Delta\omega_s := \omega_{2B} - \omega_{1A}$ as a function of the axial strain E_x and shear strain ϵ_{xy} for the magnetic field strength $B = 1$ T aligned with the symmetry axis. a) Visualization for the SiV and b) SnV. The optimal strain configuration for achieving maximal contrast is $E_x = 5.38 \cdot 10^{-4}$, $\epsilon_{xy} = 0$ for the SiV and $E_x = \epsilon_{xy} = 0$ for the SnV.

monotonically until it reaches the value $\Delta\omega_s \approx 8(12)$ GHz for the SiV (SnV). The spin splitting decreases monotonically for increasing θ_{dc} for the SiV and SnV. On the right-hand side, it becomes apparent that the cross-talk reaches its maximum at $\theta_{\mathrm{dc}} = \pi/2$ (1.4) for the SiV (SnV). From [5], it becomes apparent that the cross-talk spin splitting ratio is a relevant measure to assess the impact of the cross-talk on the spin-photon interaction. That ratio is

$$r(\theta_{\mathrm{dc}}) = \frac{\omega_s(\theta_{\mathrm{dc}})}{g_{\mathrm{max}}(\theta_{\mathrm{dc}})}, \quad g_{\mathrm{max}} := \max\{|g_{2A}|, |g_{1B}|\}. \tag{A.56}$$

When the ratio is small enough, cross-talk influences spin-photon interaction.

A.4.2. OPTIMIZATION

We assume the QD emission rates $\gamma_X = 4.34$ GHz, $\gamma_{XX} = 8.33$ GHz [9] at the optimal strain configuration for the SiV and SnV and the magnetic field strength $B = 1$ T. Due to the contrast dependence on the magnetic field orientation, we optimize for spin-photon entanglement for $0 \leq \theta_{\mathrm{dc}} \leq \pi/2$ for the SiV and SnV to extract an optimal θ_{dc} for the present configuration.

In Fig. A.3 we illustrate the performance of spin-photon entanglement as a function of the magnetic field orientation for the SiV. In Fig. A.3a) we illustrate the infidelity curve for $\theta_{\mathrm{dc}} \geq 0.7$ because the optical splitting $\Delta\omega_s$ is too small to benefit from spin-photon entanglement for $\theta_{\mathrm{dc}} < 0.7$. For $\theta_{\mathrm{dc}} > 0.7$, the infidelity decreases, where the infidelity with and without cross-talk are so close that no difference becomes apparent. The decreasing infidelity is due to the rising contrast $\Delta\omega_s$. A magnetic

field orientation $\theta_{dc} = \pi/2$ produces an optimized infidelity with the value $1 - F_{sp} = 7.92 \cdot 10^{-2}$ including crosstalk. Without crosstalk, the infidelity $1 - F_{sp} = 8.00 \cdot 10^{-2}$ is achieved at the considered magnetic field orientation. That is counterintuitive because crosstalk refers to unwanted couplings, which produce a nonlinear disturbance in the Heisenberg-Langevin equations shown in [5]. However, the optical splitting between the cross-transitions $\omega_{1B} - \omega_{2A}$ is larger than the optical splitting between the resonant transitions $\omega_{1A} - \omega_{2B}$. That means that crosstalk produces a gain of optical splitting in a nonlinear manner, resulting in a potentially lower infidelity. For the present simulations, the crosstalk is small enough that its nonlinear behavior, like frequency mixing, a property of nonlinear oscillations [10], does not deteriorate the infidelity. Local optimization improves the infidelity for the present parameters up to $1 - F_{sp} = 7.91 \cdot 10^{-2}$. In Fig. A.3b), the spin-spin entanglement success probability is illustrated as a function of the magnetic field orientation. The efficiencies with and without cross-talk differ so little that they are virtually indistinguishable. The efficiency rises monotonically for $\theta_{dc} > 0.7$ since the contrast increases in that range. At the optimal magnetic field orientation, the efficiency is $\eta_{sp} \approx 0.9187$.

In Fig. A.4, we illustrate the performance of spin-photon entanglement as a function of the magnetic field orientation for the SnV. The behavior of the infidelity on the left-hand side and efficiency on the right-hand side behaves equally compared to the SiV until the optimal magnetic field orientation $\theta_{dc} = 1.285$. For $\theta_{dc} > 1.285$, the infidelity with cross-talk rises until $\theta_{dc} \approx 1.4$, where the cross couplings also reach their maximum. The infidelity decreases afterwards because the cross couplings decrease for $\theta_{dc} > 1.4$. The efficiency in Fig. A.4b) rises monotonically, except near $\theta_{dc} = 1.4$. At the orientation $\theta_{dc} = 1.33$ we find the infidelity $8.16 \cdot 10^{-2}$ with crosstalk and $6.40 \cdot 10^{-2}$ without crosstalk. Compared to the SiV crosstalk leads to an increase in the infidelity. However, local optimization using Nelder-Mead's algorithm [6] is able to improve the infidelity with crosstalk up to $1 - F_{sp} = 6.09 \cdot 10^{-2}$, which is better than the infidelity without crosstalk. That is due to the increase in optical splitting generated by crosstalk. It is not possible to define an optical splitting here because of the nonlinear nature of the Heisenberg-Langevin equations shown in [5]. However, it provides an intuitive understanding of the observed phenomenon. We find the optimal infidelity $1 - F_{sp} = 6.09 \cdot 10^{-2}$ and efficiency $\eta_{sp} = 0.9935$.

We summarize the optimal $\theta_{dc}, \kappa, \delta_c, \delta_0$ with $\delta_0 = \omega_{1A} - \omega_0$, $\delta_c = \omega_{1A} - \omega_c$, the respective cooperativities which lead to a specific success rate η_{sp} and infidelity $1 - F_{sp}$ in Tab. A.1. We find $1 - F_{sp}^{SiV} > 1 - F_{sp}^{SnV}$ because $\Delta\omega_s^{SnV} > \Delta\omega_s^{SiV}$. Furthermore, we observe $\eta_{sp}^{SnV} > \eta_{sp}^{SiV}$. That is because $\gamma_{1A}^{SnV}, \gamma_{2B}^{SnV} < \gamma_{1A}^{SiV}, \gamma_{2B}^{SiV}$. Furthermore, it becomes apparent that

A

$C^{\mathrm{SiV}} < C^{\mathrm{SnV}}$ which is because $\gamma^{\mathrm{SiV}} \approx 10\gamma^{\mathrm{SnV}}$ for both transitions $1A$ and $2B$.

Both the optimized configurations for the SiV and SnV have a disadvantage due to experimental restrictions. The considered magnetic field configuration for the SiV requires microwave spin control to achieve a spin $\pi/2$ rotation for a qubit with the splitting $\omega_s \approx 26$ GHz. That is an experimental challenge. The optimized cooperativity $C_{1A}, C_{2B} \approx 300$ for the SnV is so large that it has not yet been experimentally demonstrated. That represents a disadvantage of the configuration.

To provide data which are closer to state-of-the-art cavities and microwave spin control restrictions we assume the magnetic field $B = 0.3$ T and $\theta_{\mathrm{dc}} = \pi/2$ for the SiV and find $1 - F_{\mathrm{sp}} < 7.37 \cdot 10^{-2}$ for $\gamma < 1.6$ GHz at $C_{1A} = 25$. For that, we assumed crosstalk, which could improve the infidelity from $1 - F_{\mathrm{sp}} = 8.09 \cdot 10^{-2}$ to $1 - F_{\mathrm{sp}} = 7.37 \cdot 10^{-2}$ using Nelder-Mead's optimization algorithm [6]. We conclude that broadband QDs are compatible with SiV cavities and magnetic field constraints, enabling high-fidelity spin $\pi/2$ microwave rotations.

For the SnV, we illustrate the spin-spin entanglement infidelity as a function of the cooperativity at $\theta_{\mathrm{dc}} = 1.33$. In Fig. A.5a), we visualize that. We observe that the infidelity decreases for an increasing cooperativity. Due to experimental restrictions [11] we extract the infidelity at $C_{1A}, C_{2B} \approx 25$ and find $1 - F_{\mathrm{sp}} \approx 0.45$. In Fig. A.5b), we visualize the infidelity as a function of the cooperativity and bandwidth. We observe that for the fidelity $F_{\mathrm{sp}} > 0.95$ at $C_{1A} = 25$, a bandwidth of $\gamma < 0.1$ GHz is required. We conclude that higher cooperativities are of great relevance for the SnV.

Table A.1.: Optimized parameters with the respective values for the efficiency η_{sp} and infidelity $1 - F_{\mathrm{sp}}$ for the SiV and SnV with $\delta_c = \omega_{1A} - \omega_c$ and $\delta_0 = \omega_{1A} - \omega_0$ for the QD emission rates $\gamma_{\mathrm{X}} = 4.34$ GHz and $\gamma_{\mathrm{XX}} = 8.33$ GHz.

Centers	θ_{dc} [rad]	κ [GHz]	δ_c [GHz]	δ_0 [GHz]
SiV	$\pi/2$	37.70	-4.07	5.44
SnV	1.33	6.69	-4.50	-4.51
	$\lvert g_{1A}\rvert$ [GHz]	$\lvert g_{2B}\rvert$ [GHz]	$\lvert g_{2A}\rvert$ [GHz]	$\lvert g_{1B}\rvert$ [GHz]
SiV	12.5	13.17	1.72	3.13
SnV	5.17	5.22	1.76	1.77
	C_{1A}	C_{2B}	η_{sp}	$1 - F_{\mathrm{sp}}$
SiV	11.39	13.11	0.9187	$7.91 \cdot 10^{-2}$
SnV	155.83	161.86	0.9935	$6.09 \cdot 10^{-2}$

A.4.3. SENSITIVITY

The optimized parameters shown in Tab. A.1 cannot be hit exactly, for example, due to fabrication uncertainties. Therefore, we analyze the dependence of the system's performance on the cavity parameters κ and δ_c. We only show the infidelity here since we optimized only for high fidelity spin-spin entanglement. In Fig. A.6 we visualize the infidelity as a function of the cavity parameters for the SiV and SnV. We find that the infidelity changes less in the considered region for the SiV than SnV. That is due to the local nature of the optimum and does not generally have to be true. Based on the illustrations, we conclude that the SiV and SnV's spin-spin entanglement infidelity is robust to fabrication uncertainties.

In Fig. A.7 we visualize the optimized amplitude and phase spectra for the SiV and SnV, neglecting cross-talk. For the SnV we use optimized parameters at $\theta_{\mathrm{dc}} = \pi/2$ for illustrative purposes. We observe flatness for the phase spectra for the SiV and SnV in a local environment of the optimized central frequency, which is due to robust optimization to broadband photons. We do not illustrate the spectra taking crosstalk into account because of the nonlinear nature of the upcoming terms in the Heisenberg-Langevin equations shown in [5]. Nonlinear systems cannot be described by a single transfer function since a linear input-output relation can only describe LTI (linear time-invariant) systems [12]. It is conceptually possible to illustrate such spectra for a damped input signal on a range of central frequencies. However, they depend on the photon-emitting duration, which is why we omit such visualizations here.

A.4.4. FILTERING

Assuming we use the quantum dot from [9] and aim for narrower photon bandwidths, frequency filtering becomes essential. We model the filter as an empty, symmetric cavity with negligible losses. The transfer function mapping an input mode to a narrower output mode is the transmittivity of an empty cavity [13]

$$F(\omega) = \frac{2\sqrt{\kappa_{f,l}\kappa_{f,r}}}{\mathrm{i}\omega + \kappa_f} \tag{A.57}$$

with the total cavity loss rate $\kappa_f = \kappa_{f,l} + \kappa_{f,r} + \kappa_{f,\mathrm{loss}}$, the loss rate on the left $\kappa_{f,l}$ and right hand side $\kappa_{f,r}$, respectively and the intrinsic losses $\kappa_{f,\mathrm{loss}}$. We assume negligible loss $\kappa_{f,\mathrm{loss}} = 0$ and a symmetric cavity, i.e. $\kappa_{f,l} = \kappa_{f,r} = \kappa_f/2$. In that case the transmittivity reads

$$F(\omega) = \frac{\kappa_f}{\mathrm{i}\omega + \kappa_f}. \tag{A.58}$$

The incoming mode S shown in Eq. (A.7) passes through the filter which leads to the output mode

$$S_f(\omega) = F(\omega)S(\omega) = \frac{\kappa_f}{\mathrm{i}\omega + \kappa_f}\frac{\epsilon_0}{\mathrm{i}\omega + \gamma/2}. \tag{A.59}$$

To get the bandwidth $\tilde{\gamma}$ after filtering we need the cavity bandwidth

$$\kappa_f = \frac{\tilde{\gamma}}{2}\sqrt{\frac{\gamma^2 + \tilde{\gamma}^2}{\gamma^2 - \tilde{\gamma}^2}}. \tag{A.60}$$

To model spin-photon interaction with crosstalk assuming the photon is emitted from a QD and passing subsequently through a Fabry-Perot interferometer we use the Heisenberg-Langevin equation shown in [5] and the input mode in time domain. To derive the input mode after filtering in time domain a_{in} we evaluate the convolution between the functions

$$s(t) = \epsilon_0 e^{(\mathrm{i}\omega_0 - \gamma/2)t}, \quad f(t) = e^{(\mathrm{i}\omega_0 - \kappa_f)t}. \tag{A.61}$$

It is

$$a_{\mathrm{in}}(t) = \int_0^t s(\tau)f(t-\tau)\,\mathrm{d}\tau = \frac{2\epsilon_0}{2\kappa_f - \gamma}f(t)\left(e^{(2\kappa_f - \gamma)/2t} - 1\right). \tag{A.62}$$

For optimizing a spin-photon CPHASE gate it is sufficient to optimize a cavity which is compatible with the QD from [9]. To evaluate the fidelity and efficiency we assume that the incoming mode is given by Eq. (A.59) when the model in frequency domain is sufficient and Eq. (A.62) when time domain simulations are required to capture crosstalk effects and the G4V cavity as well as the emission frequency of the mode do not change. Since $2e_0/(2\kappa_f - \gamma)$ might be larger than e_0 one has to carefully choose e_0 to not produce unwanted driving between the states $|1\rangle, |A\rangle$ and $|2\rangle, |B\rangle$. Furthermore, the one has to multiply the factor $\mathcal{N}_{X,XX}$ from Eqs. (A.48)-(A.50) with κ_f^2.

Assuming the QD from [9] we apply filtering to make it compatible with the SiV at the magnetic field strength $B = 0.3$ T and orientation $\theta_{\mathrm{dc}} = \pi/2$. We analyze that case because it leads to a spin splitting $\omega_s \approx 8$ GHz which is possible to address with microwaves to produce a spin $\pi/2$ rotation with state-of-the-art experimental techniques [14]. At the field strength $B = 1$ T it has not yet been experimentally realized and represents future work in microwave spin control for G4Vs.

To optimize a spin-photon CPHASE gate for the SiV at $B = 0.3$ T and $\theta_{\mathrm{dc}} = \pi/2$ we first optimize the SiV cavity and central frequency of the emitted photons. For that purpose we are restricted to assume a narrower bandwidth because spin-photon entanglement does not work

at $\gamma_X = 4.34$ GHz and $\gamma_{XX} = 8.33$ GHz without filtering at the considered magnetic field strength. We assume a QD with $\gamma_X = \gamma_{XX} = 1.56$ GHz without filtering to optimize a SiV cavity. By first optimizing the parameters in frequency domain as shown in App. A.2 and subsequently improving the parameters when including crosstalk we find the fidelity $F = 7.37 \cdot 10^{-2}$ at the parameters $\kappa = 17.82$ GHz, $\delta_c = \omega_{1A} - \omega_c = -38.56$ GHz, $\delta_0 = \omega_{1A} - \omega_0 = 4.57$ GHz, $C_{1A}, C_{2B} \approx 25$. We specifically restricted the cooperativity to 25 because these are state-of-the-art SiV cavities [11] making the present simulations a meaningful contribution. When assuming the QD from [9] with the rates $\gamma_X = 4.34$ GHz and $\gamma_{XX} = 8.33$ GHz with the above mentioned SiV cavity modeled by (κ, δ_c) and emission frequency governed by δ_0 we find that $\tilde{\gamma}_X < 4$ GHz and $\tilde{\gamma}_{XX} < 7.3$ GHz is sufficient to achieve the infidelities $1 - F_{\text{sp}} < 7.89 \cdot 10^{-2}$ and efficiencies $\eta_{\text{sp}} < 0.3311$. That infidelity bound was used because it is on the same order of magnitude as the optimized spin-spin entanglement infidelity for the SiV at $B = 1$ T and the broadband QD from [9] with the rates $\gamma_X = 4.34$ GHz and $\gamma_{XX} = 8.33$ GHz which is shown in Tab. A.1. Such a low infidelity is achieved even at so broad spectra using filtering subject to experimental constraints for the magnetic field strength $B = 0.3$ T because of the steeper mode spectrum after filtering. That leads to compensation of fidelity loss even if the spectrum is such broad.

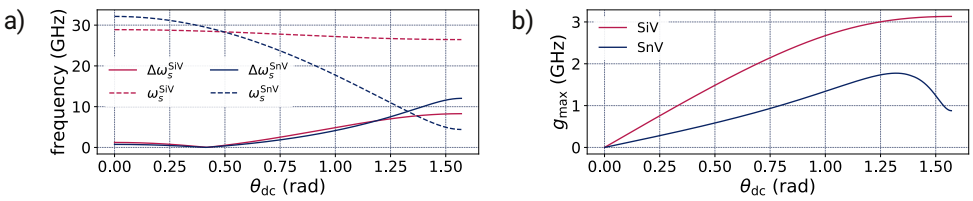

Figure A.2.: a) Contrast $\Delta\omega_s$ and spin splitting ω_s as a function of the magnetic field orientation θ_{dc} for the SiV and SnV. b) Maximal cross coupling strength $g_{\text{max}} := \max\{|g_{2A}|, |g_{1B}|\}$ as a function of θ_{dc}.

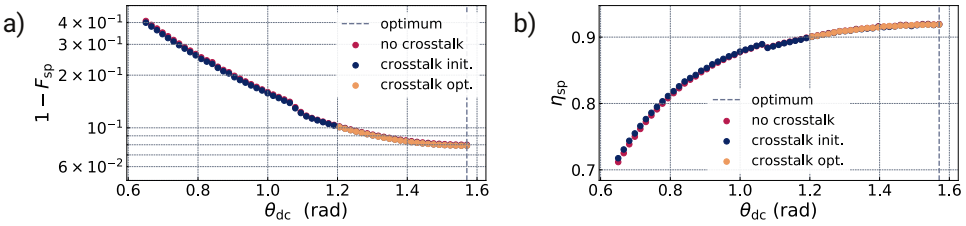

Figure A.3.: SiV's performance as a function of the magnetic field orientation with and without cross-talk. a) Infidelity $1-F_{sp}$ of the spin-spin entangled state as a function of the magnetic field orientation θ_{dc} with and without cross-talk. b) Spin-spin entanglement success probability η_{sp} as a function of θ_{dc} with and without cross-talk. The dashed gray line denotes the magnetic field orientation θ_{dc} where the infidelity is minimal.

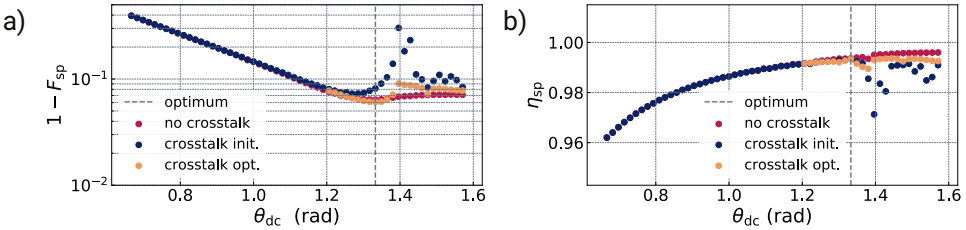

Figure A.4.: SnV's performance as a function of the magnetic field orientation with and without cross-talk. a) Infidelity $1-F_{sp}$ of the spin-spin entangled state as a function of the magnetic field orientation θ_{dc} with and without cross-talk. b) Spin-spin entanglement success probability η_{sp} as a function of θ_{dc} with and without cross-talk. The dashed gray line denotes the magnetic field orientation θ_{dc} where the infidelity is minimal.

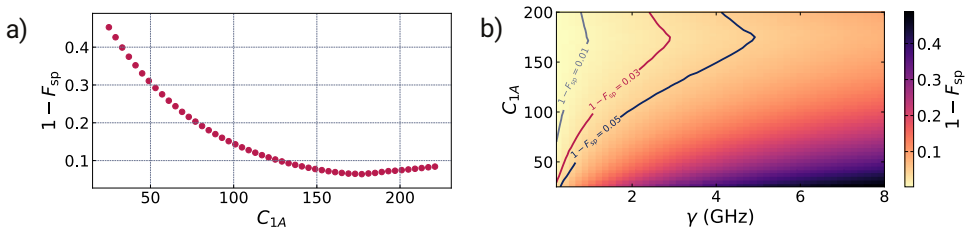

Figure A.5.: Spin-spin entanglement infidelity depending on the cooperativity. a) Spin-spin entanglement infidelity $1-F_{sp}$ of the SnV as a function of the cooperativity C_{1A}. At $C_{1A}, C_{2B} \approx 25$ it is $1-F_{sp} \approx 0.45$ at $\gamma_X = 4.34$ GHz, $\gamma_{XX} = 8.33$ GHz. b) Spin-spin entanglement infidelity $1-F_{sp}$ of the SnV as a function of the cooperativity C_{1A} and bandwidth $\gamma = \gamma_{X,XX}$.

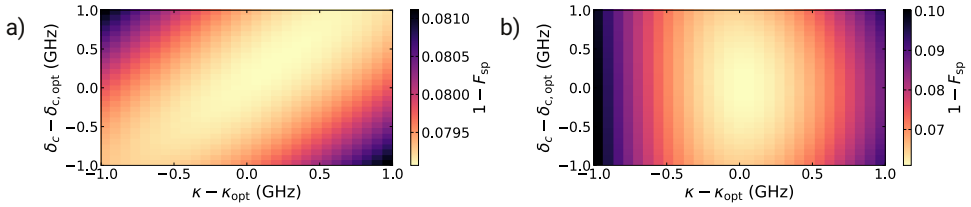

Figure A.6.: Sensitivity of the spin-spin entanglement infidelity $1-F_{sp}$. a) The infidelity is visualized as a function of the detuning deviation of the cavity mode $\delta_c - \delta_{c,opt}$ and cavity loss deviation $\kappa - \kappa_{opt}$ for the SiV. b) The same visualization is produced for the SnV. The optimal cavity parameters used for the present graph are listed in Tab. A.1.

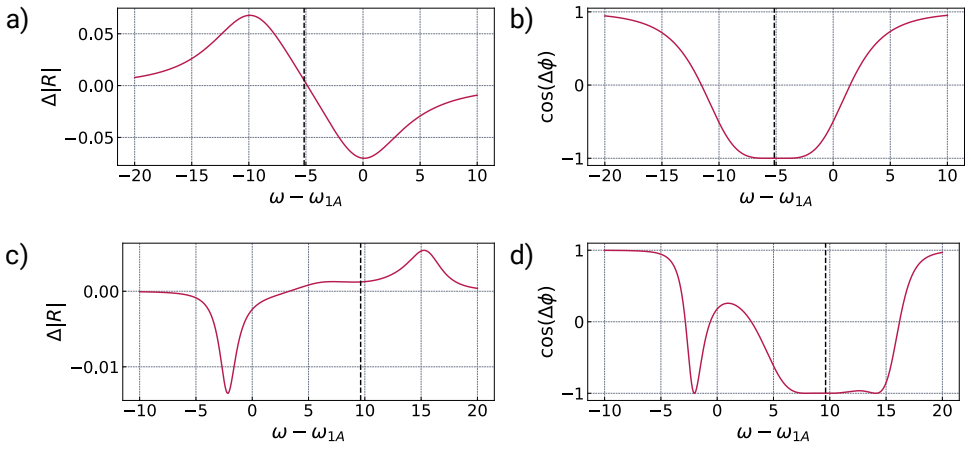

Figure A.7.: Visualization of the optimized amplitude and phase spectra for the SiV (a), (b) in the first row and SnV (c), (d), where the dashed black line denotes the optimized central frequency ω_0. It is $\Delta|R| = |R_2| - |R_1|$ and $\Delta\phi = \phi_2 - \phi_1$.

A.5. EXPECTED NUMBER OF END-TO-END ENTANGLEMENT ESTABLISHMENTS PER OPERATIONAL CYCLE

Based on the definition, the expected number of end-to-end entanglement establishments over the whole repeater chain per operational cycle is given by

$$\mathrm{E}[n_{\mathrm{end}}] = \sum_{l=1}^{m_{\mathrm{s}}} l P_{\mathrm{end}}(n_{\mathrm{end}} = l) \tag{A.63}$$

where $P_{\mathrm{end}}(n_{\mathrm{end}} = l)$ is the possibility to establish l end-to-end entanglements in one cycle. It can be rewritten as

$$\mathrm{E}[n_{\mathrm{end}}] = \sum_{l=1}^{m_{\mathrm{s}}} \sum_{k=l}^{m_{\mathrm{s}}} P_{\mathrm{end}}(n_{\mathrm{end}} = l) \tag{A.64}$$

$$= \sum_{l=1}^{m_{\mathrm{s}}} P_{\mathrm{end}}(n_{\mathrm{end}} \geq l)\,. \tag{A.65}$$

Assuming deterministic entanglement swapping, establishing at least l end-to-end entanglements implies that each elementary link has also established at least l entanglements. Consequently, we have

$$P_{\mathrm{end}}(n_{\mathrm{end}} \geq l) = P_{\mathrm{ele}}^{N}(n_{\mathrm{ele}} \geq l)\,, \tag{A.66}$$

where $P_{\mathrm{ele}}(n_{\mathrm{ele}} \geq l)$ is the possibility for an elementary link to establish at least l elemental entanglements within one cycle. It is given by

$$P_{\mathrm{ele}}(n_{\mathrm{ele}} \geq l) = \sum_{k=l}^{m_{\mathrm{s}}} P_{\mathrm{ele}}(n_{\mathrm{ele}} = l) \tag{A.67}$$

$$= \sum_{k=l}^{m_{\mathrm{s}}} \frac{m_{\mathrm{s}}!}{(m_{\mathrm{s}}-k)!k!} p_{\mathrm{arm}}^{k} (1-p_{\mathrm{arm}})^{m_{\mathrm{s}}-k}\,. \tag{A.68}$$

A.6. OPTIMIZED PARAMETERS

The optimized values of $\{N, n_{\mathrm{loc}}, n_{\mathrm{dis,n}}, n_{\mathrm{dis,e}}\}$ and the corresponding secret-key rate $R_{sk,opt}$ for different $\{F_{\mathrm{sp}}, L, m, \varepsilon_{\mathrm{n-n}}\}$ values are presented in Tab. A.2. Note that the optimum N, n_{loc}, $n_{\mathrm{dis,n}}$, and $n_{\mathrm{dis,e}}$ are searched within a wide enough range and the smallest possible step of one. However, the the searching range of n_{loc} is $\{\mathrm{round}\{\exp[\ln(20) + n\tau]\}\}$, where $\mathrm{round}(\cdot)$ denotes rounding to the nearest integer, $n = 0, 1, 2, \cdots, 99$, and $\tau = [\ln(20{,}000) - \ln(20)]/99$.

A

Table A.2.: Optimized values (N, n_{loc}, $n_{\mathrm{dis,n}}$, $n_{\mathrm{dis,e}}$) and the corresponding secret-key rates ($R_{\mathrm{sk,opt}}$).

$\varepsilon_{\mathrm{n-n}}$	F_{sp}	L	$m = 100$					$m = 1000$				
			N	n_{loc}	$n_{\mathrm{dis,n}}$	$n_{\mathrm{dis,e}}$	R_{sk}	N	n_{loc}	$n_{\mathrm{dis,n}}$	$n_{\mathrm{dis,e}}$	R_{sk}
0.01	0.95	100	2	20	0	0	2.14×10^{4}	2	20	0	0	2.31×10^{5}
0.01	0.95	200	2	40	0	0	3.64×10^{3}	2	40	0	0	4.20×10^{4}
0.01	0.95	300	2	114	0	0	6.33×10^{2}	2	107	0	0	8.35×10^{3}
0.01	0.95	400	4	114	0	1	1.66×10^{2}	4	114	0	1	2.29×10^{3}
0.01	0.95	500	4	200	0	1	57.4	4	174	0	1	927
0.01	0.95	600	5	214	0	2	19.6	5	174	0	2	416
0.01	0.95	700	6	214	0	2	6.54	5	247	0	2	196
0.01	0.95	800	6	283	0	2	2.34	5	350	0	2	89.6
0.01	0.95	900	6	462	0	2	0.692	6	304	0	2	46.0
0.01	0.95	1000	6	611	0	2	0.157	6	431	0	2	22.9
0.01	0.95	1100	7	495	0	3	0.0303	6	611	0	2	10.9
0.01	0.95	1200	7	753	0	3	0.00614	6	866	0	2	4.79
0.01	0.98	100	2	20	0	0	4.62×10^{4}	2	20	0	0	5.00×10^{5}
0.01	0.98	200	2	40	0	0	7.88×10^{3}	2	40	0	0	9.09×10^{4}
0.01	0.98	300	2	114	0	0	1.37×10^{3}	7	46	0	1	1.88×10^{4}
0.01	0.98	400	7	70	0	1	562	7	65	0	1	9.92×10^{3}
0.01	0.98	500	8	87	0	1	278	8	75	0	1	5.59×10^{3}
0.01	0.98	600	8	107	0	1	138	8	100	0	1	3.31×10^{3}
0.01	0.98	700	9	114	0	1	66.6	8	132	0	1	1.99×10^{3}
0.01	0.98	800	11	123	0	2	33.7	8	162	0	1	1.19×10^{3}
0.01	0.98	900	11	151	0	2	17.7	9	162	0	1	751
0.01	0.98	1000	12	141	0	2	8.94	9	214	0	1	472
0.01	0.98	1100	12	174	0	2	4.38	11	174	0	2	322
0.01	0.98	1200	12	230	0	2	1.86	11	200	0	2	219
0.10	0.95	100	2	20	0	0	500	2	20	0	0	5410
0.10	0.95	200	2	40	0	0	85.2	2	40	0	0	983
0.10	0.95	300	2	114	0	0	14.8	2	107	0	0	195
0.10	0.95	400	2	283	0	0	2.11	2	264	0	0	37.4
0.10	0.95	500	2	866	0	0	0.197	2	655	0	0	6.08
0.10	0.95	600	2	2000	0	0	0.0122	2	1739	0	0	0.695
0.10	0.95	700	2	5312	0	0	0.000570	2	4954	0	0	0.0466
0.10	0.95	800	2	14110	0	0	2.18×10^{-5}	2	14110	0	0	0.00207
0.10	0.95	900	2	20000	0	0	5.98×10^{-7}	2	20000	0	0	6.10×10^{-5}
0.10	0.95	1000	2	20000	0	0	9.06×10^{-9}	2	20000	0	0	9.15×10^{-7}
0.10	0.95	1100	2	18652	0	0	1.06×10^{-10}	2	20000	0	0	1.03×10^{-8}
0.10	0.95	1200	2	16223	0	0	1.31×10^{-12}	2	20000	0	0	1.09×10^{-10}
0.10	0.98	100	2	20	0	0	1.81×10^{4}	2	20	0	0	1.96×10^{5}
0.10	0.98	200	2	40	0	0	3.09×10^{3}	2	40	0	0	3.57×10^{4}
0.10	0.98	300	2	114	0	0	538	2	107	0	0	7091
0.10	0.98	400	2	283	0	0	76.6	2	264	0	0	1355
0.10	0.98	500	2	866	0	0	7.16	2	655	0	0	221
0.10	0.98	600	2	2000	0	0	0.444	2	1739	0	0	25.2
0.10	0.98	700	2	5312	0	0	0.0207	2	4954	0	0	1.69
0.10	0.98	800	2	14110	0	0	0.000791	2	14110	0	0	0.0751
0.10	0.98	900	2	20000	0	0	2.17×10^{-5}	2	20000	0	0	0.00221
0.10	0.98	1000	2	20000	0	0	3.29×10^{-7}	2	20000	0	0	3.32×10^{-5}
0.10	0.98	1100	2	18652	0	0	3.84×10^{-9}	2	20000	0	0	3.73×10^{-7}
0.10	0.98	1200	2	16223	0	0	4.75×10^{-11}	2	20000	0	0	3.97×10^{-9}

REFERENCES

[1] J. Borregaard, H. Pichler, T. Schröder, M. D. Lukin, P. Lodahl, and A. S. Sørensen. “One-Way Quantum Repeater Based on Near-Deterministic Photon-Emitter Interfaces”. en. In: *Phys. Rev. X* 10.2 (June 2020), p. 021071.

[2] T. T. Tran, M. Kianinia, K. Bray, S. Kim, Z.-Q. Xu, A. Gentle, B. Sontheimer, C. Bradac, and I. Aharonovich. “Nanodiamonds with photostable, sub-gigahertz linewidth quantum emitters”. In: *APL Photonics* 2.11 (Nov. 2017), p. 116103.

[3] T. B. Propp. “[Dissertation] Fundamental Limits to Single-Photon Detection”. In: *arXiv:2210.04089* ().

[4] S. C. Endres, C. Sandrock, and W. W. Focke. “A simplicial homology algorithm for Lipschitz optimisation”. en. In: *J. Glob. Optim.* 72.2 (Oct. 2018), pp. 181–217.

[5] Y. Strocka, M. Belhassen, T. Schröder, and G. Pieplow. “Software Framework for Optically Accessible Quantum Memory Using Group-IV Color Centers in Diamond”. In: *arXiv:2510.07045* ().

[6] P. V. et al. “SciPy 1.0: Fundamental Algorithms for Scientific Computing in Python”. In: *Nat. Methods* 17 (2020), pp. 261–272.

[7] D. Collins and J. Stephens. “Depolarizing-channel parameter estimation using noisy initial states”. In: *Phys. Rev. A* 92.3 (Sept. 2015), p. 032324.

[8] G. Pieplow, M. Belhassen, and T. Schröder. “Efficient microwave spin control of negatively charged group-IV color centers in diamond”. In: *Phys. Rev. B* 109.11 (Mar. 2024), p. 115409.

[9] C. Schimpf, M. Reindl, D. Huber, B. Lehner, S. F. Covre Da Silva, S. Manna, M. Vyvlecka, P. Walther, and A. Rastelli. “Quantum cryptography with highly entangled photons from semiconductor quantum dots”. In: *Science Advances* 7.16 (Apr. 2021).

[10] C. Vanhille, C. Campos-Pozuelo, and D. N. Sinha. “Nonlinear frequency mixing in a resonant cavity: Numerical simulations in a bubbly liquid”. In: *Ultrasonics* 54.8 (Dec. 2014), pp. 2051–2054.

A

[11] M. K. Bhaskar, R. Riedinger, B. Machielse, D. S. Levonian, C. T. Nguyen, E. N. Knall, H. Park, D. Englund, M. Lončar, D. D. Sukachev, and M. D. Lukin. “Experimental demonstration of memory-enhanced quantum communication”. en. In: *Nature* 580.7801 (Apr. 2020), pp. 60–64.

[12] H. Trentelman, A. Stoorvogel, M. Hautus, and L. Dewell. “Control Theory for Linear Systems”. In: *Appl. Mech. Rev.* 55.5 (Sept. 2002), B87–B87.

[13] A. Reiserer and G. Rempe. “Cavity-based quantum networks with single atoms and optical photons”. In: *Rev. Mod. Phys.* 87.4 (Dec. 2015), pp. 1379–1418.

[14] I. Karapatzakis, J. Resch, M. Schrodin, P. Fuchs, M. Kieschnick, J. Heupel, L. Kussi, C. Sürgers, C. Popov, J. Meijer, C. Becher, W. Wernsdorfer, and D. Hunger. “Microwave Control of the Tin-Vacancy Spin Qubit in Diamond with a Superconducting Waveguide”. In: *Phys. Rev. X* 14.3 (Aug. 2024).

B

APPENDICES FOR CH. 3

B.1. NOISE MODEL FOR STABILIZER MEASUREMENTS

In this appendix, we describe the noise modeling for the stabilizer circuits. As discussed before, the stabilizer circuit can be decomposed in two steps. The first step is the GHZ state generation using an entanglement generation scheme, and the second step is the application of locally controlled gates and measurement of the communication qubits. The detailed noise modeling of the entanglement generation is described in the respective appendices. We apply circuit-level noise and decoherence noise to all the qubits involved in the stabilizer circuit at all times. We describe these noise channels in detail here.

B.1.1. CIRCUIT-LEVEL NOISE

We consider the gate set $\{X^{\text{c/m}}, Y^{\text{c/m}}, Z^{\text{c/m}}, H^{\text{c/m}}, CZ, CiY, \text{CNOT}, \text{SWAP}\}$ as the native gate set for the module, where c/m denotes whether the single qubit gate is applied to the communication qubit or memory qubit. Circuit-level noise [1] implies that we apply noise during state preparation, single-qubit gates, two-qubit gates, and measurement operations. We model this as a depolarizing channel characterized by error probability p_g, which we call gate error. The measurement error, denoted as p_m, is modeled as the probability of a flipped measurement outcome. State preparation, idling, and single-qubit gate noise are modeled as the ideal operation followed by a single qubit depolarizing channel as [2]:

$$\mathcal{N}_{\text{gate}}^{\text{single-qubit}}(\rho) = (1-p_g)\rho + \frac{p_g}{3}\sum_{P_j} P_j \rho P_j \tag{B.1}$$

where $P_j \in \{X, Y, Z\}$ are the Pauli matrices for single qubit. While the two-qubit gate noise (here ρ is now a two-qubit density matrix) is

modeled via the two-qubit depolarizing channel:

$$\mathbb{N}_{\text{gate}}^{\text{two-qubit}}(\rho) = (1-p_g)\rho + \frac{p_g}{15}\sum_{(P_j,P_k)\neq(\mathbb{I},\mathbb{I})}(P_j\otimes P_k)\rho(P_j\otimes P_k)^\dagger \tag{B.2}$$

This channel is applied after the noiseless application of any two-qubit gates involving a communication and memory qubit. We choose $p_g = p_m = p$ as the physical error rate for the simulations and sweep p in our simulations to parameterize all the circuit-level noise.

B.1.2. DECOHERENCE NOISE

Decoherence noise: We adopt a continuous time decoherence model of all qubits. The probability to decohere (modeled as an effective depolarizing channel) is $1-\exp(-t/T^{\text{dec}})$ where t measures time and T^{dec} is the characteristic decoherence time. During an entanglement generation attempt, the memory qubits have a decoherence time of $T_{\text{link}}^{\text{dec}}$. When there is no active entanglement generation attempts in a module, all qubits (including the communication qubit) have a decoherence time of $T_{\text{idle}}^{\text{dec}}$. In general, $T_{\text{idle}}^{\text{dec}} \geq T_{\text{link}}^{\text{dec}}$ for the solid-state hardware considered in this work [3–5]. We model it as a continuous function of time with relevant coherence times as stated in Fig. 3.9, with all operations and gates tagged with their time duration. We implement the decoherence channel in terms of its Kraus operator sum representation as [2]:

$$\mathcal{N}^{\text{dec}}(\rho) = \sum_{j=1}^{K} K_j \rho K_j^\dagger \tag{B.3}$$

where ρ is any general single qubit density matrix and K_j are the Kraus operator elements, which satisfy $\sum_{j=1}^{K} K_j K_j^\dagger = \mathbb{I}$.

The T_1 time decay is described by the generalized amplitude damping (GAD) noise channel with Kraus operators:

$$\begin{aligned}
K_1^{\text{GAD}} &= \frac{1}{\sqrt{2}}\begin{bmatrix} 1 & 0 \\ 0 & \sqrt{1-\gamma_1} \end{bmatrix} \\
K_2^{\text{GAD}} &= \frac{1}{\sqrt{2}}\begin{bmatrix} 0 & \sqrt{\gamma_1} \\ 0 & 0 \end{bmatrix} \\
K_3^{\text{GAD}} &= \frac{1}{\sqrt{2}}\begin{bmatrix} \sqrt{1-\gamma_1} & 0 \\ 0 & 1 \end{bmatrix} \\
K_4^{\text{GAD}} &= \frac{1}{\sqrt{2}}\begin{bmatrix} 0 & 0 \\ \sqrt{\gamma_1} & 0 \end{bmatrix}
\end{aligned} \tag{B.4}$$

where $\gamma_1 = 1 - e^{-t/T_1}$ is the decay factor with t the time duration of the operation and T_1 the coherence time applicable.

T_2 time decay is the pure dephasing noise channel modeled via phase damping (PD) with coherence times T_2. This has the Kraus operators:

$$K_1^{\text{PD}} = \begin{bmatrix} 1 & 0 \\ 0 & \sqrt{1-\gamma_2} \end{bmatrix}, \; K_2^{\text{PD}} = \begin{bmatrix} 0 & 0 \\ 0 & \sqrt{\gamma_2} \end{bmatrix}. \tag{B.5}$$

Again with $\gamma_2 = 1 - e^{-t/T_2}$. These decoherence noise channels are applied for given operations or gate times, including link generation times, idling, and measurement times. When both these channels are applied together, they give rise to an effective depolarizing channel.

B.2. SUPEROPERATOR APPROACH TO QEC SIMULATION

This appendix describes the core of our QEC simulations using the superoperator approach for the noisy stabilizer measurement circuits. This approach is adopted from the former work on fully distributed architectures from the references [6, 7]. We adopted this method to simulate our WT4 and WT3 architectures' noisy stabilizer measurements. To simulate noise beyond the circuit-level noise model, we need to simulate the full-density matrix of the noisy stabilizer circuit. For an n qubit system, we would need 2^{2n} density matrix elements to be stored and would need very large matrix multiplications for applying any unitary operator. The problem becomes rapidly intractable as the number of qubits grows. This is where the superoperator representation is efficient. The idea is to estimate the noisy superoperator that describes the noisy stabilizer measurements on a unit cell of the surface code architecture and then use that noisy superoperator to simulate the other many unit cells of the code, depending upon its distance in each logical operator. Here, the underlying assumption is that errors are not correlated between distant modules of the distributed code. This is true because all modules are independent and only interact during the entanglement generation protocols via their communication qubits.

As we will describe, the noise applied to the code via the superoperator application is done by sampling Pauli errors to align with the stabilizer simulations. This is computationally easy to decode, in contrast to full-density matrix simulations of all the code data qubits. This is equivalent to Pauli twirling the more general noisy channel. Since the stabilizer measurement operators then incorporate only Pauli errors, they give deterministic measurement outcomes that can be fed to the decoder of choice. Now, we describe the analytical treatment of the superoperator approach.

B.2.1. SUPEROPERATOR ANALYTICAL MODEL

Represent the Hilbert space of all the qubits involved in the stabilizer measurement circuit as $\mathcal{H}$. This involves all the data qubits of the

stabilizer and the communication qubits. We can see this total Hilbert space as the direct product of the subspace of data qubits, which undergo the unitary transformation during the stabilizer measurement, and the communication qubits, which are measured out at the end of this transformation, as $\mathcal{H} = \mathcal{H}_D \otimes \mathcal{H}_c$. Our stabilizer circuit involves a GHZ creation over the desired communication qubits of the nodes, followed by the application of controlled gates and measurements. The density matrix of the GHZ state created via a chosen scheme is the input to this circuit. The action of the noisy stabilizer circuit $\mathcal{S}$ is to perform the transformation:

$$\mathcal{S}(\rho_D \otimes \rho_c) = \rho'_D \tag{B.6}$$

where ρ_D is the state of the data qubits, ρ_c state of the communication qubits. And ρ'_D is the reduced density matrix of the data qubits after the communication qubits are measured out. Suppose we figure out a Pauli decomposition of the effective transformation using Kraus operators on the post-measurement state and their corresponding probabilities. In that case, we can use these to sample errors on the code lattice for the decoding. Choi-Jamiolkowskii isomorphism [8] can be exploited to find this desired decomposition of the stabilizer circuit action. Consider each of the incoming data qubits to be one qubit of the Bell pair $|\Phi_+\rangle = \frac{1}{\sqrt{2}}(|00\rangle + |11\rangle)$. The map $\mathcal{S}$ acts only the data qubits, while their entangled counterparts remain unchanged. Then, the initial joint state to the stabilizer circuit can be expressed as:

$$|\rho\rangle = \frac{1}{\sqrt{2^{n_D}}} \sum_{i=0}^{2^{n_D}-1} |i\rangle|i\rangle \tag{B.7}$$

Where n_D is the total number of data qubits in a stabilizer unit cell. Here, $|i\rangle|i\rangle$ denote joint qubit computational basis states over the stabilizer unit-cell data qubits and the auxiliary system which together form Bell-pairs as described above and can be expanded and also be written in the binary form. For instance, if $n_D = 4$, then $\rho = \frac{1}{4}|\Phi_+\rangle^{\otimes 4} = \frac{1}{4}(|0000\rangle|0000\rangle + \ldots + |1111\rangle|1111\rangle)$. The noisy stabilizer circuit acts as:

$$\rho_{\mathcal{S}} = (\mathcal{S} \otimes \mathbb{I})|\rho\rangle\langle\rho| = \sum_j p_j (K_j \otimes \mathbb{I})|\rho\rangle\langle\rho|(K_j \otimes \mathbb{I})^\dagger \tag{B.8}$$

where each Kraus operator K_j can be expressed in the computational basis as $K_j = \sum_{x,y}[K_j]_{xy}|x\rangle\langle y|$. Then, the action of each Kraus operator

element yields an interesting fact:

$$\begin{aligned}[K_j]|\rho\rangle &= \frac{1}{\sqrt{2^{n_D}}}\sum_{x,y}[K_j]_{xy}|x\rangle\langle y|\sum_i |i\rangle|i\rangle \\ &= \frac{1}{\sqrt{2^{n_D}}}\sum_{x,y}\sum_i [K_j]_{xy}\delta_{yi}|x\rangle|i\rangle \\ &= \frac{1}{\sqrt{2^{n_D}}}\sum_{x,y}[K_j]_{xy}|x\rangle|y\rangle\end{aligned} \tag{B.9}$$

This equation reveals the relationship between the Kraus operators $[K_j]$ and their action on a computational basis. The output state density matrix can be diagonalized to reveal the Kraus operators.

B.2.2. USING THE SUPEROPERATOR DECOMPOSITION

The idea in App. B.2.1 can be readily applied to the noisy parity projections for the stabilizer measurements. If ρ_D is the state of incoming data qubits to the stabilizer measurement circuit, and Π_M is the associated projector of the measurement, then the output state is $\rho'_D = \Pi_M(\rho_D)/\mathrm{Tr}[\Pi_M(\rho_D)]$. However, because the stabilizer measurement is noisy, we also get erroneous outcomes, which leads to the effective projector:

$$\Pi_M^{\mathrm{eff}}(\rho_D) = \sum_e (a_e^M E_e \Pi_M^{\mathrm{ideal}}(\rho_D)E_e^\dagger + b_e^{\bar{M}} E_e \Pi_{\bar{M}}^{\mathrm{ideal}}(\rho_D)E_e^\dagger) \tag{B.10}$$

where $\bar{M}$ denotes a faulty measurement, and e runs over all the possible Pauli errors on the data qubits. The errors on the data qubits $E_e = P_1P_2\ldots P_w$ with $P_j \in \{I, X, Y, Z\}$ are the Pauli errors on the data qubits involved in the stabilizer measurement ($w = 4$ for WT4 and $w = 8$ for WT3 architecture, respectively; note that it is not the weight of the stabilizer but the number of data qubits involved in one unit cell of the architecture's lattice). Here, we assumed the Pauli basis decomposition for the Kraus operators in the spirit of the previous argument. However, instead of diagonalizing the resulting density matrix, we can instead find the coefficients a_e and b_e for known error permutation e on the data qubits. Assuming the form $[K_j] = (P_1P_2\ldots P_w)\Pi_{M/\bar{M}}^{\mathrm{ideal}}$ and get the output state:

$$\rho_j = (K_j \otimes \mathbb{I})|\rho\rangle\langle\rho|(K_j \otimes \mathbb{I})^\dagger \tag{B.11}$$

Using this pre-computed output state, we can directly calculate the overlap with the noisy output state of the stabilizer circuit to get the error probabilities as:

$$p_j = F(\rho_{\mathcal{S}}, \rho_j) = \mathrm{Tr}\left[\sqrt{\sqrt{\rho_j}\rho_{\mathcal{S}}\sqrt{\rho_j}}\right] \tag{B.12}$$

This method fully decomposes data qubit, measurement errors, and their corresponding error probabilities. We use the software stack developed by us for these superoperator calculations, called CircuitSimulator. We can randomly sample from this error probability distribution to apply errors on the code lattice and decode those errors using a decoder of choice [6, 9]. This part of the simulation is handled by our QEC simulator for surface codes, called Qsurface, which can handle monolithic or distributed surface code simulations for an input superoperator. We describe this part of the simulations in the next subsection.

B.3. DISTRIBUTED SURFACE CODE SIMULATIONS

This appendix describes the QEC simulations for the WT4 and WT3 architecture. The input to these simulations is the superoperator in a tabular format using methods in the App. B.2 to decompose the superoperator. Error probability for each Pauli string Kraus operator is calculated and arranged in a tabular form, along with measurement errors, either when there is GHZ success within the cutoff time t_{cut} or a GHZ state generation failure. For all these possible scenarios, it has a total number of rows equal to $4^4 \times 2 \times 2 = 1024$. Once we sample GHZ success, data qubit, and measurement errors from this error-probability distribution based on the weights, the effective joint measurement outcome is deterministic, either ± 1, for each sampled error. These stabilizer outcomes are fed to the decoder thereafter. The decoder module in our simulation workflow does not take into account specific error mechanisms and is independent of the architecture and entangling scheme considered.

In comparison to a monolithic architecture, the fully distributed implementation can be achieved in a non-fault-tolerant way through a single auxiliary qubit interacting sequentially with the four data qubits via gate teleportation [10]. Such a scheme is, however, sub-optimal in our case since it requires repeated entanglement distribution between a single module and its neighbors while keeping the auxiliary qubit coherent, which is challenging in solid-state hardware [3–5]. Which is why we consider a fully distributed architecture. We also briefly mention the modeling of cut-off times imposed on the stabilizer measurements. Suppose some stabilizers' GHZ state generation is unsuccessful within this time window. In that case, we abandon the stabilizer measurement and substitute the value from the latest successful stabilizer measurement before carrying on with the next sub-round of the stabilizer measurements. Now, we describe how these Monte Carlo simulations are executed for each of our architectures, with examples.

B.3.1. QEC SIMULATIONS FOR WT4 ARCHITECTURE

The compact tabular format of the WT4 superoperator is shown in Fig. B.1. The "Error" column describes the data qubit errors on the stabilizer data qubits, the "GHZ Success" column tells whether the GHZ generation was successful or not, and the "Meas. Error" column states whether there is a measurement error on the communication qubits during the stabilizer measurement, and the "Plaquette (Z)" and "Vertex (X)" columns describe the probability of these error combinations for each stabilizer type. This is a compact form of the tabular superoperator constructed in Ref. [9]. For a QEC cycle, we start with R_1^Z stabilizers. For each stabilizer, we sample for error probabilities from the "Plaquette (Z)" column and output one row. Say we sampled {IIII, TRUE, TRUE} (shown in light-red). This means there is no data qubit error on the stabilizer data qubits; the GHZ state was successfully generated, but there is a measurement error on the communication qubits. Therefore, we apply no data qubit error on the data qubits. We will flip the outcome when we measure the stabilizer due to the measurement error. Then, we move on to the next stabilizer and sample from the superoperator until the sub-round is completed.

Another instance can be understood from the X stabilizer measurements (shown in yellow); after sampling, we randomly output {IIIX, FALSE, TRUE}. This means the fourth data qubit has an X error. However, there was also a GHZ failure, so we cannot perform the stabilizer measurement. Therefore, we will copy the previous stabilizer outcome value to this current stabilizer, but we apply the X error on the data qubit caused due to noise during the stabilizer attempt. The measurement error does not matter when GHZ state generation fails, as we see that both TRUE/FALSE scenarios for measurement error have the same weight. This way, we apply all the different error combinations to the stabilizer data qubits. After all the sub-rounds in a layer are done, we measure that layer, including the measurement errors sampled for each stabilizer. For the final layer, we do perfect measurements to have an even number of syndromes (this is a simplification for the simulation purpose). Once all the layers are completed for the QEC cycle, we send the 3D syndrome graph data composed of the stabilizer outcomes to the decoder, either the Minimum Weight Perfect Matching (MPWM) or the Union-Find (UF) (weighted growth version) decoder.

B.3.2. QEC SIMULATIONS FOR WT3 ARCHITECTURE

The WT3 superoperator is a little more complicated. It helps to first look at the WT3 unit cell structure and identify different data qubits involved, as shown in Fig. B.2.

Let us look at one unit cell of the WT3 toric surface code, consisting of modules A, B, C, & D with the corresponding labeled data qubits. We

B

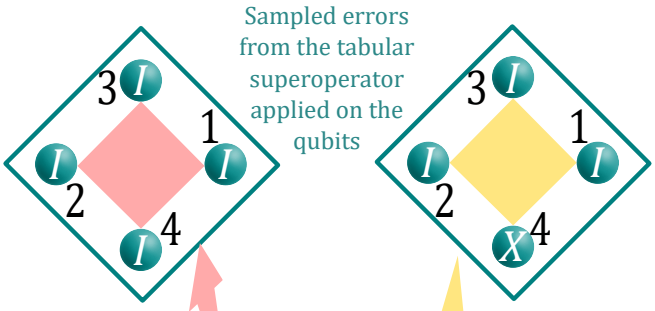

Error	GHZ Success	Meas. Error	Plaquette (Z)	Vertex (X)
IIII	TRUE	FALSE	0.9981637477558829	0.9981637477558829
IIII	TRUE	TRUE	0.0008957581465132801	0.0008957581465132789
IIII	FALSE	FALSE	9.996556342505978e-06	9.996556342505978e-06
IIII	FALSE	TRUE	9.996556342505978e-06	9.996556342505978e-06
IIIX	TRUE	FALSE	1.6624368583583534e-05	0.00010820737104832903
IIIX	TRUE	TRUE	1.3722603055920634e-05	5.464908456512845e-05
IIIX	FALSE	FALSE	2.8693439384000947e-10	2.8693439384000947e-10
IIIX	FALSE	TRUE	2.8693439384000947e-10	2.8693439384000947e-10
IIIY	TRUE	FALSE	1.6624368583583534e-05	1.6624368583583534e-05
IIIY	TRUE	TRUE	1.3722603055920634e-05	1.3722603055920634e-05
IIIY	FALSE	FALSE	2.8693439384000947e-10	2.8693439384000947e-10
IIIY	FALSE	TRUE	2.8693439384000947e-10	2.8693439384000947e-10
IIIZ	TRUE	FALSE	0.00010820737104837063	1.6624368583585804e-05

Figure B.1.: Application of data qubit errors on the code WT4 lattice, using the tabular superoperator calculated from Sec. B.2.2. For each plaquette and vertex stabilizer, we sample errors from the superoperator based on the given error probability and apply the respected errors in the right order.

consider the same noise model as the WT4 surface code. However, additional idling is involved on data qubits for WT3 surface code. Consider the current stabilizer measurement on the light-yellow, round-1 Z-type stabilizer. Modules A, B, and C are active in the stabilizer measurement. But module D is entirely idle during this sub-round. Here, we first point out the noise action on various qubits involved.

During the generation of the GHZ state by a chosen entanglement generation scheme, modules A, B, and C attempt entanglement generation; during this attempt, all the memory qubits (consisting of data qubits 1,2,3,4,5,6) are subjected to the decoherence with coherence times $T_{\text{link}}^{\text{dec}}$ (labeled with **). The attempt could be a Bell pair generation (EM scheme) or direct GHZ state (RFL and CAR schemes). We refer to data qubits 5 and 6 as active-idle qubits because they are idle in the active modules. While module D does not attempt any entanglement generation during this stabilizer sub-round (entirely idle module), and the memory qubits 7 and 8 are subjected to the decoherence $T_{\text{idle}}^{\text{dec}}$ (labeled with *) at all times. We refer to these qubits as fully idle data qubits. While certain neighboring round-1 Z stabilizers attempt GHZ generation, the considered R_1^Z stabilizer might succeed in GHZ generation. In which case, the stabilizer will be immediately measured out, and there will be some idling on all the eight data qubits, again with the coherence times $T_{\text{idle}}^{\text{dec}}$.

The WT3 superoperator's tabular form has an additional column, "Idle", that indicates the noise on the four idling qubits. Instead of creating another idling superoperator, we use the compact form shown in Fig. B.3, with the same number of rows as the WT4 superoperator. The simulation works as follows. If we again consider the R_1^Z stabilizer, and we sample {IIII, TRUE, TRUE} for the "Plaquette (Z)" (shown in light-yellow), we can apply the noise on data qubits 1,2,3,4, following the same argument as WT4 simulations. However, we must also apply the idling noise on the idling data qubits 5,6,7,8. Given that the stabilizer has a GHZ success, we now sample using the "Idle" column only from the rows that have "GHZ Success = TRUE" (shown in red). Say we sampled the error configuration "IIIX", in which case we will serially apply this configuration to the idling data qubits (in the order 5,6,7,8). We loop over all the stabilizer unit cells within a sub-round to apply all the data qubit errors, and we repeat this for all the sub-rounds for each type of stabilizer. This completed one layer of measurements in the QEC cycle. After applying all the data qubit errors, we measure the layer, including the measurement errors that were previously recorded for each stabilizer. Finally, again, we do perfect measurements in the final layer and send the 3D syndrome graph to the decoder.

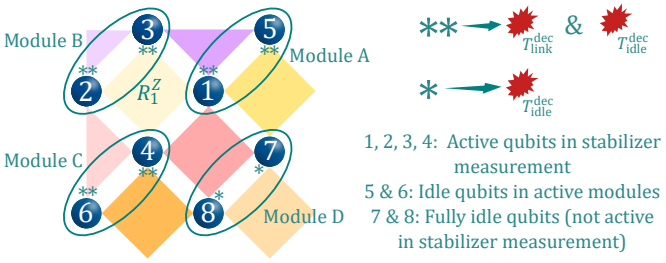

Figure B.2.: Unit-cell for WT3 surface code layout, for a R_1^Z stabilizer. There are 8 data qubits involved in the current stabilizer measurement, out of which 4 are active stabilizer qubits and 4 are idling qubits. These qubits undergo different decoherence rates depending on GHZ success and failure of the current stabilizer.

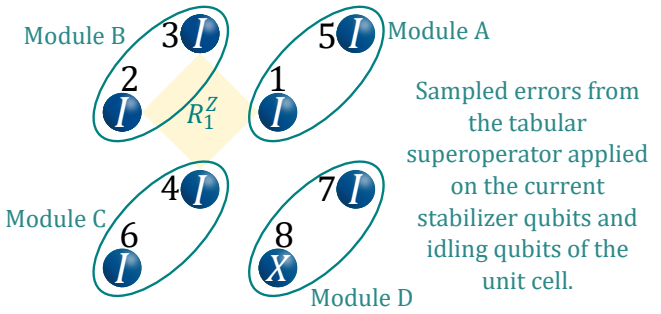

Error	GHZ Success	Meas. Error	Plaquette (Z)	Vertex (X)	Idle
IIII	TRUE	FALSE	0.9982194440061815	0.9982194440061815	0.4996787965602666
IIII	TRUE	TRUE	0.0006817668941716804	0.0006817668941716755	0.4996787965602666
IIII	FALSE	FALSE	4.497149643388714e-06	4.49714964338871e-06	4.49714964338871e-06
IIII	FALSE	TRUE	4.497149643388714e-06	4.49714964338871e-06	4.49714964338871e-06
IIIX	TRUE	FALSE	4.0768328890295396e-05	4.773858643570361e-05	2.638568278730491e-05
IIIX	TRUE	TRUE	1.3652600993303435e-05	2.000263855419068e-05	2.638568278730491e-05
IIIX	FALSE	FALSE	2.374732823451964e-10	2.374732823451964e-10	2.374732823451964e-10

Figure B.3.: Application of data qubit errors on the WT3 code lattice, using the tabular superoperator calculated from Sec. B.2.2. We show a R_1^Z stabilizer unit cell as an example where we apply the errors on data qubits of the current R_1^Z stabilizer and idling errors on other data qubits in the unit cell.

B.3.3. FLAG FAULT-TOLERANCE OF THE WT3 ARCHITECTURE

The distributed implementation of the WT4 code is fault-tolerant by construction, given the fault-tolerant creation of the GHZ states, as there is no propagation of errors (hook errors) [11] from one node to another. However, the bare WT3 architecture is not fault-tolerant w.r.t. hook errors, as there can be weight-2 error propagation from single qubits errors within each node due to local two-qubit controlled gates. A flagged version of the WT3 stabilizer measurement circuit could be considered to detect and correct for these hook errors [12]. We describe one way to implement the flagged circuit in this appendix. This error propagation is shown in Fig. B.4(a). An X error can propagate from the communication qubit to both data qubits within the module, which goes undetectable. This error propagation can be detected using a flag qubit [13]. The error is intentionally propagated to the flag qubit, where it is detected upon the measurement. This flagged stabilizer circuit (Fig. B.4(b)) can be used after the logical initialization (in the first layer of the first QEC cycle) of the code to detect such hook errors. Please note that this circuit does not provide a unique detection pattern for this error because, for instance, an X error on qubit-2 after the first cnot would also lead to the same detection pattern (flip of f_B measurement outcome). However, detecting such errors helps to decode errors better as this information can be combined with additional syndrome data to improve the decoding. For instance, in case of a hook error (as shown), another Z-stabilizer of qubit-3 will also flip, and this condition can be pre-programmed in the decoder to improve the logical error rates of the surface code. However, for the scope of this work, we only limit ourselves to simulating the unflagged version of the WT3 architecture.

B.3.4. SIMULTANEOUS STABILIZER MEASUREMENTS VS. SUB-ROUND STRUCTURE

A natural question arises: what is the impact of dividing the stabilizer measurement round into sub-rounds on decoding the QEC code? In a monolithic architecture, all the stabilizers in each layer are measured simultaneously via intertwined stabilizer circuits [11, 14]. We can consider a small example in the case of perfect measurements. For two neighboring Z type stabilizers Z_{abcd} and Z_{befg}, any incoming error X_b will flip both the stabilizers and is trivial to correct for the decoder. However, if we first measure Z_{abcd} in the first sub-round and Z_{befg} in the second sub-round, there may be X_b error that can occur between the two sub-rounds, triggering only the later Z_{befg} stabilizer. This deceives the decoder to infer that a measurement error as occurred on one of the communication qubits b,e,f,g. Thereby missing the data qubit error correction via X_b and increasing the X-logical error probability. This kind of error occurs more often in the WT3 architecture as it has

twice the number of sub-rounds, which makes catching easy recovery configurations challenging for the decoder. More detailed analytical or numerical analysis of these errors is beyond the scope of this present work, and we leave this for future work.

B.4. EMISSION BASED SCHEME AND DISTILLATION PROTOCOLS

This section provides a full analytical treatment of the emission-based scheme and its performance evaluation in the presence of circuit-level noise. We first describe the entanglement generation through a Bell-pair between two modules via the single-click protocol [15].

B.4.1. SINGLE-CLICK PROTOCOL

Consider two modules as identical emitter setups, A and B, where each emitter (the communication qubit of each module acts as the emitter qubit) can be initialized in the arbitrary state

$$|\Psi\rangle_{\text{init}}^{\text{A/B}} = \sqrt{1-\alpha}|0\rangle + \sqrt{\alpha}|1\rangle \tag{B.13}$$

where α is the bright state population parameter. This state can be initialized for each emitter with fidelity F_{prep}. This gives the density matrix

$$\rho_{\text{init}}^{\text{A/B}} = (1-\alpha)|0\rangle\langle 0| + (2F_{\text{prep}}-1)\sqrt{\alpha(1-\alpha)}|0\rangle\langle 1| + (2F_{\text{prep}}-1)\sqrt{\alpha(1-\alpha)}|1\rangle\langle 0| + \alpha|1\rangle\langle 1| \tag{B.14}$$

where the preparation infidelity noise is modelled as a dephasing channel over the state. Each of the emitters is now excited via a π-pulse, which causes the bright state $|1\rangle$ to emit a photon ($|1\rangle \rightarrow |11_{\text{ph}}\rangle$) while the dark state $|0\rangle$ does not lead to any emission ($|0\rangle \rightarrow |00_{\text{ph}}\rangle$), where the second ket is for the photon number, denoted with subscript 'ph'. The resulting density matrix for each emitter-photon is

$$\rho_{\text{emit}}^{\text{A/B}} = (1-\alpha)|00_{\text{ph}}\rangle\langle 00_{\text{ph}}| + (2F_{\text{prep}}-1)\sqrt{\alpha(1-\alpha)}|00_{\text{ph}}\rangle\langle 11_{\text{ph}}| + (2F_{\text{prep}}-1)\sqrt{\alpha(1-\alpha)}|11_{\text{ph}}\rangle\langle 00_{\text{ph}}| + \alpha|11_{\text{ph}}\rangle\langle 11_{\text{ph}}| \tag{B.15}$$

However, there could be an excitation error due to the application of this excitation pulse, which can occur due to an extra photon being emitted or unintentionally exciting the dark state. We describe this as excitation error probability p_{EE}, and this phenomenon is modeled as a dephasing channel applied to either the emitter or the emitted photon state. The

resulting density matrix is

$$\rho_{\text{emit}}^{\text{A/B}} = (1-\alpha)|00_{\text{ph}}\rangle\langle 00_{\text{ph}}| + (2F_{\text{prep}}-1)(1-2p_{\text{EE}})\sqrt{\alpha(1-\alpha)}|00_{\text{ph}}\rangle\langle 11_{\text{ph}}| + (2F_{\text{prep}}-1)(1-2p_{\text{EE}})\sqrt{\alpha(1-\alpha)}|11_{\text{ph}}\rangle\langle 00_{\text{ph}}| + \alpha|11_{\text{ph}}\rangle\langle 11_{\text{ph}}| \quad \text{(B.16)}$$

for each emitter-photon setup. After this step, the flying photons are sent to a middle station where both photons are interfered with via a beam splitter. However, there is noise in the fiber, which carries the photons.

We consider the phase uncertainty λ due to the path length difference between the interferometer's two arms. This can be realized as a dephasing channel with some error probability λ. This is calculated as:

$$\lambda = \frac{1}{2}\left(1 + \frac{I_1(\sigma(\varphi)^{-2})}{I_0(\sigma(\varphi)^{-2})}\right) \quad \text{(B.17)}$$

Where I_0 and I_1 are modified Bessel functions of the zeroth and first order, and $\sigma(\varphi)$ is the standard deviation of the phase instability. Typically, this value is around 0.984 [9, 16, 17] for the relevant phase uncertainty in the recent experiments. This dephasing channel is applied to one of the photons (the one from emitter A). Then we obtain

$$\rho_{\text{em-ph}}^{\text{A}} = (1-\alpha)|00_{\text{ph}}\rangle\langle 00_{\text{ph}}| + (2F_{\text{prep}}-1)(1-2p_{\text{EE}})(2\lambda-1)\sqrt{\alpha(1-\alpha)}|00_{\text{ph}}\rangle\langle 11_{\text{ph}}| + (2F_{\text{prep}}-1)(1-2p_{\text{EE}})(1-2\lambda)\sqrt{\alpha(1-\alpha)}|11_{\text{ph}}\rangle\langle 00_{\text{ph}}| + \alpha|11_{\text{ph}}\rangle\langle 11_{\text{ph}}| \quad \text{(B.18)}$$

Moreover, as the fiber is also noisy, we have photon loss through the fiber. We combine this effect with also the photon detector efficiency. Each excitation's total photon detection probability is parameterized by η_{ph}. This is a product of the total transmissivity between the emitter and the photon detector (accounts for photon loss), the detector efficiency, and the probability that the desired photon is emitted during the detection time window and within the zero-phonon line of the emitter. We model this overall effect as an amplitude-damping channel on both the emitter photons. The Kraus operators for the amplitude damping (AD) channel are:

$$K_1^{\text{AD}} = \begin{bmatrix} 1 & 0 \\ 0 & \sqrt{\eta_{\text{ph}}} \end{bmatrix}, \; K_2^{\text{AD}} = \begin{bmatrix} 0 & \sqrt{1-\eta_{\text{ph}}} \\ 0 & 0 \end{bmatrix} \quad \text{(B.19)}$$

According to Eqn. B.3, operating with the amplitude-damping channel on the emitted photons from both the modules, we get the output states

before the photon detection as:

$$\begin{aligned}\rho^{\mathrm{A}}_{\text{em-ph}} = {} & (1-\alpha)|00_{\mathrm{ph}}\rangle\langle 00_{\mathrm{ph}}| + \\ & (2F_{\mathrm{prep}}-1)(1-2p_{\mathrm{EE}})\sqrt{\eta_{\mathrm{ph}}}(2\lambda-1)\sqrt{\alpha(1-\alpha)}|00_{\mathrm{ph}}\rangle\langle 11_{\mathrm{ph}}| + \\ & \alpha(1-\eta_{\mathrm{ph}})|10_{\mathrm{ph}}\rangle\langle 10_{\mathrm{ph}}| + \\ & (2F_{\mathrm{prep}}-1)(1-2p_{\mathrm{EE}})\sqrt{\eta_{\mathrm{ph}}}(1-2\lambda)\sqrt{\alpha(1-\alpha)}|11_{\mathrm{ph}}\rangle\langle 00_{\mathrm{ph}}| + \\ & \alpha\eta_{\mathrm{ph}}|11_{\mathrm{ph}}\rangle\langle 11_{\mathrm{ph}}|\end{aligned} \tag{B.20}$$

$$\begin{aligned}\rho^{\mathrm{B}}_{\text{em-ph}} = {} & (1-\alpha)|00_{\mathrm{ph}}\rangle\langle 00_{\mathrm{ph}}| + \\ & (2F_{\mathrm{prep}}-1)(1-2p_{\mathrm{EE}})\sqrt{\eta_{\mathrm{ph}}}\sqrt{\alpha(1-\alpha)}|00_{\mathrm{ph}}\rangle\langle 11_{\mathrm{ph}}| + \\ & \alpha(1-\eta_{\mathrm{ph}})|10_{\mathrm{ph}}\rangle\langle 10_{\mathrm{ph}}| \\ & + (2F_{\mathrm{prep}}-1)(1-2p_{\mathrm{EE}})\sqrt{\eta_{\mathrm{ph}}}\sqrt{\alpha(1-\alpha)}|11_{\mathrm{ph}}\rangle\langle 00_{\mathrm{ph}}| + \\ & \alpha\eta_{\mathrm{ph}}|11_{\mathrm{ph}}\rangle\langle 11_{\mathrm{ph}}|\end{aligned} \tag{B.21}$$

For the photon detector, we assume the regime with negligible dark count probability, similar to other schemes, about 10^{-6}, and we neglect it. We consider the photon indistinguishability μ for the joint Bell-pair measurement for the perfect interference. The measurement projector for the two-photon measurement can be described with the following POVMs acting only on the photonic degrees of freedom [18].

$$\begin{aligned}E_{00} = {} & |0_{\mathrm{ph}}0_{\mathrm{ph}}\rangle\langle 0_{\mathrm{ph}}0_{\mathrm{ph}}| \\ E_{01} = {} & \frac{1}{2}\Bigg(\frac{\sqrt{1+\sqrt{\mu}}+\sqrt{1-\sqrt{\mu}}}{\sqrt{2}}\left(|0_{\mathrm{ph}}1_{\mathrm{ph}}\rangle\langle 0_{\mathrm{ph}}1_{\mathrm{ph}}| + |1_{\mathrm{ph}}0_{\mathrm{ph}}\rangle\langle 1_{\mathrm{ph}}0_{\mathrm{ph}}|\right) + \\ & \frac{\sqrt{1-\sqrt{\mu}}-\sqrt{1+\sqrt{\mu}}}{\sqrt{2}}\left(|0_{\mathrm{ph}}1_{\mathrm{ph}}\rangle\langle 1_{\mathrm{ph}}0_{\mathrm{ph}}| + |1_{\mathrm{ph}}0_{\mathrm{ph}}\rangle\langle 0_{\mathrm{ph}}1_{\mathrm{ph}}|\right) + \\ & \sqrt{1+\mu}|1_{\mathrm{ph}}1_{\mathrm{ph}}\rangle\langle 1_{\mathrm{ph}}1_{\mathrm{ph}}|\Bigg) \\ E_{10} = {} & \frac{1}{2}\Bigg(\frac{\sqrt{1+\sqrt{\mu}}+\sqrt{1-\sqrt{\mu}}}{\sqrt{2}}\left(|0_{\mathrm{ph}}1_{\mathrm{ph}}\rangle\langle 0_{\mathrm{ph}}1_{\mathrm{ph}}| + |1_{\mathrm{ph}}0_{\mathrm{ph}}\rangle\langle 1_{\mathrm{ph}}0_{\mathrm{ph}}|\right) + \\ & \frac{\sqrt{1+\sqrt{\mu}}-\sqrt{1-\sqrt{\mu}}}{\sqrt{2}}\left(|0_{\mathrm{ph}}1_{\mathrm{ph}}\rangle\langle 1_{\mathrm{ph}}0_{\mathrm{ph}}| + |1_{\mathrm{ph}}0_{\mathrm{ph}}\rangle\langle 0_{\mathrm{ph}}1_{\mathrm{ph}}|\right) + \\ & \sqrt{1+\mu}|1_{\mathrm{ph}}1_{\mathrm{ph}}\rangle\langle 1_{\mathrm{ph}}1_{\mathrm{ph}}|\Bigg) \\ E_{11} = {} & \frac{\sqrt{1-\mu}}{\sqrt{2}}|1_{\mathrm{ph}}1_{\mathrm{ph}}\rangle\langle 1_{\mathrm{ph}}1_{\mathrm{ph}}|\end{aligned} \tag{B.22}$$

Here E_{00} corresponds to no photon detection. E_{01} and E_{10} correspond to one photon detected in the right and left detector, respectively. And E_{11} means two photons being detected, one at each detector. For the successful entanglement generation, we herald on a single click, that is, one photon being detected at either the right or left detector. For a left/right detector click (via E_{10}/E_{01}), the output states would be

$$\rho_{\text{out}}^{\text{left/right}} = \frac{(\mathbb{I}\otimes E_{10/01})(\rho_{\text{em-ph}}^{\text{A}}\otimes\rho_{\text{em-ph}}^{\text{B}})(\mathbb{I}\otimes E_{10/01})^\dagger}{\text{Tr}[(\mathbb{I}\otimes E_{10/01})(\rho_{\text{em-ph}}^{\text{A}}\otimes\rho_{\text{em-ph}}^{\text{B}})(\mathbb{I}\otimes E_{10/01})^\dagger]} \tag{B.23}$$

where the tensor product $\rho_{\text{em-ph}}^{\text{A}}\otimes\rho_{\text{em-ph}}^{\text{B}}$ follows the order

$$|\text{em-1}\rangle|\text{em-2}\rangle|\text{ph-1}\rangle|\text{ph-2}\rangle\,. \tag{B.24}$$

And we identify the denominator as the success probability $P_{\text{single}}^{\text{left/right}}$ of the respective single-click. We get the raw output entangled state after performing a partial trace over the photons:

$$\begin{aligned}\rho_{\text{out}}^{\text{left}} = \frac{1}{4+\alpha\eta_{\text{ph}}(\mu-3)}\Big(&2(1-\alpha)|01\rangle\langle 01| + 2(2F_{\text{prep}}-1)^2(1-2p_{\text{EE}})^2\\ &(1-\alpha)(2\lambda-1)\sqrt{\mu}(|01\rangle\langle 10| + |10\rangle\langle 01|) + 2(1-\alpha)|10\rangle\langle 10| +\\ &\alpha(4+\eta_{\text{ph}}(\mu-3))|11\rangle\langle 11|\Big)\end{aligned} \tag{B.25}$$

$$\begin{aligned}\rho_{\text{out}}^{\text{right}} = \frac{\alpha\eta_{\text{ph}}}{2}\Big(&(1-\alpha)|01\rangle\langle 01| + (2F_{\text{prep}}-1)^2(1-2p_{\text{EE}})^2\\ &(1-\alpha)(1-2\lambda)\sqrt{\mu}(|01\rangle\langle 10| + |10\rangle\langle 01|) + (1-\alpha)|10\rangle\langle 10| +\\ &\frac{\alpha}{2}(4+\eta_{\text{ph}}(\mu-3))|11\rangle\langle 11|\Big)\end{aligned} \tag{B.26}$$

To convert these states into the desired Bell-state $|\Psi^+\rangle$ we apply an X^{c} gate to one of the emitters and apply a phase correction on one of the emitters if the right detector clicks. Both these gates are noisy and characterized by depolarization noise with gate error p_g. We include gate error for the post-correction gates, in contrast, to Ref. [9]. This gives the corrected output density matrices $\rho_{\text{final}}^{\text{left}}$ and $\rho_{\text{final}}^{\text{right}}$.

$$\begin{aligned}\rho_{\text{final}}^{\text{left}} &= (X^{\text{c}}\otimes\mathbb{I})\rho_{\text{out}}^{\text{left}}(X^{\text{c}}\otimes\mathbb{I})\\ \rho_{\text{final}}^{\text{right}} &= (X^{\text{c}}\otimes Z^{\text{c}})\rho_{\text{out}}^{\text{right}}(X^{\text{c}}\otimes Z^{\text{c}})\end{aligned} \tag{B.27}$$

The average density matrix from the single click protocol is, therefore:

$$\rho_s = P^{\text{left}}_{\text{single}}(\mathbb{N}^{\text{single-qubit}}_{\text{gate}} \otimes \mathbb{I})\rho^{\text{left}}_{\text{final}}(\mathbb{N}^{\text{single-qubit}}_{\text{gate}} \otimes \mathbb{I}) + P^{\text{right}}_{\text{single}}(\mathcal{N}^{\text{single-qubit}}_{\text{gate}} \otimes \mathcal{N}^{\text{single-qubit}}_{\text{gate}})\rho^{\text{right}}_{\text{final}}(\mathcal{N}^{\text{single-qubit}}_{\text{gate}} \otimes \mathcal{N}^{\text{single-qubit}}_{\text{gate}}) \tag{B.28}$$

It turns out that $P^{\text{left}}_{\text{single}} = P^{\text{right}}_{\text{single}}$ and the total success probability of the single-click protocol is the sum of both:

$$P^{\text{succ}}_{\text{single}} = \frac{1}{2}\alpha\eta_{\text{ph}}\big(4 - \alpha\eta_{\text{ph}}(3-\mu)\big) \tag{B.29}$$

We calculate the overall fidelity of the single-click protocol as

$$F_{\text{single}} = \text{Tr}\Big[\sqrt{\sqrt{\Phi^+}\rho_s\sqrt{\Phi^+}}\Big]^2 \tag{B.30}$$

where $\Phi^+ = |\Phi^+\rangle\langle\Phi^+|$ is the target Bell-pair density matrix. The full-analytical expression of the average fidelity is:

$$F_{\text{single}} = \frac{\alpha\eta_{\text{ph}}}{36P^{\text{succ}}_{\text{single}}}\Big(36(1-\alpha)(1+\phi)+(9p_g-4p_g^2)\big(36\phi-4\alpha(8+\eta_{\text{ph}}(\mu-3))\big)\Big) \tag{B.31}$$

where

$$\phi = \sqrt{\mu}(2F_{\text{prep}}-1)^2(2\lambda-1)(1-p_{\text{EE}})^2 \tag{B.32}$$

captures the overall noise in the photon generation and detection.

B.4.2. DOUBLE CLICK PROTOCOL

The raw output state ($\rho^{\text{left/right}}_{\text{out}}$) from the single-click protocol has a contribution from the pure bright-state term $|11\rangle\langle 11|$, which leads to an overall mixed state. See Eqn. B.25 and Eqn. B.26. Double-click (Barrett-Kok) protocol eliminates this term by the application of X^c gate on each emitter on the raw output state after the single click. Another round of single-click protocol is performed and heralded on the consecutive single-click. This eliminates the $|00\rangle\langle 00|$ term (after X^c gates) because it does not emit photons in the second round. The detection pattern now has four possibilities: left ⊗ left, left ⊗ right, right ⊗ left, and right ⊗ right, as the photon detector click patterns. However, for the double-click protocol [19], we initialize the initial state with $\alpha = 1/2$, and the phase uncertainty λ gets eliminated due to the symmetry of the protocol. The total success probability for the double-click protocol is:

$$P^{\text{succ}}_{\text{double}} = \sum_{a}\Big(P^{a}_{\text{single}}P^{a\otimes a}_{\text{single}} + P^{a}_{\text{single}}P^{a\otimes \bar{a}}_{\text{single}}\Big) \tag{B.33}$$

where a $\in \{\text{left}, \text{right}\}$, and $\overline{\text{left}} = \text{right}$, and vice versa. All these terms are equal, and we get the total probability with post-correction with single-qubit gates as:

$$P_{\text{double}}^{\text{succ}} = \frac{\eta_{\text{ph}}^2}{36}\Big(18 + 12p_g\big(2 + \eta_{\text{ph}}(\mu - 3)\big) + p_g^2\eta_{\text{ph}}^2(\mu - 3)^2\Big) \tag{B.34}$$

This expression reduces to $\eta_{\text{ph}}^2/2$ without gate error, as considered in Ref. [9]. The full analytical expression for the average fidelity of the double-click protocol is:

$$\begin{aligned}
F_{\text{double}} =& \Big(3p_g\big(-54(1+\eta_{\text{ph}}) + p_g(96 + 36\eta_{\text{ph}} + \\
& p_g(-32 - (-9 + 4p_g)\eta_{\text{ph}}(-8 + 3\eta_{\text{ph}})))\big) + \\
& 2p_g\big(2\big(1 - 2F_{\text{prep}}\big)^2\big(1 - 2p_{\text{EE}}\big)^4(-189 + 4p_g(81 + 4p_g(-15 + 4p_g))) + \\
& (27 - 2p_g(9 + 2p_g(-9 + 4p_g)))\eta_{\text{ph}} + 3p_g^2(-9 + 4p_g)\eta_{\text{ph}}^2\big)\mu + \\
& (9 - 4p_g)p_g^3\eta_{\text{ph}}^2\mu^2 + 162\big(1 + \big(1 - 2F_{\text{prep}}\big)^2\big(1 - 2p_{\text{EE}}\big)^4\mu\big)\Big)\Big/ \\
& \Big(18\big(18 + p_g\big(24 + \eta_{\text{ph}}(12 + p_g\eta_{\text{ph}}(-3 + \mu))(-3 + \mu)\big)\big)\Big)
\end{aligned} \tag{B.35}$$

When no gate error is considered, $p_g = 0$, then this reduces to $F_{\text{double}} = (1 + \frac{\phi^2}{(1-2F_{\text{prep}})^2})/2$, given $\lambda = 1$. This is slightly different from the limiting expression in Ref. [9] because of the change in the definition of the preparation fidelity. In our work, the preparation fidelity refers to the state preparation of the emitter state only, initialized with the bright-state parameter. In contrast, in Ref. [9], it refers to the emitter-photon state preparation fidelity, and the dephasing noise channel is applied to the emitted photon (which is applied in both rounds, incurring an extra quadratic factor in the ϕ^2 term).

B.4.3. SINGLE-CLICK VERSUS DOUBLE-CLICK

The $P_{\text{succ}}^{\text{link}}$ for single-click protocol depends on bright state parameter α, and changing this parameter has a tradeoff between fidelity and success probability. This is evident from Eqn. B.29 and Eqn. B.31. For double-click, the $P_{\text{succ}}^{\text{link}}$ is quadratically dependent on the effective photon detection probability η_{ph}, which is very small (for the NTP) and therefore unfavorable for threshold performance. Through the single-click protocol, the $P_{\text{succ}}^{\text{link}}$ is linear in η_{ph} (which is higher) and we can trade in some $P_{\text{succ}}^{\text{link}}$ to reduce the infidelity of the Bell state, and satisfy the numerical bounds on $P_{\text{succ}}^{\text{link}}$ and fidelity as discussed in the results section. However, the fidelity was still low (less than 0.90) for

the existence of a threshold (inclusive of the physical gate error), even for very low values of α. A similar exploration was also done in Ref. [9] on single-click vs. the double-click protocol without the gate error. In this view, we use the single-click protocol for NTP and double-click for FP to optimize the logical error rates in these regimes.

B.4.4. FUSION AND DISTILLATION PROTOCOLS

We describe an example of a fusion and distillation protocol using elementary Bell pairs. As an example (shown in Fig. 3.3(c)), we consider how to generate a GHZ state between three modules, A, B, and C, while using auxiliary Bell pairs along the way to increase fidelity. First, a Bell pair, $|\Phi^+\rangle_{AB}$, is generated between the communication qubits of modules A and B and swapped to memory qubits within each module through local two-qubit gates. Another Bell pair $|\Phi^+\rangle_{AB}$ is generated and is used to distill the prior one by measuring the stabilizer $X_A X_B$ (distilled state denoted by *). Similarly, a Bell pair, $|\Phi^+\rangle_{BC}$, is generated between modules B and C and distilled. Finally, a cnot operation is applied between the two Bell pair qubits at module B, followed by a measurement of one of the qubits (the communication qubit), which results in a three-qubit GHZ state $|\Phi^+\rangle_{ABC}$ between A-B-C up to a local single qubit rotation. This GHZ state can be further distilled via a Bell pair $|\Phi^+\rangle_{AC}$.

Now we give explicit examples of the EM fusion protocols for which we found a threshold. These protocols were searched using the 'dynamic program' first introduced in Ref. [20] and later used in Ref. [9]. We searched the GHZ fusion and distillation protocols pool of WT4 and WT3 GHZ states for maximum stabilizer fidelity output. Following that, a threshold calculation was run for a set of the best protocols chosen based on stabilizer fidelity. Finally, the protocol with the highest threshold and least logical error rates was chosen for each case. These are the protocols we showcase in Fig. B.6, for which we obtained thresholds. Using these binary tree diagrams, we sketch the operations involved in the GHZ creation chronologically via the EM protocol. Details of the protocol operations are provided in the caption of Fig. B.6. It consists of elementary Bell-pair generation between the modules and their distillation and fusion with other modules. For each protocol, we report the maximum number of Bell-pairs used as its k value and the maximum number of memory qubits used by a node for that protocol (this includes memory qubits used as data qubits). In all these protocols, the maximum number of auxiliary qubits used is two, but WT4 architecture has one data qubit per node, while WT3 architecture has two data qubits per node. There are two extra coherence times parameter sets for which we obtained thresholds. These are not part of the main script, but we motivate these (Set-mix and Set-D) in App. B.9

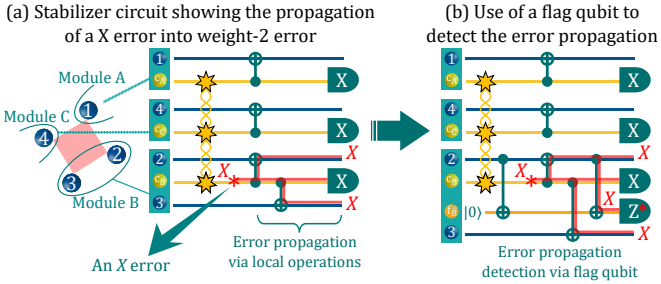

Figure B.4.: Detection of error propagation (hook errors) using flag qubit within one module (Module B) of WT3 architecture stabilizer. (a) Shows the example of an X error on a communication qubit (c_B) that propagates to two data qubits (2 & 3) within one module via local cnot operations. (b) Depicts the usage of additional memory qubit (auxiliary) as flag qubit (f_B) where the error also propagates to the flag qubit (initialized in $|0\rangle$) and is detected via its Z measurement flip (shown as Z^*).

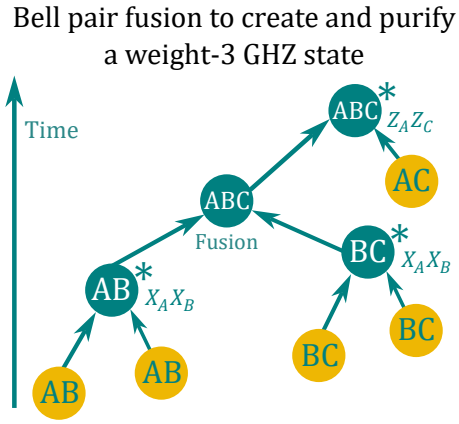

Figure B.5.: An example of a GHZ state fusion protocol with distillation used to create a high-fidelity WT3 GHZ state presented as a tree graph. Events in yellow indicate Bell pair generation between the respective modules, while the teal-colored arrows labeled with a multi-Pauli operator indicate a distillation event by measuring that operator. Modules with a teal color indicate the distilled entangled state.

and App. B.8.

B.5. REFLECTION SCHEME

The key mechanism of the RFL scheme is the photon-mediated cnot gate in the protocol. This direct spin-photon cnot operation can be achieved by reflecting a time-bin encoded single photonic qubit from a single-sided cavity with a strongly coupled communication qubit [21, 22]. Ideally, the photon is prepared in a state $\frac{1}{\sqrt{2}}(|e\rangle_{\text{ph}} + |l\rangle_{\text{ph}})$ while the communication qubit is prepared in $|0\rangle$. Assuming that the $|0\rangle$ state does not couple to the cavity field and that the incoming photon is on resonance with the cavity, scattering of the early photon result in the transformation $\frac{1}{\sqrt{2}}(|e\rangle_{\text{ph}}+|l\rangle_{\text{ph}})|0\rangle \rightarrow \frac{1}{\sqrt{2}}(-|e\rangle_{\text{ph}}+|l\rangle_{\text{ph}})|0\rangle$, i.e. the photon is reflected from the cavity with a π-phase shift. Before the scattering of the late photon, a Hadamard gate is applied to the communication qubit, transforming $|0\rangle$ into $\frac{1}{\sqrt{2}}(|0\rangle + |1\rangle) = |+\rangle$. If the $|1\rangle$ state is strongly coupled to the cavity field, scattering of the late photon will result in the transformation, $\frac{1}{\sqrt{2}}(-|e\rangle_{\text{ph}} + |l\rangle_{\text{ph}})|+\rangle \rightarrow \frac{1}{\sqrt{2}}(|e\rangle_{\text{ph}}|+\rangle + |l\rangle_{\text{ph}}|-\rangle)$ up to a global phase where $|-\rangle = \frac{1}{\sqrt{2}}(|0\rangle - |1\rangle)$. This is because scattering from the $|1\rangle$ state will reflect the photon without a π-phase shift in the strongly coupled regime. A final Hadamard gate on the communication qubit taking $|+\rangle \rightarrow |0\rangle$ and $|-\rangle \rightarrow |1\rangle$ completes the cnot operation. By reflecting a single photonic qubit with consecutive modules, this scheme allows for the direct generation of a GHZ state as shown schematically in Fig. 3.4 in the main script. The generation is heralded by a final measurement of the photonic qubit in the X-basis, which can be achieved with photonic switching and a fiber delay.

Here, we describe the reflection scheme step by step in mathematical detail. We consider the scattering of a photonic time-bin qubit from a single spin-coupled cavity and then generalize this to the case where the photon scatters off multiple cavities. The spin is initialized in the $|0\rangle$ state, and the photonic state is an equal superposition of the early and late time-bin states. Hence, the photon-spin state is $\frac{1}{\sqrt{2}}(|\text{E}0\rangle + |\text{L}0\rangle)$.

Let r_0 and r_1 denote the photonic reflection coefficients corresponding to the cases when the spin is in the uncoupled state $|0\rangle$ and coupled state $|1\rangle$, respectively. After the early time-bin component of the photon scattered, the unnormalized state of the system becomes $\frac{1}{\sqrt{2}}(r_0|\text{E}0\rangle + |\text{L}0\rangle)$. Then, a Hadamard gate is executed on the spin, which transforms the direct product state into $\frac{1}{\sqrt{2}}(r_0|\text{E}+\rangle + |\text{L}+\rangle)$. Next, the late-time-bin component of the photon is scattered, and the state of the system becomes $\frac{1}{\sqrt{2}}\left(r_0|\text{E}+\rangle + \frac{1}{\sqrt{2}}(r_0|\text{L}0\rangle + r_1|\text{L}1\rangle)\right)$. Finally, a second Hadamard gate is executed on the spin, and the state of the system

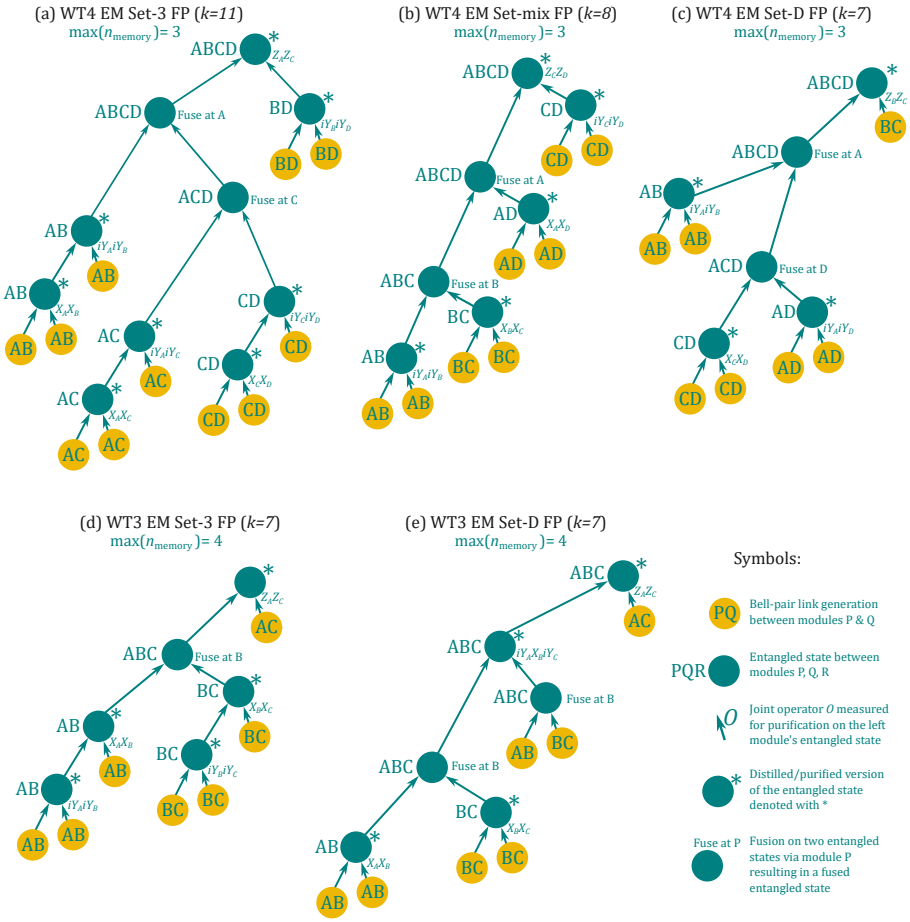

Figure B.6.: Optimised emission-based (EM) scheme fusion and distillation protocols for various architectures and schemes, for which we obtained (highest) thresholds. We sketch these protocols as binary-tree diagrams, similar to Ref. [9], with time running vertically up. We also show optimized protocols for two extra coherence time sets, namely Set-mix and Set-D, introduced in App. B.9 and App. B.8. (a), (b) and (c) show the protocols for WT4 architecture, while (d) and (e) show protocols for WT3 architecture. The total number of Bell-pairs used in a fusion protocol is shown as its k value. These protocols consist of operations such as the Bell-pair generation (via double-click protocol for all these examples), the fusion of Bell-pair with other entangled states to increase the weight of the resulting entangled state distributed between the modules, and purification/distillation operations by measuring some joint operators (stabilizers of that entangled state). Through these protocols, the total number of memory qubit requirements can be estimated for each case. We show the maximum number of memory qubits required (including the data qubits) in a module for each reported protocol below its label.

becomes

$$|\Psi_1\rangle = \frac{1}{\sqrt{2}}\left(r_0|\mathrm{E}0\rangle + \frac{r_0+r_1}{2}|\mathrm{L}0\rangle + \frac{r_0-r_1}{2}|\mathrm{L}1\rangle\right). \tag{B.36}$$

For multiple cavities, the above procedure generalizes straightforwardly. Consequently, the final state of the multiple spin qubits and the photon will be

$$\begin{aligned}|\Psi_N\rangle =& \frac{1}{\sqrt{2}}\Bigg[r_0^n|\mathrm{E}\rangle|0\rangle^{\otimes n} + \\ & |\mathrm{L}\rangle\left(\frac{r_0+r_1}{2}|0\rangle + \frac{r_0-r_1}{2}|1\rangle\right)^{\otimes n}\Bigg],\end{aligned} \tag{B.37}$$

where n is the number of the spins.

At the final step, an optical switch and a delay line are used to measure the photon in the X basis ($|\pm\rangle_{\mathrm{ph}} = (|\mathrm{E}\rangle \pm |\mathrm{L}\rangle)/\sqrt{2}$). If the photon is detected in the $|+\rangle_{\mathrm{ph}}$ state, the spins will be projected into an (unnormalized) state

$$|\Psi_+\rangle = \frac{1}{2}\left[r_0^n|0\rangle^{\otimes n} + \left(\frac{r_0+r_1}{2}|0\rangle + \frac{r_0-r_1}{2}|1\rangle\right)^{\otimes n}\right]. \tag{B.38}$$

One can see from Eqn. (B.38) that, when $r_0 \approx -r_1$, it resembles the GHZ state $|\mathrm{GHZ}\rangle = (|0\rangle^{\otimes n} + |1\rangle^{\otimes n})/\sqrt{2}$. If the photon is detected in the $|-\rangle$ state, the spins will be projected into a state

$$|\Psi_-\rangle = \frac{1}{2}\left[r_0^n|0\rangle^{\otimes n} - \left(\frac{r_0+r_1}{2}|0\rangle + \frac{r_0-r_1}{2}|1\rangle\right)^{\otimes n}\right]. \tag{B.39}$$

In this case, when $r_0 \approx -r_1$, the resulting state is close to the state $(|0\rangle^{\otimes n} - |1\rangle^{\otimes n})/\sqrt{2}$. In this case, a Z gate can be applied on the first spin qubit to recover the state $|\mathrm{GHZ}\rangle$. Note that the states in Eqs. (B.38)-(B.39) are not normalized. The sum of the norms of these two states gives the success probability of the protocol in the absence of additional photon loss:

$$P_{\mathrm{succ}}^{\mathrm{GHZ}} = \langle\Psi_+|\Psi_+\rangle + \langle\Psi_-|\Psi_-\rangle. \tag{B.40}$$

The reflection coefficients, r_0 and r_1 can be expressed in terms of the different spin-photon interface parameters as [23]:

$$r_{1,0} = 1 - \frac{2\frac{\kappa_c}{\kappa_c+\kappa_l}}{1 + 2\mathrm{i}\frac{\omega}{\kappa_c+\kappa_l} + \frac{4C_1}{1+2\mathrm{i}\delta_{1,0}/\gamma}}, \tag{B.41}$$

where δ_0 and δ_1 are the detunings between the corresponding spin transition and the input photon frequency and ω is the detuning between

the cavity resonance frequency and the input photon. The two spin transitions have a fixed detuning Δ hence $\delta_0 - \delta_1 = \Delta$ (see Fig. 3.11 in the main text).

To determine the optimal performance, we optimize these two detunings and find a region where the fidelity of the GHZ state reaches a global maximum while the success rate is nearly flat, as shown in Fig. B.7 and Fig. B.8. Hence, the location of the maximum fidelity of the GHZ state determines the optimum values of ω and δ as listed in the table in Fig. 3.11 in the main text. For the simulation of the surface code performance, our simulation also includes faulty Hadamard gates and Z gates as well as additional photon loss from e.g. the optical circulators.

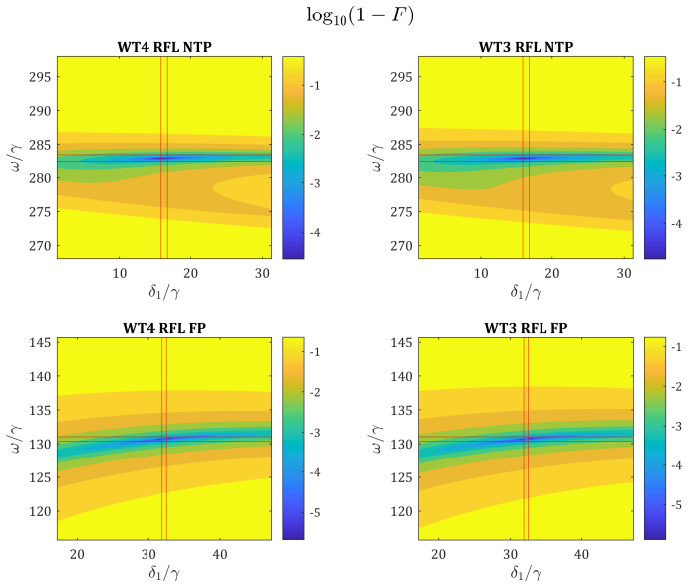

Figure B.7.: Scanning of the base-10 logarithm of the infidelity of the GHZ state over the variables of ω and δ_1. The subtitles of the figures denote different cases of state-of-the-art parameters NTP and FP for WT4 and WT3 GHZ states. The found optimum ω and δ_1 and their deviations of σ/γ are indicated with the two horizontal and two vertical red lines with the same separations of $2\sigma/\gamma$. The gate error is set to 0 in this calculation.

B.6. CARVING SCHEME WITH SINGLE PHOTON SOURCE

First, we describe the brief principle of the CAR scheme. In the setup, the communication qubit state $|0\rangle$ is uncoupled while state $|1\rangle$ is strongly

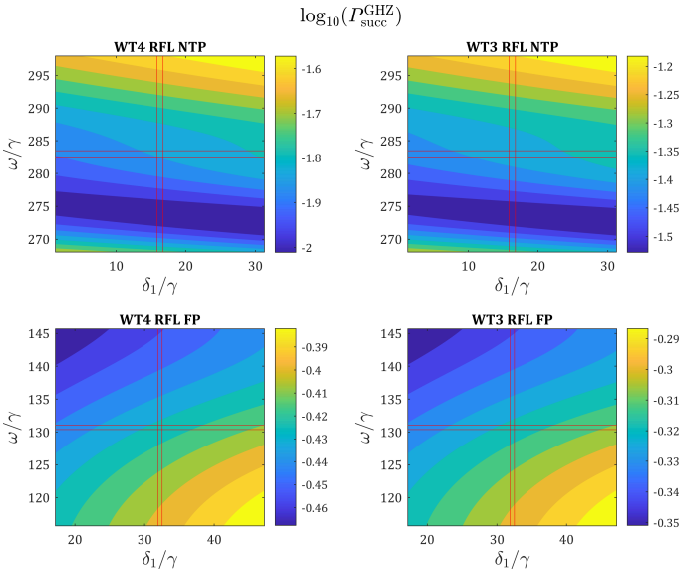

Figure B.8.: Scanning of the base-10 logarithm of the success rate of the GHZ state generation over the variables of ω and δ_1. The plotting follows the same fashion as Fig. B.7.

coupled to the incoming photon through the cavity/waveguide field as in the RFL scheme. Consequently, an incoming photon will be reflected if the qubit is in state $|1\rangle$ and transmitted if the qubit is in state $|0\rangle$ because of interference between the incoming and scattered fields [24]. This can be used to project an initially un-entangled multi-qubit state to a GHZ state probabilistically using a setup as depicted in Fig. 3.5(a) of the main script.

The communication qubits are initially all prepared in the state $|+\rangle$, and a single photon is sent through the setup. The first beam splitter creates a superposition of the photon propagating in the upper (subscript "u") or lower (subscript "l") arm. Notably, the photon can only be transmitted through an arm if all communication qubits in that arm are in state $|0\rangle$. The final beam splitter erases the information about which arm the photon propagated through. The subsequent detection of the photon projects all communication qubits in the lower or upper arm in state $|0\rangle$. Consequently, the detection of the photon will project the communication qubits into a state $\frac{1}{\sqrt{2}}\Big(|0\,0\,0\cdots\rangle_{\text{u}}|+\,+\,+\cdots\rangle_{\text{l}} \pm |+\,+\,+\cdots\rangle_{\text{u}}|0\,0\,0\cdots\rangle_{\text{l}}\Big)$, with the phase determined by which detector recorded the photon. Each qubit state is flipped by applying not gates, and a second photon is sent through the setup. The detection of this photon will project the communication qubits into a GHZ state up to single qubit rotations.

Here, we describe our model of the carving protocol with a perfect single-photon source in more detail. For simplicity, we first consider a setup with only two spins, one at the upper and one at the lower optical route. We will later generalize to more spins. The initial state of the spin reads $|\psi_0\rangle = \frac{1}{2}(|00\rangle + |01\rangle + |10\rangle + |11\rangle) = \frac{1}{2}(1,1,1,1)^{\mathsf{T}}$. When the first photon from the single-photon source passes the first beam splitter, it turns into a superposition state $\frac{1}{\sqrt{2}}(|\mathrm{U}\rangle + |\mathrm{D}\rangle)$, where $|\mathrm{U}\rangle$ is the photon state traveling along the upper route and $|\mathrm{D}\rangle$ the lower route. The unnormalized state describing the transmission of the photon through the spin-cavity systems is:

$$\left|\psi_1^{\mathrm{pre}}\right\rangle = \frac{1}{2\sqrt{2}}\left[\begin{pmatrix} t_0 \\ t_0 \\ t_1 \\ t_1 \end{pmatrix}|\mathrm{U}\rangle + \begin{pmatrix} t_0 \\ t_1 \\ t_0 \\ t_1 \end{pmatrix}|\mathrm{D}\rangle\right] \tag{B.42}$$

where t_0 and t_1 are transmission coefficients for the $|0\rangle$ and $|1\rangle$ states of the spins, respectively.

When the photon is detected after the second beam splitter, the state of the spins will be projected into

$$\left|\psi_1^{+}\right\rangle = \frac{1}{2}\begin{pmatrix} 2t_0 \\ t_0 + t_1 \\ t_0 + t_1 \\ 2t_1 \end{pmatrix} \tag{B.43}$$

if the photon is detected by detector d_+ and

$$\left|\psi_1^{-}\right\rangle = \frac{1}{2}\begin{pmatrix} 0 \\ t_0 - t_1 \\ t_1 - t_0 \\ 0 \end{pmatrix} \tag{B.44}$$

if the photon is detected by detector d_-. We focus on the state $\left|\psi_1^{+}\right\rangle$ state for now but a similar procedure is applied if the outcome is state $\left|\psi_1^{-}\right\rangle$. First, we apply not gates on the spins transforming the state to

$$\left|\psi_1^{+\mathrm{not}}\right\rangle = \frac{1}{2}\begin{pmatrix} 2t_1 \\ t_0 + t_1 \\ t_0 + t_1 \\ 2t_0 \end{pmatrix}. \tag{B.45}$$

We then attempt to transmit a second photon. Assuming again that the second photon is transmitted and detected by detector d_+, the spin state is projected to

$$\left|\psi_2^{++}\right\rangle = \frac{1}{4}\begin{pmatrix} 2t_0 \\ t_0 + t_1 \\ t_0 + t_1 \\ 2t_1 \end{pmatrix} \odot \begin{pmatrix} 2t_1 \\ t_0 + t_1 \\ t_0 + t_1 \\ 2t_0 \end{pmatrix}, \tag{B.46}$$

where $\odot$ is the symbol of the Hadamard product or element-wise product. Here one can see that if $|t_0| \gg |t_1|$, the normalized state $|\psi_2^{++}\rangle$ will resemble a Bell state $\frac{1}{\sqrt{2}}(0,1,1,0)^{\mathsf{T}}$. This is also true for the other detection patterns up to single-qubit gate corrections. Note that the protocol is heralded by the detection of both photons. If either the first or the second photon is not detected, the protocol is re-initialized.

Above, we only considered the transmission and detection of two photons. However, more photons could be scattered in order to increase the fidelity of the state at the expense of a lower success probability. For the general case with n_{wt} spins and n_{sc} scattered photons, one can write an iterative relationship between the spin states after the $(n_{\mathrm{sc}}-1)$th and n_{sc}th scatterings as

$$|\psi_{n_{\mathrm{sc}}}\rangle = \begin{cases} \mathbf{T} \odot |\psi_{n_{\mathrm{sc}}-1}\rangle, & n_{\mathrm{sc}} = 1. \\ \mathbf{T} \odot O_{\mathrm{not}} |\psi_{n_{\mathrm{sc}}-1}\rangle, & n_{\mathrm{sc}} \geq 2. \end{cases} \tag{B.47}$$

where $|\psi_{n_{\mathrm{sc}}}\rangle$ is the spin state after n_{sc}th photon scatterings, and O_{not} is an operation with not gates on every spin. The $\mathbf{T}$ is a vector of transmission coefficients defined as

$$\mathbf{T} = \begin{cases} \frac{\mathbf{t}_{\mathrm{u}}+\mathbf{t}_{\mathrm{d}}}{2}, & \text{photon detected by detector } d_+, \\ \frac{\mathbf{t}_{\mathrm{u}}-\mathbf{t}_{\mathrm{d}}}{2}, & \text{photon detected by detector } d_-, \end{cases} \tag{B.48}$$

where

$$\mathbf{t}_{\mathrm{u}} = \begin{pmatrix} t_0 \\ t_1 \end{pmatrix}^{\otimes n_{\mathrm{u}}} \otimes \begin{pmatrix} 1 \\ 1 \end{pmatrix}^{\otimes n_{\mathrm{d}}} \tag{B.49}$$

$$\mathbf{t}_{\mathrm{d}} = \begin{pmatrix} 1 \\ 1 \end{pmatrix}^{\otimes n_{\mathrm{u}}} \otimes \begin{pmatrix} t_0 \\ t_1 \end{pmatrix}^{\otimes n_{\mathrm{d}}} \tag{B.50}$$

where n_{u} and n_{d} are number of spins in the upper and lower optic routes, respectively.

After at least two rounds of photon scattering, the state of the spins will resemble the state $(|111\cdots\rangle_{\mathrm{u}}|000\cdots\rangle_{\mathrm{l}} \pm |000\cdots\rangle_{\mathrm{u}}|111\cdots\rangle_{\mathrm{l}})/\sqrt{2}$ with the $\pm$ sign depending on the parity of the number of photons detected at detector d_-. To recover the GHZ state $|\phi_+\rangle$, not gates can be applied on the spins at one of the optical routes, and a Z gate may be used on one of the spins to correct the $\pm$ sign. The corresponding gate errors will be added to the density matrix of the resulting GHZ state. The success possibility of the protocol is the trace of the unnormalized density matrix multiplied by the efficiency of the single photon detectors, single-photon source, and in/out coupling losses.

The different transmission coefficients t_0 and t_1 correspond to two different optical transitions. Therefore, the two transitions have different

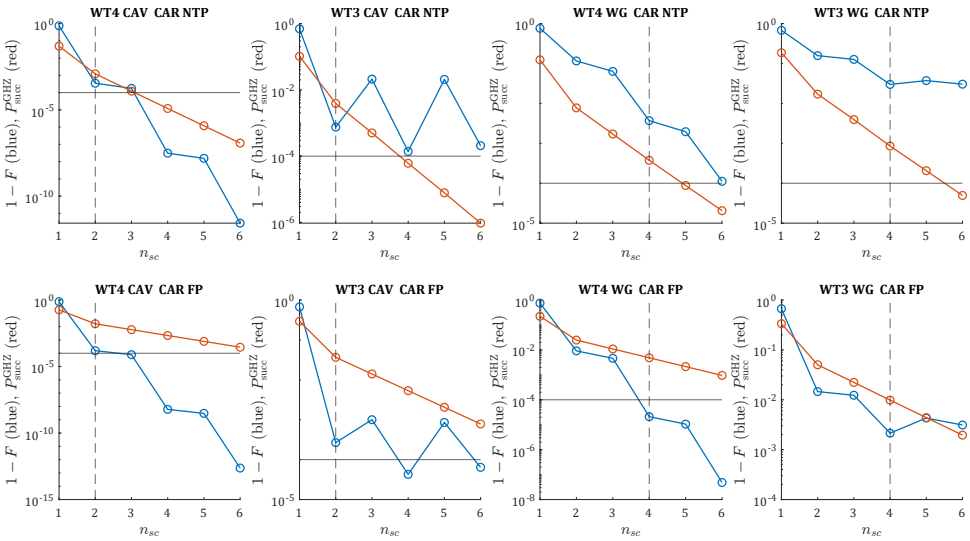

Figure B.9.: The scan of fidelity and success rate over the number of scattering times in the carving scheme with a single photon source. The title in each plot denotes different architectures, entangling schemes, and parameter sets. The red curves represent the success rate, and the blue curves represent the infidelity. The horizontal solid black lines denote the minimum requirement of the success rate of 10^{-4}. The vertical dashed black lines denote the selected optimum numbers of scattering times. They are also listed in the table in Fig. 3.12 and 3.13 in the main text.

detuning, δ_0 and δ_1, with respect to the input photons. For the cavity-included setup, according to Ref. [23], the transmission coefficient formula reads

$$t_{0,1}^{\mathrm{cav}}(\delta) = \frac{\frac{2\kappa_c}{2\kappa_c+\kappa_l}}{1+2\mathrm{i}\frac{\omega}{2\kappa_c+\kappa_l}+\frac{4C_2}{1+2\mathrm{i}\delta_{0,1}/\gamma}}, \tag{B.51}$$

For the waveguide-included setup, according to Ref. [25], the transmission coefficient formula reads

$$t_{0,1}^{\mathrm{wg}}(\delta) = \frac{1+2\mathrm{i}\delta_{0,1}/\gamma}{1+P+2\mathrm{i}\delta_{0,1}/\gamma}. \tag{B.52}$$

Notably, the t^{wg} can be viewed as t^{cav} when taking the limit of $\kappa_c \to \infty$.

The symbols in Eqn. (B.51) and (B.52) are explained in Fig. 3.12 and 3.13 in the main text.

To maximize the GHZ state fidelity, $t(\delta_0)$ should take the maximum modulus and $t(\delta_1)$ the minimum modulus. Besides, the two spin transitions have a fixed detuning Δ hence $\delta_0 - \delta_1 = \Delta$. Based on these, the optimum values of δ_1 and ω can be determined analytically which gives $\delta_1 = 0$ for both the cavity and waveguide cases and $\omega = \frac{4C_2\Delta(2\kappa_a+\kappa_c)}{1+4\Delta^2}$ for the cavity case. As in the reflection scheme, δ_1 and ω are also assumed to fluctuate following Gaussian distributions with the same deviations σ around the optimal values. The density matrix of the resulting GHZ state is calculated as an average over δ_1 and ω.

The optimal number of scattering times n_{sc} is determined by looking for the lowest infidelity in the regime where the success rate is above 10^{-4}. We found the optima by scanning the GHZ fidelity and success rates over the number of scattering times, as shown in Fig. B.9.

B.7. CARVING SCHEME WITH COHERENT LIGHT SOURCE

Here, we describe the calculation method for the carving scheme with coherent light. We will use the following properties of the coherent light. (1) A beam splitter converts a coherent light beam into two independent beams of coherent light: $|\alpha\rangle \to \left|\frac{\alpha}{\sqrt{2}}\right\rangle_+ \left|\frac{\alpha}{\sqrt{2}}\right\rangle_-$. (2) If there are two coherent light beams incident on both input ports of the beam splitter, the conversion of the beam splitter is: $|\alpha\rangle|\beta\rangle \to \left|\frac{\alpha+\beta}{\sqrt{2}}\right\rangle_+ \left|\frac{\alpha-\beta}{\sqrt{2}}\right\rangle_-$. (3) A coherent light beam after scattering from a spin-system will be split into three independent coherent light beams in the linear regime considered here (i.e. the pulse is assumed long enough that only a single photon from the beam scatters from the spin at a time) : $|\alpha\rangle \to |r\alpha\rangle|d\alpha\rangle|t\alpha\rangle$, where r, d and t are the reflection, dissipation, and transmission coefficients of the spin. They have the relationships $|r|^2 + |d|^2 + |t|^2 = 1$.

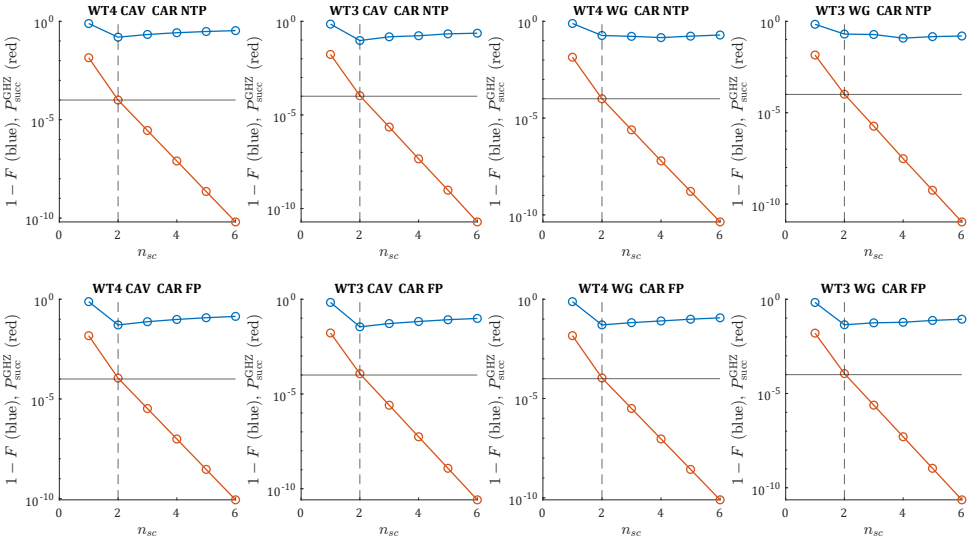

Figure B.10.: The scan of fidelity and success rate over the number of scattering times in the carving scheme with a single photon source. The title in each plot denotes different architectures, entangling schemes, and parameter sets. The red curves represent the success rate, and the blue curves represent the infidelity. The horizontal solid black lines denote the minimum requirement of the success rate of 10^{-4}. The vertical dashed black lines denote the selected optimum numbers of scattering times. They are also listed in the table in Fig. 3.12 and 3.13 in the main text.

We first take the case with two spins, one at the upper route and one at the lower routes, as an example to demonstrate the calculation method and then generalize to the case with n_{wt} spins. The spins are initially in a state $|\psi_0\rangle = \frac{1}{2}(1,1,1,1)^{\mathrm{T}}$. When the coherent light beam $|\alpha\rangle$ from the light source passes the first beam splitter, it turns into the state $\left|\frac{\alpha}{\sqrt{2}}\right\rangle_{\mathrm{u}}\left|\frac{\alpha}{\sqrt{2}}\right\rangle_{\mathrm{d}}$, where the subscripts denote the upper ("$_{\mathrm{u}}$") and lower ("$_{\mathrm{d}}$") routes. Next, when the beams have passed through the spin-systems, the state of the spins-systems and light field becomes:

$$\left|\psi_1^{\mathrm{p}}\right\rangle = \frac{1}{2}\begin{pmatrix} \left|\frac{r_0\alpha}{\sqrt{2}}\right\rangle_{\mathrm{u}}\left|\frac{d_0\alpha}{\sqrt{2}}\right\rangle_{\mathrm{u}}\left|\frac{t_0\alpha}{\sqrt{2}}\right\rangle_{\mathrm{u}}\left|\frac{r_0\alpha}{\sqrt{2}}\right\rangle_{\mathrm{d}}\left|\frac{d_0\alpha}{\sqrt{2}}\right\rangle_{\mathrm{d}}\left|\frac{t_0\alpha}{\sqrt{2}}\right\rangle_{\mathrm{d}} \\ \left|\frac{r_0\alpha}{\sqrt{2}}\right\rangle_{\mathrm{u}}\left|\frac{d_0\alpha}{\sqrt{2}}\right\rangle_{\mathrm{u}}\left|\frac{t_0\alpha}{\sqrt{2}}\right\rangle_{\mathrm{u}}\left|\frac{r_1\alpha}{\sqrt{2}}\right\rangle_{\mathrm{d}}\left|\frac{d_1\alpha}{\sqrt{2}}\right\rangle_{\mathrm{d}}\left|\frac{t_1\alpha}{\sqrt{2}}\right\rangle_{\mathrm{d}} \\ \left|\frac{r_1\alpha}{\sqrt{2}}\right\rangle_{\mathrm{u}}\left|\frac{d_1\alpha}{\sqrt{2}}\right\rangle_{\mathrm{u}}\left|\frac{t_1\alpha}{\sqrt{2}}\right\rangle_{\mathrm{u}}\left|\frac{r_0\alpha}{\sqrt{2}}\right\rangle_{\mathrm{d}}\left|\frac{d_0\alpha}{\sqrt{2}}\right\rangle_{\mathrm{d}}\left|\frac{t_0\alpha}{\sqrt{2}}\right\rangle_{\mathrm{d}} \\ \left|\frac{r_1\alpha}{\sqrt{2}}\right\rangle_{\mathrm{u}}\left|\frac{d_1\alpha}{\sqrt{2}}\right\rangle_{\mathrm{u}}\left|\frac{t_1\alpha}{\sqrt{2}}\right\rangle_{\mathrm{u}}\left|\frac{r_1\alpha}{\sqrt{2}}\right\rangle_{\mathrm{d}}\left|\frac{d_1\alpha}{\sqrt{2}}\right\rangle_{\mathrm{d}}\left|\frac{t_1\alpha}{\sqrt{2}}\right\rangle_{\mathrm{d}} \end{pmatrix} \tag{B.53}$$

where the subscriptions "$_0$" and "$_1$" of the reflection, dissipation, and transmission coefficients are regarding the $|0\rangle$ and $|1\rangle$ states of the spin, respectively.

When the beams are interfered at the second beam splitter, the state of the spin-systems and photonic field becomes:

$$\left|\psi_1^{\mathrm{b}}\right\rangle = \frac{1}{2}\begin{pmatrix} \left|\frac{r_0\alpha}{\sqrt{2}}\right\rangle_{\mathrm{u}}\left|\frac{d_0\alpha}{\sqrt{2}}\right\rangle_{\mathrm{u}}\left|\frac{r_0\alpha}{\sqrt{2}}\right\rangle_{\mathrm{d}}\left|\frac{d_0\alpha}{\sqrt{2}}\right\rangle_{\mathrm{d}}\left|\frac{2t_0\alpha}{\sqrt{2}}\right\rangle_{+}|0\rangle_{-} \\ \left|\frac{r_0\alpha}{\sqrt{2}}\right\rangle_{\mathrm{u}}\left|\frac{d_0\alpha}{\sqrt{2}}\right\rangle_{\mathrm{u}}\left|\frac{r_1\alpha}{\sqrt{2}}\right\rangle_{\mathrm{d}}\left|\frac{d_1\alpha}{\sqrt{2}}\right\rangle_{\mathrm{d}}\left|\frac{t_0+t_1}{\sqrt{2}}\alpha\right\rangle_{+}\left|\frac{t_0-t_1}{\sqrt{2}}\alpha\right\rangle_{-} \\ \left|\frac{r_1\alpha}{\sqrt{2}}\right\rangle_{\mathrm{u}}\left|\frac{d_1\alpha}{\sqrt{2}}\right\rangle_{\mathrm{u}}\left|\frac{r_0\alpha}{\sqrt{2}}\right\rangle_{\mathrm{d}}\left|\frac{d_0\alpha}{\sqrt{2}}\right\rangle_{\mathrm{d}}\left|\frac{t_1+t_0}{\sqrt{2}}\alpha\right\rangle_{+}\left|\frac{t_1-t_0}{\sqrt{2}}\alpha\right\rangle_{-} \\ \left|\frac{r_1\alpha}{\sqrt{2}}\right\rangle_{\mathrm{u}}\left|\frac{d_1\alpha}{\sqrt{2}}\right\rangle_{\mathrm{u}}\left|\frac{r_1\alpha}{\sqrt{2}}\right\rangle_{\mathrm{d}}\left|\frac{d_1\alpha}{\sqrt{2}}\right\rangle_{\mathrm{d}}\left|\frac{2t_1\alpha}{\sqrt{2}}\right\rangle_{+}|0\rangle_{-} \end{pmatrix} \tag{B.54}$$

where the subscripts "$_+$" and "$_-$" denote the two sides of the second beam splitter.

We now perform partial traces over the reflection and dissipation modes and project the transmission modes onto the cases where only detector d_+ or d_- records a photon. One may use the following formula to accomplish the calculation: for arbitrary coherent states $|\beta\rangle$ and $|\gamma\rangle$,

$$\sum_{l=0}^{\infty}\langle l|\beta\rangle\langle\gamma|l\rangle = \mathrm{e}^{-\frac{|\beta-\gamma|^2}{2}}\mathrm{e}^{\frac{\beta\gamma^*-\beta^*\gamma}{2}}, \tag{B.55}$$

and

$$\sum_{l=1}^{\infty}\langle l|\beta\rangle\langle\gamma|l\rangle = \sum_{l=0}^{\infty}\langle l|\beta\rangle\langle\gamma|l\rangle - \langle 0|\beta\rangle\langle\gamma|0\rangle = \mathrm{e}^{-\frac{|\beta-\gamma|^2}{2}}\mathrm{e}^{\frac{\beta\gamma^*-\beta^*\gamma}{2}} - \mathrm{e}^{-\frac{|\beta|^2+|\gamma|^2}{2}}. \tag{B.56}$$

where $|l\rangle$ are the Fock states.

After one traces out the reflection and dissipation modes and projects the transmission modes on the corresponding bases, one gets the density matrix of the spin systems after the first round of light scattering. One can then apply not gates on it and calculate the effect of another round of photon scattering on top of this similar to the procedure for a perfect single photon source described above.

Based on the calculation above, one can see that the overall effect of photon scattering is that it multiplies each entry of the spin density matrix with a certain coefficient. Therefore, one can derive an iteration relationship of the density matrix of the spin as

$$\rho_{n_{\mathrm{sc}}} = \begin{cases} \mathbf{T}_{\mathrm{coh}} \circledcirc \rho_{n_{\mathrm{sc}}-1}, & n_{\mathrm{sc}} = 1 \\ \mathbf{T}_{\mathrm{coh}} \circledcirc \left(O_{\mathrm{not}} \rho_{n_{\mathrm{sc}}-1} O_{\mathrm{not}}\right), & n_{\mathrm{sc}} \geq 2 \end{cases} \tag{B.57}$$

where $\rho_{n_{\mathrm{sc}}}$ is the density matrix after scattering n_{sc}th coherent states, and O_{not} is the operation of not gates on every spin. The coefficient matrix $\mathbf{T}_{\mathrm{coh}}$ is defined as

$$\mathbf{T}_{\mathrm{coh}} = \begin{cases} \left(\bigodot_{j=1}^{n_{\mathrm{wt}}} S_j^{\mathrm{R}} \circledcirc S_j^{\mathrm{D}}\right) \circledcirc S^{+}, \text{ detection on "+" side} \\ \left(\bigodot_{j=1}^{n_{\mathrm{wt}}} S_j^{\mathrm{R}} \circledcirc S_j^{\mathrm{D}}\right) \circledcirc S^{-}, \text{ detection on "−" side} \end{cases} \tag{B.58}$$

where n_{wt} is the total number of spins,

$$S_j^{\mathrm{R}} = \sum_{l=0}^{\infty} \left([\langle l|] \circledcirc \mathbf{R}_j\right) \left(\mathbf{R}_j^{\dagger} \circledcirc [|l\rangle]^{\mathrm{T}}\right), \tag{B.59}$$

$$S_j^{\mathrm{D}} = \sum_{l=0}^{\infty} \left([\langle l|] \circledcirc \mathbf{D}_j\right) \left(\mathbf{D}_j^{\dagger} \circledcirc [|l\rangle]^{\mathrm{T}}\right), \tag{B.60}$$

$$\begin{aligned} S^{+} = \sum_{l=1}^{\infty} &\left([\langle l|] \circledcirc \mathbf{T}_{+}\right) \left(\mathbf{T}_{+}^{\dagger} \circledcirc [|l\rangle]^{\mathrm{T}}\right) \circledcirc \\ &\left([\langle 0|] \circledcirc \mathbf{T}_{-}\right) \left(\mathbf{T}_{-}^{\dagger} \circledcirc [|0\rangle]^{\mathrm{T}}\right), \end{aligned} \tag{B.61}$$

and

$$\begin{aligned} S^{-} = &\left([\langle 0|] \circledcirc \mathbf{T}_{+}\right) \left(\mathbf{T}_{+}^{\dagger} \circledcirc [|0\rangle]^{\mathrm{T}}\right) \circledcirc \\ &\sum_{l=1}^{\infty} \left([\langle l|] \circledcirc \mathbf{T}_{-}\right) \left(\mathbf{T}_{-}^{\dagger} \circledcirc [|l\rangle]^{\mathrm{T}}\right), \end{aligned} \tag{B.62}$$

where $[\langle l|]$ is a column vector whose elements are all $\langle l|$. And, $\mathbf{R}_j$, $\mathbf{D}_j$, $\mathbf{T}_{+}$, and $\mathbf{T}_{-}$ are vectors whose entries are wavefunctions of the

reflection, dissipation, and transmission coherent light beams. Similar to Eqn. B.54, they form a relationship

$$\left|\psi_1^{\mathrm{b}}\right\rangle = \left(\bigodot_{j=1}^{n_{\mathrm{wt}}} \mathbf{R}_j \odot \mathbf{D}_j\right) \odot \mathbf{T}_+ \odot \mathbf{T}_- \odot |\psi_0\rangle\,. \tag{B.63}$$

Their entries are defined as

$$\begin{aligned} \mathbf{R}_j[k] &= \left|\vec{\alpha}_j^{\mathrm{r}}[k]\right\rangle \\ \mathbf{D}_j[k] &= \left|\vec{\alpha}_j^{\mathrm{d}}[k]\right\rangle \\ \mathbf{T}_+[k] &= |\vec{\alpha}_{\mathrm{t}+}[k]\rangle \\ \mathbf{T}_-[k] &= |\vec{\alpha}_{\mathrm{t}-}[k]\rangle \end{aligned} \tag{B.64}$$

where $\vec{\alpha}_j^{\mathrm{r}}$ is defined as

$$\vec{\alpha}_j^{\mathrm{r}} = \begin{cases} \frac{\alpha}{\sqrt{2}} \begin{pmatrix} t_0 \\ t_1 \end{pmatrix}^{\otimes(j-1)} \otimes \begin{pmatrix} r_0 \\ r_1 \end{pmatrix} \otimes \begin{pmatrix} 1 \\ 1 \end{pmatrix}^{\otimes(n_{\mathrm{wt}}-j)}, & j \le n_{\mathrm{u}} \\ \frac{\alpha}{\sqrt{2}} \begin{pmatrix} 1 \\ 1 \end{pmatrix}^{\otimes(n_{\mathrm{u}})} \otimes \begin{pmatrix} t_0 \\ t_1 \end{pmatrix}^{\otimes(j-n_{\mathrm{u}}-1)} \otimes \begin{pmatrix} r_0 \\ r_1 \end{pmatrix} \otimes \begin{pmatrix} 1 \\ 1 \end{pmatrix}^{\otimes(n_{\mathrm{wt}}-j)}, & j \ge n_{\mathrm{u}} \end{cases}. \tag{B.65}$$

The vector $\vec{\alpha}_j^{\mathrm{d}}$ follows a similar definition as $\vec{\alpha}_j^{\mathrm{r}}$, which can be derived by replacing r_0 and r_1 with d_0 and d_1. And, $\vec{\alpha}_{\mathrm{t}\pm} = \frac{1}{\sqrt{2}}(\vec{\alpha}_{\mathrm{u}} \pm \vec{\alpha}_{\mathrm{d}})$ with

$$\vec{\alpha}_{\mathrm{u}} = \frac{\alpha}{\sqrt{2}} \begin{pmatrix} t_0 \\ t_1 \end{pmatrix}^{\otimes n_{\mathrm{u}}} \otimes \begin{pmatrix} 1 \\ 1 \end{pmatrix}^{\otimes n_{\mathrm{d}}} \tag{B.66}$$

$$\vec{\alpha}_{\mathrm{d}} = \frac{\alpha}{\sqrt{2}} \begin{pmatrix} 1 \\ 1 \end{pmatrix}^{\otimes n_{\mathrm{u}}} \otimes \begin{pmatrix} t_0 \\ t_1 \end{pmatrix}^{\otimes n_{\mathrm{d}}}, \tag{B.67}$$

with n_{u} and n_{d} the number of spins in the upper and lower optical routes, respectively. By now, we get the unnormalized density matrix of the spin after n_{sc} rounds of light scattering. The trace of the density matrix gives the success rate for generating the GHZ state.

The optimum values of δ_1 and ω are the same as in the carving scheme with a single-photon source as discussed in App. B.6. However, the optimal values of α and the number of scattering times n_{sc} must be determined.

On the one hand, having more light-scattering rounds can potentially increase the GHZ fidelity, as in the carving scheme with a deterministic single-photon source. On the other hand, it also means more reflection and dissipation modes that will leak the quantum information of the

system into the environment. We found that for all the cases in the carving scheme with coherent light, the optimum number of light-scattering rounds is $n_{sc} = 2$ because the fidelity gain from more scattering rounds doesn't outweigh the information leakage.

Regarding the determination of α, the larger the α, the larger the success rate, but the lower the fidelity. For small α, the coherent light resembles a probabilistic single-photon source. Hence, the fidelity of this scheme will approach the scheme with a deterministic single-photon source. However, the success rate will be much lower than it. On the other hand, when α is large, the success rate will approach the scheme with a deterministic single-photon source, but the fidelity will decrease. To get the maximum fidelity, we set the α, letting the success rate take the minimum requirement value of 10^{-4} at $n_{sc} = 2$ as shown in Fig. B.10. However, the fidelities in that circumstance are still too low to realize modular quantum computing with surface code. Hence, the carving scheme with a coherent light source is not promising.

B.8. EXAMPLE: DIAMOND DEFECT CENTER IMPLEMENTATION

To demonstrate a particular physical implementation of our formalism, we give an example of diamond defect center-based hardware. We define a coherence times parameter set (called Set-D) inspired by nitrogen-vacancy (NV) centers in diamond [17, 18, 26–29]. NV centers may, however, not be suited for the direct entangling schemes due to the difficulty of coupling these defect centers to nanophotonic cavities and waveguides. Nonetheless, we anticipate that other defect centers, such as SnV or SiV, where strong coupling to nanophotonic cavities and waveguides has been experimentally demonstrated, can achieve similar coherence and operational times.

The coherence parameters' values for Set-D are inspired by Ref. [28] and shown in Fig. B.11. We consider separate T_1 and T_2 times for the generalized amplitude and phase damping channels inspired by the experiments. The values indicate a relatively strong dephasing noise (Z-biased). Set-D is also a special set for the inclusion of dynamical decoupling (DD) methods that reduce noise during gate pulse sequences [30]. In this model, gate pulses can only be applied during the focusing point between two DD pulses. This refocusing time is expressed as $t_{DD} = t_{pulse} + 2n_{DD}t_{link}$, where t_{pulse} is the time duration of a π-pulse for DD sequence. For a given value of t_{pulse} inspired from the experiments, n_{DD} was optimized in Ref. [9]. We also use the same values of $t_{pulse} = 10^{-3}$ s and $n_{DD} = 18$ for Set-D. These parameters are not used for other sets in the simulations.

Another quantity for more insight into the distributed systems is link

B

Parameter Sets	Set - 1	Set - 2	Set - 3	Set - mix	Set - D
$T_{\text{link}}^{\text{dec}}$	10^4	10^5	10^6	10^4	$T_{1,\text{link}}^{\text{m}} = 0.3$ s $T_{2,\text{link}}^{\text{m}} = 0.075$ s
$T_{\text{idle}}^{\text{dec}}$	10^5	10^5	10^6	10^6	$T_{1,\text{idle}}^{\text{c}} = 300$ s $T_{2,\text{idle}}^{\text{c}} = 1$ s $T_{1,\text{idle}}^{\text{m}} = 300$ s $T_{2,\text{idle}}^{\text{m}} = 10$ s
Operation times					
t_{link}	1	1	1	1	6×10^{-6} s
t_{meas}	1	1	1	1	4×10^{-6} s
t_P^{c}	0.01	0.01	0.01	0.01	$t_{X,Y}^{\text{c}} = 0.14 \times 10^{-6}$ s $t_{Z,H}^{\text{c}} = 10^{-6}$ s
t_P^{m}	100	100	100	100	$t_{X,Y}^{\text{m}} = 10^{-3}$ s $t_{Z,H}^{\text{m}} = 0.5 \times 10^{-3}$ s
t_{CZ}, t_{CX}, t_{CiY}	100	100	100	100	0.5×10^{-3} s
t_{SWAP}	300	300	300	300	1.5×10^{-3} s

Figure B.11.: Table describing the coherence and operation times, including two additional parameter sets, Set-mix and Set-D. All values except Set-D are expressed w.r.t. absolute value of $t_{\text{link}} = 10^{-5}$ s, which is assumed to take one unit of time. Set-D is a special set with absolute values in seconds.

efficiency η^*, as also explored in Ref. [9] in the context of NV centers using an EM scheme. We can express the entanglement generation efficiency (EGE) for EM or direct GHZ generation schemes as:

$$\eta^* = \frac{2P_{\text{succ}}^{\text{link/GHZ}}}{t_{\text{link/GHZ}}\left((T_{1,\text{link/GHZ}}^{\text{dec}})^{-1} + (T_{2,\text{link/GHZ}}^{\text{dec}})^{-1}\right)} \tag{B.68}$$

The entanglement generation efficiency captures the average number of Bell pairs or GHZ states that can be generated within the coherence times of the memory qubits. We also calculate the link (entanglement generation) efficiency for all schemes in App. B.9 via tables in Fig. B.16 and B.17 and Fig. B.18 and B.19.

B.9. THRESHOLD SIMULATION DETAILS

In this appendix, we provide details on the numerical calculations of the distributed surface code thresholds. We also introduce two additional parameter sets for the coherence and operational times: Set-mix and Set-D. Set-mix is a set composed of $T_{\text{link}}^{\text{dec}}$ from Set-1 and $T_{\text{idle}}^{\text{dec}}$ from Set-3. The motivation is to analyze the performance of technologies that exhibit excellent quantum memory capabilities with long-lasting $T_{\text{idle}}^{\text{dec}}$ times. Set-D is inspired by nitrogen-vacancy (NV) center implementation of distributed surface code, explored in Ref. [9]. See App. B.8 for more details on the physical model based on defect centers in diamond. Fig. B.11 presents a summary of all the five parameter sets together. For Set-D, we use the absolute values of the parameters and not relative numbers w.r.t. t_{link} times. We use different $T_{\text{1/2,idle/link}}^{\text{dec}}$ times as shown, inspired via the experiments with dynamical decoupling (DD) incorporated gates. Before performing the full threshold calculations, we first plot the GHZ success probability and infidelity against the varied parameter, p, for circuit-level noise. This gives us estimate on which values of p are the most relevant. Making use of the numerical bounds which we found on the success probability and fidelities. This makes it handy to calculate the other values and scan the parameter space where we would find a threshold for that setting. This is shown in Fig. B.12 for the direct GHZ generation schemes for both the WT-3/4 modular architectures.

B.9.1. CUT-OFF TIME OPTIMIZATION

As described in the main text, the cut-off time t_{cut} caps the maximum time allowed for GHZ generation for any scheme during the stabilizer measurement. Assuming $t_{\text{cut}}^{100\%}$ is the average time allowed for successful GHZ for a certain number of attempts, we can define some $t_{\text{cut}}^{x\%}$ where we get a GHZ success within x% attempts for entanglement

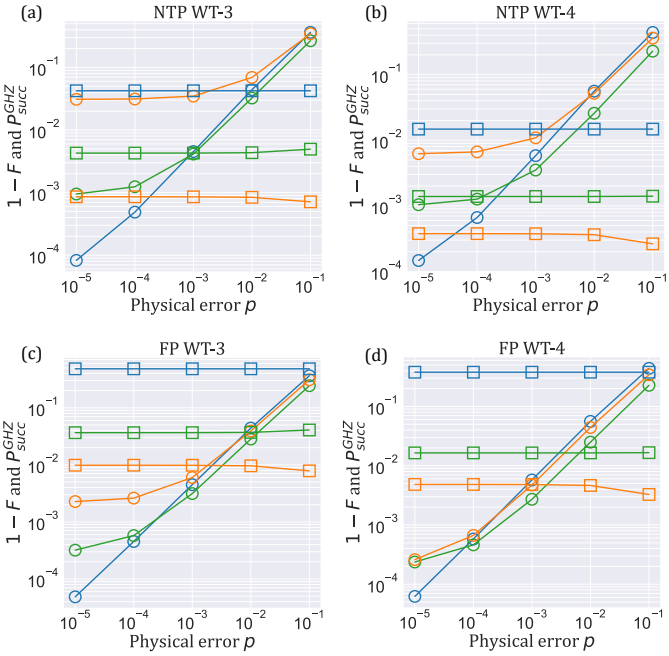

Figure B.12.: Success rates $P_{\text{succ}}^{\text{GHZ}}$ (squares) and GHZ state infidelity $1-F$ (circles) of RFL scheme (blue), CAV CAR (green) with SPS and WG CAR (orange) with SPS, as a function of physical error probability. The subtitles of the plots denote the parameter used (NTP/FP) and the surface code architecture (WT-3/4). Due to different state mixing in the protocol run via the depolarizing channel, there is a weak dependence of $P_{\text{succ}}^{\text{GHZ}}$ on the physical error. This is numerically evident in the plots.

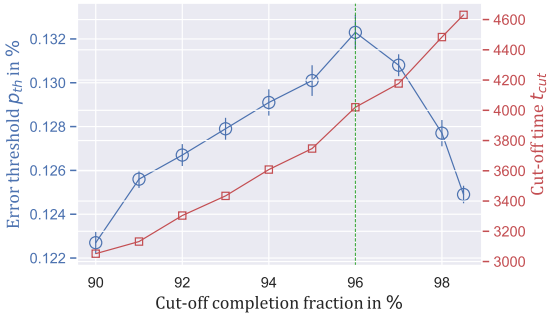

Figure B.13.: Distributed surface code threshold p_{th} (blue) and cut-off time t_{cut} (red) w.r.t. GHZ cut-off completion fraction x. For each value of x, we find $t_{\text{cut}}^{x\%}$, which gives a certain threshold. A binary search for the highest value of p_{th} results in an optimal value of x. The optimal value (highest) is shown in green. This plot was created for WT4 EM Set-3 FP.

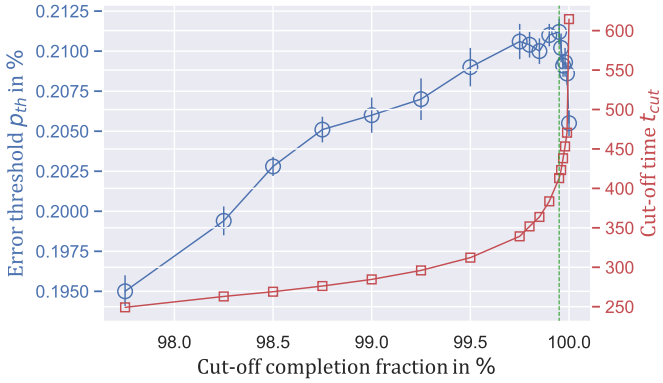

Figure B.14.: Distributed surface code threshold p_{th} (blue) and cut-off time t_{cut} (red) w.r.t. GHZ cut-off completion fraction x for WT4 RFL Set-mix NTP. Read Fig. B.13's caption for details.

generation using any scheme. $t_{\text{cut}}^{100\%}$ is computed in prior in our simulations. Then, we start with a trial value of x (typically around $98\% - 99\%$ for direct schemes or lower for EM schemes) to estimate logical error rates (p_L) in a wide spectrum of physical error rates p. We sweep x in our noisy stabilizer simulator and deduce the $t_{\text{cut}}^{x\%}$ value. For each fixed value of $t_{\text{cut}}^{x\%}$, we perform the threshold simulations to get the logical error rates and estimate the threshold for the code. If the logical error rates are low enough (typically less than 0.2), we search ahead for a threshold. If the logical error rates are greater than 0.90, we abandon the search as there is a negligible chance of threshold within that regime, which we verified numerically.

$t_{\text{cut}}^{x\%}$ increases exponentially as x increases (see Fig. B.13 and Fig. B.14). Starting from a low value of x, first, the code threshold p_{th} increases with x, because more t_{cut} allows for more error syndrome collection. However, if we keep increasing x, the code threshold starts to saturate to a maximum where more t_{cut} does not assist in more syndrome data collection but starts contributing to more noise via decoherence. If we increase x further, we see a rapid fall in the threshold near very high values of x. We perform a binary search over the variable x to find the highest value of p_{th}, including the error bars. Using the respective entanglement generation scheme, we report the highest value as the code threshold p_{th} for that architecture.

B.9.2. THRESHOLD ESTIMATION

Now, we describe the threshold estimation in detail. A trial (guessed) value of $t_{\text{cut}}^{x\%}$ is chosen. Using a superoperator table for a certain input physical error probability p, we calculate the logical error probability p_L (or logical success probability/rate $1 - p_L$). A wide range of input p values is considered such that a threshold lies within this range by numerically observing the behavior of p_L with increasing lattice sizes (6,8,10,12). When a threshold exists, we narrow the search to a small range of p values for the fitting procedure. We use the fitting function of the form [31]:

$$p_L = A + B\gamma + C\gamma^2 \tag{B.69}$$

where $\gamma = (p - p_{\text{th}})L^{1/\nu_0}$, with L as different lattice sizes for different curves. The fitting parameters $A, B, C, p_{\text{th}}, \nu_0$ are found from numerical optimization using the least-squares method. This is discussed in great detail in Ref. [9].

Here, we show an example of threshold estimation in B.15 where we perform the fitting procedure for logical success curves for various even-sized code distances.

B.9.3. DETAILED THRESHOLD SIMULATION DATA

Finally, we provide all the simulation data for all the architectures and schemes in combination with all the coherence parameter sets, including the recently introduced Set-mix and Set-D. This is presented via full-page tables in Fig. B.16 and B.17 (WT4) and Fig. B.18 and B.19 (WT3). Each block of rows describes the simulation results for a particular coherence parameter set. The columns describe different combinations of architecture layout, scheme, and NTP/FP parameters.

The first row within each block describes the success probability $P_{\text{succ}}^{\text{link/GHZ}}$, which has been introduced earlier. While previously we reported thresholds found using the Union-Find (UF) decoder [32] by optimizing the binary search for threshold values, we report a much higher threshold (p_{th} at MWPM) in this data using the minimum-weight perfect matching (MWPM) decoder [33]. The UF threshold value is listed next, also the threshold value we reported in the main text. This was preferred because the UF decoder is fast with linear time complexity in the number of qubits. We find the logical success rate $(1-p_L)$ at the threshold value using the MWPM decoder for more insight into the threshold performance. The optimal GHZ cut-off completion fraction (x%) is also listed. This is the completion fraction at which the peak performance of the architecture was found using the respective scheme. The completion fraction is relatively less for EM schemes as these require fusion operations that take longer for GHZ generation. The decoherence vs. syndrome data rate trade-off is satisfied much earlier for EM schemes during QEC cycles. This can also be seen in Fig. B.13 for the EM scheme and Fig. B.14 for the RFL scheme. After that, we report the entanglement generation efficiency (η^*, described in Eqn. B.68). The next number is the cut-off time t_{cut} at the optimal GHZ cut-off completion rate. The cut-off time is crucial to define the logical clock speed of the quantum computer via the duration of the QEC cycle. It is decided by t_{cut} or the two-qubit gate times t_p^{m} (on the memory qubits), whichever is higher. GHZ fidelity at the threshold value using the UF decoder is also reported, which indicates the quality of the entanglement generation scheme used. The fidelity is calculated for only the direct schemes where the average fidelity was calculated using the average density matrix of the output GHZ state from the scheme. For the EM scheme, this was not possible due to the different protocols used for fusion. However, we can calculate the output Bell pair fidelity for any physical error rate using Eqn. B.31 and Eqn. B.35, as the case may be. Finally, we report the stabilizer fidelity (at the UF threshold) for the entire stabilizer circuit protocol using any scheme considering the noisy two-qubit gates on the memory and noisy measurements. An improvement in two-qubit gate times or fidelity will drastically improve the stabilizer fidelity.

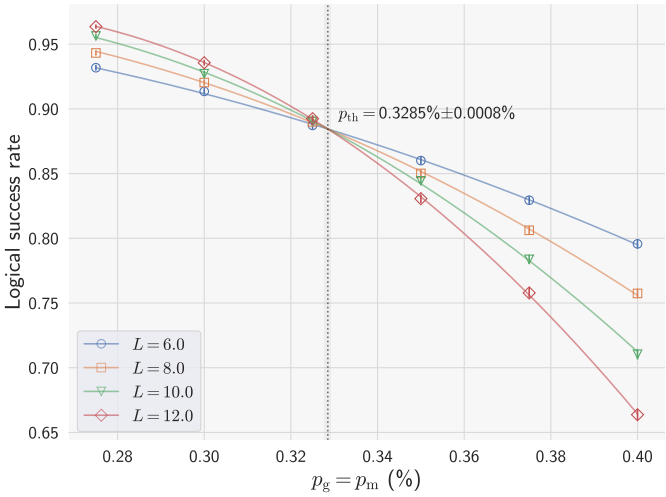

Figure B.15.: Example threshold plot for WT4 RFL (Set-3) NTP. The plot shows the logical success rates $1-p_L$ against physical error rates $p = p_g = p_m$ for different even-valued distances for the distributed surface code. The fitting function reveals the code threshold within some error bar.

Scheme	EM	RFL	CAV CAR SGL	WG CAR SGL
Arch.	WT-4	WT-4	WT-4	WT-4
Parameters	NTP	NTP	NTP	NTP
Set-1 $p_{\mathrm{succ}}^{\mathrm{link/GHZ}}$	0.0001	0.0147	0.0013	0.0003
Set-1 (p_{th} in %) using MWPM	NT	0.1907 % $\pm$ 0.0018 %	NT	NT
Set-1 (p_{th} in %) using UF	NT	0.1707 % $\pm$ 0.0013 %	NT	NT
Set-1 (LSR at MWPM p_{th})	NT	0.8552 $\pm$ 0.0040	NT	NT
Set-1 (optimal t_{cut} completion in %)	NT	98.00 %	NT	NT
Set-1 EGE (η^*)	NT	147	NT	NT
Set-1 (t_{cut})	NT	258.81	NT	NT
Set-1 (GHZ fidelity at UF p_{th})	NT	99.37 %	NT	NT
Set-1 (Stabilizer fidelity at UF p_{th})	NT	93.51 %	NT	NT
Set-2 $p_{\mathrm{succ}}^{\mathrm{link/GHZ}}$	0.0001	0.0147	0.0013	0.0003
Set-2 (p_{th} in %) using MWPM	NT	0.3040 % $\pm$ 0.0013 %	NT	NT
Set-2 (p_{th} in %) using UF	NT	0.2807 % $\pm$ 0.0008 %	NT	NT
Set-2 (LSR at MWPM p_{th})	NT	0.8663 $\pm$ 0.0029	NT	NT
Set-2 (optimal t_{cut} completion in %)	NT	98.50 %	NT	NT
Set-2 EGE (η^*)	NT	1470	NT	NT
Set-2 (t_{cut})	NT	269.01	NT	NT
Set-2 (GHZ fidelity at UF p_{th})	NT	99.07 %	NT	NT
Set-2 (Stabilizer fidelity at UF p_{th})	NT	93.18 %	NT	NT
Set-3 $p_{\mathrm{succ}}^{\mathrm{link/GHZ}}$	0.0001	0.0147	0.0013	0.0003
Set-3 (p_{th} in %) using MWPM	NT	0.3538 % $\pm$ 0.0010 %	0.3626 % $\pm$ 0.0022 %	0.0226 % $\pm$ 0.0012 %
Set-3 (p_{th} in %) using UF	NT	0.3285 % $\pm$ 0.0008 %	0.3298 % $\pm$ 0.0011 %	0.0180 % $\pm$ 0.0011 %
Set-3 (LSR at MWPM p_{th})	NT	0.8656 $\pm$ 0.0022	0.8750 $\pm$ 0.0038	0.8327 $\pm$ 0.0025
Set-3 (optimal t_{cut} completion in %)	NT	99.93 %	98.10 %	96.03 %
Set-3 EGE (η^*)	NT	14700	1300	300
Set-3 (t_{cut})	NT	398.61	1901.01	5339.01
Set-3 (GHZ fidelity at UF p_{th})	NT	98.93 %	99.21 %	98.86 %
Set-3 (Stabilizer fidelity at UF p_{th})	NT	94.23 %	92.52 %	92.57 %
Set-mix $p_{\mathrm{succ}}^{\mathrm{link/GHZ}}$	0.0001	0.0147	0.0013	0.0003
Set-mix (p_{th} in %) using MWPM	NT	0.2340 % $\pm$ 0.0013 %	NT	NT
Set-mix (p_{th} in %) using UF	NT	0.2112 % $\pm$ 0.0008 %	NT	NT
Set-mix (LSR at MWPM p_{th})	NT	0.8453 $\pm$ 0.0032	NT	NT
Set-mix (optimal t_{cut} completion in %)	NT	99.95 %	NT	NT
Set-mix EGE (η^*)	NT	147	NT	NT
Set-mix (t_{cut})	NT	413.01	NT	NT
Set-mix (GHZ fidelity at UF p_{th})	NT	99.25 %	NT	NT
Set-mix (Stabilizer fidelity at UF p_{th})	NT	94.89 %	NT	NT
Set-D $p_{\mathrm{succ}}^{\mathrm{link/GHZ}}$	0.0001	0.0147	0.0013	0.0003
Set-D (p_{th} in %) using MWPM	NT	0.2626 % $\pm$ 0.0015 %	NT	NT
Set-D (p_{th} in %) using UF	NT	0.2411 % $\pm$ 0.0008 %	NT	NT
Set-D (LSR at MWPM p_{th})	NT	0.8716 $\pm$ 0.0030	NT	NT
Set-D (optimal t_{cut} completion in %)	NT	99.23 %	NT	NT
Set-D EGE (η^*)	NT	294	NT	NT
Set-D (t_{cut} in s)	NT	0.0114481	NT	NT
Set-D (GHZ fidelity at UF p_{th})	NT	99.18 %	NT	NT
Set-D (Stabilizer fidelity at UF p_{th})	NT	94.14 %	NT	NT

Figure B.16.: First part of Weight-4 full threshold simulations data. We give code thresholds for each architecture and scheme using two decoders, success probabilities, entanglement generation efficiency, cut-off times, GHZ, and stabilizer fidelity. NT denotes no threshold.

B

Scheme	EM	RFL	CAV CAR SGL	WG CAR SGL
Arch.	WT-4	WT-4	WT-4	WT-4
Parameters	FP	FP	FP	FP
Set-1 $p_{\text{succ}}^{\text{link}/GHZ}$	0.1	0.3782	0.0164	0.0048
Set-1 (p_{th} in %) using MWPM	NT	0.3683 % $\pm$ 0.0012 %	0.2689 % $\pm$ 0.0011 %	NT
Set-1 (p_{th} in %) using UF	NT	0.3443 % $\pm$ 0.0010 %	0.2387 % $\pm$ 0.0015 %	NT
Set-1 (LSR at MWPM p_{th})	NT	0.8698 $\pm$ 0.0026	0.8632 $\pm$ 0.0021	NT
Set-1 (optimal t_{cut} completion in %)	NT	99.82 %	98.56 %	NT
Set-1 EGE (η^*)	NT	3782	164	NT
Set-1 (t_{cut})	NT	108.81	250.41	NT
Set-1 (GHZ fidelity at UF p_{th})	NT	99.00	99.44 %	NT
Set-1 (Stabilizer fidelity at UF p_{th})	NT	94.13	93.42 %	NT
Set-2 $p_{\text{succ}}^{\text{link}/GHZ}$	0.1	0.3782	0.0164	0.0048
Set-2 (p_{th} in %) using MWPM	NT	0.3730 % $\pm$ 0.0010 %	0.3813 % $\pm$ 0.0013 %	0.2431 % $\pm$ 0.0010 %
Set-2 (p_{th} in %) using UF	NT	0.3488 % $\pm$ 0.0008 %	0.3450 % $\pm$ 0.0011 %	0.2158 % $\pm$ 0.0011 %
Set-2 (LSR at MWPM p_{th})	NT	0.8703 $\pm$ 0.0021	0.8682 $\pm$ 0.0024	0.8665 $\pm$ 0.0020
Set-2 (optimal t_{cut} completion in %)	NT	99.82 %	99.75 %	98.26 %
Set-2 EGE (η^*)	NT	37820	1640	480
Set-2 (t_{cut})	NT	108.81	317.01	603.21
Set-2 (GHZ fidelity at UF p_{th})	NT	98.99 %	99.22 %	99.25 %
Set-2 (Stabilizer fidelity at UF p_{th})	NT	94.10 %	93.83 %	92.95 %
Set-3 $p_{\text{succ}}^{\text{link}/GHZ}$	0.1	0.3782	0.0164	0.0048
Set-3 (p_{th} in %) using MWPM	0.1449% $\pm$ 0.0008 %	0.3783 % $\pm$ 0.0015 %	0.4462 % $\pm$ 0.0022 %	0.3885 % $\pm$ 0.0010 %
Set-3 (p_{th} in %) using UF	0.1323 % $\pm$ 0.0008 %	0.3513 % $\pm$ 0.0010 %	0.4072 % $\pm$ 0.0010 %	0.3541 % $\pm$ 0.0007 %
Set-3 (LSR at MWPM p_{th})	0.8656 $\pm$ 0.0032	0.8669 $\pm$ 0.0033	0.8806 $\pm$ 0.0037	0.8938 $\pm$ 0.0018
Set-3 (optimal t_{cut} completion in %)	96.00 %	100 %	99.90 %	99.25 %
Set-3 EGE (η^*)	100000	378200	16400	4800
Set-3 (t_{cut})	4020.16	114.81	350.01	704.61
Set-3 (GHZ fidelity at UF p_{th})	-	98.97 %	99.09 %	98.82 %
Set-3 (Stabilizer fidelity at UF p_{th})	91.94	94.21 %	93.64 %	92.93 %
Set-mix $p_{\text{succ}}^{\text{link}/GHZ}$	0.1	0.3782	0.0164	0.0048
Set-mix (p_{th} in %) using MWPM	0.0537 % $\pm$ 0.0004 %	0.3704 % $\pm$ 0.0013 %	0.3146 % $\pm$ 0.0013 %	NT
Set-mix (p_{th} in %) using UF	0.0424 % $\pm$ 0.0004 %	0.3455 % $\pm$ 0.0010 %	0.2820 % $\pm$ 0.0013 %	NT
Set-mix (LSR at MWPM p_{th})	0.8711 $\pm$ 0.0018	0.8707 $\pm$ 0.0028	0.8612 $\pm$ 0.0025	NT
Set-mix (optimal t_{cut} completion in %)	95.00 %	99.82 %	99.80 %	NT
Set-mix EGE (η^*)	1000	3782	164	NT
Set-mix (t_{cut})	2754.08	108.81	322.41	NT
Set-mix (GHZ fidelity at UF p_{th})	-	98.99 %	99.35 %	NT
Set-mix (Stabilizer fidelity at UF p_{th})	91.94 %	94.11 %	94.32 %	NT
Set-D $p_{\text{succ}}^{\text{link}/GHZ}$	0.1	0.3782	0.0164	0.0048
Set-D (p_{th} in %) using MWPM	0.1511 % $\pm$ 0.0011 %	0.3740 % $\pm$ 0.0012 %	0.3483 % $\pm$ 0.0010 %	0.0556 % $\pm$ 0.0026 %
Set-D (p_{th} in %) using UF	0.1389 % $\pm$ 0.0005 %	0.3484 % $\pm$ 0.0008 %	0.3144 % $\pm$ 0.0014 %	0.0380 % $\pm$ 0.0024 %
Set-D (LSR at MWPM p_{th})	0.8664 $\pm$ 0.0043	0.8687 $\pm$ 0.0026	0.8788 $\pm$ 0.0016	0.8878 $\pm$ 0.0039
Set-D (optimal t_{cut} completion in %)	99.404 %	100 %	99.86 %	98.00 %
Set-D EGE (η^*)	2000	7564	328	96
Set-D (t_{cut} in s)	0.0260401	0.0006421	0.0138801	0.0284721
Set-D (GHZ fidelity at UF p_{th})	-	98.98 %	99.29 %	99.82 %
Set-D (Stabilizer fidelity at UF p_{th})	93.88 %	94.25 %	94.19 %	94.83 %

Figure B.17.: Second part of Weight-4 full threshold simulations data. We give code thresholds for each architecture and scheme using two decoders, success probabilities, entanglement generation efficiency, cut-off times, GHZ, and stabilizer fidelity. NT denotes no threshold.

Scheme	EM	RFL	CAV CAR SGL	WG CAR SGL
Architecture	WT-3	WT-3	WT-3	WT-3
Parameters	NTP	NTP	NTP	NTP
Set-1 $p_{\mathrm{succ}}^{link/GHZ}$	0.0001	0.0423	0.0041	0.0009
Set-1 (p_{th} in %) using MWPM	NT	$0.1841\ \% \pm 0.0013\ \%$	NT	NT
Set-1 (p_{th} in %) using UF	NT	$0.1717\ \% \pm 0.0011\ \%$	NT	NT
Set-1 (LSR at MWPM p_{th})	NT	0.8174 ± 0.0013	NT	NT
Set-1 (optimal t_{cut} completion in %)	NT	99.25 %	NT	NT
Set-1 EGE (η^*)	NT	423	NT	NT
Set-1 (t_{cut})	NT	268.81	NT	NT
Set-1 (GHZ fidelity at UF p_{th})	NT	99.53 %	NT	NT
Set-1 (Stabilizer fidelity at UF p_{th})	NT	95.51 %	NT	NT
Set-2 $p_{\mathrm{succ}}^{link/GHZ}$	0.0001	0.0423	0.0041	0.0009
Set-2 (p_{th} in %) using MWPM	NT	$0.2453\ \% \pm 0.0014\ \%$	$0.0309\ \% \pm 0.0011\ \%$	NT
Set-2 (p_{th} in %) using UF	NT	$0.2353\ \% \pm 0.0010\ \%$	$0.0167\ \% \pm 0.0010\ \%$	NT
Set-2 (LSR at MWPM p_{th})	NT	0.8355 ± 0.0033	0.8256 ± 0.0026	NT
Set-2 (optimal t_{cut} completion in %)	NT	98.57 %	93.00 %	NT
Set-2 EGE (η^*)	NT	4230	410	NT
Set-2 (t_{cut})	NT	260.41	583.21	NT
Set-2 (GHZ fidelity at UF p_{th})	NT	99.41 %	99.84 %	NT
Set-2 (Stabilizer fidelity at UF p_{th})	NT	94.88 %	91.11 %	NT
Set-3 $p_{\mathrm{succ}}^{link/GHZ}$	0.0001	0.0423	0.0041	0.0009
Set-3 (p_{th} in %) using MWPM	NT	$0.3412\ \% \pm 0.0011\ \%$	$0.3132\ \% \pm 0.0013\ \%$	NT
Set-3 (p_{th} in %) using UF	NT	$0.3350\ \% \pm 0.0010\ \%$	$0.3062\ \% \pm 0.0009\ \%$	NT
Set-3 (LSR at MWPM p_{th})	NT	0.8486 ± 0.0022	0.8519 ± 0.0027	NT
Set-3 (optimal t_{cut} completion in %)	NT	99.80 %	99.00 %	NT
Set-3 EGE (η^*)	NT	42300	4100	NT
Set-3 (t_{cut})	NT	288.61	852.61	NT
Set-3 (GHZ fidelity at UF p_{th})	NT	99.21 %	99.18 %	NT
Set-3 (Stabilizer fidelity at UF p_{th})	NT	95.29 %	94.56 %	NT
Set-mix $p_{\mathrm{succ}}^{link/GHZ}$	0.0001	0.0423	0.0041	0.0009
Set-mix (p_{th} in %) using MWPM	NT	$0.2739\ \% \pm 0.0009\ \%$	NT	NT
Set-mix (p_{th} in %) using UF	NT	$0.2629\ \% \pm 0.0006\ \%$	NT	NT
Set-mix (LSR at MWPM p_{th})	NT	0.8292 ± 0.0021	NT	NT
Set-mix (optimal t_{cut} completion in %)	NT	99.9 %	NT	NT
Set-mix EGE (η^*)	NT	423	NT	NT
Set-mix (t_{cut})	NT	300.01	NT	NT
Set-mix (GHZ fidelity at UF p_{th})	NT	99.35 %	NT	NT
Set-mix (Stabilizer fidelity at UF p_{th})	NT	95.85 %	NT	NT
Set-D $p_{\mathrm{succ}}^{link/GHZ}$	0.0001	0.0423	0.0041	0.0009
Set-D (p_{th} in %) using MWPM	NT	$0.2962\ \% \pm 0.0019\ \%$	NT	NT
Set-D (p_{th} in %) using UF	NT	$0.2877\ \% \pm 0.0035\ \%$	NT	NT
Set-D (LSR at MWPM p_{th})	NT	0.8473 ± 0.0040	NT	NT
Set-D (optimal t_{cut} completion in %)	NT	99.777 %	NT	NT
Set-D EGE (η^*)	NT	846	NT	NT
Set-D (t_{cut} in s)	NT	0.0065841	NT	NT
Set-D (GHZ fidelity at UF p_{th})	NT	99.30 %	NT	NT
Set-D (Stabilizer fidelity at UF p_{th})	NT	95.54 %	NT	NT

Figure B.18.: First part of Weight-3 full threshold simulations data. We give code thresholds for each architecture and scheme using two decoders, success probabilities, entanglement generation efficiency, cut-off times, GHZ, and stabilizer fidelity. NT denotes no threshold.

B

Scheme	EM	RFL	CAV CAR SGL	WG CAR SGL
Architecture	WT-3	WT-3	WT-3	WT-3
Parameters	FP	FP	FP	FP
Set-1 $P_{\text{succ}}^{\text{link/GHZ}}$	0.1	0.4823	0.0366	0.0098
Set-1 (p_{th} in %) using MWPM	NT	0.2906 % $\pm$ 0.0010 %	0.1935 % $\pm$ 0.0012 %	NT
Set-1 (p_{th} in %) using UF	NT	0.2784 % $\pm$ 0.0009 %	0.1787 % $\pm$ 0.0007 %	NT
Set-1 (LSR at MWPM p_{th})	NT	0.8305 $\pm$ 0.0024	0.8158 $\pm$ 0.0029	NT
Set-1 (optimal t_{cut} completion in %)	NT	100 %	99.25 %	NT
Set-1 EGE (η^*)	NT	4823	366	NT
Set-1 (t_{cut})	NT	211.21	279.61	NT
Set-1 (GHZ fidelity at UF p_{th})	NT	99.39 %	99.56 %	NT
Set-1 (Stabilizer fidelity at UF p_{th})	NT	95.95 %	95.80 %	NT
Set-2 $P_{\text{succ}}^{\text{link/GHZ}}$	0.1	0.4823	0.0366	0.0098
Set-2 (p_{th} in %) using MWPM	NT	0.2954 % $\pm$ 0.0012 %	0.2717 % $\pm$ 0.0012 %	0.1701 % $\pm$ 0.0021 %
Set-2 (p_{th} in %) using UF	NT	0.2849 % $\pm$ 0.0010 %	0.2603 % $\pm$ 0.0009 %	0.1522 % $\pm$ 0.0020 %
Set-2 (LSR at MWPM p_{th})	NT	0.8312 $\pm$ 0.0028	0.8349 $\pm$ 0.0028	0.8396 $\pm$ 0.0045
Set-2 (optimal t_{cut} completion in %)	NT	100 %	99.012 %	97.518 %
Set-2 EGE (η^*)	NT	48230	3660	980
Set-2 (t_{cut})	NT	211.21	275.41	421.21
Set-2 (GHZ fidelity at UF p_{th})	NT	99.38 %	99.39 %	99.38 %
Set-2 (Stabilizer fidelity at UF p_{th})	NT	95.92 %	95.01 %	93.96 %
Set-3 $P_{\text{succ}}^{\text{link/GHZ}}$	0.1	0.4823	0.0366	0.0098
Set-3 (p_{th} in %) using MWPM	0.1024 % $\pm$ 0.0008 %	0.3624 % $\pm$ 0.0008 %	0.3775 % $\pm$ 0.0010 %	0.3613 % $\pm$ 0.0008 %
Set-3 (p_{th} in %) using UF	0.0928 % $\pm$ 0.0008 %	0.3521 % $\pm$ 0.0010 %	0.3678 % $\pm$ 0.0007 %	0.3441 % $\pm$ 0.0007 %
Set-3 (LSR at MWPM p_{th})	0.8292 $\pm$ 0.0030	0.8451 $\pm$ 0.0018	0.8528 $\pm$ 0.0020	0.8683 $\pm$ 0.0015
Set-3 (optimal t_{cut} completion in %)	97 %	100 %	99.90 %	99.25 %
Set-3 EGE (η^*)	100000	482300	36600	9800
Set-3 (t_{cut})	4042.16	211.21	315.01	492.01
Set-3 (GHZ fidelity at UF p_{th})	-	99.24 %	99.16 %	98.89 %
Set-3 (Stabilizer fidelity at UF p_{th})	93.70 %	95.39 %	94.99 %	93.93 %
Set-mix $P_{\text{succ}}^{\text{link/GHZ}}$	0.1	0.4823	0.0366	0.0098
Set-mix (p_{th} in %) using MWPM	NT	0.3534 % $\pm$ 0.0009 %	0.2923 % $\pm$ 0.0009 %	0.0350 % $\pm$ 0.0012 %
Set-mix (p_{th} in %) using UF	NT	0.3457 % $\pm$ 0.0010 %	0.2806 % $\pm$ 0.0009 %	0.0132 % $\pm$ 0.0011 %
Set-mix (LSR at MWPM p_{th})	NT	0.8485 $\pm$ 0.0019	0.8348 $\pm$ 0.0019	0.7929 $\pm$ 0.0032
Set-mix (optimal t_{cut} completion in %)	NT	100 %	99.80 %	99.00 %
Set-mix EGE (η^*)	NT	4823	366	98
Set-mix (t_{cut})	NT	211.21	302.41	474.61
Set-mix (GHZ fidelity at UF p_{th})	NT	99.26 %	99.34 %	99.74
Set-mix (Stabilizer fidelity at UF p_{th})	NT	95.46 %	95.50 %	96.46 %
Set-D $P_{\text{succ}}^{\text{link/GHZ}}$	0.1	0.4823	0.0366	0.0098
Set-D (p_{th} in %) using MWPM	0.1063 % $\pm$ 0.0012 %	0.3612 % $\pm$ 0.0012 %	0.3180 % $\pm$ 0.0010 %	0.0898 % $\pm$ 0.0023 %
Set-D (p_{th} in %) using UF	0.0981 % $\pm$ 0.0007 %	0.3528 % $\pm$ 0.0010 %	0.3079 % $\pm$ 0.0009 %	0.0694 % $\pm$ 0.0021 %
Set-D (LSR at MWPM p_{th})	0.8695 $\pm$ 0.0038	0.8506 $\pm$ 0.0026	0.8561 $\pm$ 0.0020	0.8761 $\pm$ 0.0039
Set-D (optimal t_{cut} completion in %)	99.135 %	99.998 %	99.55 %	98.705 %
Set-D EGE (η^*)	2000	9646	732	196
Set-D (t_{cut} in s)	0.0467120	0.0017201	0.0065841	0.0163121
Set-D (GHZ fidelity at UF p_{th})	-	99.25 %	99.29 %	99.60 %
Set-D (Stabilizer fidelity at UF p_{th})	95.65 %	95.40 %	95.04 %	95.91 %

Figure B.19.: Second part of Weight-3 full threshold simulations data. We give code thresholds for each architecture and scheme using two decoders, success probabilities, entanglement generation efficiency, cut-off times, GHZ, and stabilizer fidelity. NT denotes no threshold.

REFERENCES

[1] O. Higgott, T. C. Bohdanowicz, A. Kubica, S. T. Flammia, and E. T. Campbell. “Improved Decoding of Circuit Noise and Fragile Boundaries of Tailored Surface Codes”. In: *Phys. Rev. X* 13 (3 July 2023), p. 031007.

[2] M. A. Nielsen and I. L. Chuang. *Quantum Computation and Quantum Information: 10th Anniversary Edition*. Cambridge University Press, 2010.

[3] D. J. Reilly. “Engineering the quantum-classical interface of solid-state qubits”. In: *npj Quantum Information* 1.1 (Oct. 2015), p. 15011.

[4] A. Gold, J. P. Paquette, A. Stockklauser, M. J. Reagor, M. S. Alam, A. Bestwick, N. Didier, A. Nersisyan, F. Oruc, A. Razavi, B. Scharmann, E. A. Sete, B. Sur, D. Venturelli, C. J. Winkleblack, F. Wudarski, M. Harburn, and C. Rigetti. “Entanglement across separate silicon dies in a modular superconducting qubit device”. In: *npj Quantum Information* 7.1 (Sept. 2021), p. 142.

[5] O. Crawford, J. R. Cruise, N. Mertig, and M. F. Gonzalez-Zalba. “Compilation and scaling strategies for a silicon quantum processor with sparse two-dimensional connectivity”. In: *npj Quantum Information* 9.1 (Feb. 2023), p. 13.

[6] N. H. Nickerson, Y. Li, and S. C. Benjamin. “Topological quantum computing with a very noisy network and local error rates approaching one percent”. In: *Nature Communications* 4.1 (Apr. 2013), p. 1756.

[7] N. H. Nickerson, J. F. Fitzsimons, and S. C. Benjamin. “Freely Scalable Quantum Technologies Using Cells of 5-to-50 Qubits with Very Lossy and Noisy Photonic Links”. In: *Phys. Rev. X* 4 (4 Dec. 2014), p. 041041.

[8] A. Jamiołkowski. “Linear transformations which preserve trace and positive semidefiniteness of operators”. In: *Reports on Mathematical Physics* 3.4 (Dec. 1972), pp. 275–278.

[9] S. de Bone, P. Möller, C. E. Bradley, T. H. Taminiau, and D. Elkouss. “Thresholds for the distributed surface code in the presence of memory decoherence”. In: *AVS Quantum Science* 6.3 (July 2024), p. 033801.

[10] A. Yimsiriwattana and S. J. L. J. au2. *Generalized GHZ States and Distributed Quantum Computing*. 2004.

[11] Y. Tomita and K. M. Svore. “Low-distance surface codes under realistic quantum noise”. In: *Phys. Rev. A* 90 (6 Dec. 2014), p. 062320.

[12] R. Chao and B. W. Reichardt. “Quantum Error Correction with Only Two Extra Qubits”. In: *Phys. Rev. Lett.* 121 (5 Aug. 2018), p. 050502.

[13] R. Chao and B. W. Reichardt. “Flag Fault-Tolerant Error Correction for any Stabilizer Code”. In: *PRX Quantum* 1 (1 Sept. 2020), p. 010302.

[14] M. McEwen, D. Bacon, and C. Gidney. “Relaxing Hardware Requirements for Surface Code Circuits using Time-dynamics”. In: *Quantum* 7 (Nov. 2023), p. 1172.

[15] C. Cabrillo, J. I. Cirac, P. García-Fernández, and P. Zoller. “Creation of entangled states of distant atoms by interference”. In: *Phys. Rev. A* 59 (2 Feb. 1999), pp. 1025–1033.

[16] P. C. Humphreys, N. Kalb, J. P. J. Morits, R. N. Schouten, R. F. L. Vermeulen, D. J. Twitchen, M. Markham, and R. Hanson. “Deterministic delivery of remote entanglement on a quantum network”. In: *Nature* 558.7709 (June 2018), pp. 268–273.

[17] F. Rozp ędek, R. Yehia, K. Goodenough, M. Ruf, P. C. Humphreys, R. Hanson, S. Wehner, and D. Elkouss. “Near-term quantum-repeater experiments with nitrogen-vacancy centers: Overcoming the limitations of direct transmission”. In: *Phys. Rev. A* 99 (5 May 2019), p. 052330.

[18] A. Dahlberg, M. Skrzypczyk, T. Coopmans, L. Wubben, F. Rozpundefineddek, M. Pompili, A. Stolk, P. Pawełczak, R. Knegjens, J. de Oliveira Filho, R. Hanson, and S. Wehner. “A link layer protocol for quantum networks”. In: *Proceedings of the ACM Special Interest Group on Data Communication*. SIGCOMM ’19. Beijing, China: Association for Computing Machinery, 2019, pp. 159–173.

[19] S. D. Barrett and P. Kok. “Efficient high-fidelity quantum computation using matter qubits and linear optics”. In: *Phys. Rev. A* 71 (6 June 2005), p. 060310.

[20] S. de Bone, R. Ouyang, K. Goodenough, and D. Elkouss. “Protocols for Creating and Distilling Multipartite GHZ States With Bell Pairs”. In: *IEEE Transactions on Quantum Engineering* 1 (2020), pp. 1–10.

[21] S. Ritter, C. Nölleke, C. Hahn, A. Reiserer, A. Neuzner, M. Uphoff, M. Mücke, E. Figueroa, J. Bochmann, and G. Rempe. “An elementary quantum network of single atoms in optical cavities”. In: *Nature* 484.7393 (2012), pp. 195–200.

[22] A. Reiserer and G. Rempe. “Cavity-based quantum networks with single atoms and optical photons”. In: *Reviews of Modern Physics* 87.4 (2015), pp. 1379–1418.

[23] A. Reiserer and G. Rempe. “Cavity-based quantum networks with single atoms and optical photons”. In: *Rev. Mod. Phys.* 87 (4 Dec. 2015), pp. 1379–1418.

[24] A. S. Sørensen and K. Mølmer. “Probabilistic Generation of Entanglement in Optical Cavities”. In: *Phys. Rev. Lett.* 90 (12 Mar. 2003), p. 127903.

[25] D. E. Chang, A. S. Sørensen, E. A. Demler, and M. D. Lukin. “A single-photon transistor using nanoscale surface plasmons”. In: *Nature physics* 3 (11 2017), pp. 807–812.

[26] M. Ruf, M. Weaver, S. van Dam, and R. Hanson. “Resonant Excitation and Purcell Enhancement of Coherent Nitrogen-Vacancy Centers Coupled to a Fabry-Perot Microcavity”. In: *Phys. Rev. Appl.* 15 (2 Feb. 2021), p. 024049.

[27] C. E. Bradley, S. W. de Bone, P. F. W. Möller, S. Baier, M. J. Degen, S. J. H. Loenen, H. P. Bartling, M. Markham, D. J. Twitchen, R. Hanson, D. Elkouss, and T. H. Taminiau. “Robust quantum-network memory based on spin qubits in isotopically engineered diamond”. In: *npj Quantum Information* 8.1 (Oct. 2022), p. 122.

[28] M. Pompili, S. L. N. Hermans, S. Baier, H. K. C. Beukers, P. C. Humphreys, R. N. Schouten, R. F. L. Vermeulen, M. J. Tiggelman, L. dos Santos Martins, B. Dirkse, S. Wehner, and R. Hanson. “Realization of a multinode quantum network of remote solid-state qubits”. In: *Science* 372.6539 (2021), pp. 259–264.

[29] M. H. Abobeih, Y. Wang, J. Randall, S. J. H. Loenen, C. E. Bradley, M. Markham, D. J. Twitchen, B. M. Terhal, and T. H. Taminiau. “Fault-tolerant operation of a logical qubit in a diamond quantum processor”. In: *Nature* 606.7916 (June 2022), pp. 884–889.

[30] C. E. Bradley, J. Randall, M. H. Abobeih, R. C. Berrevoets, M. J. Degen, M. A. Bakker, M. Markham, D. J. Twitchen, and T. H. Taminiau. “A Ten-Qubit Solid-State Spin Register with Quantum Memory up to One Minute”. In: *Phys. Rev. X* 9 (3 Sept. 2019), p. 031045.

[31] C. Wang, J. Harrington, and J. Preskill. “Confinement-Higgs transition in a disordered gauge theory and the accuracy threshold for quantum memory”. In: *Annals of Physics* 303.1 (2003), pp. 31–58.

[32] N. Delfosse and N. H. Nickerson. “Almost-linear time decoding algorithm for topological codes”. In: *Quantum* 5 (Dec. 2021), p. 595.

[33] J. Edmonds. “Paths, Trees, and Flowers”. In: *Canadian Journal of Mathematics* 17 (1965), pp. 449–467.

C

APPENDICES FOR CH. 4

c.1. RB EMITTER HAMILTONIAN

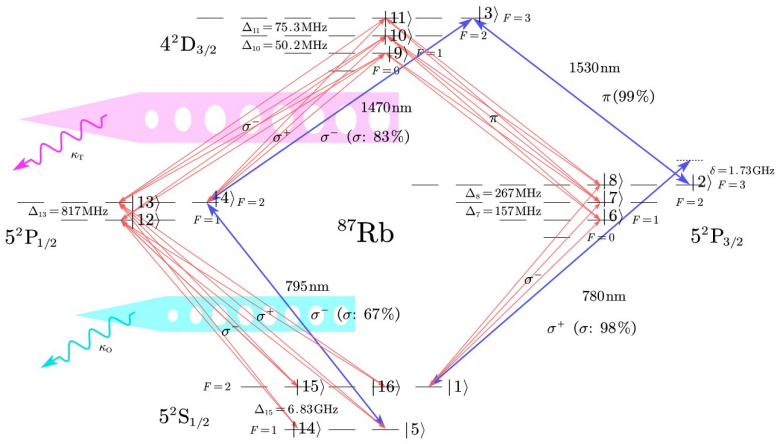

Figure C.1.: Atomic-level diagram illustrating all the relevant Rb atomic energy levels participating in the light emission procedure. States $|1\rangle$ to $|5\rangle$ are the intended used levels. They are connected with thick blue arrows as their couplings. The first two couplings are laser-induced and the later two are cavity-induced. The thin red arrows indicate the unintended drivings and coupling caused by the used laser and cavities. The choices of polarization (π, σ^+, σ^-) and wavelengths of light are noted alongside each coupling arrow. There is a detuning $\delta = 1.73$ GHz respecting the $|1\rangle - |2\rangle$ energy difference in the first laser driving. The thin red arrows represent the notable faulty couplings induced by the same lasers and cavity modes. These faulty couplings involve other states denoted as $|6\rangle$ to $|16\rangle$.

Fig. C.1 depicts all the couplings including the intended ones (thick blue arrows) and the unintended ones (thin red arrows) from the lasers and cavity modes in the ^{87}Rb atomic system with the levels involved labeled as $|1\rangle \sim |16\rangle$. From this, the Hamiltonian of the whole system, in a suitable rotating frame, can be written as

$$H = h\delta|1\rangle\langle 1| + h\Omega_1\left(|2\rangle\langle 1| + \frac{1}{c_{2,1}}\sum_{i=6}^{8} c_{i,1}|i\rangle\langle 1| + \text{H.c.}\right) + H_{\text{rig}} + H_{\text{flt}} \quad \text{(C.1)}$$

where h is the Plank constant; δ is the detuning of the first laser from the transition between the $|1\rangle$ and $|2\rangle$ states; Ω_1 is the Rabi frequency of the first laser driving; $c_{j,i}$ is the Clebsch-Gordan coefficient corresponding to the $|i\rangle - |j\rangle$ coupling which determines the relative coupling strengths of the couplings induced by the same laser or cavity coupling;

$$H_{\text{rig}} = h\Omega_2|3\rangle\langle 2| + hg_{\text{t}}|4\rangle\langle 3|\hat{a}_{\text{t}}^{\dagger} + hg_{\text{o}}|5\rangle\langle 4|\hat{a}_{\text{o}}^{\dagger} + \text{H.c.}\,; \quad \text{(C.2)}$$

and

$$\begin{aligned} &H_{\text{flt}} \\ =&-h\Delta_7|7\rangle\langle 7| - h(\Delta_7+\Delta_8)|8\rangle\langle 8| - h\Delta_{10}|10\rangle\langle 10| \\ &-h(\Delta_{10}+\Delta_{11})|11\rangle\langle 11| - h\Delta_{13}|13\rangle\langle 13| + h\Delta_{15}(|15\rangle\langle 15| + |16\rangle\langle 16|) + \\ &\left\{\frac{h\Omega_2}{c_{3,2}}\sum_{j=9}^{11}\sum_{i=6}^{8} c_{j,i}|j\rangle\langle i| + \frac{hg_{\text{t}}}{c_{4,3}}\left[\sum_{i=9}^{11}(c_{i,4}|4\rangle\langle i| + c_{12,i}|12\rangle\langle i| + c_{13,i}|13\rangle\langle i|)\right]\hat{a}_{\text{t}}^{\text{f}\dagger} + \right. \\ &\left.\frac{hg_{\text{o}}}{c_{5,4}}\left[\sum_{i=12}^{13}(c_{5,i}|5\rangle\langle i| + c_{14,i}|14\rangle\langle i| + c_{15,i}|15\rangle\langle i| + c_{16,i}|16\rangle\langle i|)\right]\hat{a}_{\text{t}}^{\text{f}\dagger} + \text{H.c.}\right\}, \end{aligned} \quad \text{(C.3)}$$

where Δ_i are the Rb atomic energy splittings as shown in Fig. C.1, and Ω_2, g_{t}, and g_{o} are the Rabi frequencies of the second laser driving, telecom-photon cavity coupling and visible-photon cavity coupling, respectively, and $\hat{a}_{\text{t}}^{\dagger}$, $\hat{a}_{\text{o}}^{\dagger}$ are the creation operators of the right telecom and visible photon, respectively. The creation operators for faulty ones are $\hat{a}_{\text{t}}^{\text{f}\dagger}$ and $\hat{a}_{\text{o}}^{\text{f}\dagger}$ assuming all the telecom or visible faulty photons are the same.

The atomic decay and the cavity leakage are characterized by the Lindblad operators below:

$$L_1 = \sqrt{\gamma_2}|1\rangle\langle 2|, \quad L_2 = \sqrt{\gamma_{3a}}|2\rangle\langle 3|, \quad L_3 = \sqrt{\gamma_{3b}}|4\rangle\langle 3|, \quad L_4 = \sqrt{\gamma_4}|5\rangle\langle 4| \quad \text{(C.4)}$$

$$L_5 = \sqrt{\kappa_{\text{t}}}\hat{a}_{\text{t}}, \quad L_6 = \sqrt{\kappa_{\text{o}}}\hat{a}_{\text{o}}, \quad L_7 = \sqrt{\kappa_{\text{t}}}\hat{a}_{\text{t}}^{\text{f}}, \quad L_8 = \sqrt{\kappa_{\text{o}}}\hat{a}_{\text{o}}^{\text{f}}. \quad \text{(C.5)}$$

where γ_i is the atomic decay rate of the $|i\rangle$ level, especially, γ_{3a} is the decay rate from the $|3\rangle$ state to the $|2\rangle$ state and γ_{3b} to the $|4\rangle$ state. The decay rates κ_t and κ_o characterize the rate of the telecom- and visible-photon cavity photons going into the fibers, respectively. The cavity loss is not considered here because it is integrated into the fiber loss and/or considered in the entanglement swap section. The decay from the faulty levels has been neglected because the population in the faulty manifold is small.

Regarding the parameters used in the simulation, the Rb atom has energy differences $\Delta_7 = 157$ MHz, $\Delta_8 = 267$ MHz, $\Delta_{10} = 50.2$ MHz, $\Delta_{11} = 75.3$ MHz, $\Delta_{13} = 817$ MHz, $\Delta_{15} = 6.83$ GHz and linewidths $\gamma_2 = 2\pi\times 6.1$ MHz, $\gamma_{3a} = 2\pi\times 0.19$ MHz, $\gamma_{3b} = 2\pi\times 1.5$ MHz, $\gamma_4 = 2\pi\times 5.7$ MHz. Besides, from the cavity simulation, we get the intended light proportions to be $p_1 = 0.98$, $p_2 = 0.99$, $p_3 = 0.83$, and $p_4 = 0.67$, and the cavity loss rates to be $\kappa_t = 2\pi\times 1.5$ GHz and $\kappa_o = 2\pi\times 1.0$ GHz. Besides, we also get the cooperativities for the telecom- and visible-photon cavities $C_t = \frac{g_t^2}{\kappa_t(\gamma_{3a}+\gamma_{3b})} = 34.4\pm 5.0$ and $C_o = \frac{g_o^2}{\kappa_o\gamma_4} = 11.2\pm 2.2$ and those determine g_t and g_o. Moreover, based on the Rb emitter simulation, the optimized $\Omega_2 = 2.0$ GHz, $\delta = 1.73$ GHz, and Ω_1 is at the order of 100 MHz and time-dependent with the temporal profile shown in Fig. 2(d) in the main text.

With the parameters above, we numerically calculate the system evolution based on the master equation

$$\frac{d\rho}{dt} = \frac{i}{h}[H,\,\rho] + \sum_k \left(\hat{L}_k\rho\hat{L}_k^\dagger - \frac{1}{2}\left\{\hat{L}_k^\dagger\hat{L}_k,\,\rho\right\}\right). \tag{C.6}$$

and get the temporal profiles of the emitted photons as shown in Fig. 2(d) in the main text. Based on the temporal profiles, we model the entanglement generation protocol with two Rb emitters. We sample the situations with varied cavity coupling and different moments within each time bin when the photons hit the photon detectors. As a result, leaving the fiber loss during distant transmission and inefficient detection aside, we get a success rate of 0.49 for generating the entangled visible photon pairs with an entangled state

$$\rho_0 = \begin{pmatrix} 0 & 0 & 0 & 0 \\ 0 & 0.5 & 0.48 & 0 \\ 0 & 0.48 & 0.5 & 0 \\ 0 & 0 & 0 & 0 \end{pmatrix}. \tag{C.7}$$

The codes of this Rb-cavity system simulation and elementary entanglement generation can be found in ref [1].

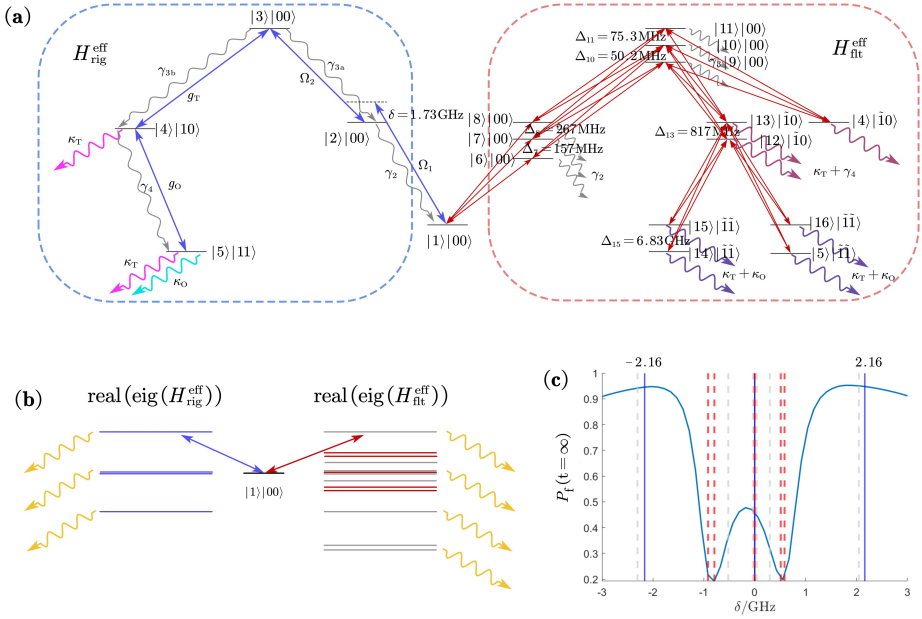

Figure C.2.: (a)Energy level diagram of the Rb-cavity system. Each quantum state is a direct product of the atomic state (first ket) and the photonic state (second ket). The atomic states are named with numbers in the decimal system. The two digits in the ket of the photonic state are either 0 or 1, meaning the vacuum or one-photon states in the telecom- (first digit) and visible- (second digit) photon cavities. The $\tilde{1}$ with a tilde means the one-photon state of faulty photons. The diagram is arranged in the way that the energy levels in the left dashed blue rounded rectangle belong to the intended subsystem and the ones in the right dashed red round rectangle consist of the faulty subsystem. (b) The spectrum, or the real parts of the eigenvalues of the effective Hamiltonians of the intended (left) and faulty (right) subsystems, respectively. The gray lines in the faulty subsystem have neglectful coupling to the $|1\rangle|00\rangle$ state. The double arrows point to the targeted states used in our simulations. (c) Right photon emission proportion (P_f) over the sweep of the first laser detuning (δ). Vertical lines denote the eigenenergies of the right subsystem (solid blue) and the faulty subsystem (dashed red and gray). The code of this calculation can be found in ref [1].

C.2. SUPPRESSION OF FAULTY-POLARIZATION ERRORS

For better analysis of the dynamic of the whole Rb-cavity system, we derive the energy-level diagram of the system incorporating the photonic states shown in Fig C.2(a) where we have separated the intended path and the faulty paths into two sides. Since the first laser driving Ω_1 is about one order weaker than the driving from the second laser and cavity couplings, it is suitable to first neglect the couplings induced by it and separate the excited systems into two parts: Specifically, the intended subsystem driven by the σ_+ polarized component of the first laser light and the faulty subsystem driven by the σ_- polarized component, as circled in with blue and red dash lines in Fig. C.2(a). These two subsystems are governed by the two Hamiltonians H_{rig} and H_{flt}, respectively, which are defined as

$$H_{\text{rig}}^{\text{eff}} = H_{\text{rig}} + \frac{h}{2\text{i}} \sum_{k=1}^{6} L_k^\dagger L_k \tag{C.8}$$

and

$$H_{\text{flt}}^{\text{eff}} = H_{\text{flt}} + \frac{h}{2\text{i}} \left(\sum_{k=7}^{8} L_k^\dagger L_k + L_4^\dagger L_4 \right), \tag{C.9}$$

Diagonalizing these two effective Hamiltonians and taking the real parts of the eigenvalues, one can get the spectrum of two subsystems as shown in Fig. C.2(b), while the imaginary parts of the eigenvalues correspond to the effective decay rates of the eigenstates or the dressed states. From the spectrum, we find it possible to couple strongly to specific dressed states of the right subspace while weakly coupling to the ones from the faulty subsystem. Thus, having the right detuning of the first laser can strongly suppress any driving from the σ_- component. Fig. C.2(c) shows the right photon emission rate sweeping over the detuning δ. One can see that the right photon emission rate peaks at regions where one of the dressed states of the right subsystem is resonantly driven while the coupling to the dressed states of the faulty subsystem is weak.

C.3. FLUCTUATING CAVITY COUPLINGS

Our simulation suggests that due to the thermal fluctuations, the Rb-telecom-cavity coupling results in an average cooperativity of 34 with a standard deviation of 5.0. This corresponds to a standard deviation in the coupling strength g_t between the Rb atom and the telecom cavity corresponding to roughly 10% of the mean coupling strength. This will degrade the fidelity with the target Bell state (see Eq. (1) in the main text) because the fluctuating couplings result in fluctuations of the temporal shape of the emitted photons, which reduces the coherence

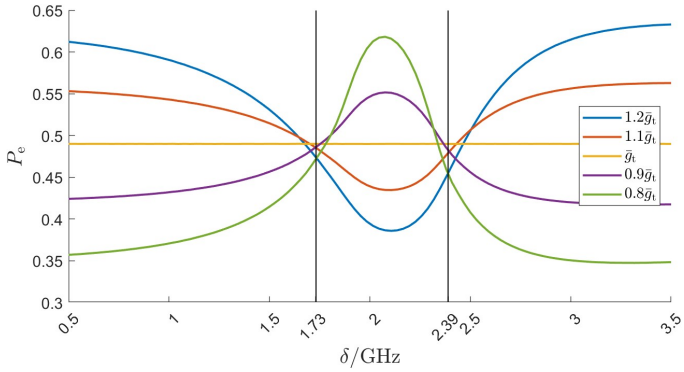

Figure C.3.: Probability that photons are emitted in the early time bin (P_e) as a function of the detuning of the first laser drive (δ). The different graphs correspond to different telecom-cavity coupling strengths variations from a mean value of g_t. The vertical lines mark the two stable points where the emission possibility is less sensitive to variations in the coupling strength. The code of this calculation can be found in Ref, [1].

of the Bell pair. As discussed in the main text, the thermal fluctuations can be reduced through cooling of the atomic motion. However, the sensitivity of the emission time of the photons to these fluctuations also depends on the detuning, δ, of the first laser drive.

To illustrate this, we plot the probability of emitting the telecom and optical photons in the early time-bin as a function of the detuning δ considering deviations from a mean coupling strength g_t in Fig. C.3. For the simulations, we fix the driving pulse to the optimal value for the mean coupling strength. From the figure, two stable points emerge where the population in the early time-bin remains stable despite fluctuations in g_t.

These two stable points can be understood by analyzing the dressed states of the subspace spanned by the states $|2\rangle|00\rangle$, $|3\rangle|00\rangle$, and $|4\rangle|10\rangle$ (see Fig. C.2 (a)). These three states form a Λ system coupled by the second laser drive and the telecom cavity field, whose Hamiltonian can be diagonalized. The first laser will drive the population from the ground state, $|1\rangle|00\rangle$, to the eigenstates of the coupled Λ system. In particular, when the detuning of the first laser drive is in the region $\delta \sim 1.5 - 2.5$ GHz, where we have efficient photon emission (see Fig. C.2(c)), we are primarily driving the population to the eigenstate

$$|\psi_{\mathrm{tar}}\rangle = \frac{1}{\sqrt{2}}\left(|3\rangle|00\rangle + \frac{g_t}{\sqrt{g_t^2+\Omega_2^2}}|4\rangle|10\rangle + \frac{\Omega_2}{\sqrt{g_t^2+\Omega_2^2}}|2\rangle|00\rangle\right), \quad \text{(C.10)}$$

from which a telecom (followed by an optical photon) can be emitted into the cavity. The effective Rabi frequency of the drive to this eigenstate is

$$\Omega_1^{\text{eff}} = \frac{\Omega_2 \Omega_1}{\sqrt{2}\sqrt{g_t^2 + \Omega_2^2}}, \tag{C.11}$$

while the effective decay rate of the eigenstate through the cavity field is

$$\kappa_t^{\text{eff}} = \frac{g_t^2 \kappa_t}{2\left(g_t^2 + \Omega_2^2\right)}. \tag{C.12}$$

It can be seen that increasing (decreasing) g_t, will decrease (increase) Ω_1^{eff} but increase (decrease) the decay rate κ_t^{eff} since we are in the regime $\Omega_2 \gtrsim g_t$. Since the effective emission rate of the photons depend on both Ω_1^{eff} and κ_t^{eff}, we find that these effects can compensate for each other at the stable points.

C.4. TRAPPING AND CAVITY DESIGNS

To couple an atom with two cavity fields, we design two nanophotonic cavities at the target frequencies fabricated parallel to each other, combined with a trap geometry that enables trapping an atom between the cavities. The individual cavities are designed by quadratic tapering of the filling fractions on a nanobeam waveguide[2]. For practical fabrication considerations, both cavities are designed with the same thickness. Due to its larger wavelength, the TE cavity at 1470 nm, requires a larger thickness for mode confinement and subsequently a high quality factor. However, for TE mode cavities for 795 nm, these thicknesses result in low modal overlap in the atom trapping region due to large mode confinement. To overcome this issue, we make use of the TM mode cavity design for 795 nm cavity, which requires a larger thickness while maintaining decent modal overlap in the trapping region.

Quality factors of both the 780 nm and 1470 nm cavities are individually optimized and brought close to each other to form a stable trap geometry. Atoms can be trapped near similar nanophotonic devices by bringing the tweezer adiabatically on top of these devices and trapping the atom in lattices formed by the incident and reflected tweezer[3–5]. In the case of two parallel cavities, trapping on top of any one of the two cavities results in minimal coupling to the other cavity due to minimal cavity mode at the trapping region. To have a significant coupling strength to both cavities, we propose trapping in between the two devices as an alternate implementation. If the separation between the parallel cavities is larger than the wavelength, and the diffraction-limited spot size of the trapping tweezer, atoms can

be trapped in the normal tweezer. However, the large rayleigh range of a normal tweezer implies an atomic wave function larger than the device's thickness. This results in a large variation in the cavity coupling strength experienced by the atom from shot to shot. To overcome this, we restrict the separation between the two parallel cavities to be significantly less than the trapping tweezer wavelength. In this case, the incident tweezer beam is reflected by the combined device structure to form a lattice-like potential similar to a single device case. For a reasonable trapping potential of atoms, the separation between the devices should be smaller than half the trapping tweezer wavelength.

While the cavities were designed to have high quality factors individually, when they are kept next to each other, the mode from one cavity can leak into the other. These additional extrinsic losses κ_{ext} through the second waveguide result in lower overall quality factors ($Q = \frac{\omega}{\kappa_{\text{ext}}+\kappa_{\text{int}}}$; ω is the resonant frequency; κ_{int} is the intrinsic losses not coupled into any waveguides; κ_{ext} includes losses into the intended waveguide mode and the additional losses to the nearby waveguide). This loss is a function of separation between the two cavities, where the loss increases with reduced separation between the cavities.

We iterate between device separation, thickness, and refractive index of the material to find a deep trap potential while maintaining high quality factors required for the results presented in the paper. To iterate over the refractive index, we assume tuning of the silicon enrichment ratio in the silicon nitride. However, the ratio of silicon in the silicon nitride also modifies the bandgap of the material. As the nitride content is reduced, the refractive index and the bandgap approaches that of bare silicon[6]. To avoid the above bandgap excitation using 780 nm laser involved in the protocol, we assume the refractive index of 2.6, assumed in the paper, results in a bandgap larger than 1.6 eV.

Atoms can be trapped in regions where cavity fields have predominantly linear polarization direction on top of nanophotonic devices [7]. However, moving the trap to the edge of the devices results in cavity field polarization to have components in more than one dimension in the trapping region, without specific control over the phase between the polarizations. This results in varying proportions of contributions from σ_+, σ_-, and π in the trapping region. The purity of the intended sigma polarization is marked in Fig. C.1. To overcome this issue, we make a careful selection of the states involved in the scheme. The level scheme involved in the protocol is chosen in a way that under correct excitation, only σ_- polarization of the cavity fields couple between atomic states. The corrections coming from the faulty excitation are labeled in the figure and are accounted for.

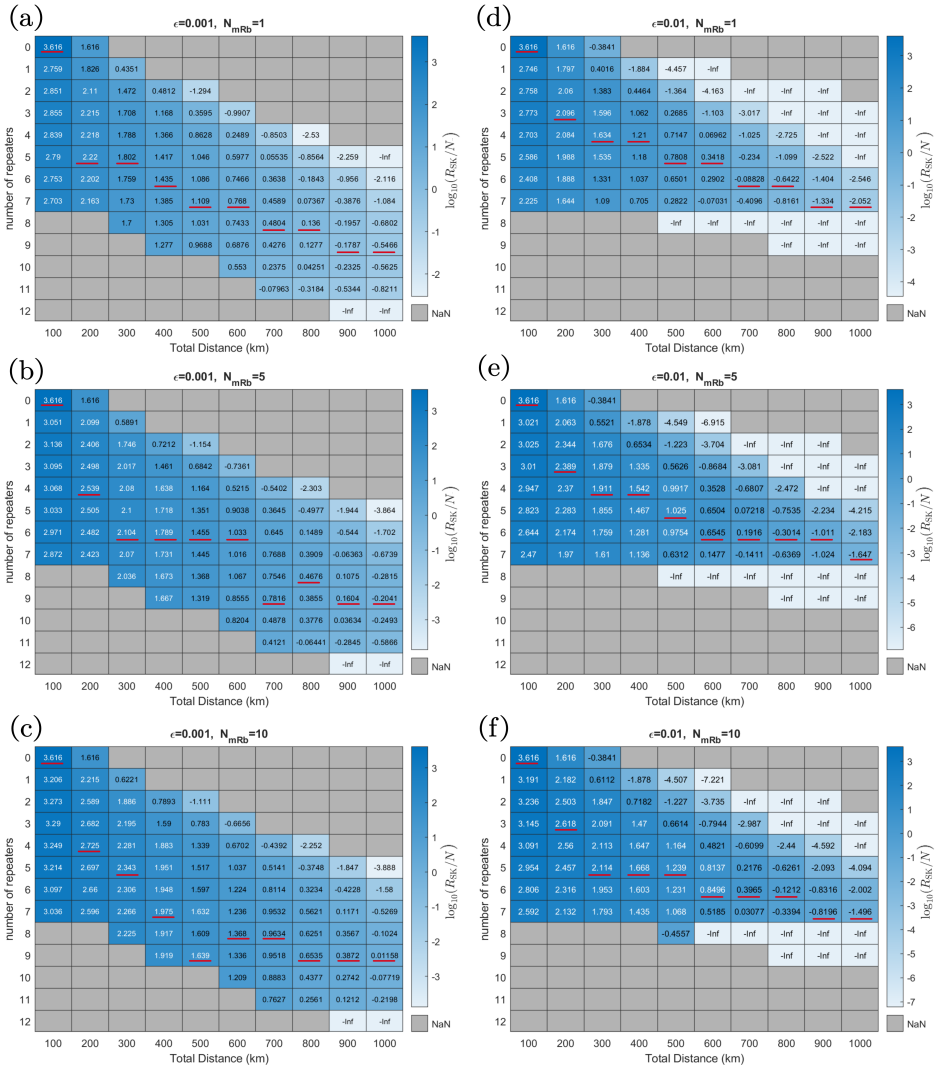

Figure C.4.: Scanning of the secret key rate per segment R_{SK}/N over the number of repeaters and total distance for swapping errors $\epsilon = 10^{-3}, 10^{-2}$ and number of auxiliary Rb memory atoms $N_{mRb} = 1, 5, 10$. The value in the heatmaps are $\log_{10}(R_{SK}/N)$, hence "-inf" meaning $-\infty$ means $R_{SK} = 0$ and the gray entries (NaN) are not calculated. The red underlines in the heatmaps identify the maximum secret key rate per segment for each total distance, determining the optimum number of repeaters.

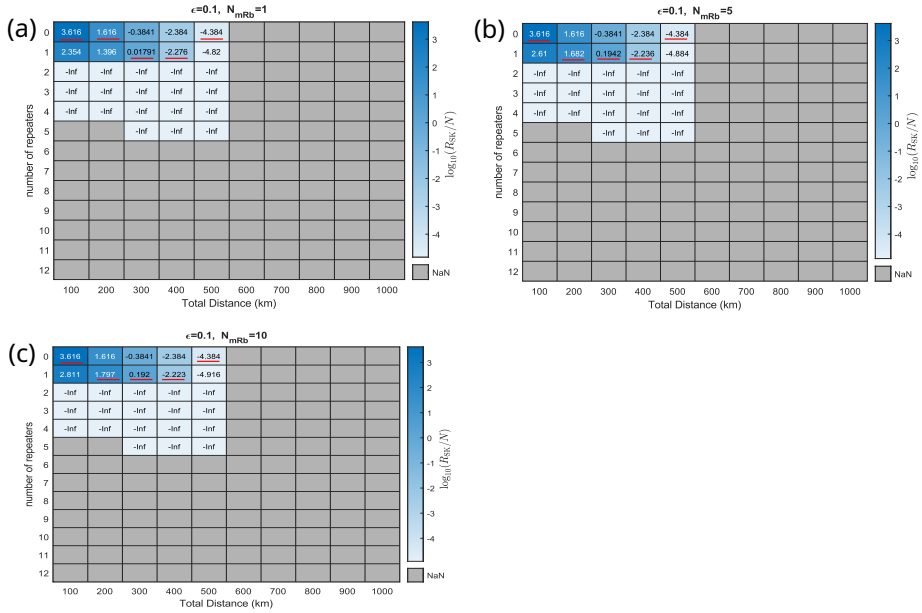

Figure C.5.: Scanning of the secret key rate per segment R_{SK}/N over the number of repeaters and total distance for swapping errors $\epsilon = 10^{-1}$ and number of auxiliary Rb memory atoms $N_{mRb} = 1, 5, 10$. The value in the heatmaps are $\log_{10}(R_{SK}/N)$, hence "-inf" meaning $-\infty$ means $R_{SK} = 0$ and the gray entries (NaN) are not calculated. The red underlines in the heatmaps identify the maximum secret key rate per segment for each total distance, determining the optimum number of repeaters.

c.5. OPTIMIZED NUMBER OF REPEATERS

The scanning of the secret key rate per segment R_{SK}/N over the number of repeaters and total distance is shown in Fig. C.4($\epsilon = 10^{-3}$ and $\epsilon = 10^{-2}$) and C.5($\epsilon = 10^{-1}$).

REFERENCES

[1] F. Gu. *Codes underlying the publication: "Hybrid Quantum Repeaters with Ensemble-based Quantum Memories and Single-spin Photon Transducers"*. 2024.

[2] Q. Quan and M. Loncar. “Deterministic design of wavelength scale, ultra-high Q photonic crystal nanobeam cavities”. In: *J. Opt. Soc. Am. A* 424 (9 2003), pp. 435–441.

[3] J. D. Thompson, T. G. Tiecke, N. P. de Leon, J. Feist, A. V. Akimov, M. Gullans, A. S. Zibrov, V. Vuletić, and M. D. Lukin. “Coupling a Single Trapped Atom to a Nanoscale Optical Cavity”. In: *Science* 340 (6137 June 2013), pp. 1202–1205.

[4] S. G. Menon, N. Glachman, M. Pompili, A. Dibos, and H. Bernien. “An integrated atom array-nanophotonic chip platform with background-free imaging”. In: *arXiv:2311.02153* (2023).

[5] A. Goban, C.-L. Hung, S.-P. Yu, J. Hood, J. Muniz, J. Lee, M. Martin, A. McClung, K. Choi, D. Chang, O. Painter, and H. Kimble. “Atom–light interactions in photonic crystals”. In: *Nature Communications 2014 5:1* 5 (1 May 2014), pp. 1–9.

[6] H. R. Philipp. “Optical Properties of Silicon Nitride”. In: *Journal of The Electrochemical Society* 120 (2 Feb. 1973), p. 295.

[7] S. G. Menon, K. Singh, J. Borregaard, and H. Bernien. “Nanophotonic quantum network node with neutral atoms and an integrated telecom interface”. In: *New Journal of Physics* 22.7 (2020), p. 073033.

ACKNOWLEDGEMENTS

I would like to express my sincere gratitude to my daily supervisor, Johannes Borregaard, for his continuous guidance and support throughout my PhD, in particular for the insightful weekly meetings that greatly shaped my research. I am also deeply grateful to Ronald Hanson for overseeing my research direction and PhD progress, and for providing an outstanding scientific environment in which this work could develop.

I would like to thank Viatcheslav Dobrovitski for his valuable guidance and discussions on the project concerning Group-IV vacancy centers in diamond, which form an important part of the foundation of this thesis.

Furthermore, I sincerely thank Simon Groeblacher, Yaroslav Blanter, Miriam Blaauboer Nicolaj Thomas Zinner, and Tim Taminiau for assessing my thesis and for serving as members of my PhD defense committee.

Finally, I would like to thank the myriad of my friends and family for their constant encouragement, life advice, and emotional support throughout this journey.

CURRICULUM VITæ

Fenglei Gu

29-07-1992 Born in Huazhou, P. R. China

EDUCATION

2020–present Ph.D. in Quantum Technologies
QuTech, Delft University of Technology, Delft, Netherlands
Thesis: Spin-photon interfaces Enabled by Group-IV-Vacancy Color Centers in Diamond and Single Rubidium Atoms
Promotor: Prof. dr. R. Hanson
Co-Promotor: Dr. V. V. Dobrovitski
External supervisor: Dr. J. Borregaard

2015–2018 M.Sc. in Atomic and molecular physics
South China Normal University, Guangzhou, P. R. China
Thesis: Holonomic Quantum Computation and Quantum Simulation Based on Dressed States
Supervisor: Dr. Zhengyuan Xue
Co-Supervisor: Dr. Danwei Zhang

2011–2015 B.Sc. in Physics
Shenzhen University, Shenzhen, P. R. China
Thesis: Light-controlled electrical Transportation Properties of Single-layer MoS2 Field Effect Transistor
Supervisor: Yunjin Yu

AWARDS

2023 Netherlands Quantum Delta Research Visitor Funding

LIST OF PUBLICATIONS

6. The Group-IV-Vacancy Color Centers in Diamond
   Fenglei Gu
   arXiv: 2509.00443

5. Hybrid Quantum Repeater Chains with Semiconductor Quantum Dots and Group-IV Color Centers in Diamond
   Yannick Strocka*, **Fenglei Gu***, Gregor Pieplow, Johannes Borregaard, Tim Schröder
   arXiv: 2511.02472

4. Modular Architectures and Entanglement Schemes for Error-Corrected Distributed Quantum Computation
   Siddhant Singh*, **Fenglei Gu***, Sebastian de Bone, Eduardo Villase, David Elkouss, Johannes Borregaard
   npj Quantum Information

3. Hybrid Quantum Repeaters with Ensemble-based Quantum Memories and Single-spin Photon Transducers
   Fenglei Gu, Shankar G Menon, David Maier, Antariksha Das, Tanmoy Chakraborty, Wolfgang Tittel, Hannes Bernien, Johannes Borregaard
   npj Quantum Information

2. Synthetic spin-orbit coupling and topological polaritons in Janeys-Cummings lattices
   Fenglei Gu, Jia Liu, Feng Mei, Suotang Jia, Danwei Zhang, Zhengyuan Xue
   npj Quantum Information

1. Nonadiabatic Holonomic Quantum Computation with Dressed-State Qubits
   Zhengyuan Xue, **Fenglei Gu**, Zhuoping Hong, Zihe Yang, Danwei Zhang, Yong Hu, Jianqiang You
   Physical Review Applied

*These authors contributed equally to the corresponding pieces of work.

ISBN/EAN: 978-94-6518-256-8